University of Alberta

Approaches to Modelling the Mass Balance of High Arctic Glaciers

by

Anthony Alan Arendt

A thesis submitted to the Faculty of Graduate Studies and Research in partial fulfillment

of the requirements for the degree of Master of Science

Department of Earth and Atmospheric Sciences

Edmonton, Alberta

Fall 1997

National Library of Canada
Acquisitions and Bibliographic Services
395 Wellington Street
Ottawa ON K1A 0N4
Canada

Bibliothèque nationale du Canada
Acquisitions et services bibliographiques
395, rue Wellington
Ottawa ON K1A 0N4
Canada

Your file Votre référence

Our file Notre référence

The author has granted a non-exclusive licence allowing the National Library of Canada to reproduce, loan, distribute or sell copies of this thesis in microform, paper or electronic formats.

L'auteur a accordé une licence non exclusive permettant à la Bibliothèque nationale du Canada de reproduire, prêter, distribuer ou vendre des copies de cette thèse sous la forme de microfiche/film, de reproduction sur papier ou sur format électronique.

The author retains ownership of the copyright in this thesis. Neither the thesis nor substantial extracts from it may be printed or otherwise reproduced without the author's permission.

L'auteur conserve la propriété du droit d'auteur qui protège cette thèse. Ni la thèse ni des extraits substantiels de celle-ci ne doivent être imprimés ou autrement reproduits sans son autorisation.

0-612-22565-8

Canada

University of Alberta

Library Release Form

Name of Author: Anthony Alan Arendt

Title of Thesis: Approaches to Modelling the Mass Balance of High Arctic Glaciers

Degree: Master of Science

Year this Degree Granted: 1997

Permission is hereby granted to the University of Alberta Library to reproduce single copies of this thesis and to lend or sell such copies for private, scholarly, or scientific research purposes only.

The author reserves all other publication and other rights in association with the copyright in the thesis, and except as hereinbefore provided, neither the thesis nor any substantial portion thereof may be printed or otherwise reproduced in any material form whatever without the author's prior written permission.

11036 - 85 Avenue
Edmonton, Alberta
T6G 0W6
Canada

October 3, 1997

University of Alberta

Faculty of Graduate Studies and Research

The undersigned certify that they have read, and recommend to the Faculty of Graduate Studies and Research for acceptance, a thesis entitled Approaches to Modelling the Mass Balance of High Arctic Glaciers submitted by Anthony Alan Arendt in partial fulfillment of the requirements for the degree of Master of Science.

Dr. M. J. Sharp

Dr. J. Wilson

Dr. Andrew Bush

Dr. Thian Y. Gan

Dr. E.L. Jackson

Date: October 3, 1997

Dedication

This thesis is dedicated to the memory of Paul M. Wolfe, whose kindness and friendship will not be forgotten.

Abstract

Comparisons are made between degree-day and energy balance model simulations for John Evans Glacier (79°40'N 74°00'W), Ellesmere Island, Nunavut, Canada. The average specific mass balance of John Evans Glacier from 1996 to 1997 was 0.016 m WE from energy balance model predictions, and 0.13 m WE from degree-day model predictions, compared with 0.15 m WE from ablation stake measurements. A physically-based surface albedo routine is developed which is driven by variations in the solar zenith angle and snow grain size, and is highly sensitive to prescribed values of surface slope and azimuth. A physically-based superimposed ice formation routine, based on heat flux calculations at the snow-ice interface, is shown to produce the best predictions of measured superimposed ice thickness and ice temperatures. For degree-day model simulations, a method of determining positive degree-day factor variations through the melt season is developed. This method relates empirically predicted effective snow grain radii to positive degree-day factors for snow.

Acknowledgements

I would like to thank my supervisor Dr. Martin Sharp for his encouragement and guidance over the years. Martin's untiring support has truly helped me realize my potential as a student. Thanks to Dr. John Wilson, Dr. Thian Gan, Dr. Andy Bush, and Dr. Ed Jackson for their input and guidance as members of my thesis committee. Thanks also to Dr. John England for cultivating my initial interest in Arctic research, to Dr. Stephen Warren, Rachel Jordan and Dr. Tom Grenfell for help with the albedo paper, and to Dr. Ian Willis for the opportunity to work with him at the University of Washington.

Special thanks to Christina MacIsaac for her help during the 1996 field season. Christina's positive attitude and ceaseless enthusiasm, even during the roughest of field conditions, made my research so much easier. Thanks also to Mark Skidmore and Rick Young for their invaluable assistance in the field.

I appreciate the help of Craig Coburn, who solved any computer problem I could possibly send his way. Darren Sjogren also helped me with the DEM, and Scott Lamoureux provided assistance with statistics. Thanks to Brian Crenna for help with mathematics and programming. Terry Thompson provided much help with field instrumentation, and Claude Labine helped with the design of the weather stations. Thanks to Randy Pakan and Michael Fisher for their assistance with figures and slides.

Financial support for the M.Sc. was provided by a scholarship from the Natural Sciences and Engineering Research Council of Canada. Field research was supported by a grant from the Canadian Circumpolar Institute, the Northern Scientific Training Program, the Geological Society of America and from an AES subvision grant and an NSERC grant to Dr. Martin Sharp. Logistical support in the field was provided by the Polar Continental Shelf Project, Department of Energy, Mines and Resources. The fieldwork was carried out with the kind permission of the Science Institute of the Northwest Territories, and the peoples of Resolute Bay and Grise Fiord.

I am fortunate to be surrounded by so many good friends. Thanks to Tom, Andy, Liang, Maria, Skids, Danielle, Luke, Nigel, Claire, Mandy, Scott, Shul and Rod. Special thanks to Wendy Davis for her friendship and support, especially during the final weeks of writing.

Finally, I would like to say thank-you to my family for their love and encouragement through the years.

Table of Contents

Chapter 1: Introduction 1

1.1 Background 1

1.2 Thesis Aims 2

1.3 Study Area 3

1.31 Site Description 3

1.32 Local Climate 3

1.33 Rationale for Site Selection 4

1.4 Outline of Thesis Objectives 4

1.5 Wider Implications of the Study 6

1.6 Outline of the Thesis 6

1.7 References 14

Chapter 2: Development and Testing of an Albedo Algorithm for High Arctic Glaciers

2.1 Introduction 16

2.2 Study Area 20

2.21 Site Description 20

2.22 Local Climate 20

2.3 Physical Controls on Snow Albedo 20

Spectral Composition of Solar Radiation 21

Solar Zenith Angle 21

Snow Grain Radius 22

Liquid Water Content 22

Concentration of Absorbing Impurities 22

Snowpack Thickness 22

2.31 Effects of Surface Slope on Albedo 23

2.4 Model Summaries 23

2.41 SNTHERM Model Description 23

2.42 SNTHERM_Albedo Algorithm 24

Diffuse Albedo 25
Direct Beam Albedo corrected for Zenith Angle 25
Combination of Diffuse and Direct Beam Components 26
All-wavelength Albedo 28
2.43 W-O Albedo Algorithm 29
2.5 Methods 29
2.51 Meteorological Data 29
2.52 Slope Corrections 30
2.53 Corrections to Measured Albedo Data 31
2.54 Potential Sources of Error 31
2.6 Measured Albedo 31
Middle Weather Station 31
Lower Weather Station 33
Upper Weather Station 33
2.7 Testing of the 2 Existing Albedo Algorithms 33
W-O Algorithm 33
SNTHERM_Albedo Algorithm 34
2.8 Development and Testing of a Combined Surface Albedo Algorithm (EBM_Albedo) 35
2.81 Correcting Albedo for a Sloping Surface 36
2.82 Optimization of Grain Sizes at each of the AWS's 36
2.83 Grain Growth Algorithm 38
2.84 Testing of the GrainSize Algorithm and Addition of New Equations 41
2.85 Albedo Predictions using EBM_Albedo at each of the Weather Stations 44
2.9 Testing of EBM_Albedo for Surface Energy Balance Calculations 46
2.10 Comparison with other studies and Implications for Glacier Mass Balance in the Arctic 47
2.11Conclusion 48

2.12 References 78

Chapter 3: Development and Testing of Superimposed Ice Formation Algorithms for High Arctic Glaciers81

3.1 Introduction 81

3.2 Study Area 84

3.21 Site Description 84

3.22 Local Climate 84

3.3 Model Descriptions 85

3.31 Physically-Based Superimposed Ice Algorithm #1 (Algorithm SI-P1) 85

3.32 Physically-Based Superimposed Ice Algorithm #2 (Algorithm SI-P2) 88

3.33 Empirical Superimposed Ice Algorithm (Algorithm SI-E) 91

3.4 Meteorological Data 91

Ice Temperature Measurements 92

Superimposed Ice Thickness 93

3.5 Results 93

3.51 Near-Surface Ice Temperatures 93

3.52 Wetting Front Migration 93

3.6 Testing of Superimposed Ice Algorithms 94

3.61 Testing of SI-P1 95

3.62 Comparison of Predicted and Measured Superimposed Ice Thickness at the M-AWS 95

3.7 Conclusion 98

3.8 References 115

Chapter 4: Development and Testing of a Surface Energy Balance Model for a High Arctic Glacier 117

4.1 Introduction 117

4.2 Study Area 119

4.21 Site Description 119

4.22 Local Climate 120

4.3 Model Description 120

4.31 Shortwave radiation 121

4.32 Longwave radiation 123

4.33 Turbulent heat fluxes 123

Roughness Length Parameterization 125

4.4 Meteorological Data 126

4.5 Elevation Data 127

4.51The Digital Elevation Model 127

4.52 GPS Data 129

4.53 Initial Snow Depth Data 130

4.54 Ablation Stake Data 131

4.55 Lapse Rates in Meteorological Measurements 132

Air Temperature 132

Other Meteorological Measurements 132

4.6 Observations and Discussion 133

4.61 Variations in Meteorological Measurements and Turbulent Fluxes 133

4.62 Spatial and Temporal Variations in Surface Albedo 134

4.63 Spatial and Temporal Variations in Surface Melt 135

Modelled Surface Melt for the Entire Glacier 137

Facies Zones at the End of the Melt Season 137

Comparison of EBM-96 and EBM-94 138

4.7 Comparison with other Studies 139
4.8 Conclusion 139
4.9 References 174

Chapter 5: Mass Balance Simulations using a Degree-Day Model for a High Arctic Glacier 177
5.1Introduction 177
5.2 Study Area 180
5.21 Site Description 180
5.22 Local Climate 180
5.3 Model Summary 181
5.31 Calculation of Air Temperature 181
5.32 Positive Degree-Days 181
5.33 Calculation of Degree-Day Factors 182
5.34 Snow and Ice Melt Algorithm 182
5.4 Meteorological Data 183
5.5 Results and Discussion 183
5.51 Air Temperature Measurements 183
5.52 Correction to Alert Air Temperature Data 184
5.53 Temperature Prediction using Cosine Function 185
5.54 Positive Degree-Days 185
5.55 Average Degree-Day Factors at the 3 Weather Stations 186
5.56 Spatial and Temporal Variations in Predicted Degree-Day Factors 187
5.57 Comparison of Degree-Day and Energy Balance Model Simulations for the 3 Weather Station Sites 189
5.58 Comparison of Degree-Day Simulations for John Evans Glacier 190
5.59 Comparison with Energy Balance Model 192
5.6 Comparison with other Studies 192
5.7 Conclusions 194

5.8 References 215

Chapter 6: General Discussion and Conclusions 217

6.1 Surface Energy Balance Models for High Arctic Glaciers 217

6.2 Degree-Day Models for High Arctic Glaciers 217

6.3 Wider Implications 218

6.4 Suggestions for Future Work 218

6.41 Surface Albedo 218

6.42 Superimposed Ice Formation 219

6.43 Surface Energy Balance Modelling 219

6.44 Degree-Day Modelling 220

6.45 Model Validation 220

6.5 References 222

LIST OF TABLES

Chapter 2

Table 2.1	Location and elevation of each automated weather station.	50
Table 2.2	Specifications of meteorological instruments.	51
Table 2.3	Periods of instrumental record at each of the 3 automated weather station sites.	52
Table 2.4	Comparison of manual and GPS methods for determining surface slope and azimuth.	52
Table 2.5	Average grain radii at the L-AWS determined from optimized grain sizes.	52
Table 2.6	Statistical attributes for model runs #1 to #3 (showing steps in the development of the EBM_Albedo algorithm) at each of the weather station sites.	53
Table 2.7	Statistical data for model runs testing the effect of changes in the initial snow depth on albedo predictions at the L-AWS.	54
Table 2.8	Description of albedo parameterizations used for each of the energy balance model simulations.	54
Table 2.9	Statistical data for model runs testing melt predictions at each of the weather station sites using different albedo parameterizations.	55

Chapter 3

Table 3.1	Location and elevation of each automated weather station.	100
Table 3.2	Specifications of meteorological instruments.	101

Table 3.3	Location of thermocouples used to measure ice or snow temperatures at the start of the measurement period for each AWS.	102
Table 3.4	Periods of instrumental record at each of the 3 automated weather station sites.	102
Table 3.5	Correlation coefficients for ice temperature predictions at the M-AWS and U-AWS.	103

Chapter 4

Table 4.1	Modifications to the surface energy balance model.	141
Table 4.2	Location and elevation of each automated weather station.	141
Table 4.3	Specifications of meteorological instruments.	142
Table 4.4	Periods of instrumental record at each of the 4 automated weather station sites.	142
Table 4.5	Snow water equivalence (SWE) at 3 sites on the glacier, prior to the start of the melt season.	143
Table 4.6	Ablation stakes set up at the start of the 1996 melt season, with associated elevations.	143
Table 4.7	Average lapse rates determined from measured hourly air temperature data on JEG.	144
Table 4.8	Statistical data for model runs testing comparing modelled SWE using the "standard" model run versus measured SWE from UDG data, converted to SWE from SNTHERM density predictions.	144
Table 4.9	Statistical data for model run comparing standard run (EBM-96) and EBM-94 with measured ablation stake data.	145

Table 4.10 Statistical data for model run comparing the old version of the energy balance model (EBM-94) with measured ablation stake data. 145

Chapter 5

Table 5.1 Location and elevation of each automated weather station. 195

Table 5.2 Time periods during which hourly and daily meteorological observations were made at each AWS. 195

Table 5.3 Coefficients of determination and significance levels (p-value) between Alert data and each of the John Evans Glacier weather stations for the period of JD 177 to JD 202. 195

Table 5.4 Analysis of variance table comparing means air temperatures at each of the John Evans Glacier weather stations with mean air temperature at Alert for the period of JD 177 to JD 202. 195

Table 5.5 Average and standard deviation of lapse rates determined from measured hourly air temperatures on John Evans Glacier. 196

Table 5.6 Statistical attributes comparing predicted positive degree-days using remote data with those using local data from the L-AWS for the period of JD 177 - 202. 196

Table 5.7 Average degree-day factors for snow melt at the 3 AWS sites, including coefficients of determination. 197

Table 5.8 Positive degree-day factors for snow ablation on glaciers. 197

Table 5.9 Correlation coefficients and standard errors for the relationship between visible (vis) and near-infrared (nir) effective grain radii as predicted by the EBM, and solved positive degree-day factors at each of the weather stations 197

Table 5.10 Statistical attributes comparing energy balance (EB) and degree-day simulations at the L-AWS for JD 177 - JD 202. 198

Table 5.11	Statistical attributes comparing energy balance (EB) and degree-day simulations at the M-AWS for JD 167 - JD 202.	198
Table 5.12	Statistical attributes comparing energy balance (EB) and degree-day simulations at the U-AWS for JD 172 - JD 210.	199
Table 5.13	List of model simulations run to test the degree-day model against the energy balance model.	199
Table 5.14	Statistical attributes for degree-day simulations compared with observed mass balance data from ablation stakes.	200

LIST OF FIGURES

Chapter 1

Figure 1.1	Map of the Canadian Arctic Islands.	8
Figure 1.2	Location of John Evans Glacier, Ellesmere Island, Nunavut, Canada.	9
Figure 1.3	Contour map of John Evans Glacier with weather station and stake locations.	10
Figure 1.4	Photograph of John Evans Glacier.	11
Figure 1.5	Surface area distribution for John Evans Glacier.	12
Figure 1.6	Temperature and precipitation records from AES meteorological station, Alert.	13

Chapter 2

Figure 2.1	Map of the Canadian Arctic Islands.	56
Figure 2.2	Location of John Evans Glacier, Ellesmere Island, Nunavut, Canada.	57
Figure 2.3	Contour map of John Evans Glacier with weather station and stake locations.	58
Figure 2.4	Surface area distribution for John Evans Glacier.	59
Figure 2.5	Temperature and precipitation records from AES meteorological station, Alert.	60
Figure 2.6	Semi-infinite direct beam albedo as a function of wavelength for various grain radii.	61
Figure 2.7	Schematic diagram of albedo model developed by Marks (1988).	62
Figure 2.8	(a) - Integrated albedo versus cos(z) for direct radiation, visible wavelengths. (b) - Integrated albedo versus cos(z) for direct radiation, near-infrared wavelengths. (c) - Integrated albedo versus square root of grain radius for diffuse albedo, visible wavelengths.	63

(d) - Integrated albedo versus square root of grain radius for diffuse albedo, near-infrared wavelengths.

Figure 2.9 Surface albedo measured at the M-AWS, uncorrected for slope or snowfall events. 64

Figure 2.10 (a) - Measured albedo at the M-AWS corrected for a sloping surface. 65

(b) - Difference between slope corrected and uncorrected albedo values at the M-AWS.

Figure 2.11 (a) - Daily average albedo at the M-AWS, corrected for a sloping surface. 66

(b) - Fractional free water content in the uppermost snow layer at the M-AWS.

(c) - Measured snowpack density at the M-AWS.

(d) - Observed snow characteristics, snow depth and grain radius at the M-AWS.

Figure 2.12 Surface albedo measured at the L-AWS, with both uncorrected and slope-corrected measurements. 67

Figure 2.13 Surface albedo measured at the U-AWS, with both uncorrected and slope-corrected measurements. 68

Figure 2.14 Comparison of measured albedo with Wal and Oerlemans' (1994) albedo parameterization. 69

Figure 2.15 Comparison of measured albedo with predictions from the SNTHERM_Albedo algorithm. 70

Figure 2.16 (a) - Optimized grain radii at the L-AWS. 71

(b) - Optimized grain radii at the M-AWS.

(c) - Optimized grain radii at the U-AWS.

Figure 2.17 Albedo simulations at the L-AWS compared with measured albedo. 72

(a) - Measured albedo corrected for a sloping surface.

(b) - Albedo simulations # 1 and # 2

(c) - Albedo simulation # 3

Figure 2.18 Modelled grain radii at each weather station site using EBM_GrainSize. 73
(a) L-AWS
(b) M-AWS
(c) U-AWS
Figure 2.19 Difference between measured and modelled albedo, using EBM_Albedo algorithm. 74
(a) L-AWS
(b) M-AWS
(c) U-AWS
Figure 2.20 Comparison of measured albedo corrected for a sloping surface and modelled albedo. 75
(a) M-AWS
(b) U-AWS
Figure 2.21 Comparison of EBM_Albedo predictions for different initial snow depths at the L-AWS. 76
Figure 2.22 Comparison of measured and modelled snow water equivalence using different albedo algorithms. 77
(a) L-AWS
(b) M-AWS
(c) U-AWS

Chapter 3

Figure 3.1	Schematic development of the near surface temperature profile during the early melt season.	104
Figure 3.2	Map of the Canadian Arctic Islands.	105
Figure 3.3	Location of John Evans Glacier, Ellesmere Island, Nunavut, Canada.	106
Figure 3.4	Contour map of John Evans Glacier with weather station and stake locations.	107
Figure 3.5	Surface area distribution for John Evans Glacier.	108
Figure 3.6	Temperature and precipitation records from AES meteorological station, Alert.	109
Figure 3.7	Measured ice temperatures. (a) M-AWS (b) U-AWS	110
Figure 3.8	SNTHERM predicted wetting front depths. (a) M-AWS (b) U-AWS	111
Figure 3.9	Observed snowpack stratigraphy. (a) JD 181, M-AWS. (b) JD 185, U-AWS.	112
Figure 3.10	Measured and predicted near surface ice temperatures. (a) M-AWS (b) U-AWS	113
Figure 3.11	Comparison of predicted and measured superimposed ice depths at the M-AWS. (a) Start day for superimposed ice formation = JD 167. (b) Start day for superimposed ice formation = JD 182.	114

Chapter 4

Figure 4.1	Map of the Canadian Arctic Islands.	146
Figure 4.2	Location of John Evans Glacier, Ellesmere Island, NWT, Canada.	147
Figure 4.3	Contour map of John Evans Glacier with weather station and stake locations.	148
Figure 4.4	3-dimensional model of John Evans Glacier.	149
Figure 4.5	Photograph of John Evans Glacier.	150
Figure 4.6	Surface area distribution for John Evans Glacier.	151
Figure 4.7	Temperature and precipitation records from AES meteorological station, Alert.	152
Figure 4.8	Photograph of main mast at the M-AWS.	153
Figure 4.9	Photograph of the UDG and net radiometer mast at the U-AWS.	154
Figure 4.10	Daily Average meteorological measurements at the L-AWS.	155,
	(a) Net radiation	156
	(b) Shortwave radiation	
	(c) Wind direction	
	(d) Maximum, minimum and average air temperature	
	(e) Relative humidity	
	(f) Windspeed	
Figure 4.11	Daily Average meteorological measurements at the M-AWS.	157,
	(a) Net radiation	158
	(b) Shortwave radiation	
	(c) Wind direction	
	(d) Maximum, minimum and average air temperature	
	(e) Relative humidity	
	(f) Windspeed	
Figure 4.12	Daily Average meteorological measurements at the U-AWS.	159,
	(a) Net radiation	160

(b) Shortwave radiation
(c) Wind direction
(d) Maximum, minimum and average air temperature
(e) Relative humidity
(f) Windspeed

Figure 4.13 Cloud cover observations in tenths. 161

Figure 4.14 Daily average lapse rates ($°Cm^{-1}$) between the 3 automated weather stations. 162

Figure 4.15 Daily averages of net longwave, shortwave, latent and sensible heat fluxes. 163
(a) L-AWS
(b) M-AWS
(c) U-AWS

Figure 4.16 Partitioning of total melt energy. 164
(a) L-AWS
(b) M-AWS
(c) U-AWS

Figure 4.17 z/L variations using the bulk transfer technique in turbulent flow. 165
(a) L-AWS
(b) M-AWS
(c) U-AWS

Figure 4.18 Variations in surface albedo on JD 167. 166
(a) 0000 hrs.
(b) 1200 hrs.

Figure 4.19 Variations in surface albedo on JD 195. 167
(a) 0000 hrs.
(b) 1200 hrs.

Figure 4.20 Seasonal variations in surface albedo. 168

Figure 4.21 Seasonal variations in surface melt. 169

Figure 4.22 Facies zones across the glacier at the end of the melt season. 170

(a) Superimposed ice remaining at the end of the season.
Snow remaining at the end of the season.
Figure 4.23 Comparison of measured and SNTHERM predicted total snowpack density. 171
Figure 4.24 Comparison of modelled versus measured snow ablation. 172
(a) L-AWS
(b) M-AWS
(c) U-AWS
Figure 4.25 Predicted specific mass balance compared with measured mass balance from the ablation stake network. 173

Chapter 5

Figure 5.1	Map of the Canadian Arctic Islands.	201
Figure 5.2	Location of John Evans Glacier, Ellesmere Island, NWT, Canada.	202
Figure 5.3	Contour map of John Evans Glacier with weather station and stake locations.	203
Figure 5.4	Surface area distribution for John Evans Glacier.	204
Figure 5.5	Temperature and precipitation records from AES meteorological station, Alert.	205
Figure 5.6	Average hourly air temperature measurements. (a) Alert weather station (b) L-AWS (c) M-AWS (d) U-AWS	206
Figure 5.7	Comparison of predicted daily air temperature using cosine function and measured daily air temperature at Alert weather station.	207
Figure 5.8	Measured and predicted positive degree-days at the L-AWS.	208
Figure 5.9	Total daily ablation for snow versus positive degree-days.	209
Figure 5.10	(a) Predicted positive degree-day factors for snow at the 3 weather stations. (b) Predicted effective grain radii at the 3 weather stations.	210
Figure 5.11	Effective visible and near-infrared grain radii versus predicted positive degree-day factors for snow.	211
Figure 5.12	Comparison of degree-day model simulations at each of the weather station sites. (a) L-AWS (b) M-AWS (c) U-AWS	212
Figure 5.13	Comparison of specific mass balance predictions from degree-day	213

calculations with measured mass balance from ablation stakes.
(a) Degree-day simulations with local (John Evans Glacier) air temperature data.
(b) Degree-day simulations with remote (Alert) air temperature data, modelled with TCA equation.
(c) Degree-day simulations with local (Alert) air temperature data.

Figure 5.14 Average specific mass balance for various degree-day model simulations. 214

List of Symbols

$I_{s,diffuse}\downarrow(Z)$	diffuse radiation incident on the surface of the earth
$I_{s,direct}\downarrow(Z)$	direct radiation incident on the surface of the earth
σ_{surf}	surface slope aspect
$K\downarrow_{N,DIR}$	direct beam radiation received by a surface normal to the sun's rays
$K\downarrow_{DIR,SLOPE}$	incoming solar radiation on a sloping surface
$\overline{T}_C$	mean absolute air temperature in the surface layer
$\sum B_n$	net balance summed over all cells in elevation band
φ	solar azimuth
ρ	air density
ϕ	phase angle
π	pi
$\alpha^0_{vis,direct}$	modelled albedo for a horizontal surface
$\alpha_{a\text{-}w}$	all-wave albedo
ρ_{ice}	density of ice
κ_{nir}	near-infrared slope coefficients for albedo decay with grain size
$\lambda_{nir,\theta}$	near-infrared offset coefficient
$\kappa_{nir,\theta}$	near-infrared slope coefficients
$\alpha_{nir,diffuse}$	near-infrared albedo when the incident radiation is entirely diffuse
$\alpha_{nir,direct}$	near-infrared direct beam albedos
$\alpha_{nir,max}$	maximum near-infrared albedos
ρ_{si}	density of superimposed ice
θ_{surf}	surface slope angle
κ_{vis}	visible slope coefficients for albedo decay with grain size
$\kappa_{vis,\theta}$	visible slope coefficients
$\alpha_{vis,diffuse}$	visible albedo when the incident radiation is entirely diffuse
$\alpha_{vis,direct}$	modelled albedo corrected for slope

$\alpha_{vis,direct}$	visible direct beam albedos
$\alpha_{vis,max}$	maximum visible albedos
ρ_{ws}	density wet snow
θ_z	solar zenith angle
A	absorptivity
A_d	number of days
ADMT	accumulated daily maximum temperatures since snowfall
a_M	stability correction constant
$Area$	Area of elevation band
β	slope angle from the horizontal
B_{sp}	Specific mass balance
cl	fractional sky clearness
c_p	specific heat capacity of air at a constant pressure
c_{tm}	contamination factor
cv	fractional cloud cover
DDF	positive degree-day factor
ecv_2	effective cloud cover for middle sky layer
ecv_3	effective cloud cover for upper sky layer
$elev$	elevation above sea level in meters
e_a	vapour pressure at the surface
e_z	vapour pressure at height z above the surface
$f_{diffuse}$	fraction of diffuse to direct beam radiation
f_{vis}	fraction of radiation in the visible band
g	acceleration due to gravity
I_{s00}	solar insolation at the top of the atmosphere
j	index numbers for insolation routine in ascending order from the air interface
k	von Karman constant

K^*	net shortwave radiation flux
K^*_{MEAS}	measured net shortwave radiation flux
$K\downarrow$	flux of incoming shortwave radiation
$K\downarrow_{DIF}$	diffuse incoming solar radiation
$K\downarrow_{DIR}$	direct beam incoming solar radiation
K_{ice}	thermal conductivity of ice
L	Monin-Obukhov length scale
$L\uparrow$	outgoing longwave radiation
L^*	net longwave radiation flux
$L\downarrow$	incoming longwave radiation
L_{ice}	latent heat of fusion of ice
L_v	latent heat of vapourization
M	water equivalent snow or ice melt
N	number of horizontally infinite plane-parallel layers in insolation routine
P	atmospheric pressure
PDD	positive degree-days
$P_{M\text{-}AWS}$	atmospheric pressure at the middle automated weather station
Pmax	maximum percent of initial snow water equivalence which forms as superimposed ice
Q^*	net allwave radiation flux
Q^*_{MEAS}	measured net allwave radiation flux
Q_E	latent heat flux
Q_G	conductive heat flux
Q_H	sensible heat flux
Q_M	melt energy flux
R	atmospheric reflectivity
r	snow grain radius
R_a	gas constant for dry air
r_{gl}	effective grain radius for glacier ice

r_{max}	maximum grain growth radius
$r_{rg,nir}$	expected growth range for near-infrared effective grain size
$r_{rg,vis}$	expected growth range for visible effective grain size
r_{nir}	effective near-infrared grain size
$r_{nir(0)}$	initial near-infrared effective grain size after a snowfall event
r_{si}	effective grain radis for superimposed ice
r_{vis}	effective visible grain size
$r_{vis(0)}$	initial visible effective grain size after a snowfall event
s	standard deviation
SI	depth of superimposed ice
SI_{max}	maximum depth of superimposed ice
T	apparent atmospheric transmissivity
t	time since last snowfall
T_0	ice temperature at a place sufficiently deep that it remains constant
TCA	mean daily air temperature
T_d	transmissivity for direct beam radation
t_d	time in days for water to completely drain from the surface
TJA	mean July air temperature
$T_{M\text{-}AWS}$	air temperature at the middle automated weather station
TMA	mean annual air temperature
t_{max}	time for maximum grain growth to occur
T_Z	cell temperature at height z
u	wind speed
u^*	friction velocity
w_0	liquid water at the surface for the previous timestep
w_l	fractional amount of liquid water at the surface
X	water equivalent thickness of superimposed ice
X_{NEW}	superimposed ice depth at the new timestep
X_{OLD}	superimposed ice depth at the old timestep

Z	snowdepth relative to the ground
z	sensor height above snow or ice surface
z_{oi}	surface roughness length for ice
z_{os}	surface roughness length for snow

CHAPTER 1: Introduction

1.1 Background

Surface energy balance and degree-day melt models have been used extensively to predict the mass balance of polar glaciers and ice sheets. These models are based upon known relationships between meteorological conditions and associated melting or accumulation of snow or ice at the glacier surface. Such modelling is useful because: (1) it provides a means of predicting the mass balance of arctic glaciers without the need for expensive fieldwork; (2) the mass balance of remote, inaccessible glaciers may be modelled if meteorological data are unavailable for these areas; and (3) the past or future mass balance of a glacier may be predicted by running the model backward or forward in time. A prediction of future mass balance responses to climate is especially important, given the fact that most general circulation models predict that greenhouse-gas induced climate change will be most pronounced at high polar latitudes, especially in winter (Hansen *et al.*, 1981; Cao *et al.*, 1992; Manabe *et al.*, 1992; McGinnis and Crane, 1994; Lynch *et al.*, 1995). It is not certain how such changes may alter the mass balance of high latitude glaciers, but it is possible that increased temperatures in the arctic may increase melt rates and cause a rise in global sea levels.

Energy balance models explicitly simulate the physical energy exchanges responsible for melting of snow or ice. These models require as inputs detailed datasets of the near-surface air temperature, relative humidity, net radiation, and wind speed. Degree-day models are based on the observed relationship between positive air temperature and the melting of snow or ice at the surface of a glacier, and are therefore much simpler and less data-intensive than energy balance models. Positive degree-days determined from air temperature measurements are converted to melt equivalents via degree-day factors which vary with surface conditions. Both of these types of models were originally developed for mid-latitude alpine glaciers, and have only recently been applied to predicting the present day mass balance of high Arctic glaciers and ice sheets, and the likely response of these glaciers and ice sheets to climate change. For the most part, degree-day and energy

balance models developed for mid-latitude glaciers have been adopted for use in the Arctic with very few modifications. This is surprising given that there are numerous differences between alpine and high polar glaciers which introduce complexities into the relationship between glacier mass balance and climate. It is likely that the remoteness of high Arctic glaciers has contributed to the lack of sufficient data to drive and test mass balance models used in the Arctic.

1.2 Thesis Aims

The purpose of this thesis is to improve upon existing energy balance and degree-day models used to simulate the mass balance of John Evans Glacier, Ellesmere Island, Nunavut, Canada. A spatially distributed energy balance model developed for John Evans Glacier has shown that the prediction of the mass balance of the glacier is highly sensitive to changes in the parameterization of superimposed ice formation, topographic shading and surface albedo (Woodward, 1995). A detailed meteorological dataset collected from 3 automated weather stations during the summer of 1996 on John Evans Glacier, together with snow depth and ablation measurements made across the glacier, provide an opportunity to test predictions from various algorithms within Woodward's (1995) model. Such tests identify inaccuracies in the existing parameterization of surface albedo. A physically-based albedo algorithm which is sensitive to diurnal variations in the solar zenith angle and changes in the effective grain size of snow or ice crystals is therefore developed. In addition, measurements of near-surface ice temperatures at 3 locations on John Evans Glacier are used to test an algorithm which simulates changes in the rate of superimposed ice formation based on the vertical gradient in temperature at the snow-ice interface. The modified surface albedo and superimposed ice routines are implemented within a spatially distributed energy balance model, and glacier-wide predictions of mass balance are compared with measured mass balance from ablation stakes located along the centerline of the glacier. The energy balance model is then used in conjunction with a degree-day model to develop a parameterization for positive degree-day factors as a function of surface characteristics.

1.3 Study Area

1.31 Site description

John Evans Glacier is a large valley glacier located at 79°40'N 74°00'W on an unnamed peninsula south of Dobbin Bay, eastern Ellesmere Island, Nunavut, Canada (Figure 1.1-1.4). Its catchment area is 211km^2, of which 47% is glaciated, and spans an altitudinal range of 50 to 1500 m (Figure 1.5). 77% of the ice surface area lies between 600m and 1100m. The catchment comprises a main trunk glacier fed from a number of sub-catchments in the western part of the basin, and 8 small valley glaciers feeding into a marginal lake 3 km from the snout of the main trunk glacier on its eastern side.

1.32 Local Climate

Mean annual and July temperatures recorded over the period 1951-1994 at the AES meteorological station at Alert, north-eastern Ellesmere Island (82°30'N 62°20'W) are shown in Figure 1.6. The mean annual sea level temperature at Alert was -17.8°C. During 1988-89, the average annual air temperature at Alert was -16.9°C. This is similar to the average annual air temperature (-17.3°C) measured for the same period at Allman Bay, located 5km south of John Evans Glacier (Figure 1.2) (G. Henry, *pers comm.*). However, July 1988 temperatures were approximately 3°C warmer at Allman Bay (located at sea level) than at Alert. Field data for the present study were collected during the summer of 1996, which was unusually cold. The mean 1996 July air temperature measured at the lower weather station (elevation 261 m) on John Evans Glacier was approximately 3°C colder than the mean July air temperature at Allman Bay in 1988 (note that some of this difference in temperature may be due to differences in surface type and elevation between Allman Bay and John Evans Glacier). Mean total precipitation from 1 August 1995 to 1 August 1996 at Alert (165.4 mm WE) was 128% higher than the mean annual total precipitation at Alert over the period 1951-1994 (128.5 mm WE).

1.33 Rationale for Site Selection

John Evans Glacier was chosen as the field area for a long term study of Arctic glacier hydrology by researchers in the Department of Earth and Atmospheric Sciences at the University of Alberta. Current research interests include the study of glacier mass balance, hydrology and ice flow dynamics. John Evans Glacier was considered a suitable catchment for an integrated project of this kind because:

1. The glacier margin is terrestrially based. Many of the glaciers on the east coast of Ellesmere Island have tidewater margins, which makes study of subglacial hydrology impossible, and complicates calculations of glacier dynamics and force balance.

2. The catchment is large (211km^2) and is easily defined as a unit, unlike many of the other large glaciers in the area which are fed from the Agassiz and Prince of Wales Ice Caps. The size of the catchment suggests the internal temperature regime may be polythermal (Blatter, 1987), which will control glacier dynamics and allow subglacial drainage.

3. The catchment has a large elevation range, from less than 100m to over 1700m. This is representative of many of the valley glaciers at this latitude.

4. The glacier lies on a precipitation gradient between the North Water polynya and the arid areas of northern Ellesmere Island (Koerner, 1979). The sparsity of previous glacier research on the east coast of Ellesmere Island means that little is known about how the polynya affects glacier mass balance in this area.

1.4 Outline of Thesis Objectives

a) To develop an algorithm which simulates the surface albedo of a high latitude glacier. The algorithm is constructed from 2 existing algorithms. The first is a physically-based algorithm designed to simulate changes in the albedo of dry snow as a function of snow grain size and solar zenith angle (Marshall and Warren, 1987; Marks, 1988; Jordan, 1991). The second is an empirical model developed specifically for the Greenland ice sheet which

incorporates the effect of free water at the surface upon the albedo of snow and ice (van de Wal and Oerlemans, 1994). A combined model is developed which is primarily physically-based, but which incorporates several empirical routines to account for snow and ice grain size variations as a function of the free water content at the surface, and particulate contamination of the snow surface. The new combined albedo model should be an improvement over previous models because it is able to simulate:

1) large diurnal cycles in snow albedo found at high polar latitudes
2) the effect of wet snow conditions, and water at the glacier surface, on albedo
3) changes between the albedos of snow, superimposed ice and glacier ice

b) To test 2 existing algorithms used to predict the maximum quantity of superimposed ice formed at the surface during the melt season. The first is the method described by Woodward (1995) based on the work of Carslaw and Jaeger (1946) and Ward and Orvig (1952), which predicts the maximum thickness of superimposed ice as a function of the ice temperature at a depth of 14 m. The second is a simple empirical method which predicts maximum superimposed ice thickness as a function of the snowpack depth prior to the start of the melt season. A new algorithm is also implemented which simulates the rate of superimposed ice formation based on the vertical gradient in temperature at the snow/ice interface (Carslaw and Jaeger, 1946; Wakahama *et al.*, 1976).

c) To test a surface energy balance model developed by Arnold *et al.* (1996) and modified by Woodward (1995) for the purpose of predicting the mass balance of John Evans Glacier. This model will include the modified albedo and superimposed ice algorithms described in (a) and (b) above. Mass balance predictions from the energy balance model will be compared with measured mass balance from ablation stake measurements made in 1996 and 1997.

d) To test the performance of a degree-day melt model in predicting the mass balance of John Evans Glacier, and to use the surface energy balance model developed in (c) above to improve degree-day simulations. This will be done by comparing predicted ablation from the energy balance model with measured temperatures at select sites across the glacier, in order to predict degree-day factors. Degree-day factors determined in this way will be related to variations in empirically estimated snow grain size, so that degree-day factors can be allowed to vary with changes in surface conditions.

1.5 Wider Implications of the Study

This study develops a number of new approaches to relating meteorological measurements to glacier mass balance in the high Arctic. The surface albedo and superimposed ice algorithms developed in this thesis are physically-based and should therefore be applicable to other glaciers and ice sheets in the Arctic. These algorithms may therefore be of value to other models currently being used to simulate glacier mass balance in the Arctic. Results from this study also point out key areas where future research into mass balance simulation of polar glaciers should be focused. In particular, this study emphasizes the effect of snow and ice crystal size variations on surface albedo (for energy balance models) and degree-day factors (for degree-day models), which has hitherto been largely ignored in mass balance simulations.

1.6 Outline of the Thesis

Chapter 1 has discussed the rationale behind the study, outlining its main objectives. Chapters 2 and 3 describe the development and testing of surface albedo and superimposed ice formation algorithms for high Arctic glaciers. Chapter 4 implements the albedo and superimposed ice routines developed in Chapters 2 and 3 within a spatially distributed surface energy balance model, and compares model simulations with measured mass balance from ablation stakes. Chapter 5 describes the development and testing of a degree-day model for high Arctic glaciers which includes a parameterization of degree-day

factors for snow as a function of snow grain size. Chapter 6 presents the conclusions of the study.

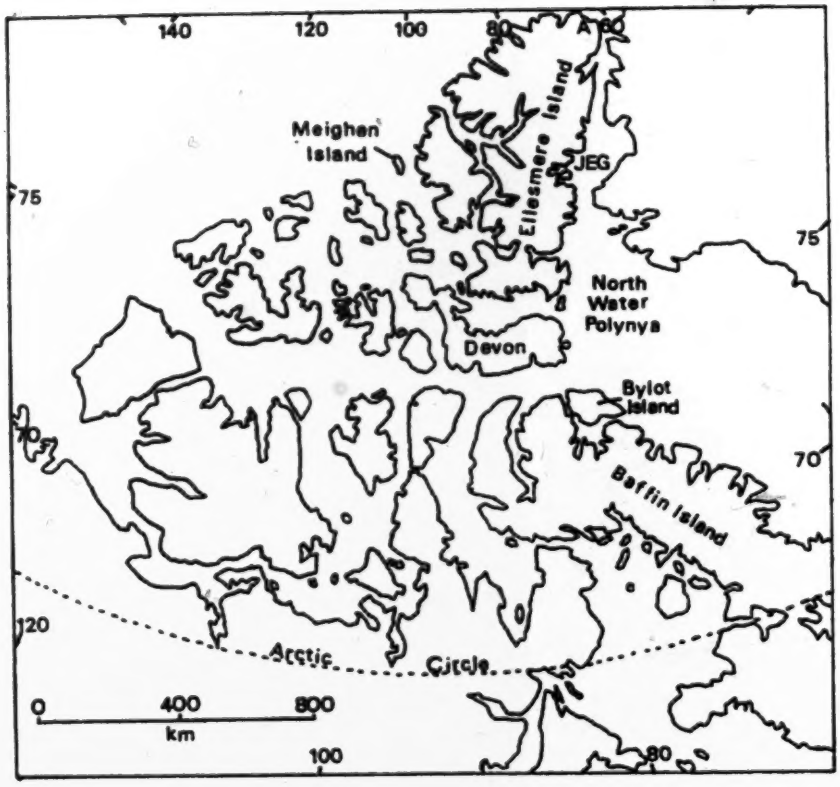

Figure 1.1: The Canadian Arctic Islands. JEG = John Evans Glacier, A = AES Meteorological Station at Alert.

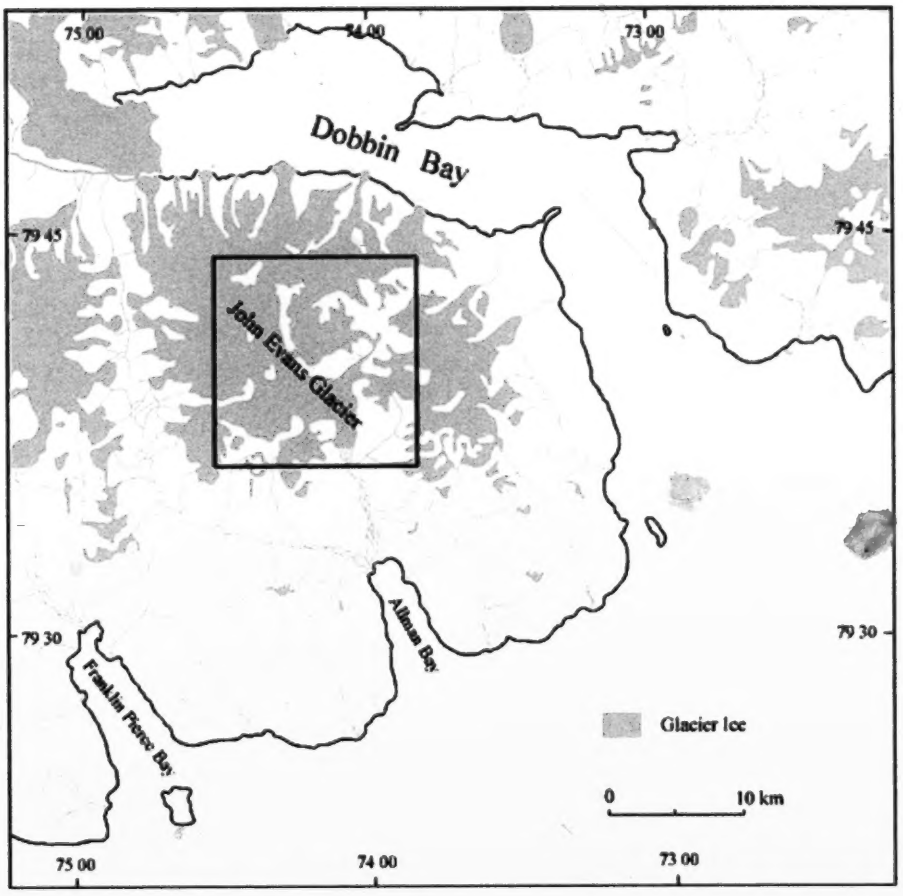

Figure 1.2: Location of John Evans Glacier, Ellesmere Island, Nunavut, Canada.

Figure 1.3: Contour map of John Evans Glacier with locations of lower, middle and upper automated weather stations (marked with arrows) and stake locations (marked with circles).

Figure 1.4: Photograph of John Evans Glacier. "L-AWS" and "M-AWS" show the location of the lower and middle automated weather stations.

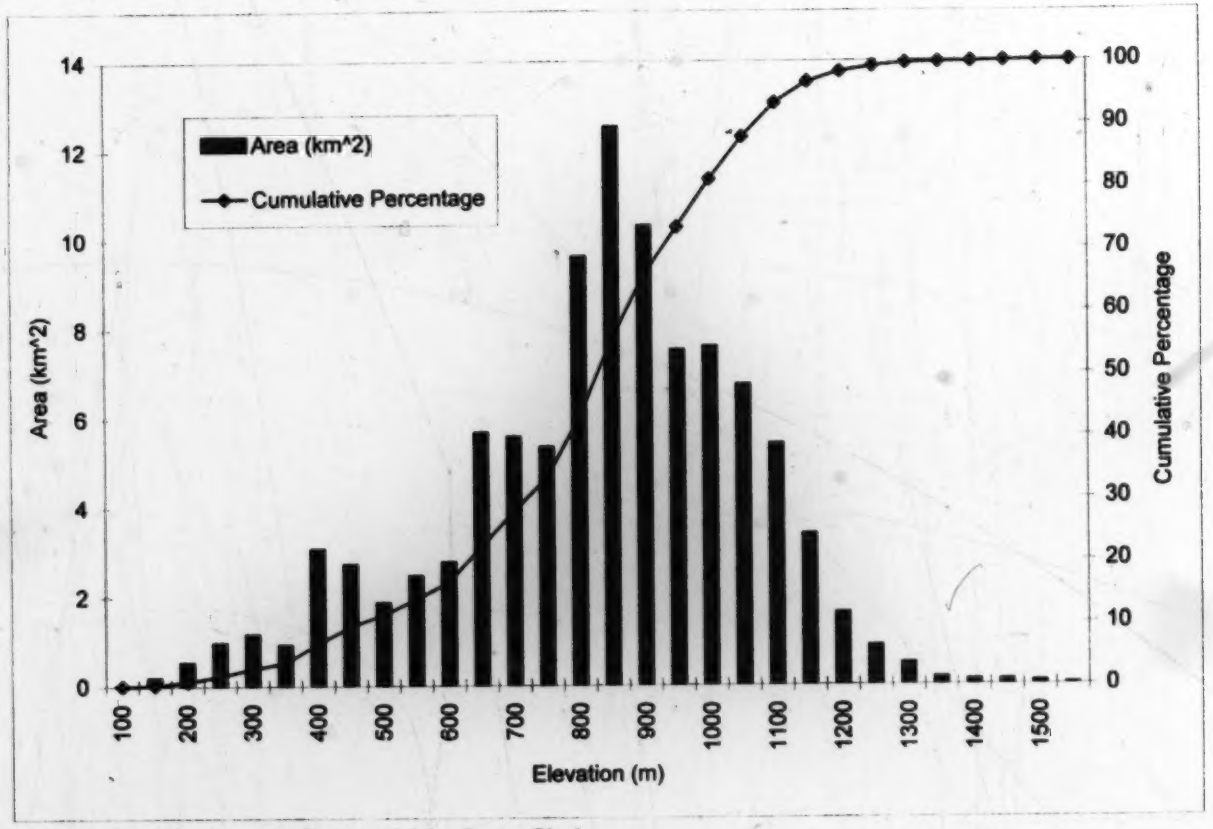

Figure 1.5: Surface area distribution of John Evans Glacier.

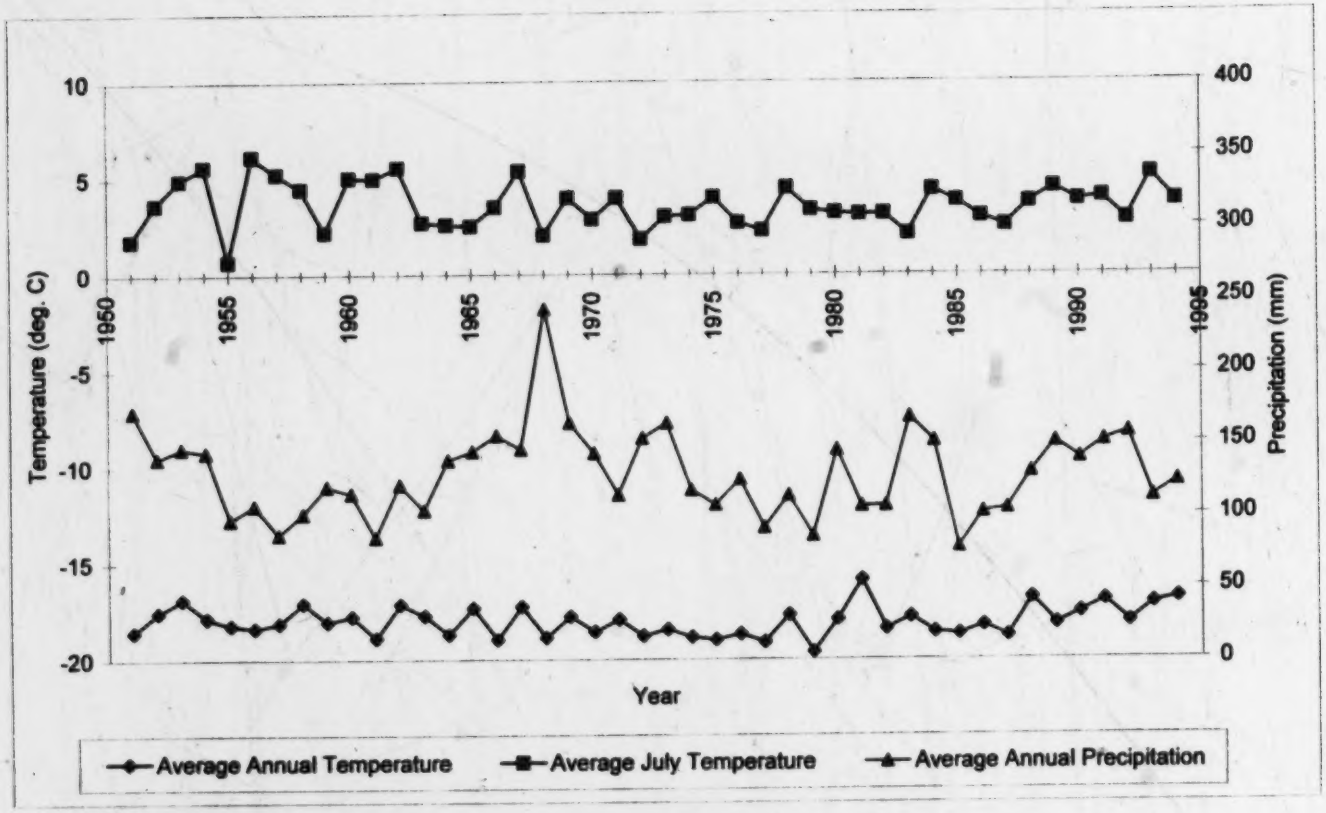

Figure 1.6 Temperature and precipitation records from AES meteorological station, Alert.

1.7 References

Arnold, N.S., Willis, I.C., Sharp, M.J., Richards, K.S. and Lawson, W.J. 1996. A distributed surface energy-balance model for a small valley glacier. I. Development and testing for Haut Glacier d'Arolla, Valais, Switzerland. *Journal of Glaciology*. 42(140): 77-89.

Blatter, H. 1987. On the Thermal Regime of an Arctic Valley Glacier: A Study of White Glacier, Axel Heiberg Island, N.W.T., Canada. *Journal of Glaciology*, 33(114): 200-211.

Carslaw, H.S. and Jaeger, J.C. 1946. Conduction of Heat in Solids. *Oxford University Press*. 510p.

Cao, H.X., Mitchell, J.F.B., and Lavery, J.R. 1992. Simulated Diurnal Range and Variability of Surface Temperature in a Global Climate Model for Present and Doubled CO_2 Climates. *Journal of Climate*, 5: 920-943.

Hansen, J., Johnson, D., Lacis, A., Lebedeff, S., Lee, P., Rind, D., and Russell, G. 1981. Climate Impact of Increasing Atmospheric Carbon Dioxide. *Science*, 213(4511): 957-966.

Jordan, R. 1991. A one-dimensional temperature model for a snow cover. Technical documentation for SNTHERM.89. *Spec. Rep.* 91-16, USA-CRREL, Hanover, NH.

Koerner, R.M. 1979. Accumulation , Ablation, and Oxygen Isotope Variations on the Queen Elizabeth Islands Ice Caps, Canada. *Journal of Glaciology*, 22(86): 25-41.

Lynch, A.H., Chapman, W.L., Walsh, J.E, Weller, G. 1995. Development of a Regional Climate Model of the Western Arctic. *Journal of Climate*, 8: 1555-1570.

Marks, D. 1988. Climate, energy exchange, and snowmelt in Emerald Lake Watershed, Sierra Nevada. *Unpublished Ph.D. Thesis*, University of California at Santa Barbara. 158 p.

Marshall, S.E. and Warren, S.G. 1987. Parameterization of snow albedo for climate models. *In: Large scale effects of seasonal snow cover*. IAHS Publ. no. 166: 43-50.

Manabe, S., Spelman, M.J., and Stouffer, R.J. 1992. Transient Responses of a Coupled Ocean-Atmosphere Model to Gradual Changes of Atmospheric CO_2. Part II: Seasonal Response. *Journal of Climate*, 5: 105-126.

McGinnis, D.L. and Crane, R.G. 1994. A Multivariate Analysis of Arctic Climate in GCMs. *Journal of Climate*, 7: 1240-1250.

van de Wal, R.S.W. and Oerlemans, J. 1994. An energy balance model for the Greenland Ice Sheet. *Global and Planetary Change*. 9: 115-131.

Wakahama, G., Kuroiwa, D., Hasemi, T., and Benson, C.S. 1976. Field Observations and Experimental and Theoretical Studies on the Superimposed Ice of McAll Glacier, Alaska. *Journal of Glaciology*, 16(74): 135-149.

Ward, W.H. and Orvig, S. 1952. The Glaciological Studies of the Baffin Island Expedition, 1950. Part IV: The Heat Exchange at the Surface of the Barnes Ice Cap During the Ablation Period. *Journal of Glaciology*, 2(13): 158-168.

Woodward, J. 1995. Superimposed ice and glacier mass balance. *Unpublished M.Sc. Thesis.* University of Alberta. 96p.

CHAPTER 2. Development and Testing of an Albedo Algorithm for High Arctic Glaciers

2.1 Introduction

Solar radiation is usually the largest contributor of melt energy to snow or ice at the surface of a glacier (Munro, 1990; Paterson, 1994; Knap and Oerlemans, 1996). The proportion of incident solar radiation which contributes to the melt energy at a glacier surface depends upon the surface albedo. Surface albedo is highly variable throughout the course of a melt season: fresh snow albedo may be as high as 95% (Liljequist, 1956), dropping to less than 60% as the snowpack ages (Bryazgin and Koptev, 1969; Grenfell and Maykut, 1977), while ice albedo ranges from 55% for clean ice to less than 20% for dirty ice (Cutler and Munro, 1996). Variations in surface albedo depend upon snow or ice crystal size, surface roughness and dirtiness, the solar zenith angle, the spectral composition of the incident solar radiation, and the amount of liquid water present at the surface (Grenfell and Perovich, 1981).

Given the high variability of albedo, and its importance in determining melt energy availability, the accurate parameterization of albedo in snow and ice melt models is essential. However, because the factors which control surface albedo are complex, albedo is often either treated as a fixed parameter, or modelled in an empirical fashion. For instance, some models assign either a single value to the albedo of a snow cover, or a series of values which correspond to general descriptions of the snow surface, such as new, old, or melting snow (e.g. Rowe *et al.*, 1995). Others assign a fixed value which is allowed to decrease once the melting snowpack reaches a critical depth (e.g.: U.S. Army Corps of Engineers (1956). Glacier surface energy balance models have used algorithms in which the albedo depends upon the accumulation of atmospheric dust and morainic material at the surface of the glacier (Oerlemans, 1992; Arnold *et al.*, 1996). Oerlemans suggested that concentrations of morainic materials increased with distance downglacier from the equilibrium line, and he defined a background albedo profile, which specified the ice surface albedo at the end of a melt season. Upon this background was superimposed an albedo profile for snow which was a smooth function of snow depth water equivalence. This allowed a smooth transition between the snow albedo and the background

albedo to occur as the snowpack melted. van de Wal and Oerlemans (1994) developed an albedo parameterization for the Greenland ice sheet in which albedo decreased with time after a new snowfall. This model also kept track of the amount of liquid water at the surface so that, during periods of melt, albedo values dropped to that of water until the water had time to runoff from the system. Including a parameterization for surface meltwater was the only way in which Zuo and Oerlemans (1996) could reproduce the observed albedo pattern and mass-balance profile along a transect on the Greenland ice sheet.

Detailed studies of the radiative transfer characteristics of individual snow crystals have led to the development of analytical models to predict variations in snow albedo across the spectrum of solar radiation (e.g. Dunkle and Bevans, 1956; Bohren and Barkstrom, 1974; Wiscombe and Warren, 1980). The most accurate of these models is that developed by Wiscombe and Warren (1980). This model predicts dry snow albedo for the entire solar spectrum (0.3 - 5 μm) on the basis of entirely observable quantities (snow grain size, solar zenith angle, the ratio of diffuse to direct incident solar radiation, and, for a thin snow layer, the snow thickness and albedo of the underlying surface) and uses no arbitrary adjustable parameters. The drawback of this model, in the context of surface energy balance modelling, is that it is computationally intensive because of the necessity to integrate calculations over the entire solar spectrum. Marshall and Warren (1987) and Marshall (1989) simplified the Wiscombe and Warren's (1980) model with the goal of integrating a physically based albedo routine into large-scale global climate models (GCMs). Their approach was to average the modelled spectral albedo over two wavelength bands, and to fit simple analytical functions to the spectrally-averaged albedo. The spectrally-averaged albedo varied with grain size, solar zenith angle, snow depth, underlying surface albedo (for thin snow), the impurity content of the snowpack, and cloud cover. Marks (1988), in a model of the surface energy balance of an alpine watershed, followed the approach of Marshall and Warren and fitted functions to spectrally-averaged albedo curves from the Wiscombe and Warren (1980) model. Marks' equations were subsequently implemented in a one-dimensional snowpack temperature model, SNTHERM (Jordan, 1991; Jordan, 1995). Jordan (1995) made several modifications to the model developed by Marks, including additional equations to correct albedo for sloping surfaces. The

routine implemented in the present version of SNTHERM is hereafter referred to as "SNTHERM_Albedo".

A surface energy balance model (EBM) developed by Arnold *et al.* (1996) and modified for use on Arctic glaciers by Woodward (1995), uses the albedo algorithm developed by van de Wal and Oerlemans (1994). This model is hereafter referred to as "EBM-94" to differentiate it from "EBM-96", a modified version of the model described in Chapter 4. Woodward investigated the sensitivity of EBM-94 for simulations of the mass balance of John Evans Glacier, Ellesmere Island, Nunavut, and showed that altering the prescribed background albedo (albedo of bare ice) from 55% to 43% resulted in a decrease in the annual specific mass balance of 74%. The sensitivity of the model to surface albedo, coupled with the fact that glaciers in the high Arctic receive up to 24 hours of continuous daylight during the melt season, indicates the importance of correctly parameterizing surface albedo in models of the energy balance of high Arctic glaciers. Although the van de Wal and Oerlemans algorithm (hereafter the "W-O" algorithm) captures some important features of the surface albedo, including a decrease in albedo with time after a new snowfall, automated measurements of hourly surface albedo collected at 3 locations on John Evans Glacier during the summer of 1996 show that albedo varied in ways which the W-O algorithm is unable to predict. The main shortcoming of the W-O algorithm is that it does not predict large diurnal variations in surface albedo.

In the light of the weaknesses of the existing models, a new albedo algorithm is developed in this paper. It incorporates some empirical elements of the W-O algorithm, but is primarily physically based, following the structure of the SNTHERM_Algorithm. A physically based model is favored because:

1) provided there are sufficient data to run the model, it is expected to be the most accurate method for simulating surface albedo;
2) unlike empirical simulations which depend upon arbitrary constants which may need to be adjusted for each site, it is expected to be readily transferable to other locations;
3) through sensitivity analyses carried out with surface energy balance models, a physically based albedo model may reveal feedback mechanisms between the

surface and the atmosphere which would not be revealed with an empirical albedo model (e.g. changes in cloud cover which affect the spectral composition of incoming solar radiation, and hence the surface albedo).

The main stages in the development of the new physically-based albedo algorithm for EBM-96 are:

1) Testing of Existing Algorithms: Both EBM-94 and the SNTHERM model are run using data from each of 3 weather stations established on John Evans Glacier in the summer of 1996, using the unmodified W-O and SNTHERM_Albedo routines respectively. Albedo predictions from each model are compared with albedo measurements from John Evans Glacier to gain insight into which elements of each algorithm need to be retained in the new algorithm.
2) Incorporation of SNTHERM_Albedo into the EBM: The code for SNTHERM_Albedo is incorporated within the EBM as a new subroutine (EBM_Albedo), which is called by the main EBM program.
3) Development of a Grain Size Algorithm: Because EBM_Albedo is driven primarily by grain size, and the EBM main program does not model grain size, a new routine is developed (EBM_GrainSize) which provides empirical predictions of grain size to EBM_Albedo.
4) Improvement to EBM_Albedo: EBM_Albedo is improved by incorporating some components of the W-O routine into EBM_GrainSize. In particular, van de Wal and Oerlemans' method for modelling free water at the surface is used to account for the effects of meltwater on the surface albedo. Other improvements include assigning specific grain sizes for superimposed ice and glacier ice, and introducing a contamination factor to account for the effects of surface contaminants on the surface albedo of snow.

These steps provide a method for combining a physically based albedo routine, developed exclusively for dry snow conditions (SNTHERM_Albedo), with an empirical model which accounts for the effect of free water in melting snow on the surface albedo of high polar glaciers (W-O routine).

2.2 Study Area

2.21 Site description

John Evans Glacier is a large valley glacier located at 79°40'N 74°00'W on an unnamed peninsula south of Dobbin Bay, eastern Ellesmere Island, Nunavut, Canada (Figure 2.1-2.3). Its catchment area is 211 km^2, of which 47% is glaciated. The glacier spans an altitudinal range of 50 to 1500 m (Figure 2.4). 77% of the ice surface area lies between 600m and 1100m. The catchment comprises a main trunk glacier fed from a number of subcatchments in the western part of the basin, and 8 small valley glaciers feeding into a marginal lake 3 km from the snout of the main trunk glacier on its eastern side.

2.22 Local Climate

Mean annual and July temperatures recorded over the period 1951-1994 at the AES meteorological station at Alert, north-eastern Ellesmere Island (82°30'N 62°20'W) are shown in Figure 2.5. The mean annual sea level temperature at Alert was -17.8°C. During 1988-89, the average annual air temperature at Alert was -16.9°C. This is similar to the average annual air temperature (-17.3°C) measured for the same period at Allman Bay, located 5km south of John Evans Glacier (Figure 2.2) (G. Henry, *pers comm.*). However, July 1988 temperatures were approximately 3°C warmer at Allman Bay (located at sea level) than at Alert. Field data for the present study were collected during the summer of 1996, which was unusually cold. The mean 1996 July air temperature measured at the lower weather station (elevation 261 m) on John Evans Glacier was approximately 3°C colder than the mean July air temperature at Allman Bay in 1988 (note that some of this difference in temperature may be due to differences in surface type and elevation between Allman Bay and John Evans Glacier). Mean total precipitation from 1 August 1995 to 1 August 1996 at Alert (165.4 mm WE) was 128% higher than the mean annual total precipitation at Alert over the period 1951-1994 (128.5 mm WE).

2.3 Physical Controls on Snow Albedo

Before attempting to model snow or ice albedo, it is important to understand the physical controls on surface albedo. Both physical and empirical albedo models are developed

from observed relationships between surface albedo and snow/ice grain radius and liquid water content, the solar zenith angle, the underlying surface albedo (for thin snow), the concentration of absorbing impurities in the snow/ice layer, and the spectral composition of solar radiation incident at the surface. Each of these factors will be described briefly in order to aid in the understanding of the equations described in this paper.

Spectral Composition of Solar Radiation: The albedo of dry snow is wavelength dependent, and is generally high in the near-ultraviolet and visible parts of the spectrum (0.3-0.7 mm), starts to drop steeply with wavelength in the near-infrared (near-IR) (0.8-1.5 mm) and remains low for longer wavelengths (Wiscombe and Warren, 1980) (Figure 2.6). As a result, the spectral composition of radiation reaching the snow surface will have an effect upon the albedo. An increase in diffuse radiation, normally caused by increased cloud cover, will increase the all-wavelength snow albedo because the radiation field will become relatively richer in visible wavelengths. When the radiation is directional, the reflectance is also directional, such that snow albedo under direct sunlight depends primarily upon the solar zenith angle.

Solar Zenith Angle: The relationship between solar zenith angle (θ) and albedo is complex, and depends upon the snow surface characteristics and the range of zenith angles involved. For a flat, smooth snow surface under clear sky conditions, albedo increases with increasing zenith angle (Wiscombe and Warren, 1980), although the effect is greatest for zenith angles greater than 50° (Petzold, 1977). In general, a smooth snow surface tends to act in a specular or mirror-like fashion, such that incident radiation at a given angle is reflected from the surface at the same angle (Oke, 1987). This effect becomes enhanced for higher zenith angles, as there is less likelihood of diffuse scattering of radiation into the snowpack. For high θ, a photon entering the snowpack has a high probability of undergoing a scattering event close to the surface (Warren, 1982). Photons incident at low θ have a higher likelihood of penetrating deeper into the snowpack, where scattering photons have a greater chance of being absorbed.

Snow Grain Radius: An increase in the radius of snow grains, which occurs naturally as the snowpack ages, reduces the snow albedo. Since refraction of light within a snowpack occurs at the snow grain boundaries and absorption occurs within the ice grains, larger snow grains are both more absorptive and more forward scattering than smaller ones. Therefore, as the snow grain size increases, radiation is transmitted into the snowpack more effectively, decreasing the albedo.

Liquid Water Content: Liquid water present in a melting snowpack tends to replace air between ice grains (Colbeck, 1975; 1979). This leads to an increase in the effective grain size, which decreases the albedo. If enough meltwater is present near the surface of the snowpack, the all-wavelength snow albedo will drop because water has a lower all-wavelength albedo than ice crystals. Liquid water also has the effect of increasing the rate of grain growth, so that the albedo tends to change more quickly after only a brief exposure to melting conditions.

Concentration of Absorbing Impurities: Snow commonly contains atmospheric aerosols, which become incorporated into the snow nuclei during the formation and/or atmospheric transport of a snow crystal. The aerosols which have an important effect upon snow albedo are dust and soot particles (Warren and Wiscombe, 1980). Because snow is weakly absorptive in the visible region of the spectrum, dust or soot contaminants in a snowpack tend to reduce the albedo in this region. Other impurities which may contaminate the surface of Arctic glaciers consist of morainic materials derived from surrounding bedrock surfaces. These contaminants also reduce the visible component of the surface reflection.

Snowpack Thickness: Short-wave radiation which is not reflected from the surface of a snowpack may be absorbed by the snow grains or be transmitted deeper within the snowpack. Because radiation transmitted into the snow is attenuated with depth at an exponential rate, there is a critical depth defining the limit of solar penetration into the snowpack (Mellor, 1977). When the snowpack thins to below this critical depth, transmitted radiation may interact with the surface underlying the snowpack. If the albedo of the underlying surface is different than the snow albedo, the net reflectivity of the snowpack may be altered.

2.31 Effects of Surface Slope on Albedo

The albedo of a sloping surface differs from that of a horizontal surface, especially in areas with high solar zenith angles. Grenfell *et al.* (1994) have shown that under clear sky conditions, potential errors in albedo measurements over a sloping surface may occur if radiation instruments are set up with the cosine collector parallel to the horizon rather than the slope. The dominant effect of slope on surface albedo is that the incident irradiance with respect to the local zenith is different from that with respect to the normal of the sloping surface. Therefore, a sensor set up to measure albedo over a sloping surface will measure an incident irradiance which is too low if the cosine collector is aligned parallel to the horizon. However, because the radiation reflected from a snow surface is largely isotropic, the reflected irradiance will be nearly the same regardless of whether the sensor is aligned parallel to the slope or the horizon (for the case of a small surface slope). Since the spectral albedo of snow is so high, an underestimation of the measured or modelled incident irradiance may result in albedo values which are too large, and may even be greater than 1.

2.4 Model Summaries

This section describes the main components of the SNTHERM_Albedo and W-O algorithms, two existing albedo routines for simulating the surface energy balance over snow and ice. Both algorithms are described here because the new albedo routine developed in Section 2.8 incorporates elements of both these algorithms. The new albedo routine is constructed on the basis of an evaluation of the strengths and weaknesses of the SNTHERM_Albedo and W-O algorithms, as described in Section 2.7. Testing of the SNTHERM_Albedo routine is carried out within the SNTHERM model, which is described briefly in Section 2.41. Testing of the W-O algorithm is carried out using EBM-94 (see Woodward, 1995 for a description of EBM-94).

2.41 SNTHERM Model Description

SNTHERM is a one-dimensional mass and energy balance model for predicting temperature profiles within strata of snow and frozen soil (Jordan, 1991). Although temperature prediction is the primary objective of the model, snow accumulation, ablation, densification and metamorphism, as well as the transport of liquid water and water vapor, are included as required components in the heat and mass balance calculations. A numerical solution to the governing heat and mass balance equations is obtained by subdividing snow and soil layers into horizontally infinite control volumes. The governing equations are subject to meteorologically determined boundary conditions at the snow/air interface. Surface fluxes are computed from user-supplied meteorological observations of air temperature, dew point temperature, wind speed, precipitation, and solar and incoming infrared radiation. The model is initialized with profiles of temperature and water content for the various strata, the accuracy of which determines the time required for the simulation to equilibrate after initiation of the computer run. The model has been modified by Rowe *et al.* (1995) to simulate snowmelt over a glacier ice surface, simply by treating the ice as a soil layer with no dry soil component. Rowe *et al.* used this modified version of the model to simulate summer snowmelt on the Greenland ice sheet, and found that their simulations of snowpack height and mass agreed well with observations. However, a drawback to the model was that it used a fixed albedo value for calculations of net solar radiation. A recent upgrade of the SNTHERM model contains an algorithm for calculating snow albedo (Jordan, 1995). In this paper, the SNTHERM albedo algorithm is used as a basis for the development of an improved algorithm.

2.42 SNTHERM_Albedo Algorithm

The SNTHERM_Albedo algorithm is intended for dry snow surfaces, and was originally adapted from Marks (1988), whose work was based on the studies of Wiscombe and Warren (1980) and Marshall and Warren (1987). Because snowpack albedo varies according to the spectral composition of radiation reaching the surface, Marks made separate calculations of the albedo for diffuse and direct components of the incident radiation. His calculation of the albedo for the diffuse component depended upon grain size, while that for the direct component also incorporated the effects of the solar zenith

angle on surface albedo. Following the approach of Marshall and Warren, Marks calculated albedo for 2 wavebands, the visible (vis, 0.3-0.7μm) and near-infrared (nir, 0.7-3.0μm), for each of the direct and diffuse components,. Marks' approach is described schematically in Figure 2.7.

Diffuse Albedo: Marshall and Warren showed the relationship between the square root of grain radius (√R) and albedo for diffuse radiation in the visible (vis, 0.3-0.7μm) and near-infrared (nir, 0.7-3.0μm) bands (Figure 2.8). Marks developed equations to fit these snow albedo curves, which estimate vis and nir albedo for incident radiation which is entirely diffuse ($\alpha_{vis,diffuse}$ and $\alpha_{nir,diffuse}$ respectively):

$$\alpha_{vis,diffuse} = \alpha_{vis,max} - \kappa_{vis} r \tag{2.1}$$

$$\alpha_{nir,diffuse} = \alpha_{nir,max} \exp\left[\kappa_{nir} r\right] \tag{2.2}$$

where $\alpha_{vis,max}$ and $\alpha_{nir,max}$ are the maximum visible and near-infrared albedos (1.0 and 0.85447 respectively), κ_{vis} and κ_{nir} are the visible and near-infrared slope coefficients for albedo decay with grain size, and r is the snow grain radius.

Direct Beam Albedo corrected for Zenith angle: Marshall and Warren also showed the relationship between snow albedo and the cosine of the solar zenith angle for incident radiation which consists entirely of direct beam radiation (Figure 2.8). Based on these curves, Marks developed a functional relationship which corrects Equation (2.1) and (2.2) for zenith angles other than 0.0:

$$\alpha_{vis,direct} = \alpha_{vis,diffuse} + \kappa_{vis,\theta} r \left(1.0/\sqrt{3.0} - \cos\theta_z\right) \tag{2.3}$$

$$\alpha_{nir,direct} = \alpha_{nir,diffuse} + \left(\kappa_{nir,\theta} r + \lambda_{nir,\theta}\right)\left(1.0/\sqrt{3.0} - \cos\theta_z\right) \tag{2.4}$$

where $\alpha_{vis,direct}$ and $\alpha_{nir,direct}$ are the visible and near-infrared direct beam albedos, $\kappa_{vis,\theta}$ and $\kappa_{nir,\theta}$ are visible and near-infrared slope coefficients, $\lambda_{nir,\theta}$ is the near-infrared offset coefficient, and θ_z is the solar zenith angle. The factor 1.0/√3.0 was introduced as a

correction by Jordan (1995), to improve the fit of the original equation developed by Marks to the theoretical curves of Marshall and Warren. This is necessary because Marks mistakenly assumed that his Equation (2.1) and (2.2) were for vertically incident direct beam radiation(i.e. solar zenith angle of 0), rather than for diffuse radiation.

Combination of Diffuse and Direct Beam Components: The visible and near-infrared albedos (α_{vis} and α_{nir}) are expressed as linear combinations of the diffuse and direct beam components:

$$\alpha_{vis} = \alpha_{vis,diffuse} f_{diffuse} + \alpha_{vis,direct}\left(1 - f_{diffuse}\right) \tag{2.5}$$

$$\alpha_{nir} = \alpha_{nir,diffuse} f_{diffuse} + \alpha_{nir,direct}\left(1 - f_{diffuse}\right) \tag{2.6}$$

where $f_{diffuse}$ is the fraction of diffuse radiation. The diffuse-direct fractions are computed using an insolation routine adapted from Shapiro (1987). Shapiro divided the atmosphere into N horizontally infinite plane-parallel layers. Following the two-stream formulation for a thin atmosphere, the angular distribution is simplified into bi-directional forward and backward components. Shapiro defined a reflectivity R and apparent transmissivity T for each layer, in which R is analogous to the backscatter. According to conservation of energy, T is given by:

$$T = 1 - R - A \tag{2.7}$$

where A is the absorptivity. Note that by this definition, T includes both unscattered and forward scattered radiation. The radiative transfer equations are then given by:

$$I_s^{j''-\frac{1}{2}}\downarrow = T_{j'} I_s^{j''+\frac{1}{2}}\downarrow + R_{j'} I_s^{j''-\frac{1}{2}}\uparrow \tag{2.8}$$

$$I_s^{j''+\frac{1}{2}}\uparrow = T_{j'} I_s^{j''-\frac{1}{2}}\uparrow + R_{j'} I_s^{j''+\frac{1}{2}}\downarrow \tag{2.9}$$

where the index j'' numbers in ascending order from the air interface. By fitting curves to data from the SOLMET data base, Shapiro tabulated values for $R_{j'}$ and $T_{j'}$ as polynomial

functions of the solar zenith angle θ_z and cloud conditions. Specifying the upper and lower boundary conditions as:

$$I_s^{N+\frac{1}{2}} = I_{s00} \tag{2.10}$$

and

$$I_s^{\frac{1}{2}}\uparrow = R_0 I_s^{\frac{1}{2}}\downarrow = \alpha_{top} I_s^{\frac{1}{2}}\downarrow \tag{2.11}$$

where I_{s00} is the solar insolation at the top of the atmosphere, leads to a system of $2N + 2$ linear equations, which can be solved for the incident flux at the earth's surface. In addition to the N-level model, Shapiro proposed a simplified three-level algorithm with layers corresponding to heights of low ($j'' = 1$) and high ($j'' = 3$) clouds. Equations 2.8 & 2.9 are then solved in closed form to obtain:

$$I_s\uparrow(\mathrm{Z}) = I_s^{\frac{1}{2}}\downarrow = \frac{T_1 T_2 T_3}{D_2} I_{s00} \tag{2.12}$$

where Z is the snow depth relative to the ground, and

$$D_2 = d_1(d_3 d_2 - R_3 R_1 T_2^2) - d_3 R_2 \alpha_{top} T_1^2 - R_3 \alpha_{top} (T_2 T_1)^2 \tag{2.13}$$

and the coefficients $d_{j''}$ are defined as

$$d_{j''} \equiv 1 - R_{j''} R_{j''-1} \tag{2.14}$$

Direct radiation is taken as that which is transmitted to the earth unscattered by the atmosphere. As a first approximation, the transmissivity, Td, is computed by assuming that radiation is scattered isotropically, so that backward and forward components are equal. In this case $T\mathrm{d} = T - R$ and the direct radiation incident on the earth is

$$I_{s,\mathrm{direct}}\downarrow(\mathrm{Z}) = T\mathrm{d}_1 T\mathrm{d}_2 T\mathrm{d}_3 I_{s00} \tag{2.15}$$

and diffuse radiation is the complement of this, or

$$I_{s,diffuse}\downarrow(Z) = I_s\downarrow(Z) - I_{s,direct}\downarrow(Z) \qquad (2.16)$$

All-wavelength Albedo: The all-wavelength albedo (α_{a-w}) is a linear combination of the vis and nir broad band albedos:

$$\alpha_{a-w} = \alpha_{vis} f_{vis} + \alpha_{nir}(1 - f_{vis}) \qquad (2.17)$$

The fraction f_{vis} of radiation in the visible band is set to 0.424, as approximated by Jordan, who integrated the clear sky spectral curve shown in Grenfell and Perovich (1981). Because this fraction will increase with cloud cover, and the curves of Marshall and Warren which are used to develop the albedo equations will be sensitive to cloud cover, this albedo routine is valid only for clear skies. As a preliminary solution to this limitation, Jordan included an equation to modify f_{vis} for cloudy sky conditions:

$$f_{vis} = 0.5 + 0.149 * (1 - cl) \qquad (2.18)$$

where cl is sky clearness calculated as:

$$cl = cv_1 + ecv_2 + ecv_3 \qquad (2.19)$$

and ecv_2, ecv_3 are effective cloud covers for the middle and upper sky layers, calculated as:

$$ecv_2 = cv_2 + (1 - cv_1) \qquad (2.20)$$

$$ecv_3 = (1 - cv_1)cv_3(1 - cv_2) \qquad (2.21)$$

and cv is the fractional cloud cover for the associated cloud layer. Note that the indexing for the cloud layers follows the convention established in the above description of the Shapiro algorithm.

2.43 W-O Albedo Algorithm

The van de Wal and Oerlemans (1994) albedo algorithm uses a series of fixed parameters to represent the albedo of fresh snow, old snow, bare ice and water. Exponential functions are then used to model the transition between each of these phases of the surface albedo. After a new snowfall, albedo is set to the prescribed value for fresh snow. Albedo then decays as a function of time towards the value for old snow, or, once all the snow has melted, towards the value for glacier ice. Free water at the surface, formed as a function of snow or ice ablation, forces the albedo towards the albedo of water.

Parameters used in testing the W-O Algorithm are the same as those used by Woodward (1995) in EBM-94. Fresh snow, old snow, bare ice and water albedos are set at 0.85, 0.65. 0.55 and 0.2 respectively. Any water formed at the surface drains completely in 1 day.

2.5 Methods

2.51 Meteorological Data

Three automatic weather stations (AWS's) were set up at low (261 m a.s.l.), middle (824 m a.s.l.) and high (1183 m a.s.l.) elevation sites on John Evans Glacier in summer 1996 (Figure 2.3; Table 2.1). Each AWS consisted of a central mast frozen into a ~1.5m deep hole drilled into the ice surface. A cross-bar was mounted on these masts so that sensors could be attached. Once the masts were frozen into the ice, they were very stable and only very strong winds could make them shake. None of the masts melted out or needed to be re-drilled into the ice. Incoming and outgoing short-wave radiation, net radiation, air temperature, relative humidity, air pressure, wind speed and wind direction were measured every ten seconds from 15 June (JD 167) to 3 August (JD 216), 1996 (Table 2.2, 2.3). The ten second values were then averaged to hourly values for use in the energy balance model. Cloud type, cover and height were estimated for 3 layers in the atmosphere. These observations were always made at 0700 and 1900 hrs., and additional observations were made whenever conditions changed from the previous observation. Snowfall was collected in a small plastic tray (surface area of 0.10 m^2) and water equivalence was determined by melting the

snow and measuring the volume of water at the end of a snowfall event.

To ensure that other sensors would not shade the sensor, K↓ was initially measured at a height of approximately 2m above the snow surface, while K↑ was initially measured at a height of approximately 1m above the surface. Although every attempt was made to adjust K↑ sensor height as the surface melted, and to ensure that all sensors were level, this was not always possible due to the difficulty in reaching each site on a regular basis. Surface albedo was calculated by dividing K↓ by K↑.

2.52 Slope Corrections

In order to correct albedo measurements for a sloping surface, both the slope angle and slope azimuth had to be determined for each AWS. In the field, AWS locations were determined using a Trimble Pathfinder global positioning system (GPS). Measurements were taken using a portable "rover" system connected to a hand held data logger. At each point, 2 sets of 200 readings were made. These were then averaged and plotted on a digital elevation model (DEM) of John Evans Glacier (see Section 4.51), to determine in which grid cell of the DEM each station was situated. The DEM was then used to determine the slope angle and azimuth for each of these specific grid cells, using simple neighbourhood functions which examine the elevations of the 9 cells surrounding a given cell (see Section 4.51 For details). Table 2.4 compares these results with field measurements of slope angle and azimuth, which were made with a hand-held Abney level and a tape measure. Azimuth was estimated by comparison with aerial photos and maps because a compass could not be used for such a purpose at this high latitude site. Because of the potential for error in estimating slope azimuth in the field, it is assumed that the GPS method of estimating slope azimuth is more accurate. Therefore, GPS obtained values are used in albedo calculations.

2.53 Corrections to Measured Albedo Data

Because field measurements of all-wavelength surface albedo were carried out with sensors with cosine collectors aligned parallel to the horizon, and because these measurements were made over a sloping surface (see Section 2.31), it was necessary to correct albedo

measurements for slope to allow comparison with model output. This was accomplished by first estimating the diffuse to direct ratio of incoming solar radiation using the Shapiro routine described above (Equation 2.7 - 2.16), and the vis to nir ratio (Equation 2.18 - 2.21). Measured albedo values were then separated into their vis/nir and direct/diffuse components using Equation 2.17, 2.5 and 2.6. Equation 2.22 was then used to correct the visible, direct component of the incident irradiance for slope, and this value was recombined with all remaining components of the irradiance, using Equation 2.17, 2.5 and 2.6, to obtain a slope-corrected all-wavelength albedo value.

2.54 Potential Sources of Error

Fresh snow landing on the K↓ sensor was a large source of error in albedo measurements. This snow prevented radiation from reaching the sensor, reducing the recorded value of K↓ from its true value. This resulted in the observation of apparent albedos which were over 100%. However, since detailed records were kept of the timing of precipitation events, albedo measurements could be easily corrected. During snowfall events, K↓ values were adjusted so that the observed albedo was 95%, a typical value observed for fresh dry snow near the start of the season.

Albedo data from the middle AWS are considered the most accurate and useful for the development of an improved albedo algorithm. This is because the field camp was located next to this station, allowing the observation of ice and snow characteristics, and the adjustment of sensors, on a regular basis. The upper and lower sites could not be visited very often, and this meant that the sensors could go off balance, be positioned at the wrong height above the surface, and become covered with ice or snow.

2.6 Measured Albedo

<u>Middle Weather Station:</u>

The surface albedo at the M-AWS, uncorrected for slope, varies on both diurnal and seasonal timescales. On a daily basis, the albedo changes by as much as 35% over the course of a day, due to changes in the solar zenith angle (θ) (Figure 2.9). Wiscombe and

Warren (1980) showed that albedo changes most rapidly with θ at large values of θ, and this result is supported by the data from this study. At John Evans Glacier, θ ranged from 56° to 77° during the melt season, and such high values probably account for the high diurnal variability in albedo. Corrections to the measured albedo at the M-AWS have the effect of enhancing or dampening the diurnal variability in albedo, depending on the position of the sun with respect to the slope. The slope azimuth at the M-AWS points towards the north, so that the slope faces directly away from the sun's position at noon, decreasing the angle of incident solar radiation. Therefore, corrected albedo values are up to 45% higher than uncorrected measurements at midday when the solar azimuth is upslope from the M-AWS, and up to 50% lower during the early morning/late evening when the sun is downslope from the M-AWS (Figure 2.10 a,b). The magnitude of the correction depends on the fraction of incoming solar radiation which is direct radiation. Measured albedo values greater than 1 occur at midday when the slope is tilted away from the incident solar beam, and the incident irradiance is underestimated, as explained in Section 2.31.

On a seasonal basis, corrected albedo at the M-AWS decreases over time after a new snowfall (Figure 2.11a). This decrease in albedo coincides with an increase in the grain size at the snow or ice surface, which results from snowpack metamorphism and an increase in the water content of the surface layer (Figure 2.11b-d). High albedo values at the start of the season are the result of fresh snow at the surface with a low grain diameter (0.25 mm). The snow remained dry until melting commenced on JD 176, during which time average daily albedo ranged between 0.80 and 0.90. After melting began, average daily albedo began to drop more rapidly than during the dry snow period, reaching a low of ~0.65 on JD 191 when superimposed ice with a grain diameter of 5 mm was exposed at the surface. The snowpack density was uniform at the start of the measurement period, and increased through time as the melt season progressed. Spikes in the density profile represent ice layers within the snowpack. Increases in density at the surface are coincident with a decrease in the measured surface albedo.

Lower Weather Station: The L-AWS was set up over a snowpack which had already undergone melting and compaction. Although the albedo measurements at this site are useful because they capture the transition from wet snow to superimposed ice to glacier ice, there are likely inaccuracies in the dataset because the station could not be visited very frequently. Albedo values ranged between 0.80 and 0.53 for wet snow, 0.70 and 0.35 for superimposed ice, and 0.50 and 0.20 for glacier ice. Average albedos for wet snow, superimposed ice and glacier ice were 0.73, 0.62 and 0.38 respectively (Figure 2.12). Correcting the albedo measurements for slope has the effect of enhancing the range of diurnal variability during periods of direct sunlight, with the largest amount of slope correction occurring at midnight, when the solar zenith angle was high and the sun was positioned upslope from the weather station.

Upper Weather Station: Because of its location high on the glacier on an unsheltered ridge, this site was frequently subject to high winds. During all visits to this site (JD 167-168, 176, 185 and 217), the upper layer of the snowpack consisted of a hard-packed wind-scoured surface with a grain diameter of less than 1 mm. Therefore, it is likely that snow grain sizes at the surface remained similar throughout much of the melt season. This site therefore provides an opportunity to observe changes in surface albedo given a largely static grain size. It is easy to differentiate between periods of direct sunlight and periods with cloud cover at this site (Figure 2.13). During sunny periods, an obvious diurnal cycle appears in the albedo record (e.g. JD 193-196), while at other times, this diurnal cycle is damped. Correcting the albedo measurements for slope enhances the difference between periods of direct sunlight (strong diurnal cycle) and those without direct sunlight.

2.7 Testing of the 2 Existing Albedo Algorithms

In this section, the W-O and SNTHERM_Albedo algorithms are tested using data from John Evans Glacier. Testing is carried out using data from the M-AWS because these data are considered to be the most accurate. Results are compared with measured albedo at the M-AWS.

W-O Algorithm: The albedo parameterization of W-O does a good job of estimating

albedo decay with time after a new snowfall event. The algorithm is sensitive to the prescribed runoff rate (see Section 2.84 for details), and the results suggest that the runoff parameter in the W-O model should be set to a value of between 1/24 and 1 day. Although some diurnal variability is introduced via the surface water content parameter, this model does not capture the large diurnal cycles in albedo measured in the field (Figure 2.14).

SNTHERM_Albedo Algorithm: Surface albedo as simulated by the SNTHERM_Albedo algorithm, using data from the M-AWS to drive the SNTHERM model, cycles diurnally between 0.65 and 0.55, with maximum values occurring around midnight and minimum values around noon each day (Figure 2.15). The SNTHERM_Albedo algorithm does not do a good job at predicting surface albedo at the M-AWS. The main problems with the SNTHERM_Albedo algorithm are:

1) It does not capture the effect of new snowfall events.
2) It does not simulate an overall decrease in albedo with time after a new snowfall event, or an increased rate of albedo decay due to the presence of liquid water at the surface of the snowpack.
3) It has no way of dealing with a bare ice or superimposed ice surface (shown as a straight line, where SNTHERM predicts all snow has melted).
4) The range of the diurnal variations is too small.
5) The modelled diurnal variations are out of phase with the measured variations.

Limitations 1-3 of the SNTHERM_Albedo algorithm probably relate to problems with the grain size predictions generated by the SNTHERM model. SNTHERM predicts grain size in a physically based fashion, based on vapor transport between individual snow grains (Colbeck, 1973). This grain radius is used in Equation 2.1 and 2.2 to drive albedo simulations. The fact that albedo predictions generated by SNTHERM_Albedo are consistently lower than observed albedo suggests that the grain radii used to initialize the model are too high. However, regardless of whether initial snow grain radii are set correctly, the fact that SNTHERM_Albedo does not adequately predict albedo decay with time suggests that either: 1) grain growth rates predicted by the SNTHERM model are too low, or 2) there are other

factors, such as free water in the snowpack, which cause a albedo to decrease in a fashion similar to that which would be produced by rapid grain growth.. Finally, SNTHERM_Albedo is unable to predict the surface albedo of superimposed or glacier ice because SNTHERM is not set up to model the grain size of these types of surfaces. However, the albedo of superimposed or glacier ice could be modelled using the SNTHERM_Albedo algorithm, simply by developing a parameterization of the grain size of these types of surfaces.

Limitations 4-5 of the SNTHERM_Albedo algorithm are probably caused by problems with the slope corrections applied to modelled albedo values. SNTHERM_Albedo does include a routine to correct predicted albedo for a sloping surface, and diurnal variations do appear in modelled values as a result of changes in the solar zenith angle with respect to the surface slope. However, the fact that the range in diurnal variations is too small, and that these variations are slightly out of phase with measured values, suggests there may be a problem with the way in which SNTHERM_Albedo corrects albedo values for a sloping surface.

2.8 Development and Testing of a Combined Surface Albedo Algorithm (EBM_Albedo)

The W-O and SNTHERM_Albedo algorithms capture some but not all of the features in the measured albedo profile at the M-AWS, and they differ in their strengths and weaknesses. The new albedo algorithm developed here builds upon the perceived strengths of the two. This new algorithm, "EBM_Albedo", is developed and implemented within the surface energy balance model (known as EBM-96) described in Chapter 4. EBM_Albedo uses the SNTHERM_Albedo equations described in Section 2.42 (Equation 2.1 to 2.21) as a starting point for model development. Two main changes are made to the SNTHERM_Albedo routine. The first is to introduce a new method for correcting albedo for a sloping surface, based on work by Grenfell *et al.* (1994). The second is to add an empirical grain growth algorithm, based on work by Marks (1988), which simulates the effective grain size of individual snow crystals. The effects of surface water, as simulated by the W-O algorithm, are incorporated into the new albedo algorithm via this grain growth algorithm. This algorithm improves albedo simulations, and allows the new albedo algorithm to be more readily incorporated into the EBM-96 energy balance

balance model. This is because EBM-96 is a computationally-intensive, spatially distributed model which is unable to generate the detailed physical simulations of snowpack layering and crystal growth produced by the one-dimensional model SNTHERM model .

2.81 Correcting Albedo for a Sloping Surface

The original SNTHERM algorithm corrected modelled albedo for a sloping surface by modifying $\cos\theta_z$ in Equation 2.3 and 2.4 to account for the orientation of the slope with respect to the incoming solar beam. It is not clear why this approach was unable to correctly simulate the effects of surface slope on albedo. An alternative approach, based on a study by Grenfell *et al.* (1994), was tested and produced better results. The approach calculates albedo for a sloping surface, assuming isotropic reflected radiance for the case of a small surface slope, as:

$$\alpha_{vis,direct} = \frac{\alpha^{0}_{vis,direct}}{\frac{\cos\left[\theta_z + \theta_{surf}\cos\varphi\right]}{\cos\theta_z}\left[1 - \frac{\theta_{surf}}{2}\right]} \qquad (2.22)$$

where $\alpha^{0}_{vis,direct}$ is the modelled albedo for a horizontal surface, $\alpha_{vis,direct}$ is the modelled albedo corrected for slope, θ_z is the solar zenith angle, θ_{surf} is the slope of the surface in radians, and φ is the solar azimuth, defined as zero when the solar azimuth is in the uphill direction from the detector (Grenfell *et al.*, 1994). Notice that Equation 2.22 was applied only to the visible portion of the spectrum, because testing carried out by Grenfell *et al.* showed Equation 2.22 to be successful between wavelengths of 0.4 to 1.4 μm. In addition, corrections for slope were applied only to the direct component of the incident irradiance because incoming solar radiation is largely isotropic under cloudy skies.

2.82 Optimization of Grain Sizes at each of the AWS's

The first step in developing a grain growth algorithm is to determine, through optimization, the grain sizes that would be required to model the measured albedo profiles

at each of the weather station sites. These simulations use the SNTHERM_Albedo algorithm with the alternative method to correct for a sloping surface as described in Section 2.81. Predicted albedos were optimized against measured albedos which were first corrected for the effects of a sloping surface as described in Section 2.53. Optimal grain sizes were determined through an iterative procedure, whereby grain size was modified by a small increment until modelled albedo was the same as measured albedo.

The predicted grain sizes for the L-AWS showed 2 main periods of rapid grain growth, from JD 181 to JD 192, and from JD 192 to JD 199. Upon these were superimposed diurnal cycles with sharp peaks in optimized grain size around midnight each day (Figure 2.16 (a); note that optimized grain sizes plotted in Figure 2.16 (a) were scaled between 0 and 200 mm for graphing purposes, since many peaks reached into the thousands of mm). Diurnal variations also appeared in the optimized grain sizes for the M-AWS and U-AWS, but grain sizes were smaller at these 2 sites than at the L-AWS (Figure 2.16b, c). At the M-AWS, there were 3 distinct peaks in optimized grain size on JD 183, 190 and 198 (Figure 2.16b). At the U-AWS, there were no distinct peaks in optimized grain size (Figure 2.16c).

Peaks in predicted grain size at the L-AWS and M-AWS coincided with the ends of periods of high melt, after which grain size dropped to a low value as the result of new snowfall events (see Figure 2.9 for timing of new snow events). Periods of grain growth probably occurred as a result of snowpack densification and wetting in response to increased surface melting. Melting probably played a large role in determining grain size variations since grain sizes showed an increased range and variability with a decrease in elevation on the glacier. For instance, at the U-AWS, where there was very little melt, grain sizes were relatively constant with maximum values up to 20 mm, whereas at the L-AWS, where there was extensive melting, grain sizes reached over 200 mm. The surface type at each of the AWS's also controlled grain size variations. The surface at the U-AWS consisted of hard-packed snow through the majority of the melt season, so grain sizes varied less and were lower than at the L-AWS, where the surface consisted of slush, superimposed ice or glacier ice.

Diurnal cycles in grain size simply reflect inadequacies in the methods used to correct surface albedo for the effects of surface slope and variations in the solar zenith angle. It appears that the slope corrections applied according to Equation 2.22 became less accurate for surfaces with larger slopes, and at times when the sun was orientated upslope from the surface. For instance, the L-AWS was located over a surface with a relatively high surface slope (4.0°). Extremely high peaks in grain size which occurred during many days at the L-AWS occurred at midnight when the sun was upslope from the station, when the sun's rays were just grazing the surface. At these times, Equation 2.22 over-predicted the surface albedo corrected for a sloping surface, and grain sizes tended towards infinity to compensate for this over prediction. This suggests that Equation 2.22 might not be suitable for locations with a high surface slope, as stated by Grenfell *et al.* (1994), or that the slope angle used in calculations at the L-AWS was incorrect.

Optimized grain size observations described above show that 2 main features of grain size variations need to be captured in a grain growth algorithm. The first is an overall increase in grain size with time after a snowfall event. The second is an increase in grain size in response to specific surface characteristics. For instance, the dramatic differences in grain size between the L-AWS and the M-AWS/ U-AWS suggest that very wet snow, superimposed ice and glacier ice should have much higher grain sizes than dry or partially wet snow.

2.83 Grain Growth Algorithm

This section describes an empirical snow grain growth algorithm developed by Marks (1988) which accounts for grain size variations after a snowfall event (Marks' unmodified algorithm will be called "GrainSize"). To account for large differences in optimized grain sizes between the L-AWS and M-AWS/U-AWS (Section 2.82), additional equations are included which simulate the effects of free-water content and snow or ice dirtiness on the surface albedo (this new algorithm will be called "EBM_GrainSize"). Based on optimized grain sizes, typical grain size values for superimposed ice and glacier ice are determined. Each step in the development of this grain growth algorithm is supported by results

showing the improvements in model predictions which result from the addition of new equations. For all steps in the development of the algorithm, results from the L-AWS are shown to illustrate the effects of various changes on surface albedo predictions. All simulations in this and subsequent sections are implemented within EBM-96, the surface energy balance model described in Chapter 4.

Description of GrainSize Algorithm developed by Marks (1988): This grain growth algorithm predicts the effective grain radius of snow, rather than a true grain radius which would correspond to actual field measurements of grain sizes. In this way, the effects of contaminants and free liquid water within the snowpack can be incorporated into the albedo algorithm through their influence upon the effective grain size. An increase in either snow contaminants or liquid water causes an increase in the effective grain radius, which in turn decreases the surface albedo. Because snow contaminants have been shown to cause a decrease in snow albedo in the visible part of the spectrum (Wiscombe and Warren, 1980), a distinction is made between effective grain radii for the vis and nir wavebands, and the factor for snow contamination is included in the equations for the vis grain radius only. The initial effective grain size after a snowfall event ($r_{vis(0)}$ and $r_{nir(0)}$), and the expected growth range for the visible and near-infrared ($r_{rg,vis}$ and $r_{rg,nir}$)are calculated as:

$$r_{vis(0)} = c_{im} r^{1/2} \tag{2.23}$$

$$r_{nir(0)} = r^{1/2} \tag{2.24}$$

$$r_{rg,vis} = c_{im}\left[r_{\max} - r\right]^{1/2} \tag{2.25}$$

$$r_{rg,nir} = \left[r_{\max} - r\right]^{1/2} \tag{2.26}$$

where r_{max} is the maximum grain radius for snow (1.6 mm), r is the grain radius at the time of deposition (r = 0.02 mm, based on observations by Marks) and c_{im} is the contamination factor. Studies of snowpack chemistry on John Evans glacier during the spring of 1995

showed that the late winter snowpack was probably very clean, because filtered samples of melted snow left no visible particles on the filter paper (M. Sharp, *pers. comm.*). Therefore, as an initial estimate, c_{im} was set at 0.

Grain growth rates, g_{th}, are approximated by a second order Chebyshev polynomial (Press *et al.*, 1989):

$$g_{th} = \cos\left[\frac{\arccos\left(\frac{t - t_{max}/2}{t_{max}/2}\right)}{2}\right] \tag{2.27}$$

where t = time since last snowfall + 1.0 (days) and t_{max} is the time in days for maximum grain growth to occur, set at 9 days (Marks, 1988). This function ranges from 0.0 to 1.0 as t approaches ∞, but achieves 80% of its range by $t = t_{max}$.

The visible and near-infrared effective grain radii (r_{vis} and r_{nir}) at time t after a snowfall event are:

$$r_{vis} = r_{vis(0)} + \left[r_{ag,vis} g_{th}\right] \tag{2.28}$$

$$r_{nir} = r_{nir(0)} + \left[r_{ag,nir} g_{th}\right] \tag{2.29}$$

Ice Grain Size: Modelling grain size during the transition between snow and ice at the surface of a high latitude glacier is complicated by the presence of superimposed ice. Superimposed ice refers to the layer of ice formed by the refreezing of meltwater at the base of a wet isothermal snowpack overlying a subzero glacier surface. Therefore, a two-phase approach, which models the surface as consisting of either snow or glacier ice, is an oversimplification for conditions found in the Arctic. Optimized grain sizes determined in Section 2.82 show that the transition from snow to superimposed ice involved a gradual increase in grain size. Therefore the approach adopted here is to prescribe constant effective grain radii for superimposed ice and glacier ice, and to implement a smooth

transition between the effective grain radii of the snow and ice surfaces. Table 2.5 shows the average grain sizes for superimposed ice and glacier ice as determined from optimized grain sizes at the L-AWS.

The transition between the effective grain radii for superimposed and glacier ice is scaled against the depth of superimposed ice:

$$r = r_{si} + \frac{SI_{max} - SI}{SI_{max}}\left(r_{gi} - r_{si}\right) \tag{2.30}$$

where SI and SI_{max} are the present and maximum depths of superimposed ice, and r_{si} and r_{gi} are the effective grain radii for superimposed and glacier ice.

2.84 Testing of the GrainSize Algorithm and Addition of New Equations

Simulations of surface albedo at each of the AWS's using the GrainSize algorithm described above are best at the U-AWS, with a decrease in accuracy towards the L-AWS (Run #1, Table 2.6, Figure 2.17 (b)). These results show that the primary weakness of the albedo simulations is at the L-AWS, where the albedo algorithm consistently over-estimates measured values. Since the L-AWS was subject to extensive melting, it is expected that the free water content of the snow might contribute to a lowering of the surface albedo. Therefore, an attempt was made to incorporate the effects of liquid water at the snow or ice surface on the surface albedo.

The effects of liquid water on the surface albedo are taken into account by multiplying the calculated grain radii by the fractional amount of free water at the surface. Liquid water at the surface is parameterized using the method described by van de Wal and Oerlemans (1994) for the Greenland ice sheet. Free water at the surface forms when ablation occurs:

$$w_l = \frac{M}{Z} + w_0 \quad \text{, where } 0 \le w \le 1 \tag{2.31}$$

where w_l is the fractional amount of liquid water at the surface, w_0 is the liquid water for the previous time step, M is the water equivalent melt and Z is the water equivalent snow

depth. If there is any water at the surface, it will runoff according to:

$$w_l = w_0 \exp\left(-\frac{2}{t_d}\right) \tag{2.32}$$

Where t_d is the time in days for water to completely drain from the site, set at 1 day based on simulations in Section 2.7.

The effective grain radii (vis and nir) are then modified to account for the effect of water:

$$r = r + rw_l \tag{2.33}$$

This equation states that the effective grain radius will double relative to dry snow when the surface is fully saturated with water (i.e.: w_l = 1.0), based on results from Marshall (1988).

Model simulations which included Equation 2.31 to 2.33 to account for the effects of liquid water on the surface albedo (Run # 2, Table 2.6 Figure 2.17 (b)) show an improvement over previous results. The greatest improvement is at the L-AWS, with no noticeable improvement at the U-AWS due to the lack of extensive melting at this site.

Although including equations to account for the effects of liquid water on the surface albedo does improve results, predicted albedo at the L-AWS still exceeds measured values. Therefore, additional equations were added to improve simulations at the L-AWS. This was done by developing a parameterization for surface contamination. Although it is questionable whether surface contamination has a significant effect on the surface albedo at John Evans Glacier, including a factor for surface contamination was the only way of forcing predicted albedo values to be as low as predicted values at the L-AWS. A possible physical explanation for this is that the L-AWS is located in the ablation zone, where the summer snowpack overlies glacier ice, which is generally dirtier than superimposed ice. Therefore, the solar beam, especially when it is shallow, might penetrate through to the underlying glacier surface which has a lower albedo than the snow.

Surface contamination is modelled as a function of elevation, based upon the assumption that dust and morainic material concentrations increase at lower elevations. Oerlemans (1992) made a similar assumption in defining a background albedo profile, which would theoretically exist at the end of an infinitely long melt season. The albedo for this profile decreased with an increase in distance downglacier from the equilibrium line. Using the Oerlemans model with an estimated equilibrium line of 900m produces a base albedo which is about 5 times higher at the equilibrium line than at the snout of the glacier. Although Oerlemans' equations for the background albedo describe a non-linear pattern, the justification for such a pattern is not clear. Therefore, since data are not available for a more detailed treatment, surface contamination is modelled as a simple function of elevation relative to the equilibrium line:

$$c_{tm} = \left(\frac{-1.0}{200.0 * elev}\right) + 5.0 \quad \text{, if } elev < 900 \text{ m} \tag{2.34}$$

$$c_{tm} = 1.0 \quad \text{, if } elev \geq 900 \text{ m} \tag{2.35}$$

where *elev* is the elevation above sea level in meters.

Including a factor for the contamination of the surface greatly improves model predictions at the L-AWS, and slightly improves simulations at the M-AWS (Run # 3, Table 2.6 Figure 2.17 (c)).

The grain size algorithm described above, including all of the additional changes described in this section (Equation 2.31 to 2.35), is called "EBM_GrainSize". Figure 2.18 shows grain sizes predicted by EBM_GrainSize at each of the weather stations. Grain radii are most variable at the L-AWS, where the maximum effective grain radius is an order of magnitude higher than at the other 2 sites. The L-AWS is the only site where surface contamination is considered, and is therefore the only station where vis and nir radii are different. Grain radii at all sites decrease to 0.02 mm whenever there is a new snowfall.

The development of EBM_GrainSize is the last step in the development of the combined

albedo model, EBM_Albedo, which is implemented in the surface energy balance model EBM-96, described in Chapter 4. As this is the final stage in development of EBM_Albedo, albedo predictions for each of the 3 weather stations derived from EBM_Albedo are discussed in detail in the next section.

2.85 Albedo Predictions using EBM_Albedo at Each of the Weather Stations

Lower Weather Station: Modelled surface albedo at the L-AWS generally underestimates measured albedo during periods when the surface consists of wet snow or superimposed ice (JD 172 to JD 187, Figure 2.19 (a); see Figure 2.12 for surface characteristics at the L-AWS). When glacier ice is exposed at the surface (JD 187 to JD 201), the model more frequently overestimates measured albedo. These results suggest the predicted grain sizes for wet snow and superimposed ice may be too low, while predicted grain sizes for glacier ice may be too high.

Middle Weather Station: The simulation for the M-AWS predicts a decrease in surface albedo with time after a new snowfall (Figure 2.20 (a)). Diurnal variations are predicted during periods of direct sunlight. However, the model underestimates the magnitude of diurnal variations observed in the field. As the melt season progresses, modelled albedo becomes higher than measured albedo, especially after JD 196 when the surface consists of large superimposed ice crystals.

Upper Weather Station: The model does a good job at simulating the trend in surface albedo at the U-AWS (Figure 2.20 (b)). During periods of direct sunlight, the magnitude of diurnal variations is lower than observed in the field.

In terms of the average difference between modelled and measured albedo, the EBM_Albedo algorithm performs best for the M-AWS (RUN # 3, Table 2.6). Although it produces the lowest coefficient of correlation (0.36, compared with 0.42 at the L-AWS and 0.48 at the U-AWS), the run for the M-AWS produces the lowest seasonal difference, standard error and absolute error of all the weather station sites. EBM_Albedo does not

perform as well at the U-AWS, probably because grain sizes were not simulated correctly at this site. The U-AWS was the windiest of the 3 weather station sites, with an average windspeed of 2.86 ms^{-1}, compared with average windspeeds of 2.22 ms^{-1} and 1.73 ms^{-1} at the M-AWS and L-AWS respectively. Therefore, grain sizes at the U-AWS may have been strongly affected by wind. Since the effects of wind on snow grain size are not considered in the EBM_GrainSize algorithm, grain size predictions at the U-AWS may be incorrect.

Simulations for the M-AWS are better than for the L-AWS because more detailed observations of surface characteristics were carried out at the M-AWS. At the L-AWS, even if the effective grain sizes used for superimposed and glacier ice were correct, EBM_Albedo would only provide correct albedo predictions if the energy balance model correctly predicted the timing of snow and superimposed ice melt correctly. To illustrate this point, a series of model simulations were run for the L-AWS, each of which used a different value for the snow depth at the start of the run (Figure 2.21). 0.2425 m WE is the value obtained from the snow depth parameterization described in Section 4.53 for the L-AWS. Values higher and lower than 0.2425 m WE (0.15, 0.20, 0.30 and 0.35 m WE) were used as initial snow depths to test the sensitivity of EBM_Albedo to changes in the timing of the exposure of superimposed ice and glacier ice (Table 2.7).

Reducing the initial snow depth at the L-AWS reduces the coefficient of determination and increases the standard and absolute errors in albedo predictions. Increasing the initial snow depth to 0.30 m WE reduces the seasonal difference and absolute error, but strongly reduces the coefficient of determination of albedo predictions at the L-AWS. Thus increasing the initial snow depth by 0.06 m WE improves the model's ability to predict the measured albedo values but not the trend in measured albedo. In comparing albedo simulations, it is important to consider that melt predictions can be sensitive to the timing of albedo variations, since deviations between measured and modelled albedo during periods of high insolation create more error in melt predictions than similar deviations during periods of low insolation. Therefore, it may be more important to properly simulate the trend in surface albedo, as indicated by the coefficient of determination, than

to properly simulate overall average values.

2.9 Testing of EBM_Albedo for Surface Energy Balance Calculations

A series of 4 simulations was run to compare melt predictions at each of the AWS's, using different albedo algorithms (Table 2.8). All simulations were carried out using EBM-96. The purpose of this analysis is to (a) compare simulations based on modelled albedo with those based on measured albedo, (b) compare the new albedo model with the W-O algorithm used in EBM-94, (c) look at the effect on melt predictions of including the influence on albedo of diurnal and seasonal variations in zenith angle, and (d) consider the effect of slope correcting albedo measurements on the quality of simulations based on measured albedo values.

RUN # 1 produced the highest coefficients of determination and lowest standard errors, and performed best at the L-AWS and M-AWS (Figure 2.22, Table 2.9). This is to be expected since RUN # 1 used measured albedo data. The 4 remaining simulations are compared for each of the weather station sites.

Lower Weather Station: All simulations except for RUN # 5 performed well at this site, however RUN # 2 performed slightly better than the others. RUN # 2 was closest in its prediction of the snow depth at the end of the simulation, and had a high coefficient of determination and a low standard error.

Middle Weather Station: Surprisingly, RUN # 4 performed best at this site, followed by RUN # 2, RUN # 1, RUN # 5 and RUN # 3. It is not clear why removing diurnal variations from EBM_Albedo (RUN # 4) improved melt simulations at the M-AWS, but it may suggest that the slope value used for the M-AWS was incorrect. If the slope angle or aspect were not defined correctly, then corrections to the surface albedo for a sloping surface, which depend in part on the solar zenith angle, might have been over or underestimated as the zenith angle changed through the day. Holding the zenith angle constant may have averaged out any errors in the slope corrections.

Upper Weather Station: RUN # 1 performed best at this site, followed by RUN # 2. RUN # 3 and RUN # 4 greatly overestimate melt, while RUN # 5 underestimates melt.

At all 3 weather stations, EBM_Albedo (RUN # 2) did a substantially better job at predicting snow ablation than the W-O algorithm (RUN # 3) implemented in the previous version of the energy balance model (EBM-94). The improvement is most dramatic at the M-AWS and U-AWS, where the W-O algorithm substantially over-predicts melt. This suggests that melt predictions from EBM-94 may have overestimated melt. Simulations using measured data without slope corrections (RUN # 5) performed quite poorly at all 3 weather stations, substantially underestimating melt. This shows that correcting albedo for a sloping surface is very important in simulating ablation at high polar sites.

2.10 Comparison with other Studies and Implications for Glacier Mass Balance in the Arctic

The surface albedo of glaciers at high polar latitudes appears to be very sensitive to surface slope because of the high solar zenith angles at these . This is in agreement with a study conducted by Grenfell *et al.* (1994) on the Antarctic ice sheet, in which significant errors were found in albedo measurements made by a sensor aligned parallel to the horizon over a sloping surface. It is therefore surprising that Zuo and Oerlemans (1996), in a study of the albedo of the Greenland ice sheet, regarded errors in sensor alignment of no more than a few degrees as being insignificant to albedo measurements. The results of this study support the conclusions of Blöschl (1991), that sites where albedo is to be monitored must be selected carefully, and that instruments should be checked frequently.

To date there have been no studies of the effects of diurnal variations in surface albedo on the mass balance of high polar glaciers. Although Zuo and Oerlemans (1996) collected hourly albedo data, their analyses are based on daily average data. This paper suggests that diurnal variations in surface albedo can be important for energy balance simulations, especially for sites where the surface is sloping. Further investigations are necessary to determine whether higher resolution modelling of surface albedo substantially improves energy balance simulations.

This paper has shown that albedo algorithms, such as the one developed for the Greenland ice sheet by van de Wal and Oerlemans (1994), provide inadequate predictions of surface albedo, and that errors introduced to melt simulations by such incorrect predictions can be substantial. In models which simulate the effects of global climate change on the mass balance of high polar glaciers and ice sheets, it may be worthwhile to implement a physically based albedo algorithm in energy balance simulations. An algorithm such as the one described in this paper might not only improve present-day energy balance simulations, but it may also be useful in simulating feedback mechanisms between the surface and the atmosphere which result from global climate change. For example, if climate change were to cause an increase in cloudiness, this would alter the spectral composition of incoming solar radiation, increasing the diffuse fraction of the solar radiation. Marshall and Warren (1987) have already implemented a physically based albedo algorithm into GCM models. It therefore seems reasonable that physically based albedo algorithms should be implemented within glacier and ice sheet energy balance models.

2.11 Conclusion

Surface energy balance models developed for Arctic glaciers require an accurate albedo algorithm to correctly predict net solar radiative fluxes at the surface. Past albedo algorithms applied to Arctic regions have not taken into account large diurnal variations in surface albedo which occur at high latitude sites. Omitting these higher order patterns in surface albedo may reduce the accuracy of energy balance calculations. This is because zenith angles are so high in the Arctic, that small differences in surface slope or azimuth can have a large impact upon surface albedo. This study has shown that for a site with a small surface slope of 4.6°, facing towards the north, the surface albedo changes by up to 50% from that which would be measured over a horizontal surface. Albedo was found to be highest around the time when incident solar radiation fluxes were also highest. Therefore, models which do not incorporate the diurnal cycling of albedo, and which do not correct for surface slope and azimuth, especially at high latitude locations, will probably produce inaccurate melt predictions.

Use of this type of albedo algorithm in energy balance models is possible only if surface characteristics, namely the effective grain size, can be accurately predicted. Since surface characteristics were monitored in this study, it was possible to develop empirical approximations of the effects of surface contamination and water content on the effective grain size. These empirical algorithms should be tested on other glaciers to determine whether similar results are obtained. If so, then this albedo model may be useful for other sites in the Arctic. Otherwise, in situations where data on surface characteristics are not available, it may be better to use a less detailed model which does not depend on measured physical parameters.

Met. Station Name	Latitude	Longitude	Elevation (m a.s.l.)
L-AWS	79°37'52"	74°04'38"	261
M-AWS	79°40'17"	74°20'59"	824
U-AWS	79°42'35"	74°33'20"	1183

Table 2.1 Location and elevation of each automated weather station.

Measurement	Instrument and model	Measurement Range	Instrument Error
Air Temperature	Campbell 107F Temperature probe	-53°C to +48°C	±0.4°C
Relative humidity sensor	HMP35CF Vaisala RH probe	0 to 100% RH	±2% RH (0 to 90% RH) ±3% RH (90 to 100% RH)
Incoming short-wave radiation	LI200s Li-COR Pyranometer	0.280-2.80 µm	±5% maximum
Outgoing short-wave radiation	Kipp and Zonen CM7 Pyranometer	0.305-2.80 µm	±2%
Net Radiation	REBS Q7 net radiometer	0.250 to 6.0 µm	wind speed dependent
Air Pressure	CS105 Barometric Pressure Sensor	600 to 1060 mb	±0.5 mb (@ 20°C)
Wind Speed	05103 R.M. Young Wind Monitor	0 to 60 m/s	1.0 m/s threshold sensitivity
Wind Direction	05103 R.M. Young Wind Monitor	360°	1.0 m/s threshold sensitivity at 10° displacement
Height of snow/ice surface	UDG01 Ultrasonic Depth Gauge	0.6 to 10 m	±1 cm or 0.4% of distance to target (whichever is greatest)

Table 2.2 Specifications of meteorological instruments. These instruments were connected to a Campbell Scientific CR 10 data logger and SM 192/716 Storage module.

Station	Start of Measurements	End of Measurements
L-AWS	JD 172, 1996	JD 212, 1996
M-AWS	JD 167, 1996	JD 202, 1996
U-AWS	JD 169, 1996	JD 216, 1996

Table 2.3: Periods of instrumental record at each of the 3 automated weather station sites.

Weather Station	Slope Azimuth (°)		Slope Angle (°)	
	GPS	Manual	GPS	Manual
Lower	8.55	45.0	4.31	4.0
Middle	144.18 200.0		5.48	4.3

Table 2.4: Comparison of manual and GPS methods for determining surface slope and azimuth. GPS data for the U-AWS were obtained but could not be plotted on the DEM because the U-AWS was located outside the DEM boundaries.

	Julian Days	Average Grain Radius (mm)
Superimposed Ice	180 - 186	33.15
Glacier Ice	186 - 201	100.18

Table 2.5: Average grain radii at the L-AWS determined from optimized grain sizes.

	L-AWS			M-AWS			U-AWS		
RUN #	1	2	3	1	2	3	1	2	3
Number of Data Pairs	936	936	936	816	816	816	960	960	960
Mean Observed	0.64	0.64	0.64	0.77	0.77	0.77	0.81	0.81	0.81
Mean Calculated	0.86	0.82	0.71	0.83	0.83	0.79	0.83	0.83	0.85
Coefficient of Determination	0.11	0.17	0.42	0.29	0.30	0.36	0.48	0.48	0.48
Seasonal Difference	-0.33	-0.28	-0.10	-0.07	-0.07	-0.02	-0.02	-0.02	-0.05
Standard Error	0.08	0.09	0.11	0.07	0.07	0.07	0.08	0.08	0.08
Absolute Error	-0.14	-0.11	-0.04	-0.04	-0.04	-0.01	-0.01	-0.01	-0.03

Table 2.6: Statistical attributes for model runs #1 to #3 (showing steps in the development of the EBM_Albedo algorithm) at each of the weather station sites.

Coefficient of Determination = $\left[\sum(x_o - \bar{x}_o)^2 - \sum(x_c - x_o)^2\right] / \sum(x_o - \bar{x}_o)^2$

Seasonal Difference = $\left[\sum(x_o - x_c)\right] / \sum(x_o)$

Standard Error = $\left[\sum(x_c - x_o)^2 / n\right]^{0.5} / \bar{x}_o$

Absolute Error = $\sum(x_o - x_c) / n\bar{x}_o$

where x_c is the calculated value, x_o is the observed value, $\bar{x}$ is the mean value, and n is the total number of observations

	s = 0.15	s=0.20	s=0.24	s=0.30	s=0.35
Mean Observed	0.64	0.64	0.64	0.64	0.64
Mean Calculated	0.56	0.57	0.71	0.66	0.72
Coefficient of Determination	0.07	0.06	0.42	0.01	0.12
Seasonal Difference	0.13	0.11	-0.10	-0.02	-0.12
Standard Error	0.23	0.23	0.11	0.19	0.14
Absolute Error	0.05	0.05	-0.04	-0.01	-0.05

Table 2.7: Statistical data for model runs testing the effect of changes in the initial snow depth on albedo predictions at the L-AWS.

Model Simulation	Albedo Parameterization
RUN # 1	measured albedo (corrected for a sloping surface)
RUN # 2	EBM_Albedo
RUN # 3	W-O Albedo Algorithm
RUN # 4	EBM_Albedo with constant solar zenith angle (66.5°)
RUN # 5	measured albedo without corrections for a sloping surface

Table 2.8: Description of albedo parameterizations used for each of the energy balance model simulations.

	L-AWS					M-AWS					U-AWS				
RUN #	1	2	3	4	5	1	2	3	4	5	1	2	3	4	5
Number of Data Pairs	582	582	582	582	582	816	816	816	816	816	960	960	960	960	960
Mean Observed	0.12	0.12	0.12	0.12	0.12	0.24	0.24	0.24	0.24	0.24	0.28	0.28	0.28	0.28	0.28
Mean Calculated	0.15	0.16	0.15	0.19	0.25	0.21	0.22	0.12	0.25	0.28	0.26	0.28	0.16	0.21	0.31
Coefficient of Determination	0.97	0.97	0.95	0.98	0.98	0.93	0.92	0.93	0.93	0.93	0.41	0.41	0.29	0.32	0.32
Seasonal Difference	-0.25	-0.33	-0.26	-0.55	-1.04	0.12	0.09	0.51	-.03	-0.14	0.10	0.02	0.43	0.25	-0.09
Standard Error	0.03	0.02	0.03	0.01	0.00	0.03	0.01	0.04	0.01	0.00	0.03	0.02	0.08	0.06	0.00
Absolute Error	0.00	0.00	0.00	-0.01	-0.02	0.01	0.01	0.03	0.00	-0.01	0.01	0.00	0.03	0.02	-0.01

Table 2.9: Statistical data for model runs testing melt predictions at each of the weather station sites using different albedo parameterizations.

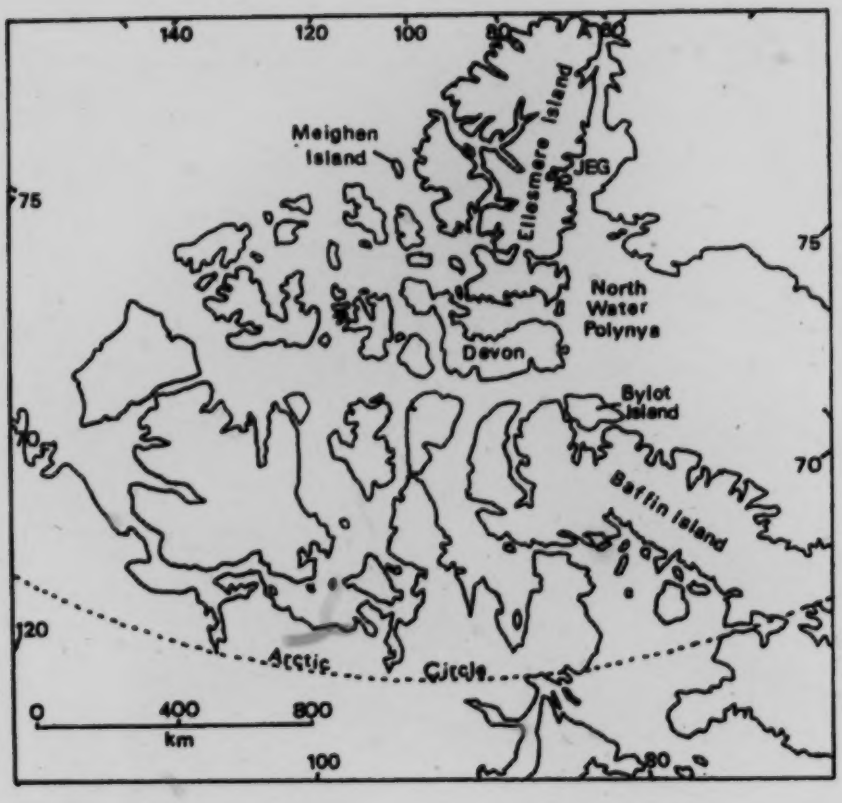

Figure 2.1: Map of the Canadian Arctic Islands. JEG = John Evans Glacier, A=AES Meteorological station at Alert.

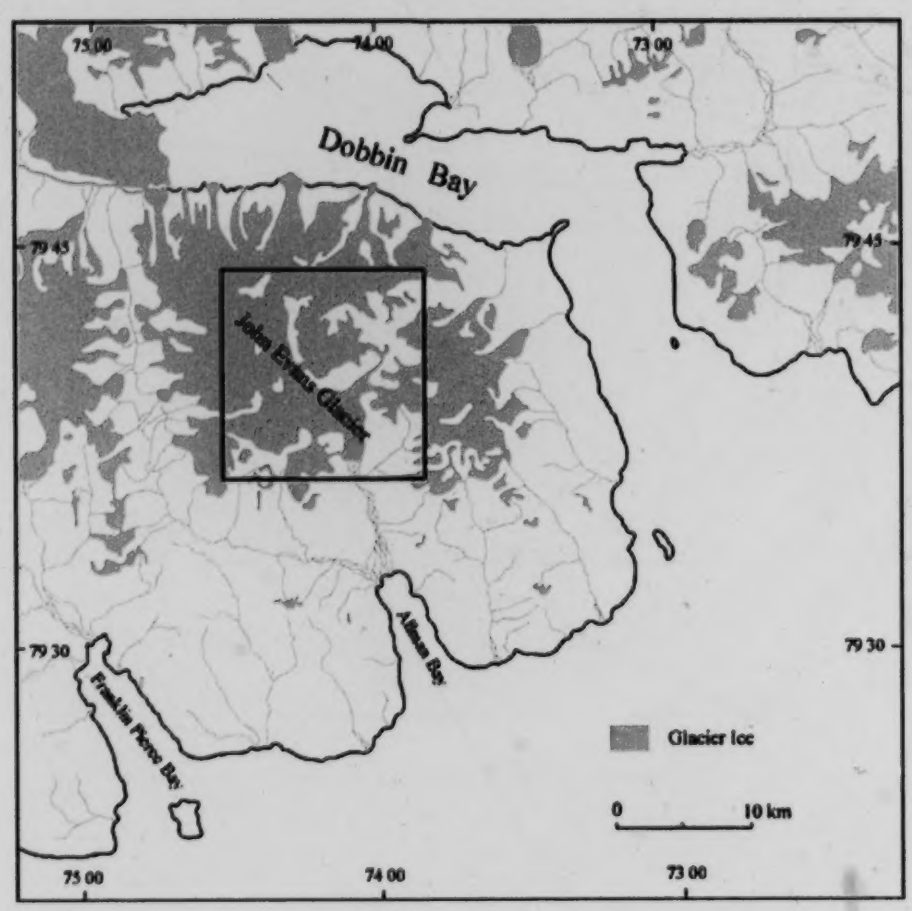

Figure 2.2: Location of John Evans Glacier, Ellesmere Island, Nunavut, Canada.

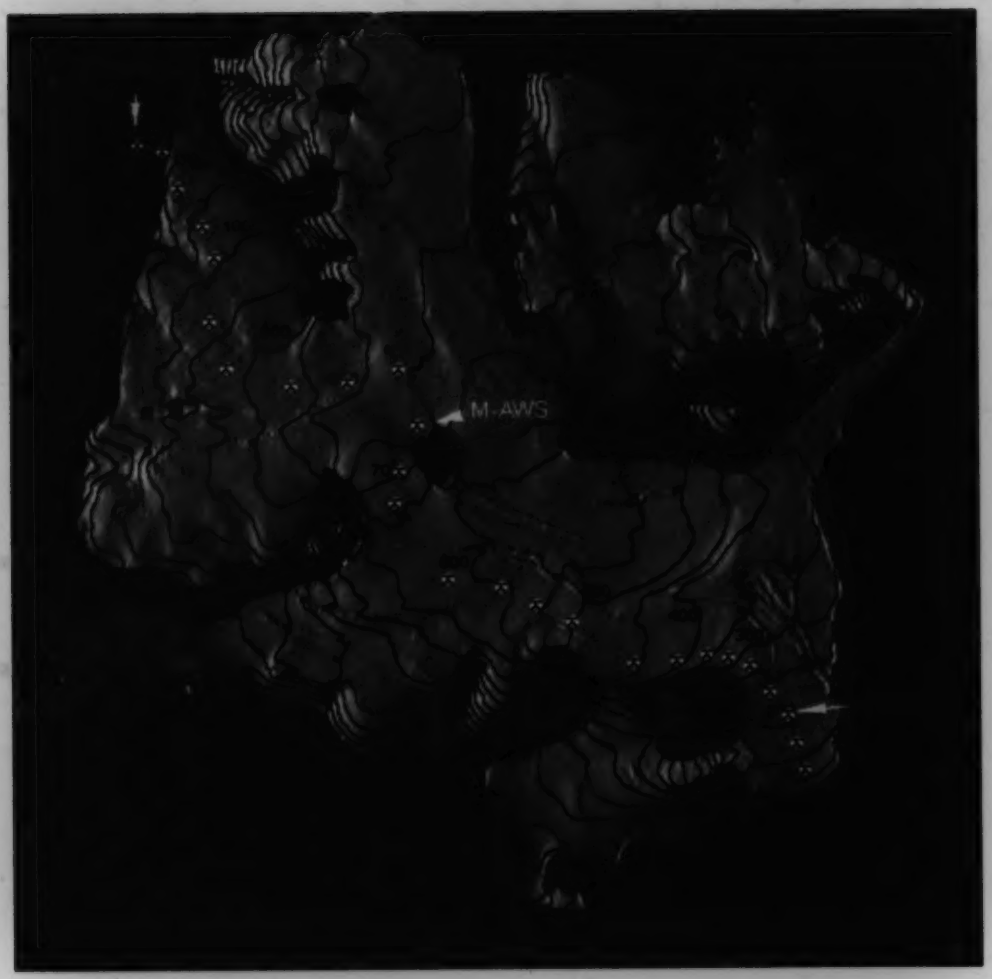

Figure 2.3: Contour map of John Evans Glacier with locations of lower, middle and upper automated weather stations (marked with arrows) and stake locations (marked with circles).

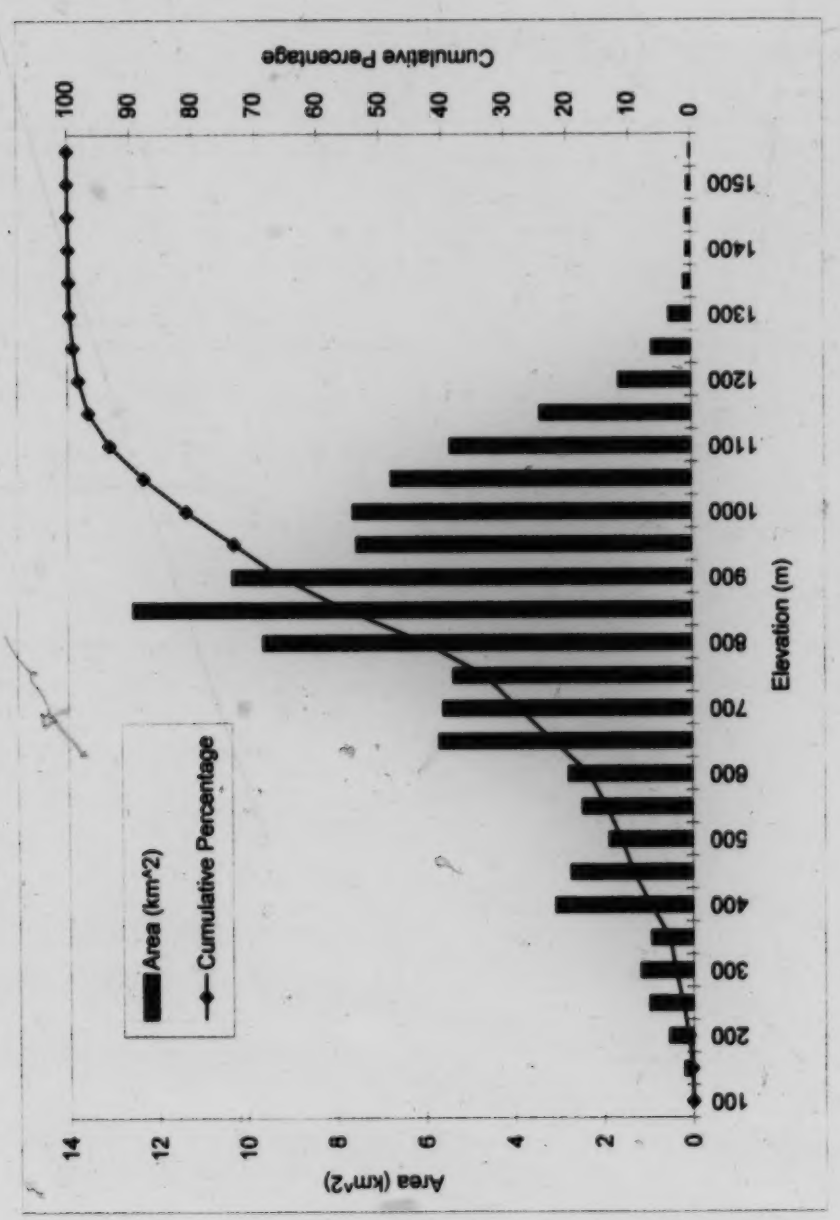

Figure 2.4: Surface area distribution of John Evans Glacier.

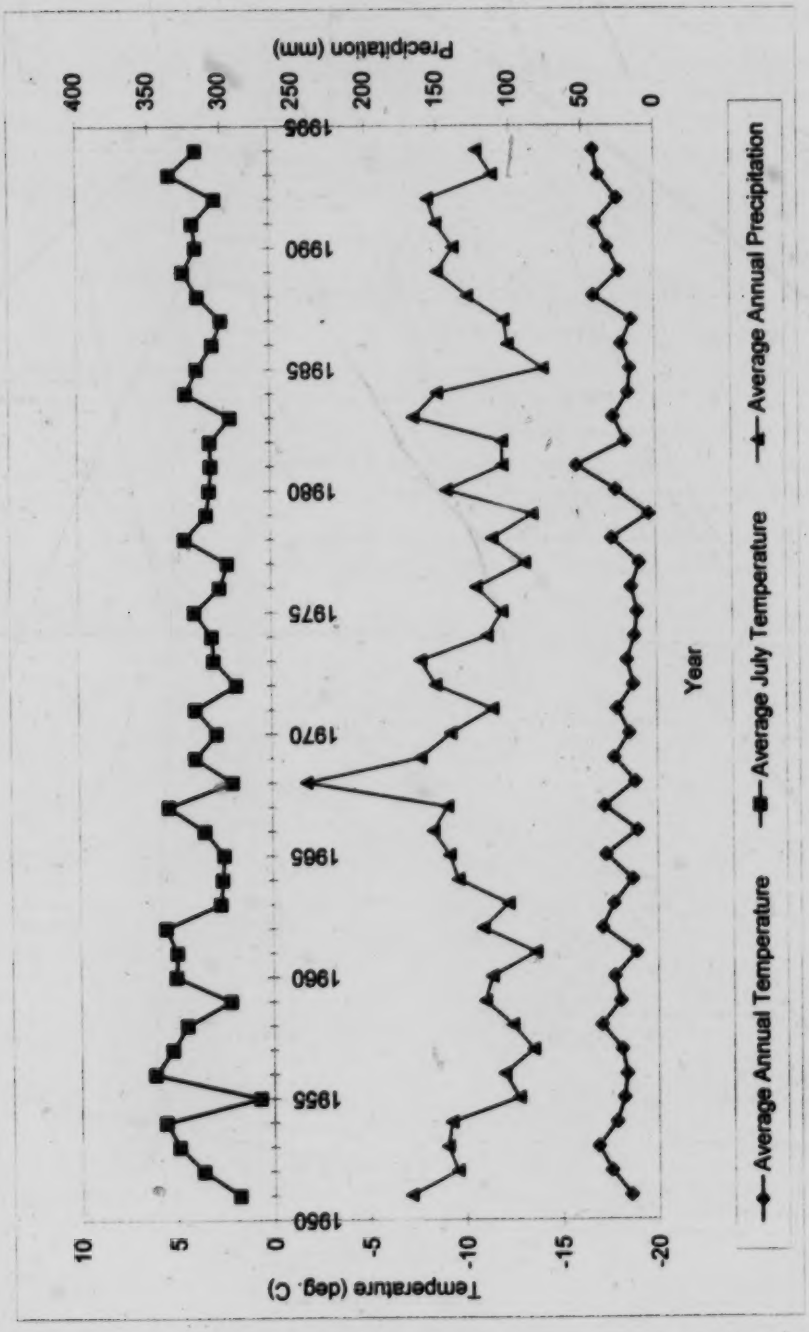

Figure 2.5: Temperature and precipitation records from AES meteorological station, Alert.

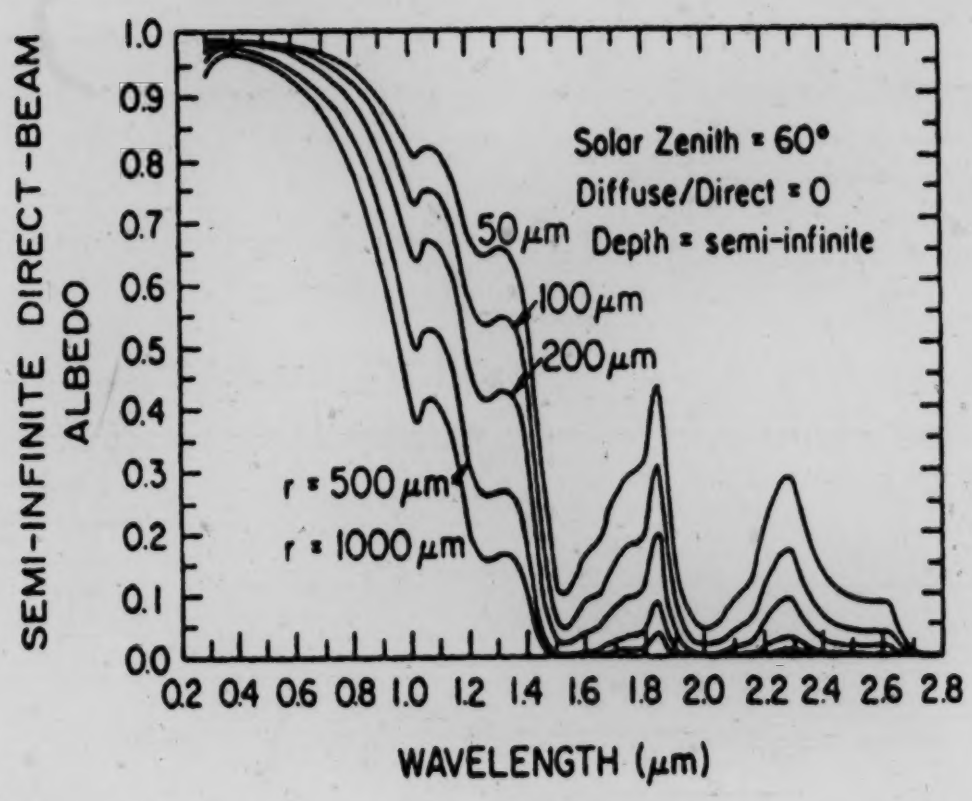

Figure 2.6 : Semi-infinite direct beam albedo as a function of wavelength for various grain radii. (Reproduced from Wiscombe and Warren, 1980, fig. 8, p. 2722).

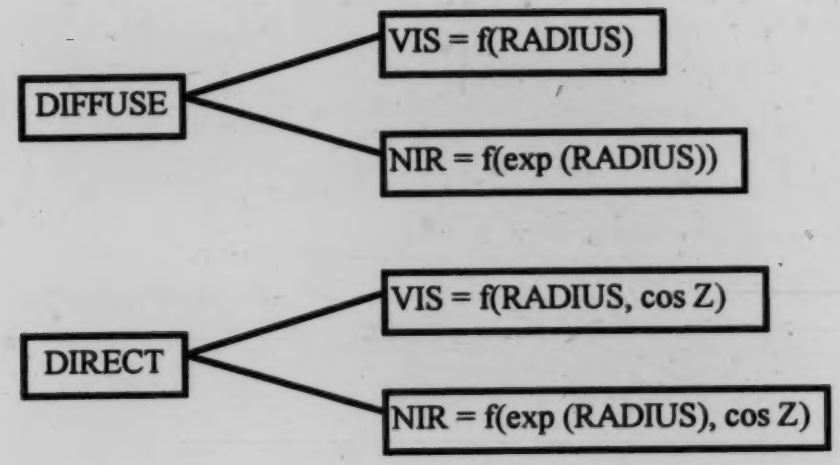

Figure 2.7: Schematic representation of the albedo model developed by Marks (1988) and adopted in the present albedo algorithm.

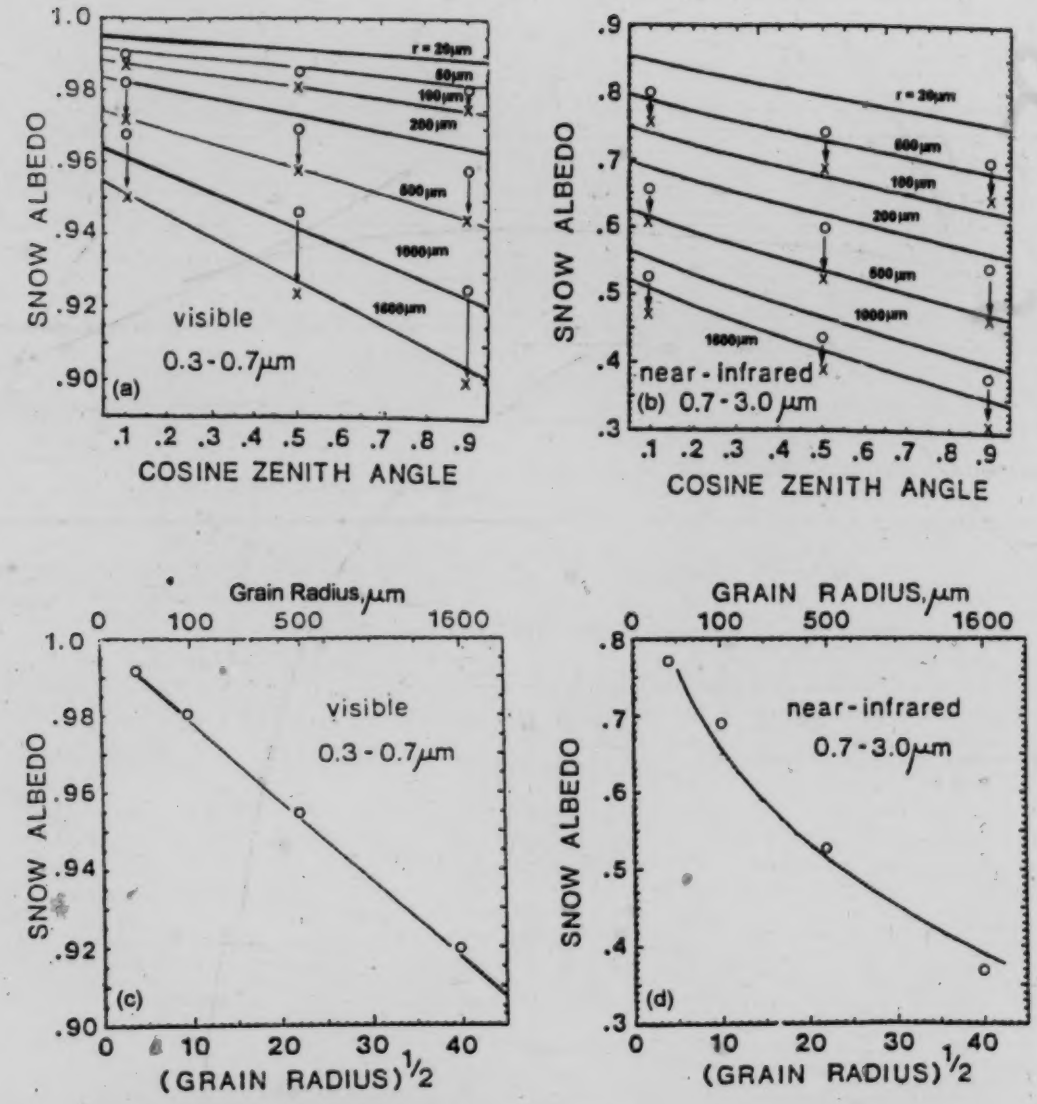

Figure 2.8 (a) & (b): Integrated albedo versus cos(z) for direct radiation from Marshall and Warren (1982). Points "O" are plotted from Marks' (1987) equations, while points "X" are from Eq. 2.3 and 2.4, which include corrections made by Jordan (1995).

Figure 2.8 (c) and (d): Integrated albedo versus square root of grain radius for diffuse albedo, from Marshall and Warren (1982). Points "O" are plotted from Eq. 2.1 and 2.2.

(Reproduced from Jordan, 1995)

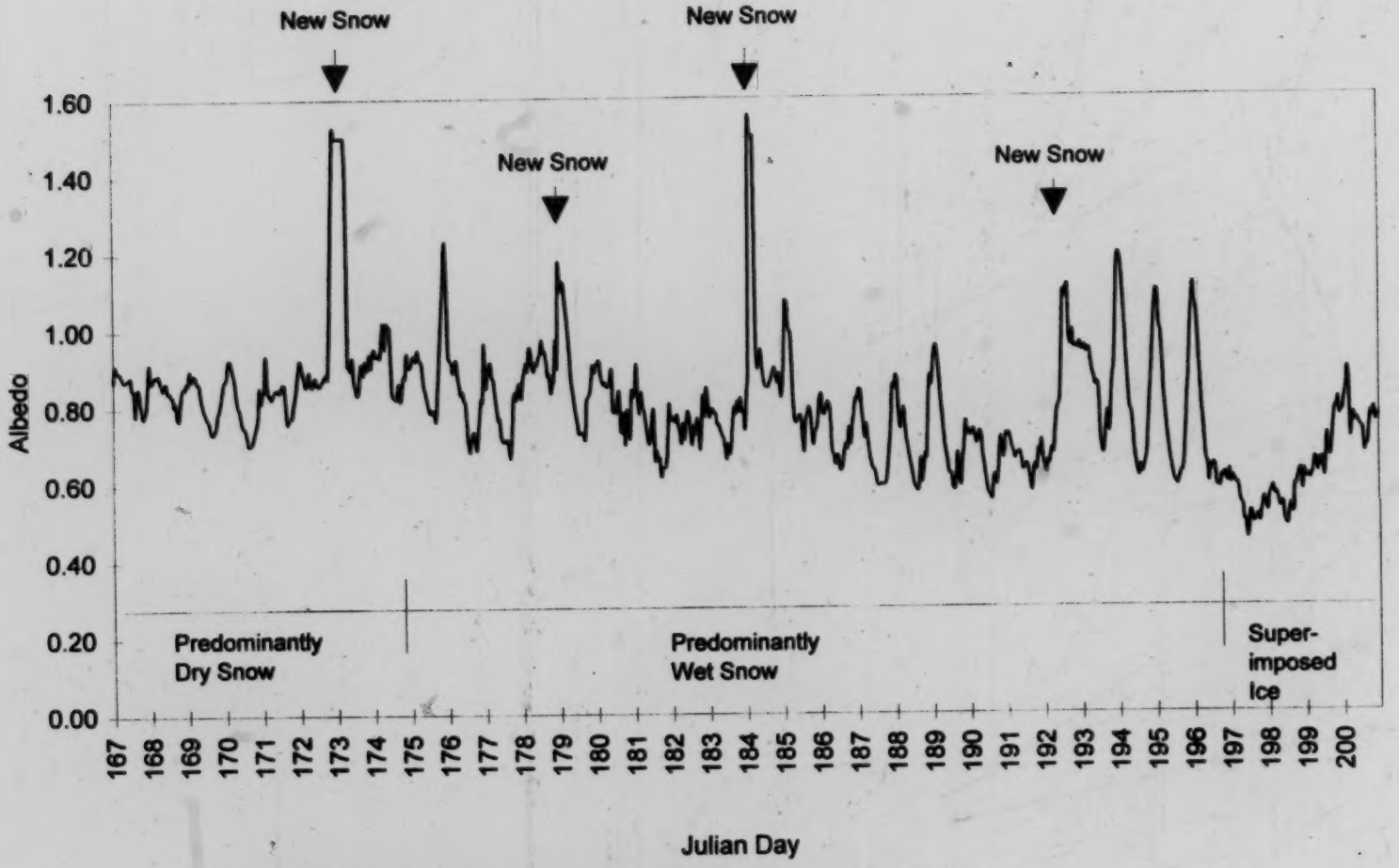

Fig. 2.9: Surface albedo measured at the M-AWS, uncorrected for slope or the effects of snowfall on the upward facing sensor.

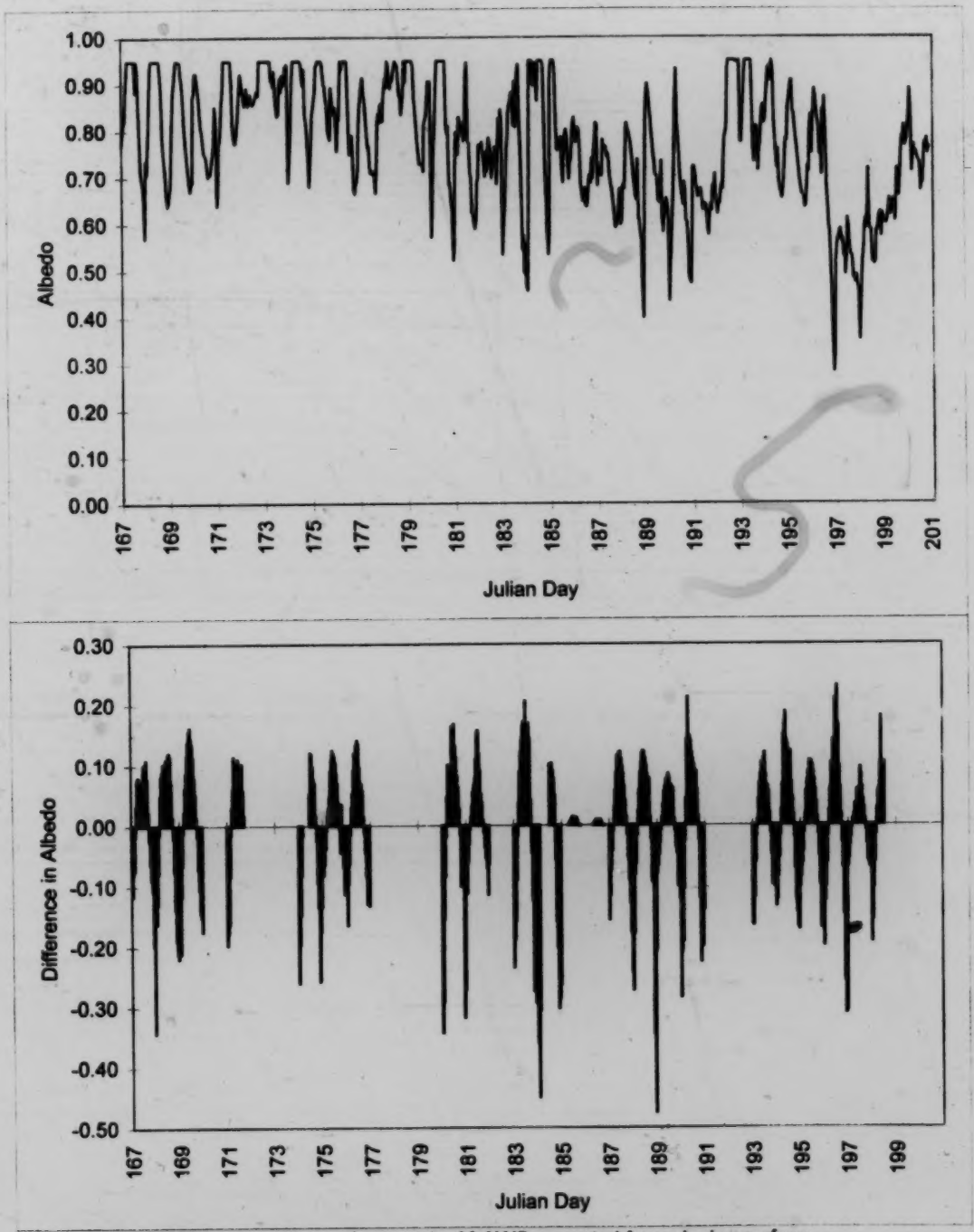

Figure 2.10: (a) Measured surface albedo at the M-AWS corrected for a sloping surface.
(b) Difference between slope-corrected and uncorrected albedo values at the M-AWS.

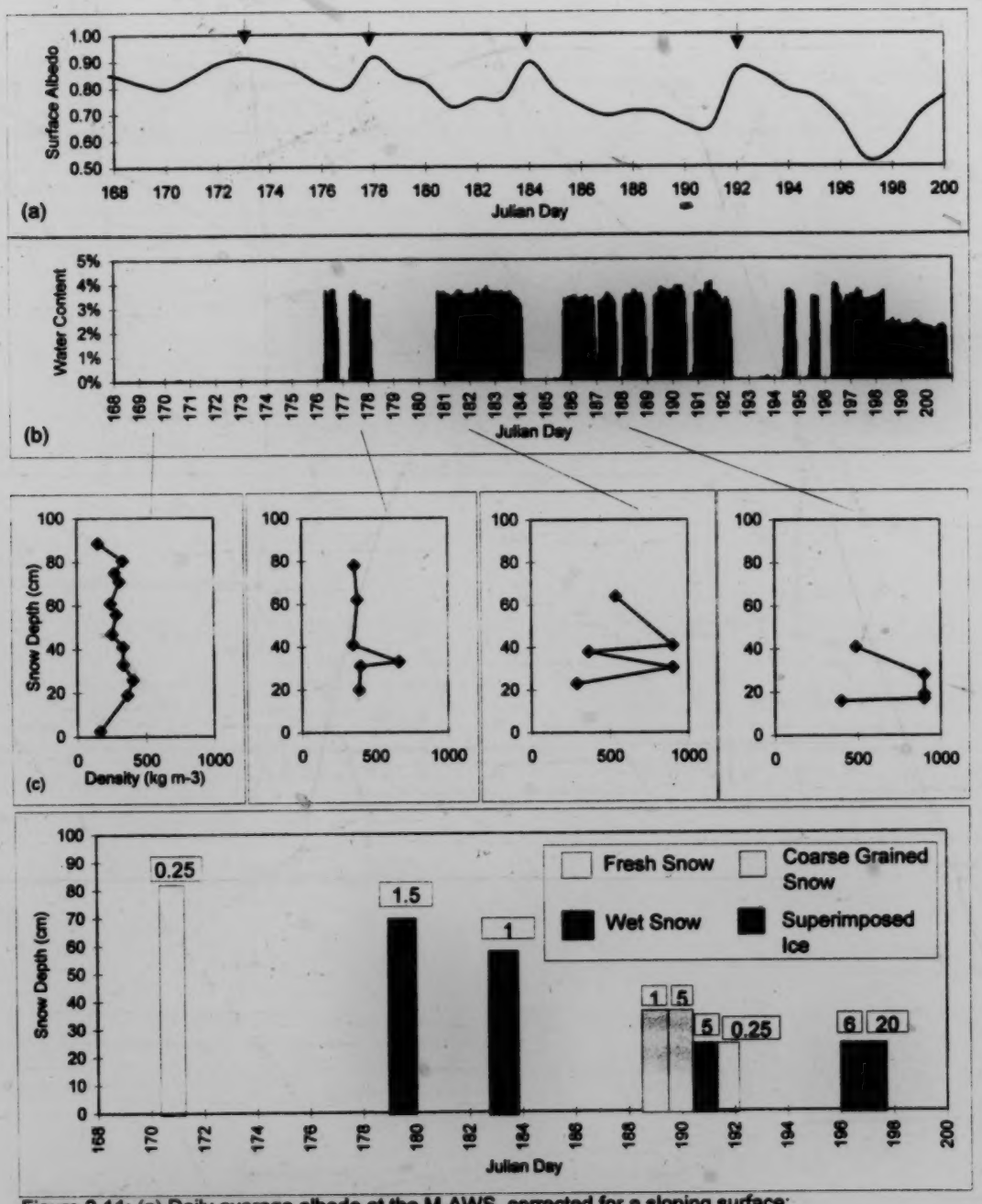

Figure 2.11: (a) Daily average albedo at the M-AWS, corrected for a sloping surface; (b) Fractional free water in the uppermost snow layer at the M-AWS, as determined from the SNTHERM model; (c) Measured snowpack density at the M-AWS; (d) Observed snow characteristics, snow depth and grain radius of snow in the uppermost layer at the M-AWS. (arrows in (a) mark the timing of new snowfall events).

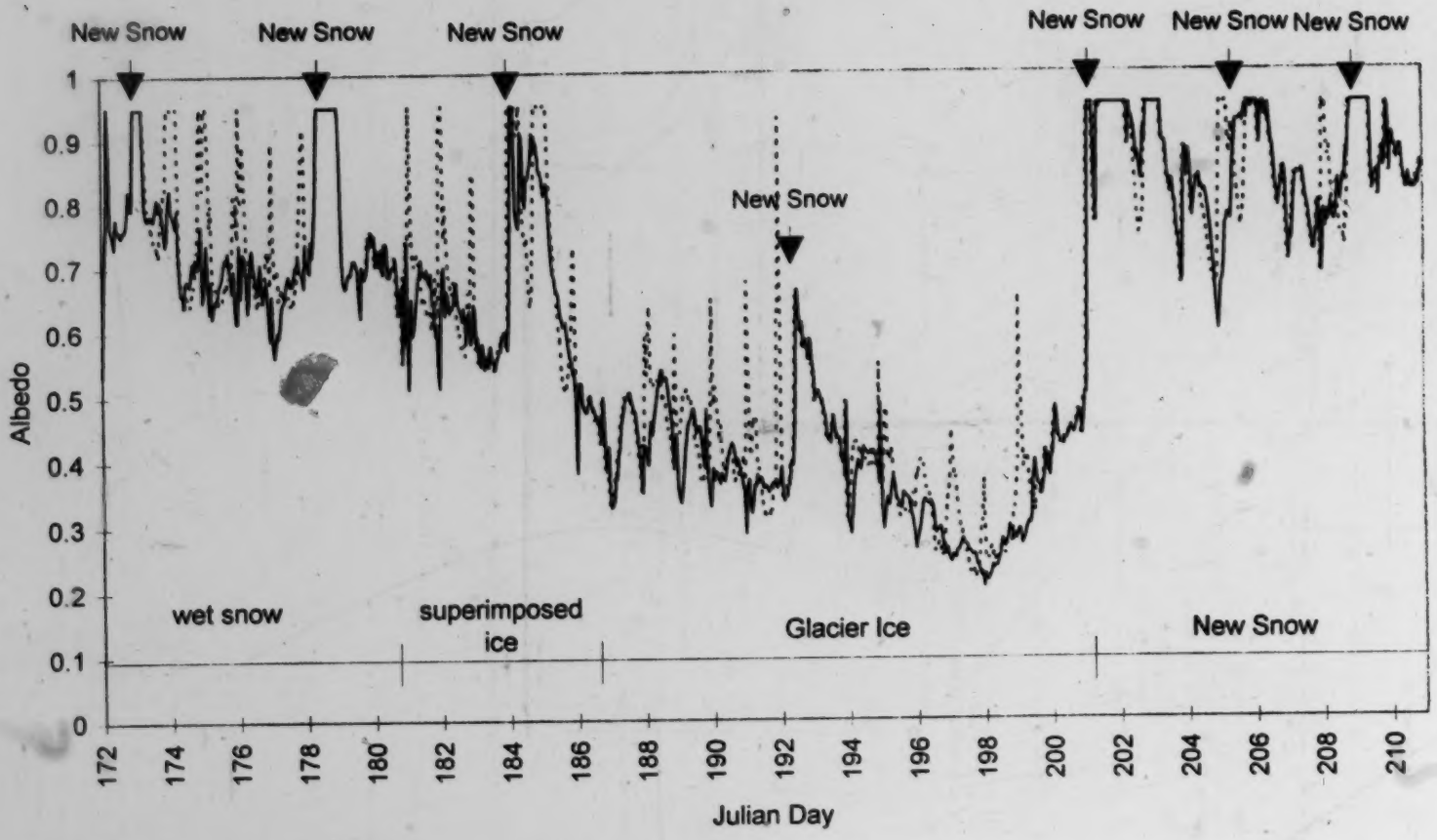

Fig. 2.12: Surface albedo measured at the L-AWS. Solid line is uncorrected for slope, dashed line is corrected for slope.

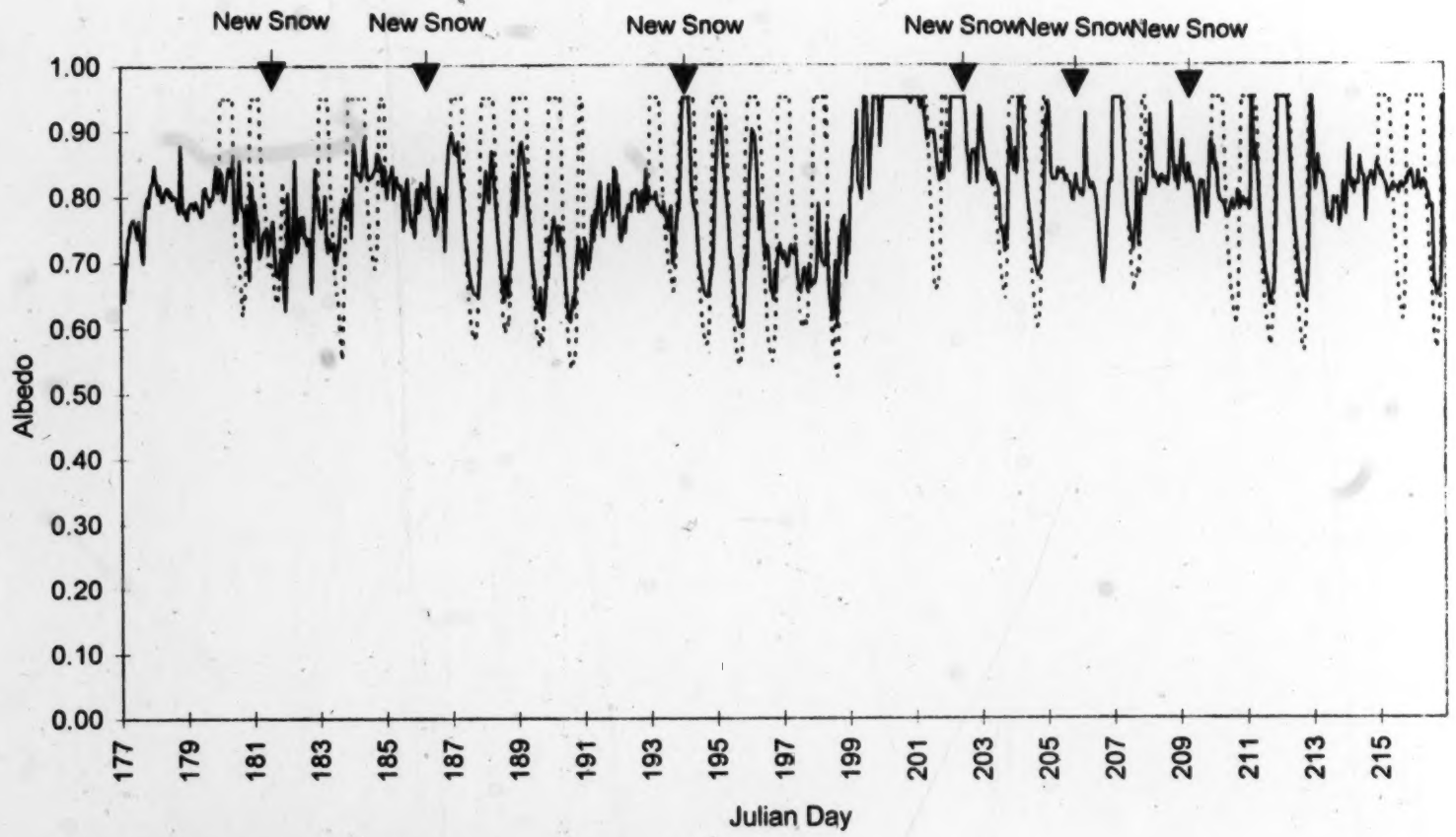

Fig. 2.13: Surface albedo measured at the U-AWS. Solid line is uncorrected for slope, dashed line is corrected for slope.

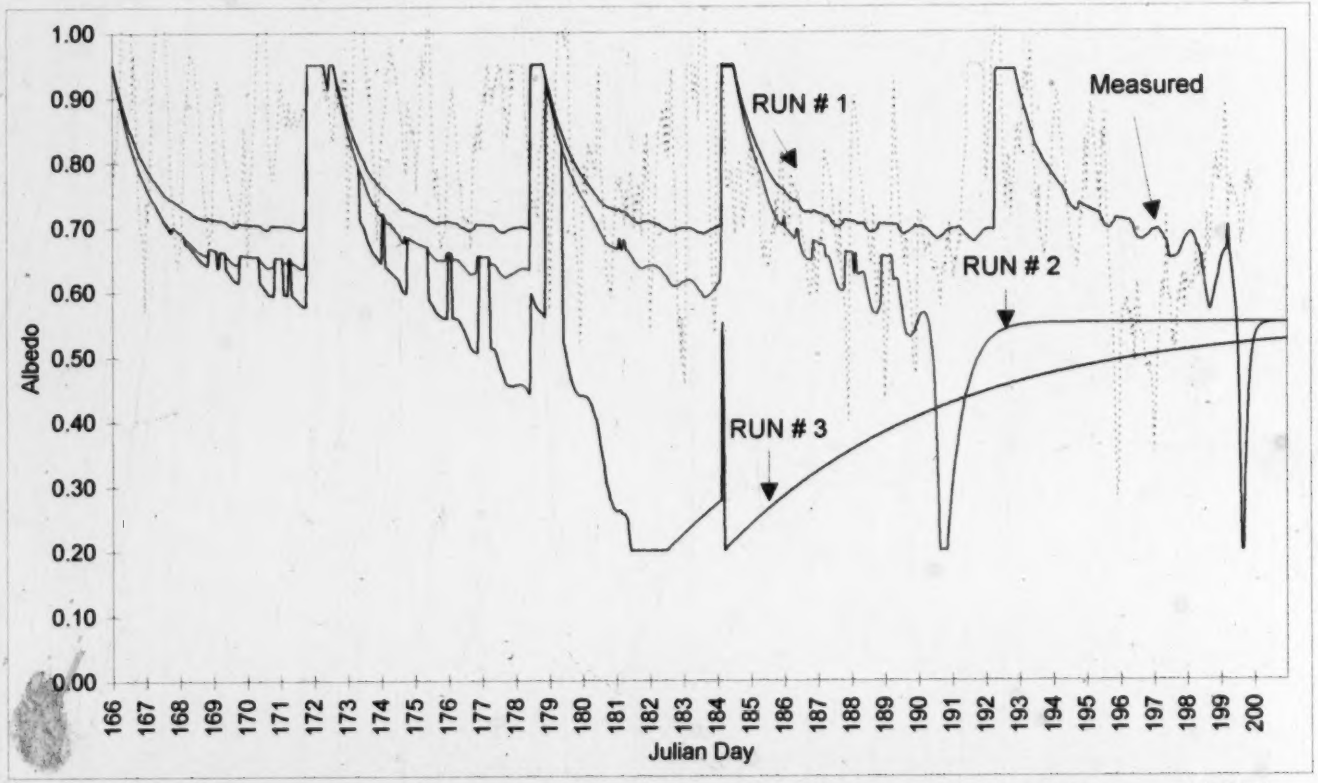

Figure 2.14: Comparison of measured albedo, corrected for a sloping surface, with Wal and Oerlemans' (1994) parameterization. Each run is differentiated by the amount of time required for surface water to runoff. Runoff times are 1/24 day, 1 day, and 13 days for runs #1 through #3 respectively.

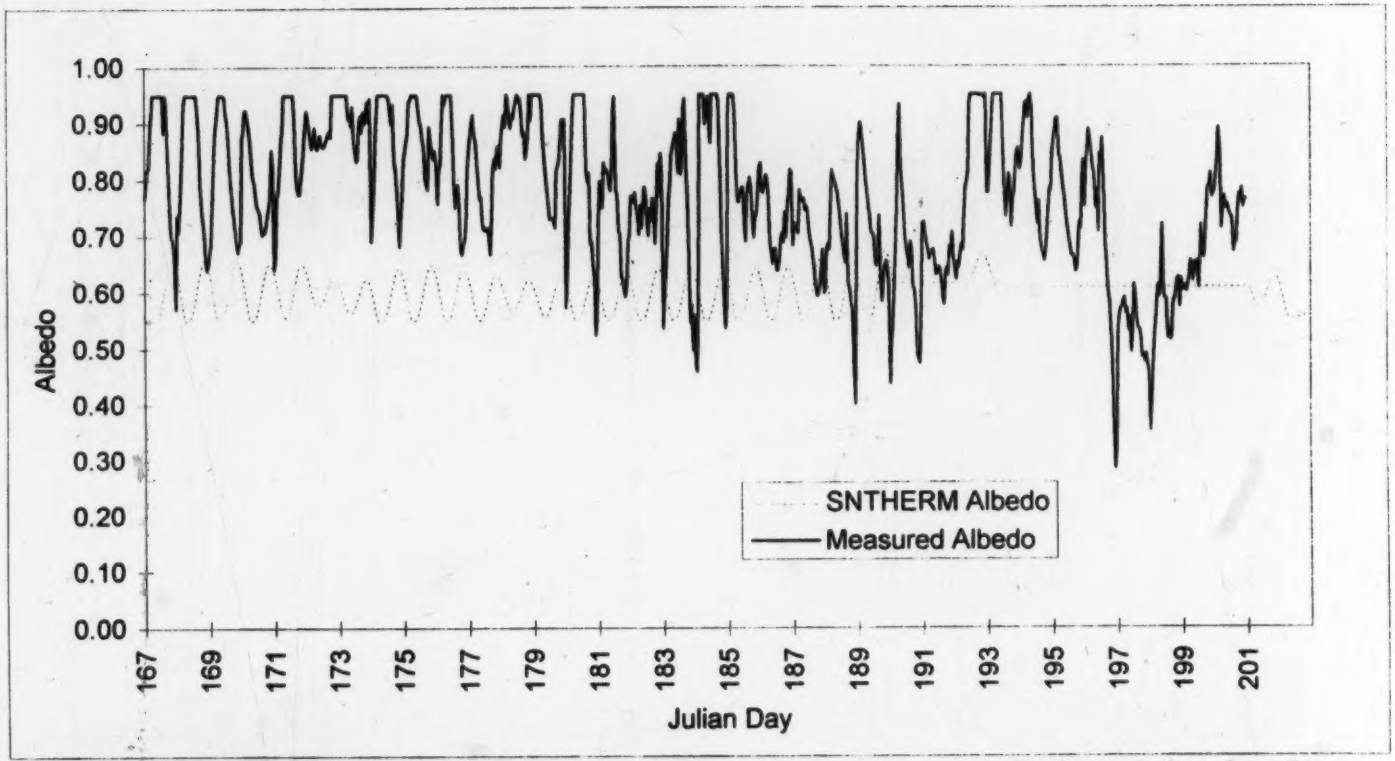

Figure 2.15: Comparison of measured albedo, corrected for a sloping surface, and albedo predictions from the SNTHERM_Albedo algorithm.

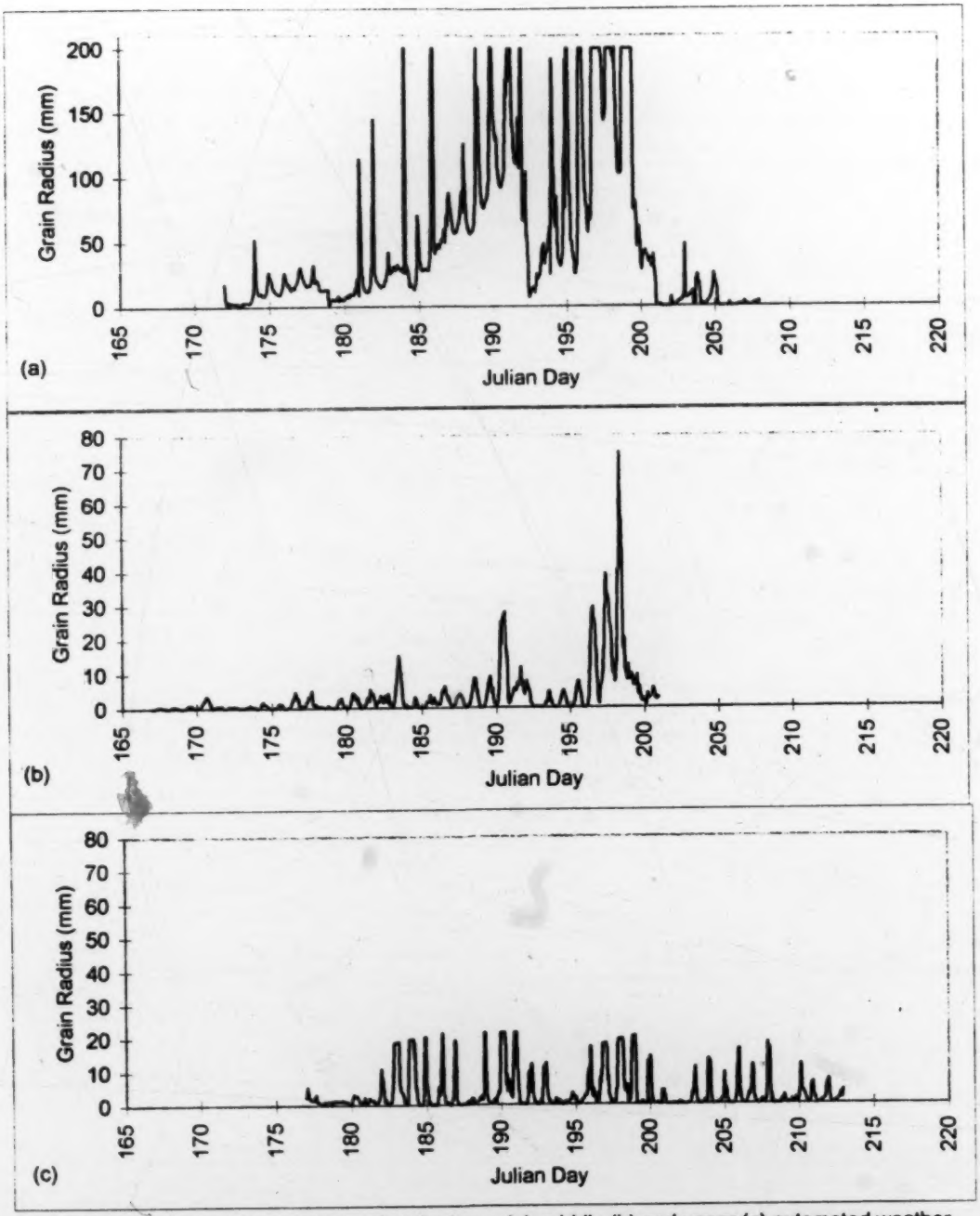

Figure 2.16: Optimized grain radii (mm) at the lower (a), middle (b) and upper (c) automated weather station sites. (note that the y-axis scale in (a) is an order of magnitude larger than in (b) and (c))

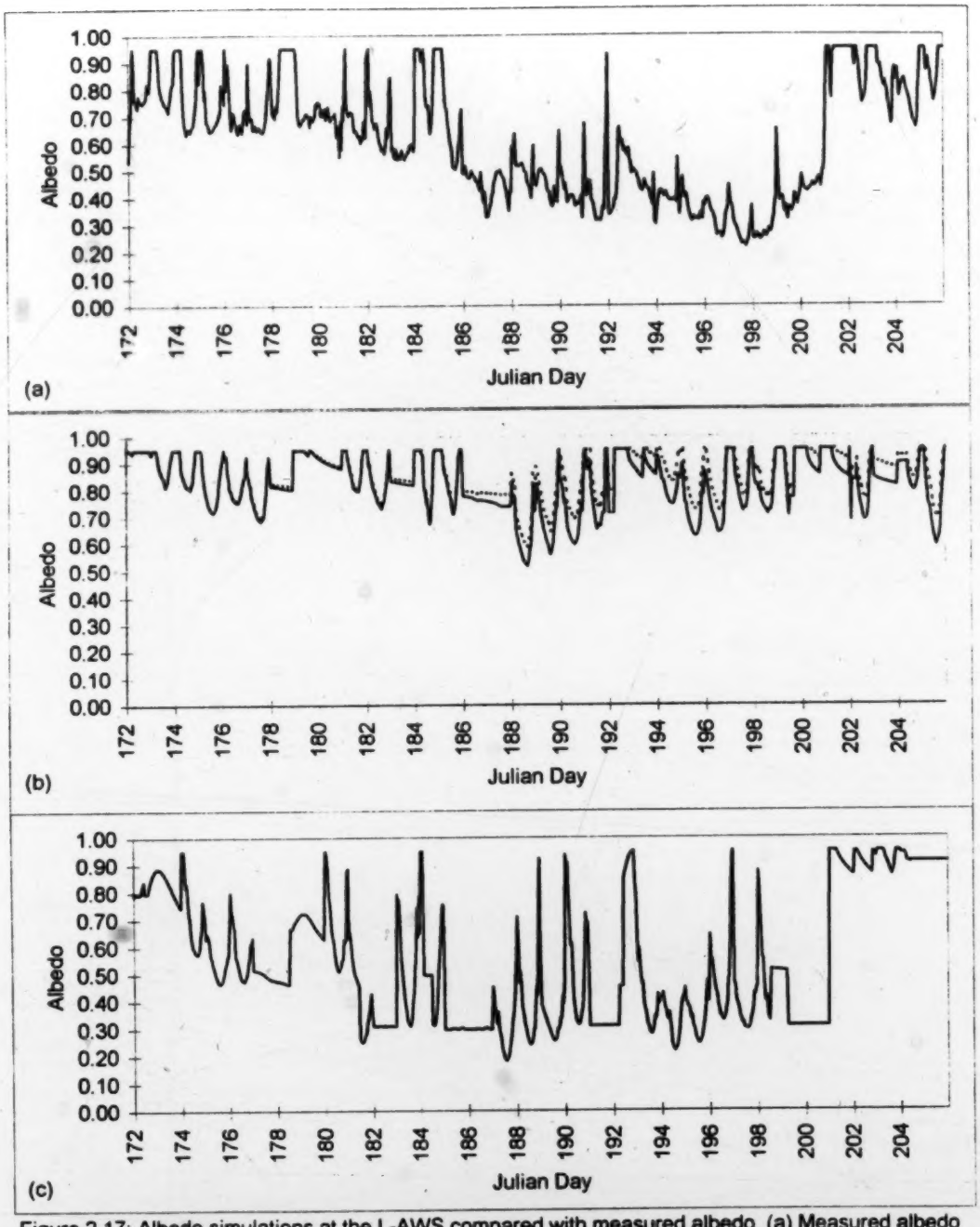

Figure 2.17: Albedo simulations at the L-AWS compared with measured albedo. (a) Measured albedo corrected for a sloping surface; (b) Run # 1 (dashed line) showing albedo simulations with no correctior for snow contamination or free water content, Run # 2 (solid line) showing albedo simulations with correction for free water content; (c) Run # 3 showing albedo simulations with corrections for free water content and snow contamination.

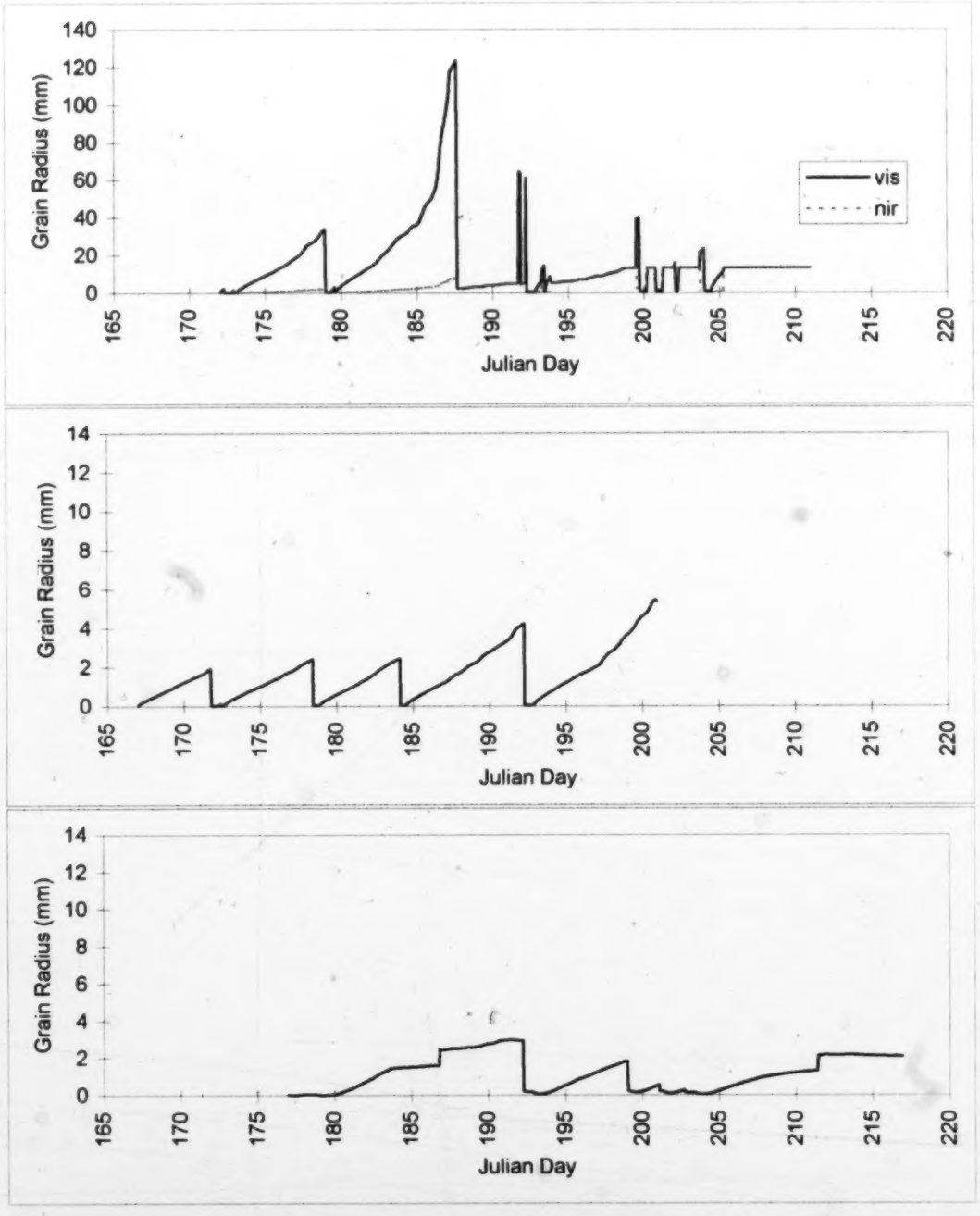

Figure 2.18: Modelled grain radii using EBM_GrainSize. (a) L-AWS; (b) M-AWS; (c) U-AWS. The visible (vis) and near-infrared (nir) grain radii are different at the L-AWS only. Notice that the scale on graph (a) is an order of magnitude greater than for (b) and (c).

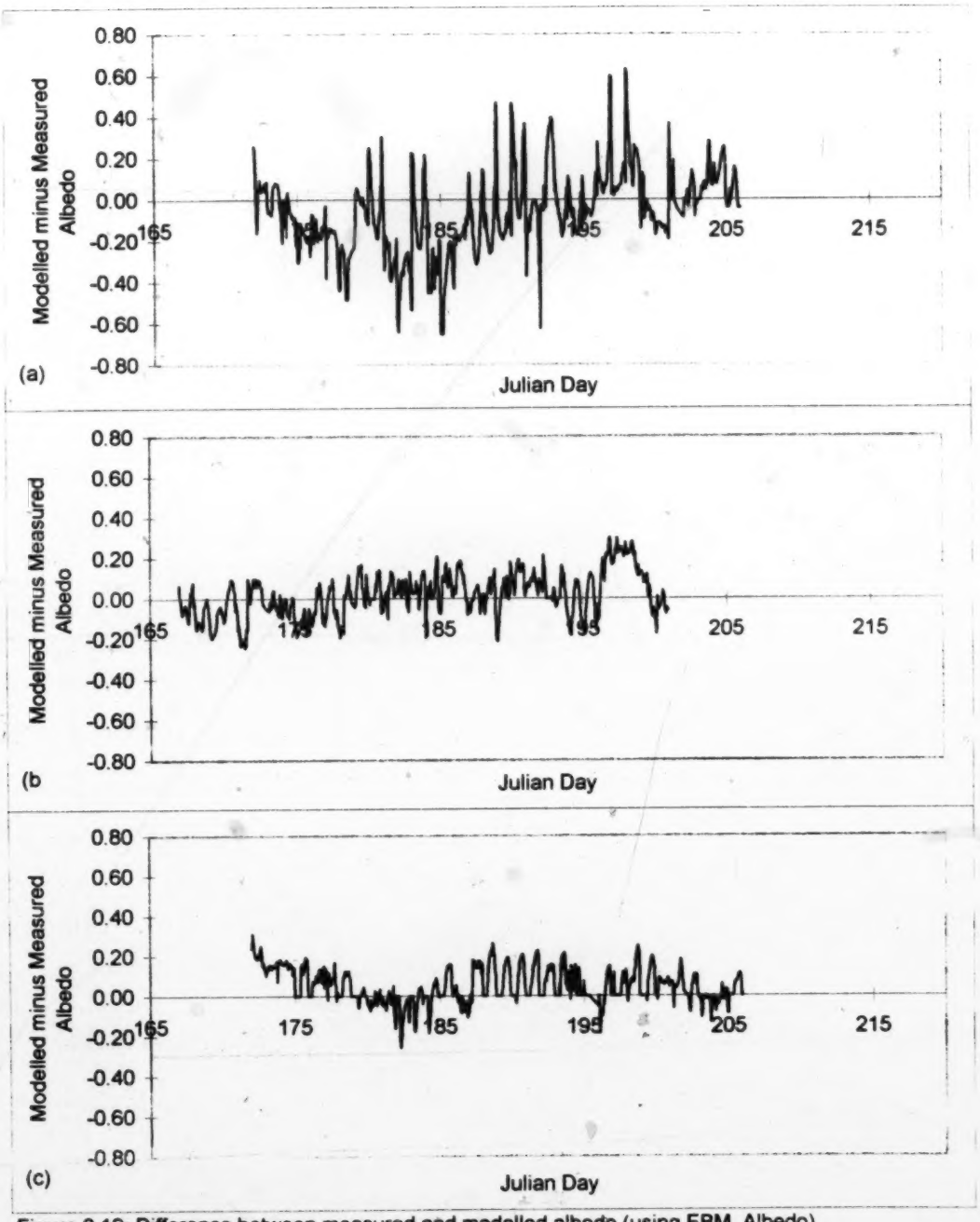

Figure 2.19: Difference between measured and modelled albedo (using EBM_Albedo)
(a) L-AWS; (b) M-AWS; (c) U-AWS.

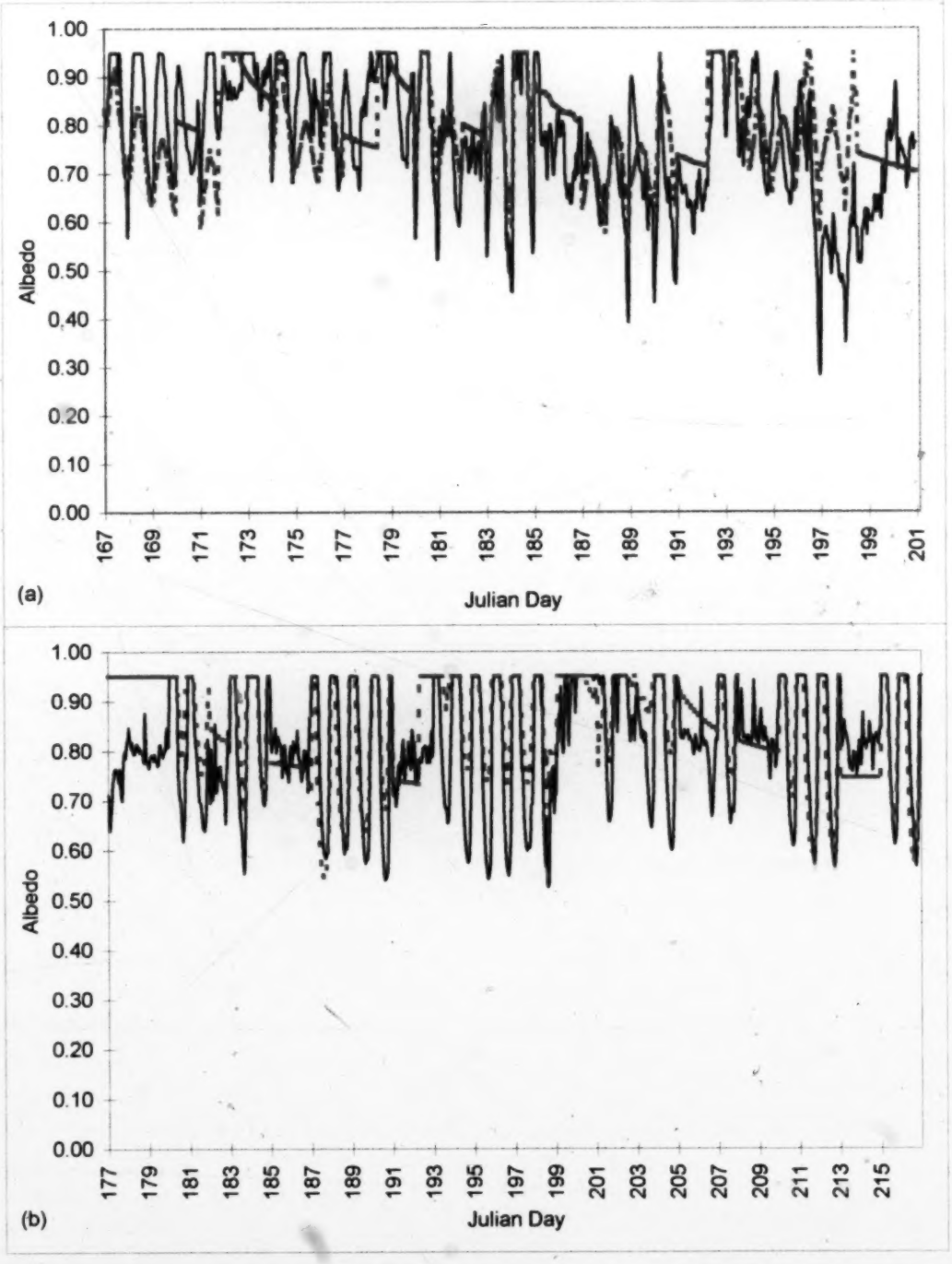

Figure 2.20: Measured albedo corrected for a sloping surface (solid line) compared with simulated albedo (dashed pink line). (a) M-AWS (b) U-AWS.

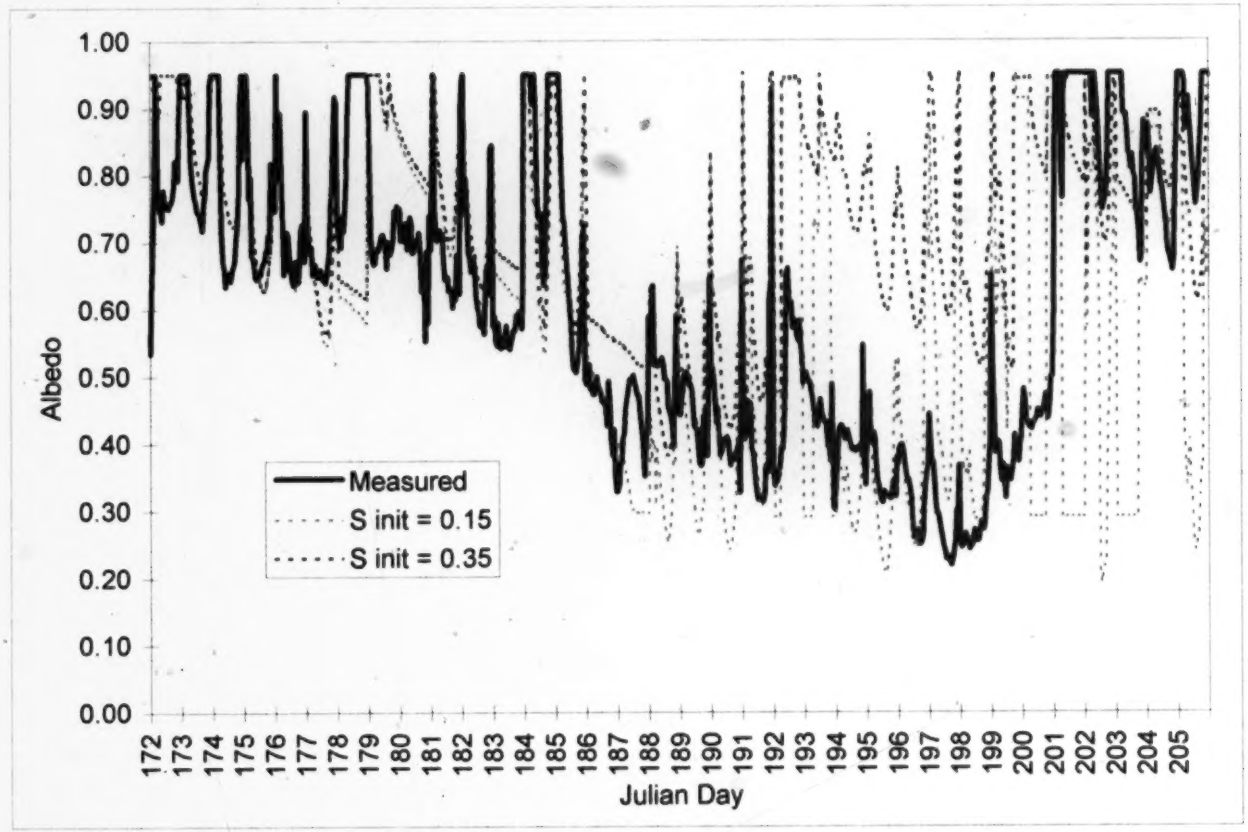

Figure 2.21: Comparison of EBM_Albedo predictions for different initial snow depths at the L-AWS.

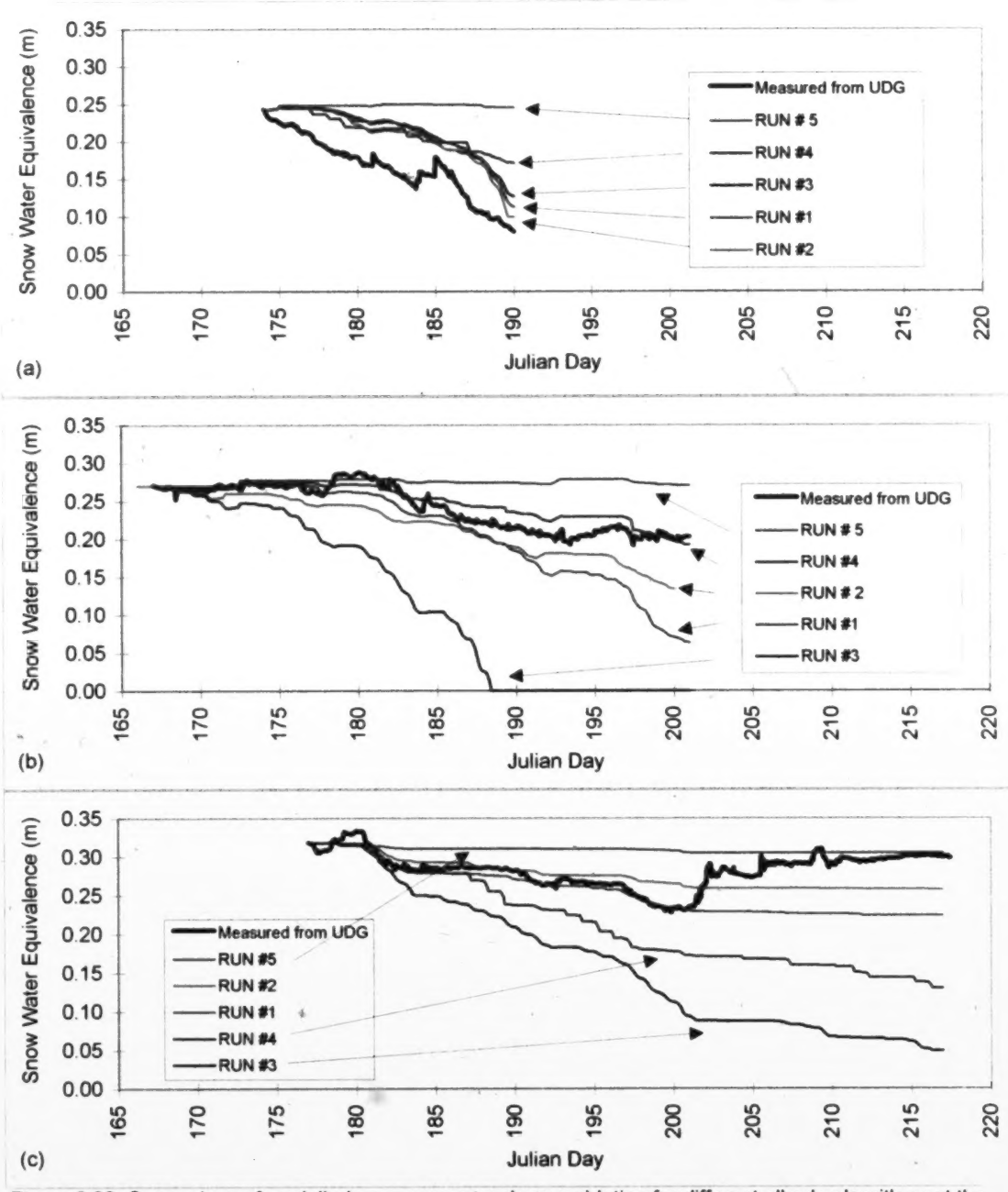

Figure 2.22: Comparison of modelled versus measured snow ablation for different albedo algorithms at the (a) L-AWS, (b) M-AWS, and (c) U-AWS. RUN # 1 uses measured albedo corrected for a sloping surface, RUN # 2 uses EBM_Albedo, RUN # 3 uses the W-O albedo algorithm, RUN # 4 is EBM_Albedo with a constant (66.5°) zenith angle, and RUN # 5 uses measured albedo without corrections for a sloping surface.

2.13 References

Arnold, N.S., Willis, I.C., Sharp, M.J., Richards, K.S. and Lawson, W.J. 1996. A distributed surface energy-balance model for a small valley glacier. I. Development and testing for Haut Glacier d'Arolla, Valais, Switzerland. *Journal of Glaciology*. 42(140): 77-89.

Blöschl, G. 1991. The influence of uncertainty in air temperature and albedo on snowmelt. *Nordic Hydrology*. 22: 95-108.

Bohren, C.F. and Barkstrom, B.R. 1974. Theory of the optical properties of snow. *Journal of Geophysical Research*. 79: 4527-4535.

Bryazgin, N.N. and Koptev, A.P. 1969. Spectral albedo of a snow ice cover. *Problemy Arktiki i Antarktiki*, 31: 79-83.

Cutler, P.M. and Munro, D.S. 1996. Visible and near-infrared reflectivity during the ablation period of Peyto Glacier, Alberta, Canada. *Journal of Glaciology*. 42(141): 333-340.

Colbeck, S.C. 1973. Theory of metamorphism of wet snow. USA Cold Regions Research and Engineering Laboratory, Research Report 313.

Colbeck, S.C. 1975. Grain and bong growth in wet snow. *Snow Mechanics Symposium*. IAHS-AISH Publ. No. 114, 51-61.

Colbeck, S.C. 1979. Grain clusters in wet snow. *Journal of Colloid Interface Science*. 72: 371-384.

Dunkle, R.V. and Beavans, J.T. 1956. An approximate analysis of the solar reflectance and transmittance of a snow cover. *Journal of Meteorology*. 13: 212-216.

Grenfell, T.C. and Maykut, G.A. 1977. The optical properties of ice and snow in the Arctic basin. *Journal of Glaciology*. 18: 445-463.

Grenfell, T.C. and Perovich, D.K. 1981. Radiation absorption coefficients of polycrystalline ice from 400 nm to 1400 nm. *Journal of Geophysical Research*. 89: 3573-3580.

Grenfell, T.C., Perovich, D. and Ogren, J. 1981. Spectral albedos of an alpine snowpack. *Cold Regions Science and Technology 4*: 121-127.

Grenfell, T.C., Warren, S.G. and Mullen, P.C. 1994. Reflection of solar radiation by the Antarctic snow surface at ultraviolet, visible, and near-infrared wavelengths. *Journal of Geophysical Research*. 99(D9): 18,669-18,684.

Jordan, R. 1991. A one-dimensional temperature model for a snow cover. Technical documentation for SNTHERM.89. *Spec. Rep.* 91-16, USA-CRREL, Hanover, NH.

Jordan, R. 1995. Unpublished updated technical documentation for SNTHERM.89 variable albedo algorithm. USA-CRREL, Hanover, NH.

Knap, W.H. and Oerlemans, J. 1996. The surface albedo of the Greenland ice sheet: satellite-derived and in situ measurements in the Søndre Strømfjord area during the 1991 melt season. *Journal of Glaciology.* 42(141): 364-374.

Liljequist, G.H. 1956. Energy exchange of an Antarctic snowfield. Short-wave radiation (Maudheim, 71°03'S, 10°56'W). *Norwegian-British-Swedish Antarctic Expedition, 1949-52, Scientific Results,* Vol. 2, Pt. 1A, Oslo, Norsk Polarinstitutt, 107 p.

Marks, D. 1988. Climate, energy exchange, and snowmelt in Emerald Lake Watershed, Sierra Nevada. Ph.D. Dissertation, University of California at Santa Barbara. 158 p.

Marshall, S.E. 1989. A physical parameterization of snow albedo for use in climate models. Ph.D. Dissertation, University of Colorado. NCAR Cooperative thesis No. 123. 161 p.

Marshall, S.E. and Warren, S.G. 1987. Parameterization of snow albedo for climate models. *In: Large scale effects of seasonal snow cover.* IAHS Publ. no. 166: 43-50.

Mellor, M. 1977. Engineering properties of snow. *Journal of Glaciology.* 19(81): 15-66.

Munro, D.S. 1990. Comparison of melt energy computations and ablatometer measurements on melting ice and snow. *Arctic and Alpine Research.* 22(2): 153-162.

Oerlemans, J. 1992. Climate sensitivity of glaciers in southern Norway: application of an energy-balance model to Nigardsbreen, Hellstugubreen and Alfotbreen. *Journal of Glaciology.* 38(129): 223-231.

Oke, T.R. 1987. Boundary Layer Climates. Second Edition. Routledge. 435 p.

Paterson, W.S.B. 1994. The Physics of Glaciers. Pergamon Press, 250 p.

Petzold, D.E. 1977. An estimation technique for snow surface albedo. *Climatological Bulletin.* (McGill University), 21: 1-11.

Press, W.H., Flannery, B.P., Teukolsky, S.A. and Vetterling, W.T. 1989. *Numerical Recipes. The Art of Scientific Computing (FORTRAN Version).* Cambridge University Press, Cambridge. 702p.

Rowe, C.M., Kuivinen, K.C. and Jordan, R. 1995. Simulation of summer snowmelt on the Greenland ice sheet using a one-dimensional model. *Journal of Geophysical Research.* 100(D8): 16,265-16,273.

Shapiro, R. 1987. A simple model for the calculation of the flux of direct and diffuse solar radiation through the atmosphere. ST Systems Corporation, Lexington, MA. Scientific Report No. 35. Under contract to Air Force Geophysics Laboratory, Report AFGL-TR-87-0200.

U.S. Army Corps of Engineers. 1956. Snow Hydrology. Summary Report of Snow Investigations, Corps of Engineers, North Pacific Division, Portland, Oregon: 141-191 and plates.

van de Wal, R.S.W. and Oerlemans, J. 1994. An energy balance model for the Greenland Ice Sheet. *Global and Planetary Change.* 9: 115-131.

Warren, S.G. 1982. Optical properties of snow. *Reviews of Geophysics and space physics.* 20(1): 67-89.

Warren, S.G. and Wiscombe, W.J. 1980. A model for the spectral albedo of snow. II. Snow containing atmospheric aerosols. *Journal of the Atmospheric Sciences.* 37(12): 2734-2745.

Wiscombe, W.J. and Warren, S.G. 1980. A model for the spectral albedo of snow. I: Pure snow. *Journal of the Atmospheric Sciences.* 37(12): 2712-2733.

Woodward, J. 1995. Superimposed ice and glacier mass balance. *Unpublished M.Sc. Thesis.* University of Alberta. 96p.

Zuo, Z. and Oerlemans, J. 1996. Modeling albedo and specific balance of the Greenland ice sheet: calculations for the Søndre Strømfjord transect. *Journal of Glaciology.* 42(141): 305-317.

CHAPTER 3. Development and Testing of Superimposed Ice Formation Algorithms for High Arctic Glaciers

3.1 Introduction

Predictions of surface ablation and runoff for high polar glaciers and ice sheets are complicated by the formation of superimposed ice (Reeh, 1989). Superimposed ice forms at the base of the snowpack on Arctic glaciers, where percolating meltwater refreezes on contact with underlying cold ice (Baird *et al.*, 1952; Arnold, 1965; Koerner, 1970; Palosuo, 1987; Jonsson and Hansson, 1990). Ice formed in this way has to be melted at least once again before it can be removed as runoff, thereby increasing the amount of energy required to remove a given amount of snow from the surface. Superimposed ice which does not melt completely in a given year remains as accumulation into subsequent years. Presently, superimposed ice formation is an important process of accumulation on Arctic glaciers. For some glaciers, such as the Meighen, Barnes, Bylot and Devon Ice Caps, superimposed ice is the dominant source of accumulation (Baird *et al.*, 1952; Koerner and Paterson, 1974).

The formation of superimposed ice is driven by the near surface ice temperature gradient. At the start of the melt season, near surface ice temperature gradients are higher than at any other time in the season. This is because the temperature of the upper ~14 m of arctic glaciers reflects the winter temperature regime, so that the temperature at the snow/ice interface end of the winter approximates the average winter air temperature (Blatter, 1985). Below a depth of ~14 m, the ice is at a temperature approximating the mean annual air temperature (Hooke, 1976). At the start of the melt season, ice temperatures at the surface are commonly colder than temperatures below 14 m (Figure 3.1 a). In the early melt season, energy supplied to the surface of the snowpack will warm the snow surface to the melting point, and further heating will melt the surface snow (Schytt, 1949) (Figure 3.1 b). Meltwater generated at the surface then percolates into the subzero snowpack and refreezes, releasing latent heat to warm the snow pack towards 0°C (Marsh and Woo, 1984). This process continues until the whole snow pack becomes isothermal at 0°C (Figure 3.1 c). Surface meltwater is then able to percolate through the snowpack to the snow/ice interface where it refreezes, again releasing latent heat.

This latent heat is conducted into the ice, warming it, and lowering the magnitude of the ice temperature gradient (Figure 3.1d and 3.1e). As the temperature gradient decreases, the rate of superimposed ice formation also decreases, so that more of the water reaching the snow/ice interface will runoff.

A number of studies have investigated ways of predicting superimposed ice formation (Ward and Orvig, 1952; Holmgren, 1971; Paterson, 1972; Wakahama *et al.*, 1976; Hooke, 1983; Greuell *et al.*, 1994). These studies estimate the thickness of superimposed ice formed by solving one dimensional heat flux equations for the upper ice layer (following Carslaw and Jaeger, 1946). The glacier ice is treated as a semi-infinite solid with a constant basal temperature and a fluctuating surface temperature. Ward and Orvig (1952) simplified this approach by assuming that, at the start of the period of superimposed ice formation, the ice to a depth of 14m is isothermal at the mean annual air temperature. Using this approach, Ward and Orvig (1952) were able to accurately model the timing and thickness of superimposed ice formation on the Barnes Ice Cap (70°00'N 74°00'W).

A surface energy balance model (EBM) developed by Arnold *et al.* (1996) and modified for use on Arctic glaciers by Woodward (1995), uses a superimposed ice algorithm based on the work of Carslaw and Jaeger (1946) with the simplifications introduced by Ward and Orvig (1952). (The model developed by Woodward (1995) is hereafter called "EBM-94" to differentiate it from "EBM-96", a modified version of the model described in Chapter 4). The approach of Woodward was to solve the equations of Carslaw and Jaeger at each grid cell at the start of model simulations to determine the maximum amount of superimposed ice which could form given the temperature at 14 m depth. Woodward (1995) showed that the net mass loss from John Evans Glacier would increase by 127% if superimposed ice did not form. Also, Woodward *et al.* (*in press*) investigated the sensitivity of mass balance simulations to changes in T_e the ice temperature at 14m depth, and found that the specific mass balance of John Evans Glacier would be reduced by 0.008 m a^{-1} per degree of warming. Therefore, correct parameterization of superimposed ice formation in energy balance simulations is important for correctly predicting the mass balance of high latitude glaciers.

A potential limitation of the work of Woodward *et al.* (*in press*) is that their superimposed ice algorithm predicts the total quantity of superimposed ice which may form in a given season, but does not simulate the rate at which superimposed ice forms. Woodward *et al.* assume that all water reaching the snow-ice interface freezes until the maximum thickness of superimposed ice is reached. In reality, if the rate of meltwater supply to the snow-ice interface exceeds that which can be refrozen given the ice temperature gradient at that time, then some runoff may occur. Temporal variations in the rate of superimposed ice formation have been taken into consideration in the models of Wakahama *et al.* (1976), Hooke (1983) and Greuell *et al.* (1994). These models solve the one-dimensional heat flux equations of Carslaw and Jaeger (1946) at each model time step, so that changes in the snow-ice interface temperature gradient resulting from meltwater refreezing can propagate through the ice column. This approach determines the maximum rate of superimposed ice formation at each time step, rather than the maximum seasonal quantity of superimposed ice.

This paper documents 3 methods for predicting superimposed ice thicknesses within the spatially distributed energy balance model described in Chapter 4. The first 2 are physically based models, and include the model of Woodward *et al.* (*in press*) and a new model following the approach of Wakahama *et al.* (1976). The third is an empirical model in which maximum superimposed ice thicknesses are determined as a percentage of total snow water equivalence at the start of the season (Pmax). Each model will be tested using data collected at 2 automated weather station sites on John Evans Glacier, Nunavut, Canada, during the summer of 1996. The superimposed ice algorithm which performs best will be implemented into the surface energy balance model described in Chapter 4.

During some phases of model development, specific information which could not be measured directly in the field has been simulated using the model SNTHERM (Jordan, 1991). SNTHERM is a one-dimensional mass and energy balance model for predicting temperature profiles within strata of snow and frozen soil. Although temperature prediction is the primary objective of the model, snow accumulation, ablation, densification and metamorphosis, as well as the transport of liquid water and water vapor, are included as required components in the heat and mass balance calculations (See

Section 2.41 for a complete description of SNTHERM). In this paper, SNTHERM is used to predict wetting front locations within the snowpack to determine the timing of the onset of superimposed ice formation.

3.2 Study Area

3.21 Site description

John Evans Glacier is a large valley glacier located at 79°40'N 74°00'W on an unnamed peninsula south of Dobbin Bay, eastern Ellesmere Island, Nunavut, Canada (Figure 3.2-3.4). Its catchment area is 211km^2, of which 47% is glaciated, and spans an altitudinal range of 50 to 1500 m (Figure 3.5). 77% of the ice surface area lies between 600m and 1100m. The catchment comprises a main trunk glacier fed from a number of sub-catchments in the western part of the basin, and 8 small valley glaciers feeding into a marginal lake 3 km from the snout of the main trunk glacier on its eastern side.

3.22 Local Climate

Mean annual and July temperatures recorded over the period 1951-1994 at the AES meteorological station at Alert, north-eastern Ellesmere Island (82°30'N 62°20'W) are shown in Figure 3.6. The mean annual sea level temperature at Alert was -17.8°C. During 1988-89, the average annual air temperature at Alert was -16.9°C. This is similar to the average annual air temperature (-17.3°C) measured for the same period at Allman Bay, located 5km south of John Evans Glacier (Figure 3.2) (G. Henry, *pers comm.*). However, July 1988 temperatures were approximately 3°C warmer at Allman Bay (located at sea level) than at Alert. Field data for the present study were collected during the summer of 1996, which was unusually cold. The mean 1996 July air temperature measured at the lower weather station (elevation 261 m) on John Evans Glacier was approximately 3°C colder than the mean July air temperature at Allman Bay in 1988 (note that some of this difference in temperature may be due to differences in surface type and elevation between Allman Bay and John Evans Glacier). Mean total precipitation from 1 August 1995 to 1 August 1996 at Alert (165.4 mm WE) was 128% higher than the mean annual total precipitation at Alert over the period 1951-1994 (128.5 mm WE).

3.3 Model Descriptions

EBM-94 was used to test 2 different superimposed ice algorithms (Woodward, 1995). The first predicted superimposed ice thicknesses empirically as a function of the water equivalent depth of snow prior to melt. The second was a physically-based model derived from theory describing heat conduction in ice. This paper describes both these models (physically-based algorithm #1, SI-P1 and empirical algorithm, SI-E), outlines the development of a new model (physically-based algorithm #2, SI-P2), and tests all 3 models against field measurements of superimposed ice thicknesses and near-surface ice temperatures. None of these 3 models deals explicitly with the refreezing of meltwater within the snowpack (i.e. above the snow/ice interface) because of the complexities involved in simulating water flow in an inhomogeneous snowpack. However, 1996 field observations showed that substantial refreezing of meltwater did occur within denser snow layers, rather than at the snow/ice interface. The inability of these models to deal with meltwater refreezing within the snowpack is therefore a limitation which needs to be addressed in future studies. For this study, the term "superimposed ice" will refer to ice which forms at the snow/ice interface only. Superimposed ice thicknesses predicted by these algorithms represent the water-equivalent thickness of superimposed ice, rather than the actual thickness of superimposed ice which would be observed in the field.

3.31 Physically-Based Superimposed Ice Algorithm #1 (Algorithm SI-P1)

EBM-94 used a superimposed ice formation algorithm which sets a limit on the maximum thickness of superimposed ice, based upon the temperature gradient in the near-surface ice layers (Woodward *et al., in press*). This algorithm was based on work by Ward and Orvig (1952) and Carslaw and Jaeger (1946) who used the equation of one-dimensional heat conduction to solve for the thickness of superimposed ice as a function of the initial ice temperature prior to the onset of superimposed ice formation, and of the length of time during which superimposed ice forms. The EBM-94 algorithm is tested against measured near-surface ice temperatures and measured superimposed ice thicknesses. The EBM-94 equations are modified slightly to reintroduce the error function omitted for simplicity by Woodward *et al.*

The growth rate of superimposed ice at the snow-ice interface may be obtained by solving the equation of one-dimensional heat conduction:

$$\frac{\partial}{\partial z}\left(\frac{\partial T}{\partial z}\right) = \frac{1}{\kappa}\frac{\partial T}{\partial t} \tag{3.1}$$

where T is the temperature (°C), t is the time (sec), κ is the thermal diffusivity of ice ($0.011 cm^2 s^{-1}$) and z is the vertical co-ordinate (cm). Equation 3.1 is restricted to the following boundary conditions:

$$T = 0, z \geq X \tag{3.2}$$

$$T \rightarrow -T_0, z \rightarrow -\infty \tag{3.3}$$

$$T = -T_0, t = 0, z < 0 \tag{3.4}$$

$$-K_{ice}\left(\frac{\partial T}{\partial z}\right)_{z=X} = -L_{ice}\rho_{ice}\frac{dX}{dt} \tag{3.5}$$

Where T_0 is the ice temperature at a location sufficiently deep that it remains constant, K_{ice} is the thermal conductivity of ice ($0.0224 Js^{-1}cm^{-1}{}^{o}C^{-1}$), L_{ice} is the latent heat of fusion of ice ($0.335 J kg^{-1}$) and ρ_{ice} is the density of ice ($0.9 g cm^{-3}$). The vertical co-ordinate, z, is defined as positive upward, where z=0 is the snow-ice interface. X represents the water equivalent thickness of superimposed ice above z=0, and, at time t, and is given as:

$$X = 2A\sqrt{\kappa t} \tag{3.6}$$

Where A is a constant given by:

$$Ae^{A^2}\left(1 + erf(A)\right) = \frac{c_{ice}T_0}{L_{ice}\sqrt{\pi}} \tag{3.7}$$

where *erf(A)* is the error function of A (see Carslaw and Jaeger, 1946, p. 51) and c_{ice} is the

specific heat of ice at 0°C (2097 J kg^{-1} °C^{-1}). For energy balance calculations, A must be solved for every grid cell since T_o is corrected for elevation via a constant lapse rate (0.004°C m^{-1}). To solve for A, Woodward *et al.* developed a linear approximation of A as a function of T_0, because they mistakenly assumed *erf(A)* could not be solved without a knowledge of the rate of change of ice temperatures with time. Although Holmgren (1971) showed *erf(A)* is small and can be ignored, sensitivity analysis in the present study showed that explicitly calculating *erf(A)* for each grid cell made a difference to overall melt computations. Superimposed ice thickness predictions at the M-AWS were 1 cm WE less when *erf(A)* was explicitly calculated than when it was not. Therefore, the linear approximation method used by Woodward *et al.* is omitted here and Equation 3.6 is solved iteratively every time there is a new T_0.

The approach of Woodward *et al.* was then to solve Equation 3.6 for the maximum thickness of superimposed ice which may be formed at a given grid cell. They did this by using a constant value for the length of the period of superimposed ice formation (10 days, based on observations made by Wolfe (1995)) and by estimating the value of T_0 for each grid cell. T_0 was approximated from measurements of the mean annual air temperature, which were assumed to represent the ice temperature at a depth of 14m. Superimposed ice was then allowed to form whenever snow melt occurred, provided that the thickness of superimposed ice was less than the maximum amount determined by Equation 3.6. After the maximum superimposed ice thickness was reached, subsequent melt was considered runoff and was removed from the cell immediately.

In order to test this algorithm against measured ice temperature data, the heat conduction equation (Equation 3.1) can be solved for temperature, so that predictions of ice temperatures after the onset of superimposed ice formation can be compared with ice temperature observations at each AWS. The temperature in the ice at depth z and time t is given by:

$$T = T_0\left[-1+\frac{erfc\left(-\frac{z}{2\sqrt{\kappa t}}\right)}{1+erfA}\right] \tag{3.8}$$

where *erfc* is the complementary error function, such that:

$$erfc\left(-\frac{z}{2\sqrt{\kappa t}}\right) = 1 - erf\left(-\frac{z}{2\sqrt{\kappa t}}\right) \tag{3.9}$$

3.32 Physically-Based Superimposed Ice Algorithm #2 (Algorithm SI-P2)

The condition required for the solution of the heat balance equations in Section 3.31 is that the supply of meltwater to the snow-ice interface is sufficient to achieve the maximum rate of accretion of superimposed ice $\left(\frac{dX}{dt}, \text{Eq.3.5}\right)$ allowed by the temperature gradient at the snow-ice interface $\left(\frac{\partial T}{\partial z}, \text{Eq.3.5}\right)$. This is probably not always true, since during cold periods there may be no input of water to the interface, and the accretion rate may be less than the potential rate modelled using the heat conduction equations. Also, during periods of high melt, the rate of meltwater supply may exceed the maximum superimposed ice accretion rate, so that ponding and/or runoff may occur before the maximum superimposed ice thickness is achieved. Finally, there may be cooling at the snow-ice interface during the melt season which may draw heat from the ice and create the potential for more superimposed ice formation later in the season. Algorithm SI-P1 does not deal with these second-order effects concerning the rates of superimposed ice formation; instead, it deals with the first-order problem of how much superimposed ice may form at a cell given the initial temperature gradient in the ice, and then allows superimposed ice to form regardless of time. The new algorithm (SI-P2) attempts to incorporate the second-order effects of the near-surface ice temperature gradient on the rate of formation of superimposed ice. It is a dynamic model in the sense that changes in the near surface ice temperature gradient are dependent upon the rate of meltwater input to

the snow-ice interface.

The boundary condition in Equation 3.5 states that the rate of formation of superimposed ice is proportional to the temperature gradient at the snow-ice interface. It shows that the release of latent heat by the formation of superimposed ice results in a decrease in the temperature gradient at the snow-ice interface. In reality, some heat released in this phase change also goes to heat the surrounding ice-water mixture present at the interface. Wakahama *et al.* (1976) account for this by rewriting Equation 3.5 as:

$$-K\left(\frac{\partial T}{\partial z}\right)_{z=X} = -\left[\rho_{si} - \rho_{ws}(1-w)\right]L\frac{dX}{dt} \tag{3.10}$$

where ρ_{si} and ρ_{ws} are the densities of superimposed ice and wet snow, respectively, and w is the free water content of wet snow.

In this algorithm, $\frac{dX}{dt}$ is solved at each time step using the following procedure:

1 - the temperature profile within the ice is determined according to Equation 3.1 using Saul'yev's Method, an alternating-direction finite differencing procedure (Carnahan *et al.*, 1969). Following the approach of Wakahama *et al.*(1976), calculations are carried out over a regular grid to a depth of 14 m using a grid spacing of 0.40 m. 14 m is chosen as the depth at which $T = T_o$ (Equation 3.3), based on findings of Hooke (1976). The upper boundary is artificially fixed in space, since: a) the growth of superimposed ice is small compared to the grid-spacing, and b) solving for the temperature field with a moving upper boundary using finite differencing is complex. A "control volume" approach (in which the grid is divided into nodes, and net energy fluxes at each nodal boundary are calculated) would be more suitable, since this approach lends itself more easily to variable sized nodes, however such a solution is beyond the scope of the present work. The time step used in the finite-difference procedure is the same as the time step of model calculations in the EBM (1 hour).

2 - Equation 3.10 is solved for $\frac{dX}{dt}$, assuming an unlimited supply of water at the

snow-ice interface. This represents the maximum rate of superimposed ice at the present time step, given the ice temperature gradient.

3 - Q_M is assumed to represent the meltwater flux at the base of the snowpack. There are then 2 possible conditions:

$$Q_M \geq \frac{dX}{dt} \tag{3.11}$$

or

$$Q_M < \frac{dX}{dt} \tag{3.12}$$

For the first case (Equation 3.11), the superimposed ice thickness at the new time step (X_{new}) is given as:

$$X_{NEW} = X_{OLD} + \frac{dX}{dt} \tag{3.13}$$

where (X_{old}) is the thickness of superimposed ice at the previous time step. This describes the condition when the meltwater supply to the snow-ice interface is greater than the potential rate of superimposed ice formation given the temperature gradient in the ice. Therefore, the maximum possible amount of superimposed ice is formed at that time step.

For the second case (Equation 3.12), insufficient meltwater reaches the base of the snowpack to heat the ice as much as is prescribed by the temperature gradient in the ice. The amount of superimposed ice formed will be:

$$X_{NEW} = X_{OLD} + Q_M \tag{3.14}$$

Since $Q_M < \frac{dX}{dt}$, the actual amount of energy released when Q_M refreezes will be less than the potential amount solved for in Equation 3.10. Therefore, to solve for the

actual energy transfer, and hence the temperature gradient at the snow-ice interface, Q_M is substituted back into Equation 3.10 as $\frac{dX}{dt}$. Then Equation 3.10 is solved for $\left(\frac{\partial T}{\partial z}\right)_{z=X}$, and the temperature profile is readjusted via Equation 3.1 before progression to the next time step.

4 - For the case when $Q_M = 0$ at a given time step, the temperature profile is recalculated with $\frac{dX}{dt}$ retaining the value calculated in the previous time step. This allows for the conduction of heat through the ice column.

3.33 Empirical Superimposed Ice Algorithm (Algorithm SI-E)

Algorithm SI-E1 is the simplest superimposed ice algorithm. Superimposed ice is allowed to form until some percentage (Pmax) of the initial pre-melt snow water equivalence is reached. Pmax has been assigned a value of 0.6, largely on intuitive grounds (e.g.: Reeh, 1991), however some field studies do support a value of this order. For instance, Wolfe (1995) obtained a value of 0.67 from studies on Quviagivaa Glacier, Ellesmere Island.

3.4 Meteorological Data

Three automatic weather stations (AWS's) were set up at low (261 m a.s.l.), middle (824 m a.s.l.) and high (1183 m a.s.l.) elevation sites on John Evans Glacier (Figure 3.3; Table 3.1 & 3.2). Each AWS consisted of 2 central masts made of galvanized steel drilled vertically ~1.5m into the ice, to which was mounted a cross-bar. Sensors were attached to the central mast and the cross-bar. Once the masts were frozen into the ice, they were very stable and only very strong winds could make them shake. None of the masts melted out or needed to be re-drilled into the ice. Incoming and outgoing short-wave radiation, net radiation, air temperature, relative humidity, wind speed and wind direction were measured at each site, while air pressure was measured only at the M-AWS (PHOTO 3.2). Ultrasonic depth gauges (UDG's) were used to monitor changes in the height of the snow or ice surface at each site. Copper-constantan thermocouples were used to obtain ice temperature

measurements to a depth of up to 4.8 m (Table 3.3). All sensors were wired to a CR10 datalogger housed in a plastic enclosure which was mounted on one of the masts. Measurements from each sensor were taken every 10 sec., and, except for the UDG, were averaged for hourly output. Because of anticipated errors in UDG measurements due to blowing snow, UDG measurements were averaged and output every 10 min.

Cloud type, cover and height were estimated for 3 layers in the atmosphere. These observations were always made at 700 and 1900 hrs., and additional observations were made whenever conditions changed from the previous observation. Snowfall was collected in a small plastic tray of area 0.10 m^2 and water equivalence was determined by melting the snow and measuring the volume of water at the end of a snowfall event.

Ice Temperature Measurements:

Temperature measurements made with thermocouples connected to a CR10 datalogger require a measurement of the temperature at the reference junction, or CR10 wiring terminal (CSI Manual, p.13-11). A 107F thermistor probe was housed in the datalogger enclosure to provide this reference temperature. As the melt season progressed, it was observed that the reference temperature within the datalogger enclosure was much higher than the outside temperature. Because such high temperatures coincided with periods of sunny weather, it was believed that radiative heating of the logger enclosure was the cause. The yellow colour and plastic material making up the enclosure likely made it susceptible to such radiative heating. High temperatures caused errors in ice temperature measurements, observed as excessive noise and/or diurnal cycling within measured temperature profiles. The best remedy that could be devised in the field involved installing a single thermocouple to measure air temperature at the same height as the 107F thermistor used for the same purpose. The difference between thermistor and thermocouple measurements of air temperature was then used to correct the remaining ice temperature thermocouple measurements. Analyses carried out in this paper use daily average ice temperatures, which hide measurement errors. However, it is likely that ice temperatures reported in this paper are erroneously high.

Superimposed Ice Thickness:

At the start of the melt season at the M-AWS, a snowpit was dug and powdered chalk was sprinkled over a small area of the glacier ice. The snowpit was then carefully refilled and the location of the chalk layer was marked using an ablation stake. Later in the season, when superimposed ice formation was thought to have ended, the site was excavated and an ice axe was used to chip away layers of superimposed ice until the chalk layer was reached. The thickness of superimposed ice which had accumulated above the chalk layer was then measured.

3.5 Results

This section describes observed near-surface ice temperatures at the M-AWS and U-AWS. These data will be compared with modeled near-surface ice temperatures in Section 3.61. Snowpit observations, supplemented by results from model simulations using the SNTHERM model, are used to determine the onset of superimposed ice formation. Data from the L-AWS were not used in this analysis, because most or all of the superimposed ice had formed at the L-AWS prior to the installation of the weather station.

3.51 Near-Surface Ice Temperatures

At the M-AWS, the snow/ice interface temperature began to rise around JD 175, and reached a plateau near 0°C around JD 185 (Figure 3.7). Ice temperatures at -1.6m, -2.3m and -3.2m were identical, with an average value of -13.6°C, until JD 181, after which they began to diverge, with temperatures nearest the surface increasing more rapidly than those at a greater depth. At the U-AWS, the snow temperature at 0.5m began to rise around JD 175, while the snow/ice interface temperature began to increase rapidly around JD 181. Ice temperatures at -1.6m, -2.3m and -3.2m averaged -19.5°C until JD 181, after which they began to diverge.

3.52 Wetting Front Migration

A prediction of the location of the wetting front within the snowpack is useful in determining the onset of superimposed ice formation (required as an initial condition in

testing SI-P1; see Section 3.61), and in predicting the location of meltwater refreezing. Although detailed observations of wetting front migration were not made in this study, it may be predicted for the U-AWS and M-AWS using SNTHERM. SNTHERM calculates fluid flow using Colbeck's (1971) gravitational form of the equations for water mass flux in snow, omitting the effects of capillarity. SNTHERM assumes horizontal homogeneity in the snowcover and does not account for inhomogeneous flow, such as the formation of fluid fingers.

Simulations for the M-AWS show that the wetting front did not reach the snow-ice interface until after JD 182 (Figure 3.8). Because JD 182 is the day after that on which ice temperatures at the M-AWS began to increase, this day was chosen as the starting date for superimposed ice formation at the M-AWS. A snowpit dug on JD 181 at the M-AWS showed that water had reached a point 30.5 cm above the ice surface (Figure 3.9 a), and this matches very well with SNTHERM predictions. At the U-AWS, the wetting front penetrated only as far as a point 18 cm above the ice on JD 183. Although water did not reach the base of the snowpack at the U-AWS, ice temperatures still rose in a manner similar to that observed at the M-AWS, and at a similar time (~JD 182). Therefore, it is likely that superimposed ice formation also began around this time, so JD 182 is set as the start date for superimposed ice formation at the U-AWS.

SNTHERM predicts a rapid flux of water towards the base of the snowpack during the warm period around JD 182 at both the M-AWS and U-AWS. However, while the wetting front remained at the snow/ice interface at the M-AWS, it retreated upwards at the U-AWS after JD 182. The fact that ice temperatures continued to rise throughout the melt season at the U-AWS, even though there was no water at the snow/ice interface, suggests that refreezing of meltwater was occurring within the snowpack at the U-AWS, and that the heat released was used to warm the snowpack and the near-surface glacier ice. A snowpit dug at the U-AWS on JD 185 showed the presence of multiple ice layers throughout the snowpack, which supports these predictions (Figure 3.9 b).

3.6 Testing of Superimposed Ice Algorithms

The predicted timing and rate of superimposed ice formation are compared with measured superimposed ice thicknesses and, for the physically-based models, with measured ice temperature profiles. The testing is carried out using data from the U-AWS and M-AWS.

3.61 Testing of SI-P1

Figure 3.10 shows measured and predicted near-surface ice temperature variations at the M-AWS and U-AWS using Equation 3.8. The start-day for superimposed ice formation and the initial ice temperatures (T_o) were determined from observations reported in Section 3.51 & 3.52. In general, temperature predictions for both sites compare well with measured values. Correlation coefficients between measured and predicted values for both sites range from 0.41 to 0.95, with an average of 0.77 (Table 3.5). Temperature predictions were worse at the M-AWS than the U-AWS, and, for both sites, the worst predictions occur at the snow/ice interface.

3.62 Comparison of Predicted and Measured Superimposed Ice Thickness at the M-AWS

All 3 superimposed ice algorithms described in this paper were implemented within the surface energy balance model described in detail in Chapter 4 (EBM-96). Superimposed ice thicknesses predicted for the M-AWS by each of the algorithms were compared with the superimposed ice thickness measured at the end of the melt season. One difficulty in implementing these routines within a larger energy balance model is determining when superimposed ice formation should begin at a given location. Model simulations using EBM-96 began on JD 167. At this time superimposed ice had already begun to form at the lower elevations, but not at the higher elevations. Testing carried out in this section will therefore examine predicted superimposed ice thicknesses for 2 different times of the onset of superimposed ice formation.

Energy balance simulations at the M-AWS were run using both JD 167 and JD 182 as the start date for superimposed ice formation (Figure 3.11). For SI-P1 and SI-E, superimposed ice thicknesses simply show the water equivalent melt which occurs at the M-AWS until the maximum superimposed ice thickness is reached. Therefore, temporal patterns in superimposed ice thicknesses for SI-P1 and SI-E arise from variations in

predicted melt rather than from any process embodied within the superimposed ice routine. For SI-P2, variations in predicted superimposed ice thicknesses result from variations in both melt and the rate of superimposed ice formation as determined by the temperature gradient at the snow/ice interface.

When superimposed ice is allowed to form from the start of the energy balance simulations, the predicted final superimposed ice thickness is closer to the measured thickness (Figure 3.11 a). The physically-based algorithms predict nearly the same final superimposed ice thickness (0.121 m WE for SI-P1 and 0.122 m WE for SI-P2), very close to the observed superimposed ice thickness of 0.12 m WE at the M-AWS. However, the timing of superimposed ice formation differs between the 2 models. Both models predict the same superimposed ice thicknesses until JD 182. After JD 182, SI-P1 predicts a higher rate of superimposed ice formation than SI-P2, although the trend for each curve remains the same. The rate of superimposed ice formation is slower for SI-P2 because the rate of meltwater supply sometimes exceeds the maximum rate of superimposed ice formation as dictated by the temperature gradient at the snow/ice interface. SI-P1 predicts a leveling-off in superimposed ice formation on JD 196 because the maximum thickness of superimposed ice has been reached. However, SI-P2 predicts a continuation in superimposed ice formation until the end of the model run, because the ice temperature is still sufficiently cold to cause superimposed ice to form. SI-E (using Pmax=0.60) follows the trend of SI-P1 but predicts a higher final value of 0.153 m WE.

When the onset of superimposed ice formation is set at JD 182, SI-E and SI-P1 both predict a final superimposed ice thickness of 0.1096 m WE, while SI-P2 predicts a final thickness of 0.0894 m WE (Figure 3.11 b). Therefore superimposed ice thickness predictions are better when superimposed ice is allowed to form from the start of energy balance simulations rather than being constrained to begin when water was observed to reach the snow/ice interface. This suggests either that the start date chosen for the onset of superimposed ice formation at the M-AWS was incorrect, or that the rate of superimposed ice formation was incorrectly simulated by SI-P2. Since there are no data available to properly predict the starting date of superimposed ice formation across the

glacier, energy balance simulations in Chapter 4 will assume that superimposed ice begins to form as soon as melting occurs at a given location. Because SI-P2 produced a very good estimate of measured superimposed ice thickness when superimposed ice formation began on JD 167 at the M-AWS, it is used for energy balance simulations in Chapter 4. The advantage to using algorithm SI-P2 is that measured ice temperature profiles at the 3 weather station sites can be used to initialize the SI-P2 algorithm. In this way, the fact that superimposed ice already began to form at some locations on the glacier can be accounted for by initializing these locations with a warmer ice temperature profile.

Results from simulations for the M-AWS suggest that SI-P1 is useful for the type of modelling being carried out in this paper, despite the fact that it may not simulate the temporal variations in superimposed ice formation. Approximations of the net mass balance across the glacier are for the most part independent of temporal variations in superimposed ice formation. As long as the maximum superimposed ice thickness is predicted accurately, it does not matter when during the season this superimposed ice formed. However, results from the M-AWS may not be representative of the entire glacier. Spatial patterns in superimposed ice thickness predicted by SI-P2 are presented in Chapter 4.

More tests are needed to determine which of the physically-based superimposed ice algorithms is more accurate. SI-P1 is useful because it is a simple and fast algorithm which produces maximum superimposed ice thickness estimates based on near surface ice temperatures. SI-P2 is more computationally intensive but allows for the prediction of the temporal patterns in superimposed ice formation, and may be more accurate at predicting superimposed ice thicknesses. The empirical model is useful because it can be used with a limited amount of data, but may produce inaccurate predictions of maximum superimposed ice thicknesses. Assuming the physically-based models are more accurate, it is possible to use them to improve the empirical model. For instance, a comparison of SI-P1 and SI-P2 results with SI-E1 for the M-AWS suggests that previously reported values for Pmax may be too high (SI-P2 predicts a Pmax value of 0.47 rather than 0.60). Future modelling which predicts the routing of meltwater through the snowpack and across the

glacier should use an algorithm such as SI-P2 which includes a consideration of temporal patterns in superimposed ice formation.

Errors in predicted superimposed ice thicknesses were not necessarily the result of inadequacies in the superimposed ice routine which produced such predictions. Problems with the energy balance model itself could equally have been to blame for discrepancies between modeled and measured superimposed ice thicknesses. However, the fact that predicted ice temperatures using SI-P1 matched well with observed ice temperatures is promising, since such predictions were made independent of the melt model. Future work should examine predicted and measured superimposed ice thicknesses at multiple locations across the glacier, and at various times during the melt season.

3.7 Conclusion

Using data collected from John Evans Glacier during the summer of 1996, the superimposed ice algorithm used by Woodward (1995) has accurately predicted the measured superimposed ice thickness and near-surface ice temperatures at the middle weather station. Previous energy balance models for high Arctic glaciers have simulated superimposed ice formation based on the Pmax approach, which is probably overly simplistic. Although the Pmax model and the model of Woodward (1995) both predicted identical maximum superimposed ice thicknesses when the onset of superimposed ice formation was set to JD 182, Woodward's model performed better when superimposed ice was allowed to form from the start of energy balance simulations. Since most energy balance models for high polar glaciers are not sophisticated enough to predict the onset of superimposed ice formation, it is suggested that Woodward's approach is better to use for such models.

This paper documents a method by which the rate of superimposed ice formation can be predicted at each time step within the energy balance model. It is not possible, given the data available in this study, to properly assess whether this superimposed ice algorithm (SI-P2) is the most accurate method for simulating superimposed ice thicknesses. Results from this paper show that, by the end of the melt season, the maximum amount of superimposed ice which formed at the M-AWS was the same using SI-P1 or SI-P2 (for simulations where the onset of

superimposed ice formation was the same as the start date for the melt model). Therefore there might not be an advantage in using SI-P2 for mass balance simulations, since it is much more computationally intensive. However, it may be important to account for variations in the rate of superimposed ice formation using SI-P2 in models which simulate the temporal and spatial patterns of runoff from the glacier.

Met. Station Name	Latitude	Longitude	Elevation (m a.s.l.)
L-AWS	79°37'52"	74°04'38"	261
M-AWS	79°40'17"	74°20'59"	824
U-AWS	79°42'35"	74°33'20"	1183

Table 3.1 Location and elevation of each automatic weather station.

Measurement	Instrument and model	Measurement Range	Instrument Error
Air Temperature	Campbell 107F Temperature probe	-53°C to +48°C	±0.4°C
Relative humidity sensor	HMP35CF Vaisala RH probe	0 to 100% RH	±2% RH (0 to 90% RH) ±3% RH (90 to 100% RH)
Incoming short-wave radiation	LI200s Li-COR Pyranometer	0.280-2.80 μm	±5% maximum
Outgoing short-wave radiation	Kipp and Zonen CM7 Pyranometer	0.305-2.80 μm	±2%
Net Radiation	REBS Q7 net radiometer	0.250 to 6.0 μm	wind speed dependent
Air Pressure	CS105 Barometric Pressure Sensor	600 to 1060 mb	±0.5 mb (@ 20°C)
Wind Speed	05103 R.M. Young Wind Monitor	0 to 60 m/s	1.0 m/s threshold sensitivity
Wind Direction	05103 R.M. Young Wind Monitor	360°	1.0 m/s threshold sensitivity at 10° displacement
Height of snow/ice surface	UDG01 Ultrasonic Depth Gauge	0.6 to 10 m	±1 cm or 0.4% of distance to target (whichever is greatest)

Table 3.2 Specifications of meteorological instruments. These instruments were connected to a Campbell Scientific CR10 data logger and SM 192/716 storage module.

Station	Thermocouple Location
L-AWS	-3.2
	-2.3
	-1.6
	0.0
	+0.3 (snow)
M-AWS	-4.8
	-3.6
	-1.8
	0.0
U-AWS	-3.2
	-2.3
	-1.6
	0.0
	+0.5 (snow)

Table 3.3: Location of thermocouples used to measure ice or snow temperatures at the start of the measurement period for each AWS. The position 0.0 represents the location of the snow-ice interface.

Station	Start of Hourly Measurements	End of Hourly Measurements
L-AWS	JD 172, 1996	JD 212, 1996
M-AWS	JD 167, 1996	JD 202, 1996
U-AWS	JD 169, 1996	JD 216, 1996

Table 3.4 Time intervals of hourly output of meteorological observations at each AWS.

Depth of Thermocouple	M-AWS	U-AWS
0m	0.41	0.60
-1.6m	0.88	0.95
-2.3m		0.95
-3.2m	0.82	0.82
-4.8m	0.75	
Average	**0.72**	**0.83**

Table 3.5: Correlation coefficients between measured and predicted ice temperature variations at the M-AWS and U-AWS. Only coefficients with $p < 0.05$ are shown.

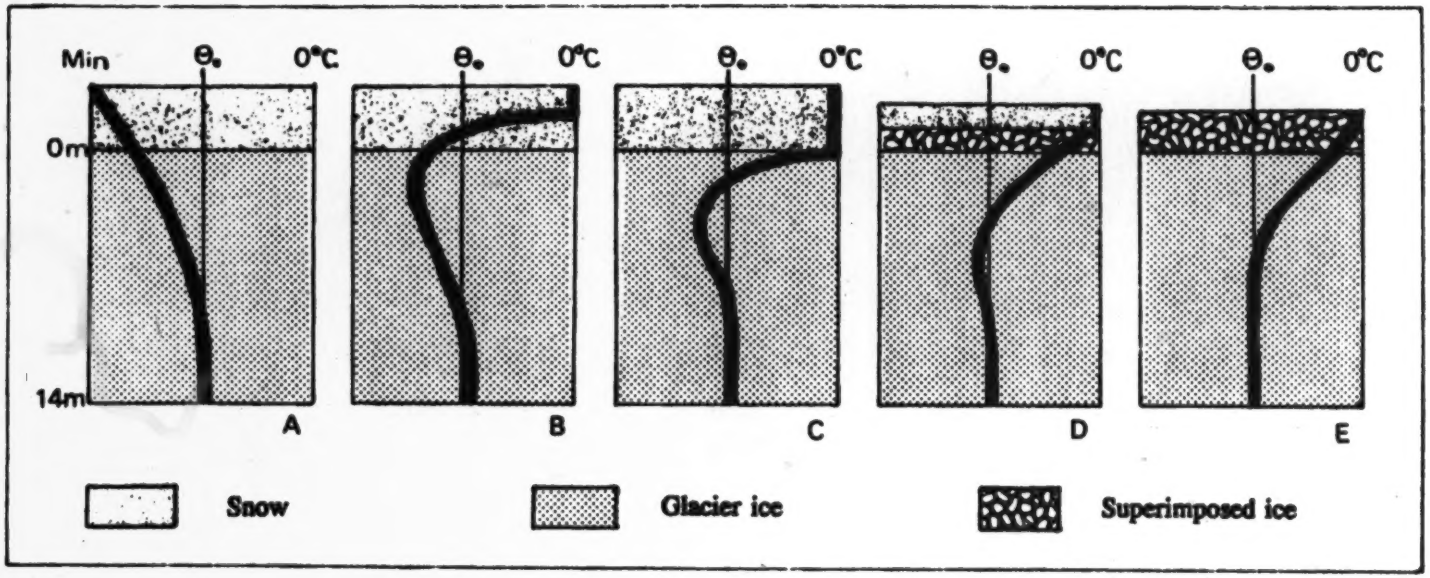

Figure 3.1: Schematic development of the near surface temperature profile during the early melt season.
(Reproduced from Woodward, 1995, p. 3)

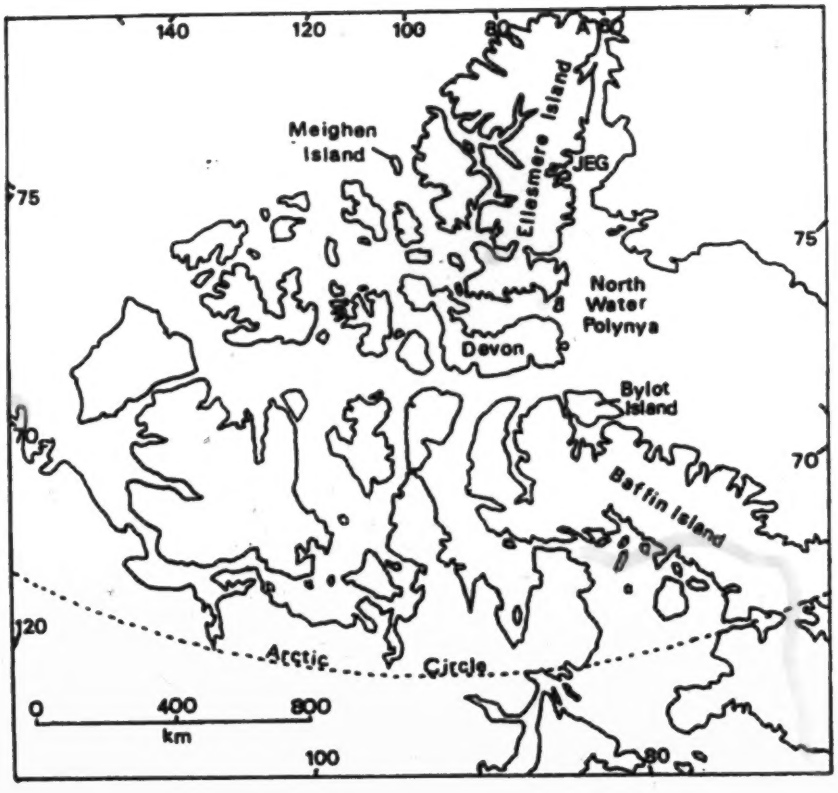

Figure 3.2: Map of the Canadian Arctic Islands. JEG = John Evans Glacier, A=AES Meteorological station at Alert.

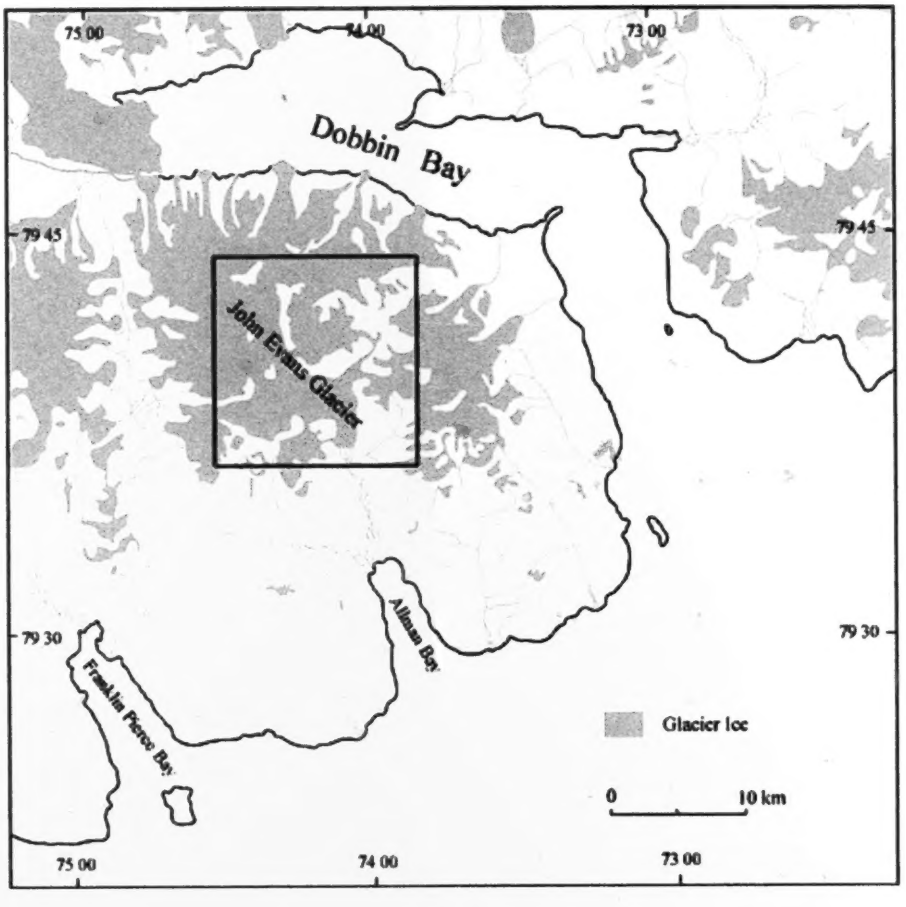

Figure 3.3: Location of John Evans Glacier, Ellesmere Island, Nunavut, Canada.

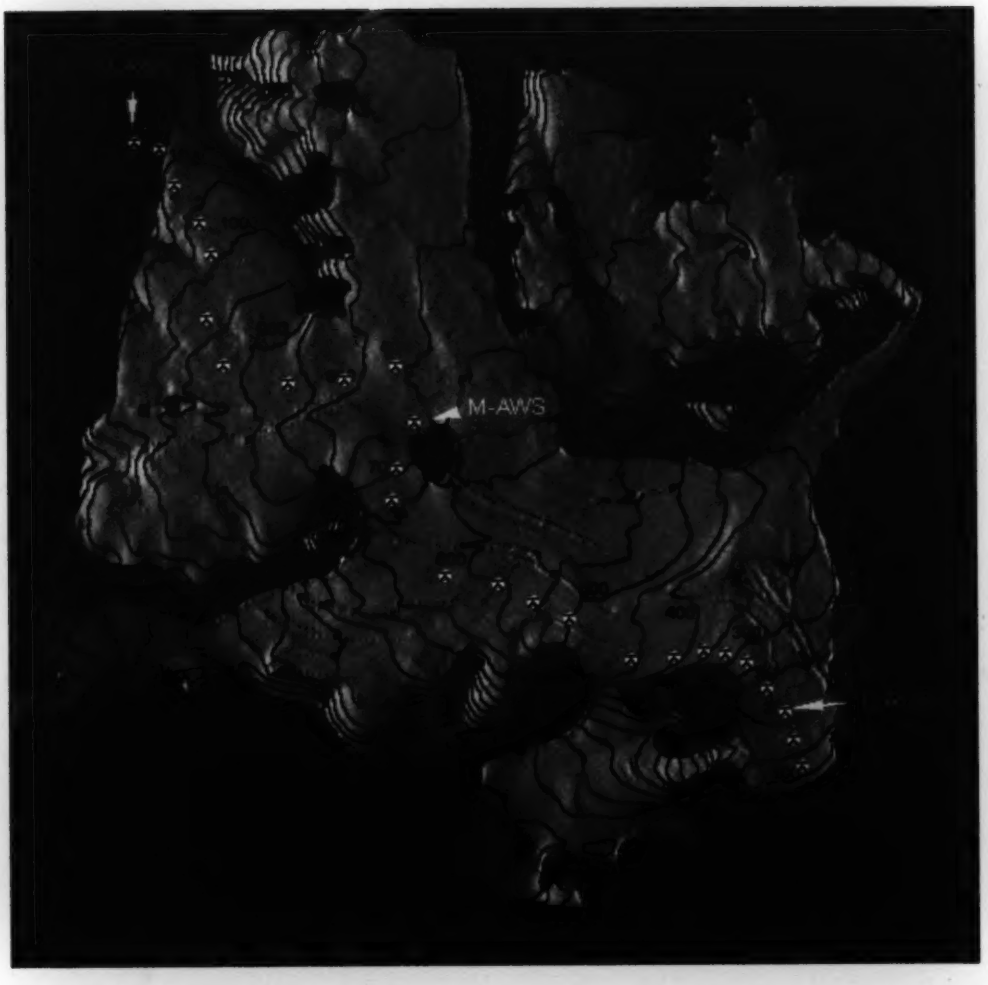

Figure 3.4: Contour map of John Evans Glacier with locations of lower, middle and upper automated weather stations (marked with arrows) and stake locations (marked with circles).

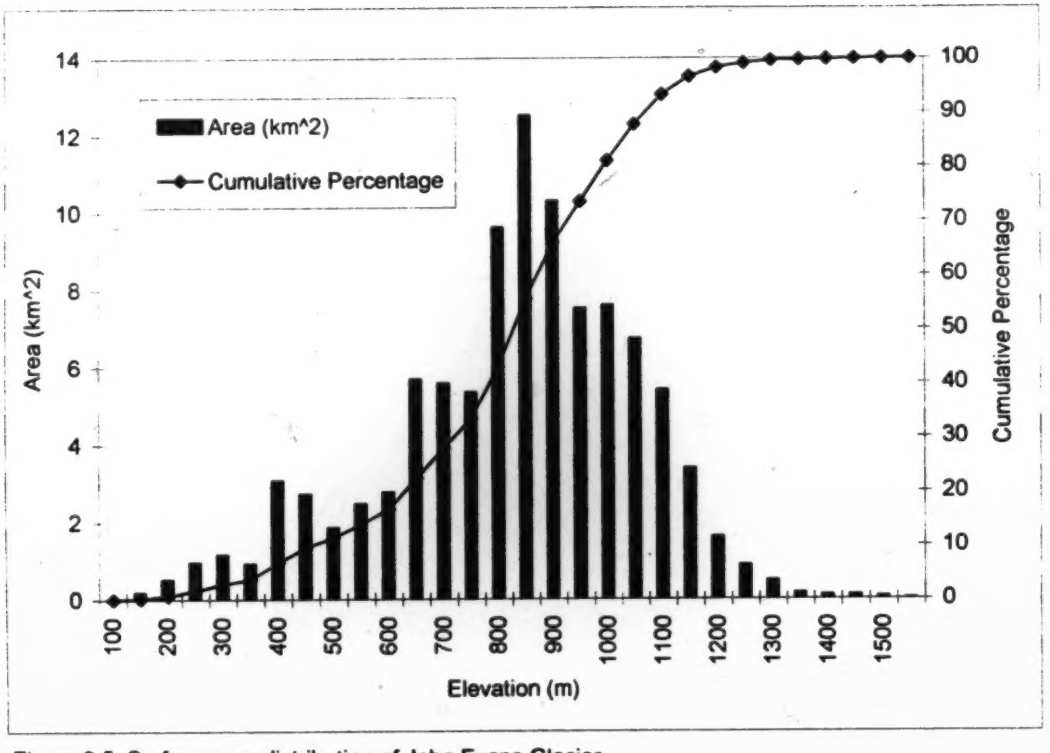

Figure 3.5: Surface area distribution of John Evans Glacier.

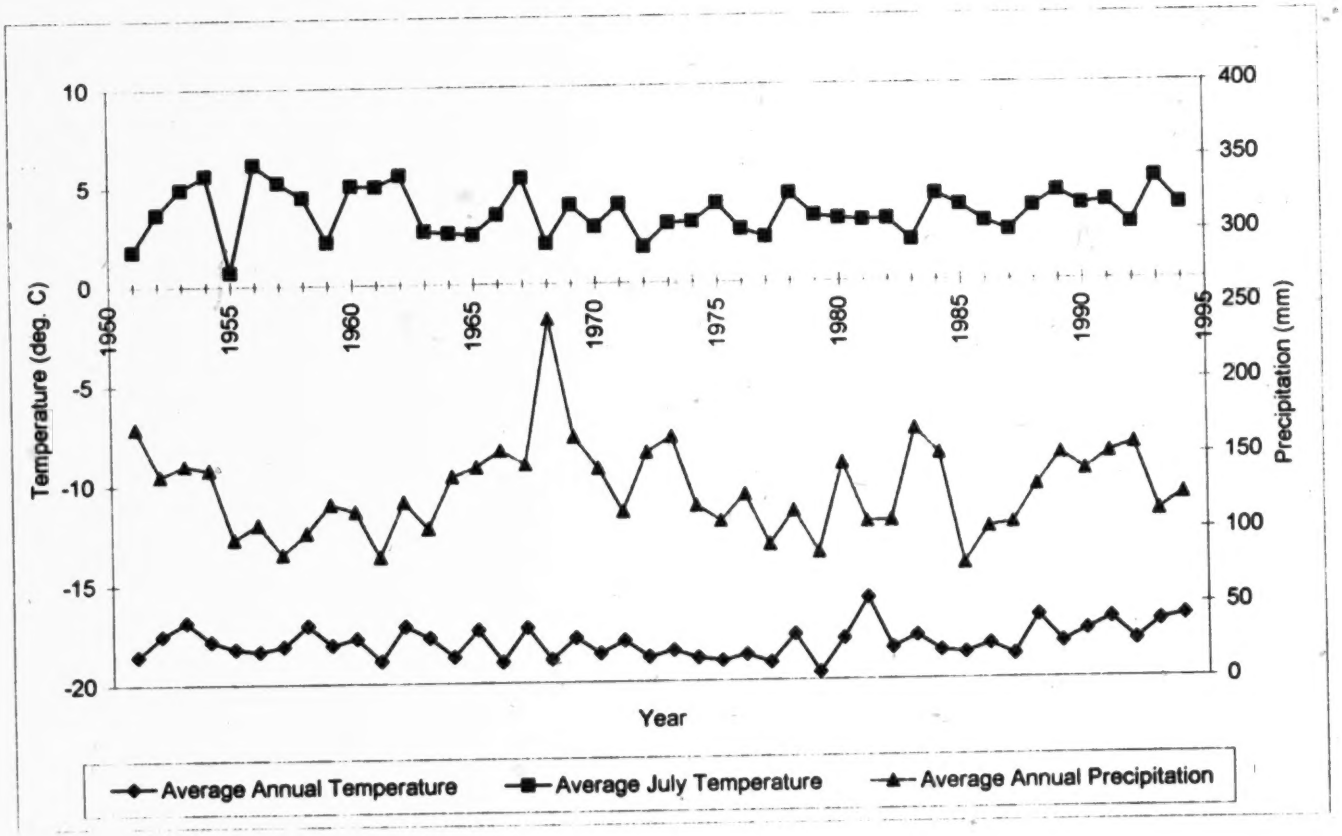

Figure 3.6 Temperature and precipitation records from AES meteorological station, Alert.

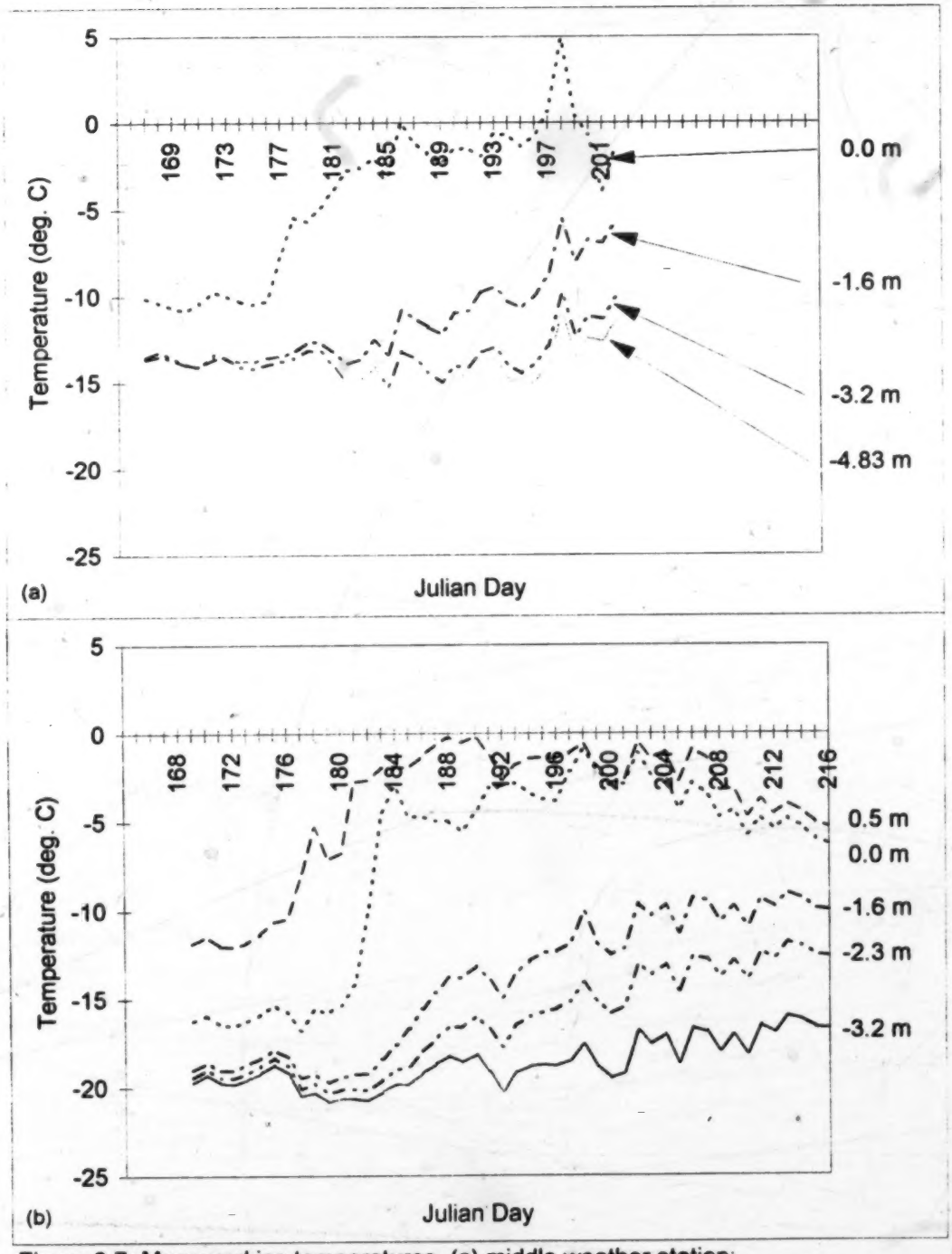

Figure 3.7: Measured ice temperatures. (a) middle weather station; (b) upper weather station.

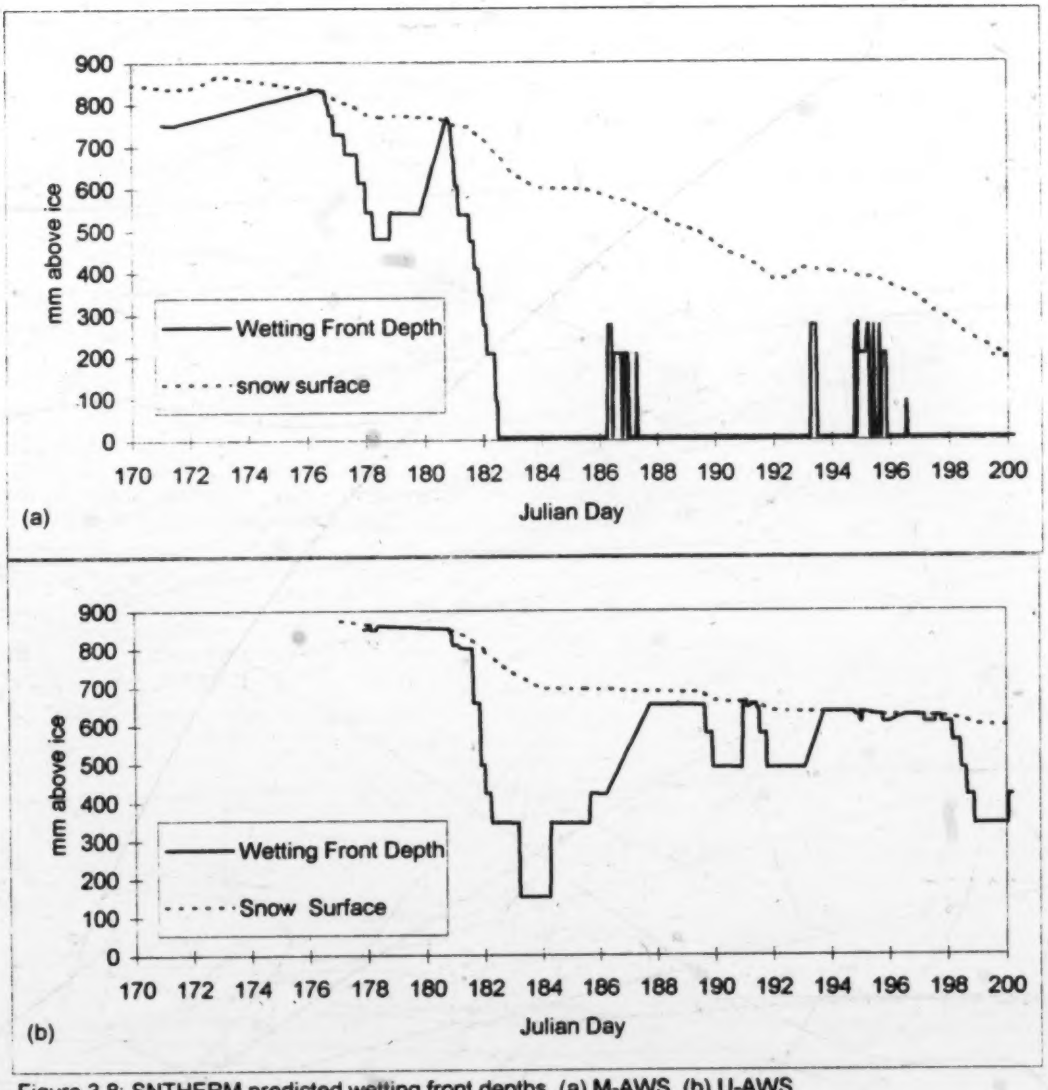

Figure 3.8: SNTHERM predicted wetting front depths. (a) M-AWS, (b) U-AWS.

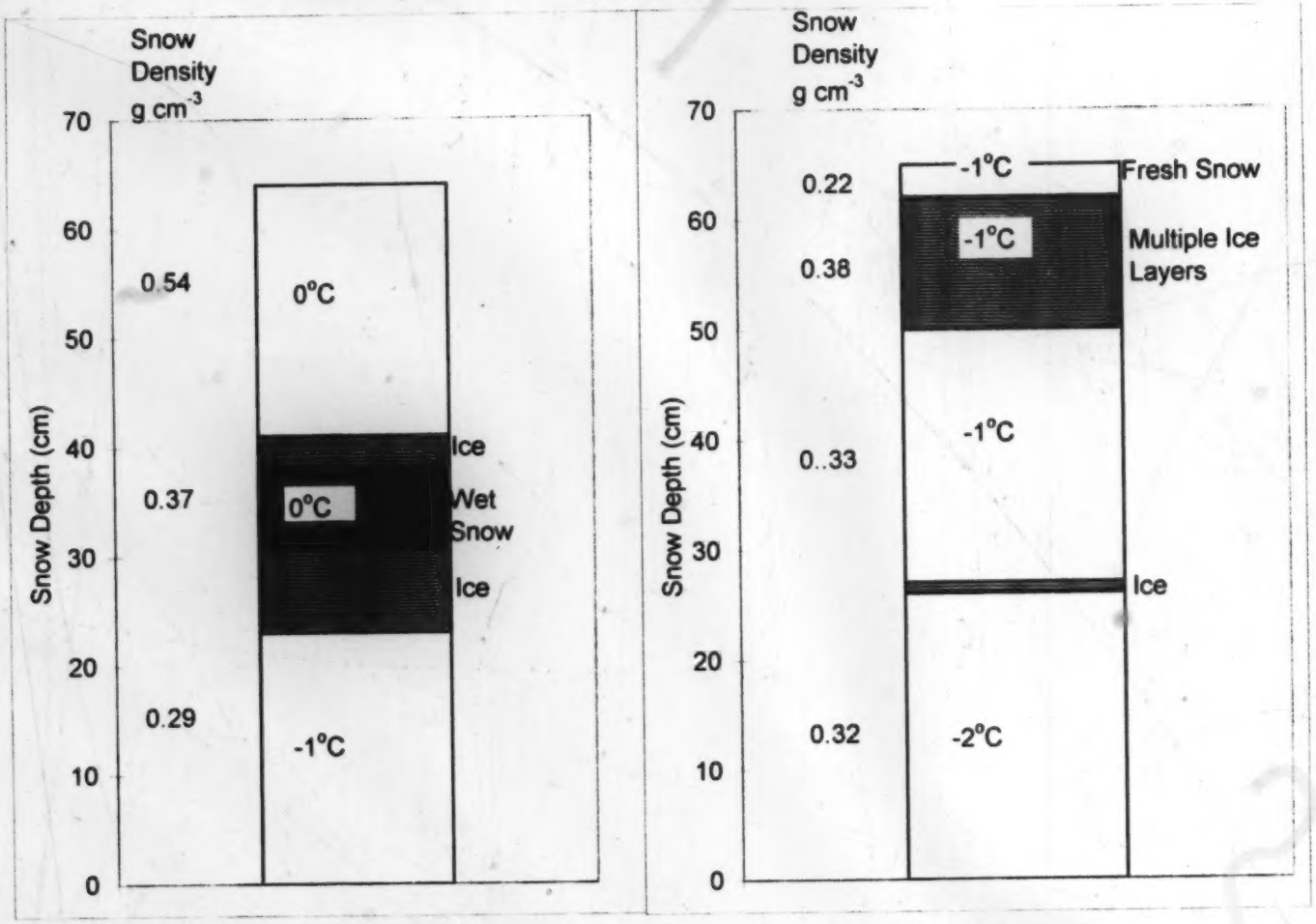

Figure 3.9: Observed snowpack stratigraphy. (a) JD 181, M-AWS. (b) JD 185, U-AWS.

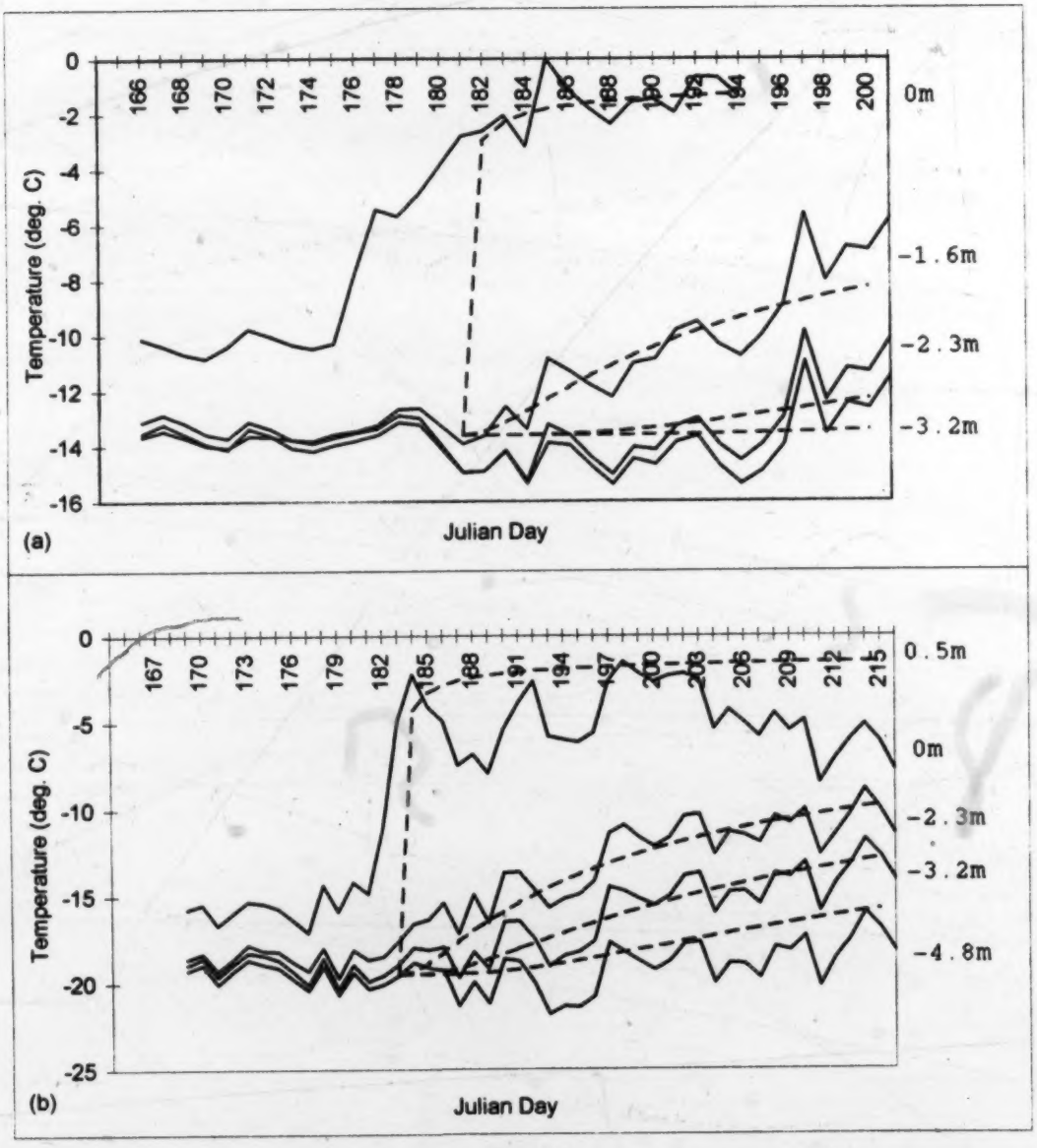

Figure 3.10: Measured and predicted near surface ice temperatures. (a) M-AWS, (b) U-AWS.

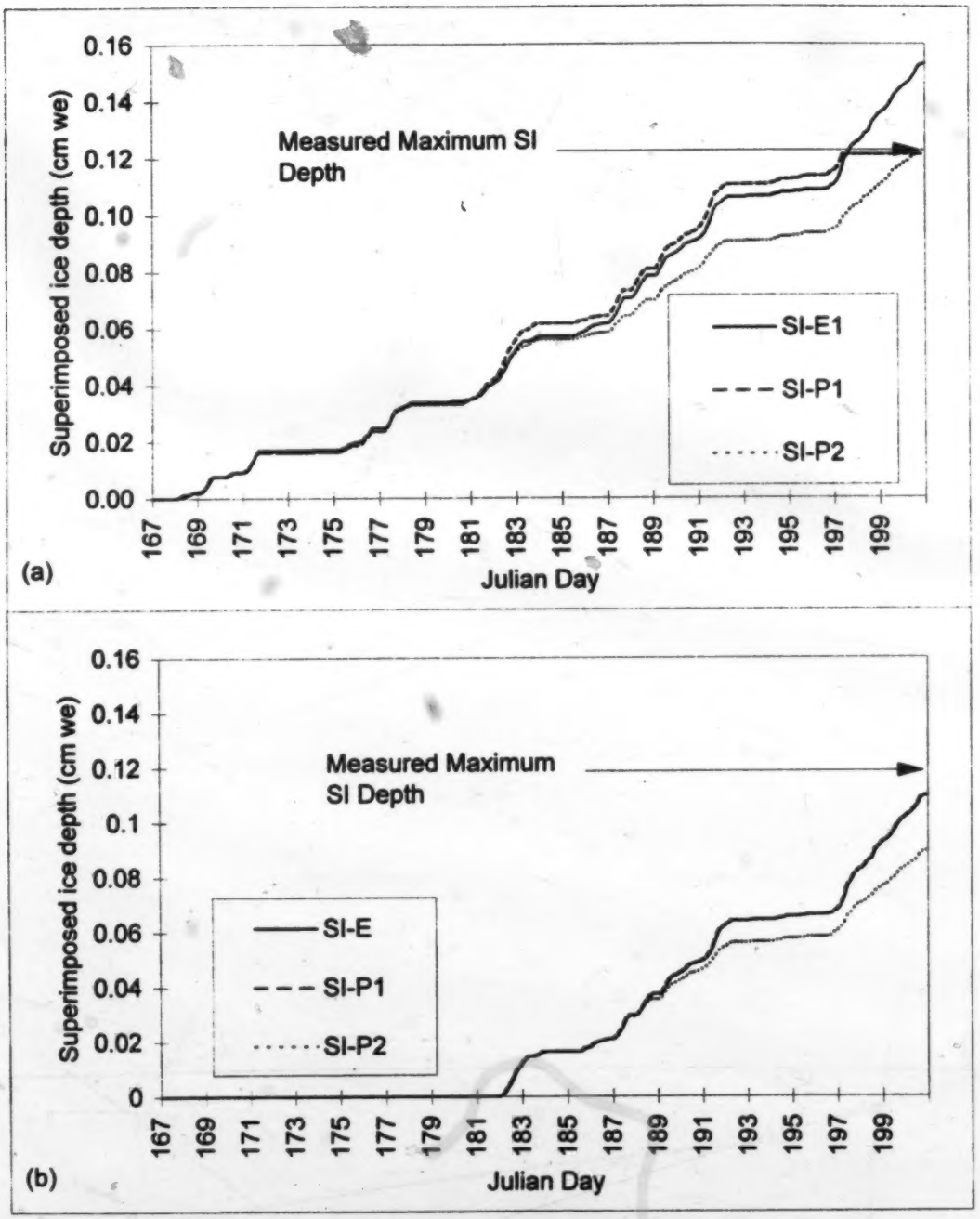

Figure 3.11: Comparison of predicted and measured superimposed ice depths at the M-AWS. (a) Start day for superimposed ice formation = JD 167.(b) Start day for superimposed ice formation = JD 182.

3.8 References

Arnold, K.C. 1965. Aspects of the Glaciology of Meighen Island, Northwest Territories, Canada. *Journal of Glaciology*. 5(40): 399-410

Arnold, N.S., Willis, I.C., Sharp, M.J., Richards, K.S. and Lawson, W.J. 1996. A distributed surface energy-balance model for a small valley glacier. I. Development and testing for Haut Glacier d'Arolla, Valais, Switzerland. *Journal of Glaciology*. 42(140): 77-89.

Baird, P.D., Ward, W.H., and Orvig, S. 1952. The Glaciological Studies of the Baffin Island Expedition, 1950. Part I: Methods of Nourishment of the Barnes Ice Cap. *Journal of Glaciology*, 2(11): 2-23.

Blatter, H. 1987. On the Thermal Regime of an Arctic Valley Glacier: A Study of White Glacier, Axel Heiberg Island, N.W.T., Canada. *Journal of Glaciology*, 33(114): 200-211.

Carnahan, B., Luther, H.A., and Wilkes, J.O. 1969. Applied Numerical Methods. *John Wiley & Sons, Inc.* p. 451-452.

Carslaw, H.S. and Jaeger, J.C. 1946. Conduction of Heat in Solids. *Oxford University Press*. 510p.

Colbeck, S.C. 1971. One-dimensional water flow through snow. USA Cold Regions Research and Engineering Laboratory, Research Report 296.

Greuell, W. and Konzelmann, T. 1994. Numerical modelling of the energy balance and the englacial temperature of the Greenland Ice Sheet. Calculations for the ETH-Camp location (West Greenland, 1155m a.s.l.). *Global and Planetary Change*. 9: 91-114.

Holmgren, B. 1971. Climate and Energy Exchange on a Sub-polar Ice Cap in Summer. Part. F. On the Energy Exchange of the Snow Surface at Ice Cap Station. Arctic Institute of North America Devon Island Expedition 1961-1963. *Meddelanden Från Uppsala Universitets Meteorologiska*. No.112.

Hooke, R.LeB. 1976. Near-Surface Temperatures in the Superimposed Ice Zone and Lower Part of the Soaked Zone of Polar Ice Sheets. *Journal of Glaciology*, 16(74): 302-304.

Hooke, R.LeB. 1983. Near-surface temperatures near and below the equilibrium line on polar and subpolar glaciers. *Zeitschrift Für Gletscherkunde*. 19(1): 1-25.

Jonsson, S. and Hansson, M. 1990. Identification of Annual Layers in Superimposed Ice From Störöyjokulen in Northeastern Svalbard. *Geografiska Annaler*, 72A: 41-54.

Koerner, R.M. 1970. Some Observations on Superimposition of Ice on the Devon Island Ice

Cap, N.W.T. Canada. *Geografiska Annaler*, 52A: 57-67.

Koerner, R.M., and Paterson, W.S.B. 1974. Analysis of a Core Through the Meighen Ice Cap, Arctic Canada, and Its Paleoclimatic Implications. *Quaternary Research*, 4: 253-263.

Marsh, P. and Woo, M. 1984. Wetting Front Advance and Freezing of Meltwater Within a Snow Cover 2. A Simulated Model. *Water Resources Research*, 20(12): 1865-1874.

Palosuo, E. 1987. Ice Layers and Superimposition of Ice on the Summit and Slope of Vestfonna, Svalbard. *Geografiska Annaler*, 69A: 289-296.

Paterson, W.S.B. 1972. Temperature distribution in the upper layers of the ablation area of the Athabasca Glacier, Alberta, Canada. *Journal of Glaciology*. 11(61): 31-41.

Reeh, N. 1991. Parameterization of melt rate and surface temperature on the Greenland Ice Sheet. *Polarforschung*, 59(3): 113-128.

Schytt, V. 1949. Re-Freezing of the Melt-Water on the Surface of Glacier Ice. *Geografiska Annaler*, 34(1-4): 222-227.

Wakahama, G., Kuroiwa, D., Hasemi, T., and Benson, C.S. 1976. Field Observations and Experimental and Theoretical Studies on the Superimposed Ice of McAll Glacier, Alaska. *Journal of Glaciology*, 16(74): 135-149.

Ward, W.H. and Orvig, S. 1952. The Glaciological Studies of the Baffin Island Expedition, 1950. Part IV: The Heat Exchange at the Surface of the Barnes Ice Cap During the Ablation Period. *Journal of Glaciology*, 2(13): 158-168.

Wolfe, P.M. 1995. Hydrometeorological Investigations on a Small Valley Glacier in the Sawtooth Range, Ellesmere Island, Northwest Territories. *Unpublished M.Sc. Thesis*. Wilfrid Laurier University. 205p.

Woodward, J. 1995. Superimposed ice and glacier mass balance. *Unpublished M.Sc. Thesis*. University of Alberta. 96p.

Woodward, J., Sharp, M. and Arendt, A. *In Press*. The influence of superimposed ice formation on the sensitivity of glacier mass balance to climate change.

Chapter 4: Development and Testing of a Surface Energy Balance Model for a High Arctic Glacier

4.1 Introduction

Energy balance models are used to calculate net transfers of energy between the atmospheric surface boundary layer and the surface of a glacier. Because they explicitly describe the physical transfers of latent, sensible and radiative energy between the atmosphere and the glacier surface, such models require as inputs detailed datasets of the near-surface air temperature, relative humidity, net radiation, and wind speed. In glacier mass balance studies, energy balance models are used to determine the energy available for surface melting and thus to predict the summer mass balance. When this is subtracted from the winter mass balance, the net balance across the glacier can be obtained.

Because of the difficulty in obtaining detailed meteorological data from high Arctic sites, there have been relatively few energy balance simulations for high Arctic glaciers. Of these studies, most have been point specific investigations, in which data from a single meteorological station are used to improve energy balance theory by comparing melt computations with measurements of surface lowering at that site (see for instance Keeler (1963), Havens et al. (1965) and Adams (1966) for White Glacier, Axel Heiberg Island, NWT; Braithwaite and Olesen (1990), Konzelmann and Braithwaite (1995), van den Broeke (1996) for the margins of the Greenland Ice Sheet; Ohmura et al. (1994) for the equilibrium zone of the Greenland Ice Sheet). The theory developed in these studies has only recently been applied on a glacier-wide scale for the purpose of modelling spatial patterns in glacier mass balance. Such spatially distributed models consist of point models applied to multiple locations across a glacier, usually using a digital elevation model (DEM) to subdivide the glacier into grid cells. These models cannot be considered 3-dimensional models because they do not explicitly account for lateral energy transfers between grid cells.

Spatially-distributed energy balance models are useful because they can be used to simulate the present-day mass balance of Arctic glaciers, possibly reducing the need for manual

measurements of glacier mass balance in the Arctic. Also, because of recent concerns about the effects of global climate change on the melt rates of polar ice sheets, spatially distributed energy balance models have been used to test the sensitivity of polar glaciers to changes in surface air temperature and other climatological parameters. A number of spatially-distributed energy balance models have been applied to the Greenland ice sheet. van de Wal and Oerlemans (1994) and van de Wal (1996) examined the sensitivity of the Greenland ice sheet to climate change using an energy balance model on a grid with 20 km spacing, and Ohmura *et al.* (1996) modelled the influence of doubling atmospheric CO_2 on the evolution of the Greenland ice sheet, using energy balance simulations within a high resolution global climate model (GCM). However, these models were limited because of their coarse grid spacing, and did not consider the effects of surface topography on incoming radiation. Also, they were driven by data from a sparsely distributed set of meteorological stations, and their predictions have not been adequately tested against measured mass balance data.

Recently, Arnold *et al.* (1996) developed a spatially-distributed energy balance model on a 20x20 m grid which used a digital elevation model to calculate the effects of shading and surface topography on incoming radiation. This model has been applied to John Evans Glacier, Nunavut, using data collected during the summer of 1994 (Woodward, 1995). Woodward made a number of modifications to the energy balance model developed by Arnold *et al.*, including the addition of routines to account for the formation of superimposed ice, the transfer of thermal energy between the snowpack and the ice surface, and the surface albedo of arctic glaciers. The sensitivity of this model to alterations in the superimposed ice, albedo, cloud cover and shading routines emphasised the importance of correctly parameterizing these components of the surface energy balance. For instance, eliminating the superimposed ice routine decreased the average specific mass balance for the catchment from -186 mm to -417 mm. Unfortunately, the 1994 dataset was limited, consisting of meteorological data from a single station situated in the proglacial area of the catchment. Also, lack of field data prevented evaluation of the accuracy of the model in simulating the formation of superimposed ice and evolution of surface albedo and in predicting mass balance.

During the summer of 1996, detailed meteorological measurements were made at 3 sites across

John Evans Glacier. These data can be used to drive the surface energy balance model (EBM-94) developed by Woodward (1995). Ablation stake and snowpit data were also collected across the catchment, and are used to determine the initial snow water equivalence across the glacier at the start of the melt season, and to test model output. Changes are made to Woodward's model, as outlined in Table 4.1.

During some phases of model development, average snow density, which could not always be measured directly in the field because of the difficulty in accessing some areas of the glacier, has been simulated using the model SNTHERM (Jordan, 1991). SNTHERM is a one-dimensional mass and energy balance model for predicting temperature profiles within strata of snow and frozen soil. Although temperature prediction is the primary objective of the model, snow accumulation, ablation, densification and metamorphosis, as well as the transport of liquid water and water vapor, are included as required components in the heat and mass balance calculations (See Section 2.41 for a complete description of SNTHERM).

4.2 Study Area

4.21 Site description

John Evans Glacier is a large valley glacier located at 79°40'N 74°00'W on an unnamed peninsula south of Dobbin Bay, eastern Ellesmere Island, Nunavut, Canada (Figure 4.1-4.5). Its catchment area is 211km^2, of which 47% is glaciated, and the glacier spans an altitudinal range of 50 to 1500 m (Figure 4.6). 77% of the ice surface area lies between 600m and 1100m. Based on contour curvature, the ELA on John Evans Glacier is around 700 m (Figure 4.3). Thus the majority of the glacier's surface area lies at or around the equilibrium line. The catchment comprises a main trunk glacier fed from a number of sub-catchments in the western part of the basin, and 8 small valley glaciers feeding into a marginal lake 3 km from the snout of the main trunk glacier on its eastern side.

4.22 Local Climate

Mean annual and July temperatures recorded over the period 1951-1994 at the AES meteorological station at Alert, north-eastern Ellesmere Island (82°30'N 62°20'W) are shown in Figure 4.7. The mean annual sea level temperature at Alert was -17.8°C. During 1988-89, the average annual air temperature at Alert was -16.9°C. This is similar to the average annual air temperature (-17.3°C) measured for the same period at Allman Bay, located 5km south of John Evans Glacier (Figure 4.2) (G. Henry, *pers comm.*). However, July 1988 temperatures were approximately 3°C warmer at Allman Bay (located at sea level) than at Alert. Field data for the present study were collected during the summer of 1996, which was unusually cold. The mean 1996 July air temperature measured at the lower weather station (elevation 261 m) on John Evans Glacier was approximately 3°C colder than the mean July air temperature at Allman Bay in 1988 (note that some of this difference in temperature may be due to differences in surface type and elevation between Allman Bay and John Evans Glacier). Mean total precipitation from 1 August 1995 to 1 August 1996 at Alert (165.4 mm WE) was 128% higher than the mean annual total precipitation at Alert over the period 1951-1994 (128.5 mm WE).

4.3 Model Description

The framework of the energy balance model is similar to that described by Arnold et al. (1996). The energy available for melt at the glacier surface is given by:

$$Q_M = Q^* + Q_H + Q_E - Q_G \qquad (4.1)$$

Where Q^*, the total radiation flux, is:

$$Q^* = K^* + L^* \qquad (4.2)$$

K^* is the net short-wave radiation flux, L^* is the net longwave radiation flux, Q_H is the sensible heat flux, Q_E is the latent heat flux and Q_G is the conductive heat flux into the glacier. For model output, all fluxes are expressed in millimetres of water per unit time. The five components of the energy balance are evaluated for each grid cell in the catchment for every hour of the model run. The treatment of each component is described in detail below.

4.31 Short-wave radiation

K^*, the net short-wave radiation flux, is given by:

$$K^* = (1-\alpha)\, K\downarrow \tag{4.3}$$

Where μ is the surface albedo and $K\downarrow$ is the flux of incoming short-wave radiation. The surface albedo is calculated using the algorithm developed in Chapter 2. $K\downarrow$ can be further divided into its direct and diffuse components:

$$K\downarrow = K\downarrow_{DIR} + K\downarrow_{DIF} \tag{4.4}$$

where $K\downarrow_{DIR}$ is the direct beam and $K\downarrow_{DIF}$ the diffuse incoming short-wave solar radiation. The ratio of diffuse to direct radiation is calculated using the routine developed by Shapiro (1987) (See Chapter 2, Equations 2.7 - 2.17). A knowledge of the ratio of direct to diffuse incoming solar radiation is important for the albedo algorithm, and is also used to determine the proportion of the incoming solar radiation which should be corrected for a sloping surface. Slope corrections are not necessary for the diffuse component of the radiation because diffuse radiation is isotropic. However, the directional component of the solar radiation, $K\downarrow_{DIR}$, needs to be adjusted to take into account the effects on radiation receipts of slope, aspect and shading from surrounding topography. Slope angle and aspect are obtained for a given cell x, y in the DEM using neighbourhood functions which examine the four surrounding cells, such that:

$$\theta_{surf} = \arctan\left(\sqrt{\left\{\frac{\left(elev_{x-1,y} - elev_{x+1,y}\right)}{2s}\right\}^2 - \left\{\frac{\left(elev_{x,y-1} - elev_{x,y+1}\right)}{2s}\right\}^2}\right) \tag{4.5}$$

$$\sigma_{surf} = \arctan\left(\sqrt{\left\{\frac{\left(elev_{x-1,y} - elev_{x+1,y}\right)}{2s}\right\} - \left\{\frac{\left(elev_{x,y-1} - elev_{x,y+1}\right)}{2s}\right\}}\right) \tag{4.6}$$

Where θ_{surf} is the slope angle from the horizontal (always positive) and σ_{surf} is the aspect of the slope measured as degrees from due south, positive to the west and negative to the east,

elev is the cell elevation and s is the grid cell resolution (25m).

Topographic shading is determined using the algorithm of Arnold *et al.* (1996). All cells in the DEM are originally designated as 'in sun'. The cell nearest the sun is selected and the algorithm "walks" from this cell along the path of the solar beam in steps equal to the DEM grid size. Two tests are then made after each "step". If the elevation of the new cell is higher than the solar beam at that point, then the start cell is designated as "in shade". If the new cell is lower than the solar beam and has already been designated as "in sun" on a previous walk, then the start cell stays designated as "in sun". If neither of these conditions is met, then the walk continues to the next cell. If neither condition is met by the time the walk reaches the opposite edge of the DEM, then the original cell is designated as "in sun". For all model simulations in this paper, the shading pattern across the glacier is recalculated for each hour of each day.

If the cell is designated as "in sun", then the direct beam radiation received by the nearest radiometer ($K\downarrow_{DIR}$) is converted to the equivalent radiation received by a surface normal to the sun's rays ($K\downarrow_{N,DIR}$) using the relationship:

$$K\downarrow_{N,DIR} = \frac{K\downarrow_{DIR}}{\cos\theta_{surf}} \tag{4.7}$$

The radiation received by an individual grid cell on the sloping glacier surface is then:

$$K\downarrow_{DIR,SLOPE} = K\downarrow_{N,DIR}\left[\sin\phi\cos\sigma_{surf} + \cos\phi\sin\sigma_{surf}\cos(\varphi - \theta_{surf})\right] \tag{4.8}$$

Where φ is the solar azimuth, defined as degrees from due south, positive to the west and negative to the east. To obtain the total incoming solar radiation, it is necessary to recombine $K\downarrow_{DIF}$ with the direct beam component, which has been corrected for a sloping surface:

$$K\downarrow = K\downarrow_{DIR,SLOPE} + K\downarrow_{DIF} \tag{4.9}$$

If the cell is designated as "in shade", only diffuse radiation is allowed to reach the glacier

surface:

$$K\downarrow = \bar{K}\downarrow_{DIF} \tag{4.10}$$

4.32 Longwave radiation

L^*, the net longwave radiation flux, is given by:

$$L^* = (L\downarrow - L\uparrow) \tag{4.11}$$

Where $L\downarrow$ is the incoming longwave radiation, and $L\uparrow$ is the outgoing longwave radiation. $L\uparrow$ has a constant value of 316 Wm^{-2}, assuming that the glacier surface is at 0°C and radiates as a black body. $L\downarrow$ is usually calculated as a function of cloud effective emissivity and air temperature. In this paper, net all-wavelength and net short-wave radiation measurements allow for the calculation of $L\downarrow$ as a residual of Equation 4.2:

$$L\downarrow = Q^*_{MEAS} - K^*_{MEAS} + L\uparrow \tag{4.12}$$

4.33 Turbulent heat fluxes

EBM-94 calculates turbulent heat fluxes using the relationships derived by Ambach (1986), based on energy balance measurements on the Greenland ice sheet. This method assumes adiabatic stratification in a Prandtl-type boundary layer, in which wind speed increases as the natural logarithm of the height above the surface, and in which vertical fluxes of energy and momentum are constant with height. Recently, Braithwaite (1995) has examined atmospheric stability over the Greenland ice sheet by comparing sensible heat fluxes for logarithmic and log-linear wind profiles, and has concluded that calculations which use a log-linear profile with corrections for atmospheric stability produce the most realistic sensible heat flux estimations. Therefore, this model (EBM-96) calculates turbulent heat fluxes for each cell using the bulk transfer technique for estimating heat exchange in turbulent flow (Munro, 1990):

$$Q_H = \frac{\rho c_p k^2 u_z T_Z}{\left[\ln\left(\frac{z}{z_o}\right) + a_M\left(\frac{z}{L}\right)\right]^2} \tag{4.13}$$

$$Q_E = \frac{0.622 \rho L_v k^2 u_z \left(e_Z - e_s\right)/P}{\left[\ln\left(\frac{z}{z_o}\right) + a_M\left(\frac{z}{L}\right)\right]} \tag{4.14}$$

where ρ is the air density (kg m^{-3}), defined as:

$$\rho = \frac{P}{R_a T_Z} \tag{4.15}$$

where R_a is the gas constant:

$$R_a = 287\left\{1 + 0.608\left[\frac{0.622}{P}\left(R_h 611 \exp\left(\frac{17.27 T_z}{237.3 + T_z}\right)\right)\right]\right\} \tag{4.16}$$

and T_Z is the cell temperature at height z (K) and P is the atmospheric pressure (Pa) (Chow *et al.*, 1988):

$$P = P_{M-AWS}\left(\frac{T_Z}{T_{M-AWS}}\right)^{g/aR_a} \tag{4.17}$$

where g is the acceleration due to gravity (m s^{-2}), and the subscript "M-AWS" refers to air pressure and temperature measurements from the middle weather station.

Continuing with the variables in Equation 4.13 and 4.14, c_p is the specific heat capacity of air at a constant pressure (J kg^{-1}), k is the von Karman constant (0.40), u is the wind speed (m s^{-1}), z is the measurement height, L_v is the latent heat of vaporisation (J kg^{-1}), z_o is the surface roughness length (see following parameterization), and e_z and e_s are the vapour pressure at height z and the surface respectively (Pa).

The stability correction constant, a_M, is given a value of 5 (Munro, 1990). The Monin-Obukov length scale, L, is calculated as:

$$L = \frac{\rho c_p u^{*3} \overline{T}_C}{kgQ_H} \tag{4.18}$$

where $\overline{T}_C$ is the mean absolute air temperature in the surface layer (K) and u^*, the friction velocity, is calculated as:

$$u^* = \frac{ku_z}{\left[\ln\left(\frac{z}{z_o}\right) + a_M\left(\frac{z}{L}\right)\right]} \tag{4.19}$$

An iterative approach is used to solve Equation 4.13 to 4.19, whereby Q_H and u^* are calculated for neutral conditions ($z/L = 0$) to obtain an initial estimate of L, which is then re-substituted to obtain subsequent values of Q_H and u^*, the whole procedure being repeated for a number of iterations until the solution converges.

The calculation of Q_H and Q_E described above assumes a stable atmosphere. Additional computations to account for the effects of instability on Q_H and Q_E were omitted because the surface boundary layer at each of the 3 weather station sites was nearly always stable throughout the melt season (see Section 4.61). Simulations of Q_H and Q_E which accounted for instability were no different than calculations using the method described above.

Roughness Length Parameterization:

Because the transfer processes of temperature, vapour pressure and momentum are different in the interfacial sub-layer close to the surface, many authors suggest using different roughness lengths for each of these processes (Sverdrup, 1935; Holmgren, 1971; Ambach, 1986). However, there is much disagreement as to the appropriate values (Braithwaite, 1995).

Therefore, following Braithwaite (1995), the surface roughness is assigned an effective value which assumes each of the roughness lengths for temperature, vapour pressure and momentum are equal. However, different roughness lengths are used for snow and ice.

The surface roughness length when the surface is snow-covered, z_{os} (mm), is defined as:

$$z_{os} = \exp(-6.19 + 2.96 \log ADMT) \tag{4.20}$$

where ADMT is the accumulated daily maximum temperature since the last snowfall. This parameterization of z_{os} is based on both microtopographic and wind profile measurements across Haut Glacier d'Arolla, a valley glacier in the Swiss Alps (Brock, 1997). It is based on the relationship between ADMT and surface melt, so that increased melt increases the roughness of the surface. Although the relationship between ADMT and z_{os} is probably specific to the Arolla glacier, it is nonetheless used here because it can be used to predict temporal variations in surface roughness. The average value of z_{os} predicted by Equation 4.20 for the M-AWS was 0.11 mm, in agreement with Ambach's (1986) value (0.1 mm) of the surface roughness for momentum for snow. Following Braithwaite (1995), the surface roughness length for ice was set constant (z_{oi} = 1.7 mm).

4.4 Meteorological Data

Three automatic weather stations (AWS's) were set up at low (261 m a.s.l.), middle (824 m a.s.l.) and high (1183 m a.s.l.) elevation sites on John Evans Glacier in summer 1996 (Figure 4.3; Table 4.2). Each AWS consisted of 2 central masts made of galvanized steel drilled vertically ~1.5m into the ice, to which was mounted a cross-bar. Sensors were attached to the central mast and the cross-bar. Once the masts were frozen into the ice, they were very stable and only very strong winds could make them shake. None of the masts melted out or needed to be re-drilled into the ice. Incoming and outgoing short-wave radiation, net radiation, air temperature, relative humidity, wind speed and wind direction were measured at each site, while air pressure was measured only at the M-AWS (Figure 4.8; Table 4.3). Air temperature sensors were housed in 6-plate Gill radiation shields, while relative humidity sensors were housed in 12-plate shields. Ultrasonic depth gauges (UDG's) were used

to monitor changes in the height of the snow or ice surface at each site. In order to avoid interference from other instruments, the UDG and net radiometer were mounted on a separate mast from the rest of the sensors (Figure 4.9). Measurement heights were initially set at 2m above the snow or ice surface for all instruments, and the height of each cross-arm was adjusted throughout the season to keep sensors at the correct height. Copper-constantan thermocouples were used to obtain ice temperature measurements to a depth of up to 4.8 m (Table 3.4). All sensors were wired to a Campbell Scientific CR10 datalogger housed in a plastic enclosure which was mounted to one of the masts. The measurement and output intervals varied according to the time of year (Table 3.5). During the melt season, measurements from each sensor were taken every 10 sec., and, except for the UDG, were averaged for hourly output. Because of anticipated errors in UDG measurements due to blowing snow, UDG measurements were output every 10 min.

Cloud type, cover and height were estimated for 3 layers in the atmosphere. These observations were made at 700 and 1900 hrs. each day, and additional observations were made whenever conditions changed from the previous observation. Cloud cover data were converted to hourly observations by extrapolation: a given observation was assumed to apply for all subsequent hours until the next observation. Snowfall was collected in a small plastic tray and water equivalence was determined by melting the snow and measuring the volume of water at the end of a snowfall event.

4.5 Elevation Data

4.51 The digital elevation model

An accurate digital elevation model (DEM) of the glacier catchment is needed by the model to calculate:

1. Shading of the glacier surface. This allows quantification of the incoming short-wave radiation in terms of its direct and diffuse components (Ohmura, 1981; Oerlemans, 1993). If a grid cell on the DEM is in shade then only diffuse radiation is allowed to reach the ground surface.

2. Aspect and slope of the glacier surface. This allows quantification of the direct short-wave radiation reaching the surface in each grid cell.

3. The elevation of each cell. Lapse rates for temperature and precipitation can then applied to weather station values to calculate temperature and precipitation for each cell. Air temperature is important for calculating both radiative and turbulent heat fluxes. Precipitation lapse rates are needed to initialise winter mass balance values and to calculate precipitation inputs for each precipitation event.

4. The surface albedo of the glacier surface. The surface albedo varies with the solar zenith angle, and is corrected for the effects of slope angle and azimuth. The surface albedo also depends upon the fraction of direct to diffuse radiation, so that if a cell is in shade, the surface albedo is different than if the cell is in sun.

The DEM for John Evans Glacier was produced photogrammetrically by Western Photogrammetry, a division of UMA Geomatics. Aerial photographs numbers A.16607.192-194, which were used for DEM construction, were supplied by the National Aerial Photographic Library, Ottawa. They were taken in 1959, are at a scale of 1:60,000 and were taken from 30,000 feet using a WILD RC5a camera under clear sky conditions. A 100 metre grid of elevations was obtained along with an irregular network of breaklines using a WILD Aviolyt BC1 Analytical system. This system has a working accuracy of ±4μm when working with well contrasted images. The photographs of John Evans Glacier show very poor contrast on the snow surfaces, and even the rock areas are poorly differentiated due to the absence of vegetation cover. The accuracy of point elevations is ±10m.

Over 15000 gridded elevations and 20000 irregular elevations were recorded and surfaced using the surfacing package QSURF developed by Hemenway (1995). The program uses a multiquadratic surfacing technique developed by Hardy (1971). Multiquadratic interpolation is an exact-fitting analytical approach to surfacing. Exact-fitting implies that the surface passes through every point in the input file. The technique then interpolates unknown intervening elevations.

As the number of data points in the input file is so large, the data set must first be broken down into a number of overlapping subsets or tiles. The adaptive tiling approach developed by Hemenway (1995) "intelligently" partitions the input data points on the basis of data density and distribution. Multiquadratic surfacing techniques are then used to produce small surface segments. These surfaced segments overlap by at least 50% and are joined using a "weighted blend" technique which applies distance from the centre of the tile to calculate the relative importance of adjacent elevation values. This results in a smooth surface with a limited boundary effect between tiles. Surface elevations were output as a raster data grid with one elevation for each 25m by 25m grid cell.

4.52 GPS Data

A Trimble Pathfinder global positioning system (GPS) was used to determine ablation stake and weather station positions so that their locations could be plotted on the DEM. Measurements were taken using a portable "rover" system connected to a hand held data logger. At every point, 2 sets of 200 readings were made. These individual readings can be up to 200m in elevation away from their actual locations. This is because satellite signals are deliberately degraded by the U.S. Department of Defence (Trimble Navigation Ltd., 1994). This effect can be overcome by a process known as differential correction, which makes use of a static "base" station, usually located at a known position, such as a geodetic survey marker. Unfortunately, it was not possible to collect base station data during this study. However, the goal of this work was to determine the x and y co-ordinates of each site (i.e. Northings and Eastings), so that these points could be plotted on the DEM. The elevation of each site was then determined from the elevation of the grid cell in which the site plotted. Therefore, the acceptable range of error for x and y GPS measurements is the DEM grid cell size (25m). Statistical analysis of each of the 400 points collected at each site shows that the range of individual measurements can be as much as 100m. However, the standard deviation of these measurements is in all cases below 25m, so that predicted mean site locations are probably never greater than 1 grid cell away from their actual location on the DEM. Given the fact that all ablation stake and weather station sites were chosen to represent the surrounding topography, and were placed on flat terrain whenever possible, these errors seem within

reason.

4.53 Initial Snow Depth Data

An estimate of the winter net balance (1995-1996) across the glacier is required as the starting condition for the energy balance simulations. Ideally, the winter balance is estimated from snow depth and density measurements made at regular intervals across the catchment, prior to the onset of melt. While a number of snow depth measurements were made in the upper sections of the glacier prior to melt, a complete profile of snow water equivalence across the entire glacier was not obtained before melting began.

A detailed snow depth and density profile was obtained during fieldwork carried out in the spring of 1995, from which a linear relationship between elevation and snow water equivalence (SWE) in cm was obtained (Woodward, 1995):

$$SWE = 0.008199\ elev + 12.81 \qquad (4.21)$$

where *elev* is the elevation in m. This paper assumes that the gradient in snow accumulation with elevation is similar between years, and therefore uses the gradient determined from 1995 field measurements (i.e.: 0.008199 cm m^{-1}) for the 1996 simulations. However, an adjustment is made to account for variations in the total quantity of snow deposition between the winters of 1994-95 and 1995-96. This is done by altering the intercept value in Equation 4.21 according to the differences between measured 1996 SWE and SWE predicted from Equation 4.21 (Table 4.5).

The new intercept value is the sum of the old value (12.81 cm) and the average amount by which 1996 measured values exceeded 1995 values (9.3 cm), resulting in the relationship:

$$SWE = 0.008199\ elev + 22.11 \qquad (4.22)$$

Snow water equivalence data measured during the spring of 1997 may be used to verify the slope value in Equation 4.22. Data from 14 snow pits dug at various elevations on John Evans Glacier during the spring of 1997 yield the following relationship between

snow water equivalence and elevation ($r^2 = 0.22$, with SE of y = 0.04 and p-value = 0.95):

$$SWE = 0.0074\ elev + 16.64 \qquad (4.23)$$

The slope in Equation 4.23 is only 0.0004 mm m^{-1} greater than the slope in Equation 4.22. This suggests that the relationship between snow water equivalence and elevation is consistent between years, and confirms that the slope value used in Equation 4.22 is reasonable. Equation 4.22 is therefore used to determine the initial snow depth in each grid cell at the start of the model run.

4.54 Ablation Stake Data

25 ablation stakes were drilled into the ice or placed vertically into the snow at approximately 50 m elevation intervals along the centerline of the glacier (Table 4.6; see Figure 4.3 for stake locations). Each stake consisted of a 3.08 m long, 3 cm diameter white PVC pipe. As many stakes as possible were drilled into the ice, however some stakes could not be visited with a drill and were simply placed vertically in the snow, with the base of the stake at the snow/ice interface. Therefore, some stakes were lost as the season progressed, although many stakes not drilled into the ice were later frozen into the ice as superimposed ice accumulated around them. The snow depth at the stake and the height of the stake above the snow were measured when each stake was set up. Stakes still remaining in 1997 were revisited and measurements of snow depth and stake height above the snow were made. A residual snow layer was observed at the base of snow pits dug near stakes in the upper areas of the glacier. Snow depth measurements in 1997 were made from the top of the snow surface to the top of the residual snow layer. Net mass balance for the 1996-1997 balance year was determined by comparing stake heights above the ice surface, prior to the start of the melt season in 1996, and stake heights measured in the spring of 1997. In the ablation zone, since the change in stake height was the result of ice melt alone, differences in stake heights were converted to water equivalent values by multiplying by the density of ice (0.90 kg m^{-3}). In the accumulation zone, the density of the residual snow layer left over from 1996 had to be estimated. This was done using the SNTHERM model, which was used to simulate variations in snowpack density throughout

the 1996 melt season at the M-AWS and U-AWS. Snowpack density at the end of the melt season as predicted by SNTHERM was 0.748 kg m^{-3} at the M-AWS and 0.417 kg m^{-3} at the U-AWS. To estimate density at intervening stakes, snow density was assumed to vary linearly between the M-AWS and U-AWS.

In order to compare melt predictions with ablation stake measurements, glacier-wide predictions are summed for each 50 m elevation band and divided by the area of the band to determine its specific mass balance (B_{sp}):

$$B_{sp} = \frac{\sum B_n}{Area} \tag{4.24}$$

where *Area* is the area of the elevation band and $\sum B_n$ is the net balance summed over all cells in the elevation band.

4.55 Lapse Rates in Meteorological Measurements

Air Temperature: Lapse rates in air temperature are important for predicting the temperature at a given cell at which it is not directly measured. In EBM-96, hourly temperature lapse rates were read as input to the model. These were calculated from differences between measured temperatures at the 3 weather stations. The glacier was split into 2 sections: an upper section between the M-AWS and U-AWS, and a lower section between the L-AWS and M-AWS. Each grid cell was assigned a lapse rate based on the difference in hourly mean temperature at the 2 weather stations between which the grid cell is located. Locations above the U-AWS were assigned the lapse rate calculated for the section between the U-AWS and M-AWS, while locations below the L-AWS were assigned the lapse rate calculated for the section between the M-AWS and L-AWS.

Other Meteorological Measurements: Variations in wind speed, net radiation, incoming short-wave radiation and relative humidity for grid cells between weather station sites were determined in the same manner as for air temperature. Although it is reasonable to assume that air temperature varied linearly with elevation on the glacier, it is probably less

reasonable to assume the same linear change for other measurements. For instance, wind speed is often controlled by topography. An air mass may be forced to accelerate as it moves towards a steep hill, after which it decelerates on the lee side of the hill. However, modelling air flow in response to topographic features is complex and is beyond the scope of this study. Therefore, a simple linear variation in meteorological measurements seems justified.

4.6 Observations and Discussion

4.61 Variations in Meteorological Measurements and Turbulent Fluxes

Daily summaries of meteorological measurements at each weather station site are shown in Figures 4.10-4.12.Cloud cover variations, usually observed at the M-AWS, are shown in Figure 4.13. Lapse rates in air temperature were highly variable, ranging between -0.015 and + 0.007°Cm^{-1} (Figure 4.14). There were 3 distinct inversions (i.e. periods when temperature increased with elevation, shown by positive lapse rates) on JD 180-183, JD 190-191 and JD 198-200. Each of these inversions occurred first in the lower sections of the glacier, as shown by the lag between peaks in positive lapse rates. These inversions, and the associated lag in their timing, may have been caused by cool, cloudy conditions at the snout caused by fog drifting in from Allman Bay (see Figure 4.2). Fog commonly moved up the glacier over the course of a day reducing temperatures, while upper sections of the glacier remained clear and therefore warmer.

Average lapse rates (Table 4.7) were lower than the dry adiabatic lapse rate (-0.0096°Cm^{-1}). This is to be expected since katabatic winds on the glacier were probably responsible for mixing cool air to lower elevations, limiting the formation of strong gradients in temperature. The mean lapse rate from the M-AWS to the U-AWS was slightly higher than the lapse rate of -0.004°C m^{-1} measured by Bøggild *et al.* (1994) for Storstrømmen, North Greenland. The mean lapse rate from the L-AWS to the M-AWS was unusually low (-0.000621°C m^{-1}), probably as a result of fog in Allman Bay as mentioned above.

Results from the energy balance model indicate that net shortwave and net longwave

radiation were the main contributors to melting or cooling at the glacier surface (Figure 4.15). At all 3 sites, K^* was the largest component of the positive melt energy, followed by Q_H (Figure 4.16). The ratio of K^* to Q_H decreased with increasing elevation. At the U-AWS, Q_H was 10% of the positive melt energy, while it was only 3% at the M-AWS and L-AWS. Q_E was also higher at the U-AWS than at the other sites. The decrease in the ratio of K^* to L^* and the turbulent fluxes (Q_H and Q_E) was probably due to an increase in albedo with an increase in elevation which reduced K^*. The atmosphere above each of the 3 weather station surfaces was usually stable, as shown by predominantly positive z/L values determined from turbulent heat flux calculations (Figure 4.17).

4.62 Spatial and Temporal Variations in Surface Albedo

Daily Variations: The surface albedo across the glacier varied with the time of day. This is because the albedo parameterization described in Chapter 2 accounts for the effects of solar zenith angle on albedo. On JD 167, albedo varied markedly between 0000 hrs. and 1200 hrs (Figure 4.18). At 0000 hrs., the sun was to the north and the zenith angle was high (~78°), so that the albedo across the glacier was also high, especially for south-facing slopes. This is because the lower the angle of incidence between the solar beam and the surface, the higher the albedo becomes (see Chapter 2). At midday, when the sun was at it's highest point in the sky (zenith angle = ~56°), the surface albedo was substantially lower (ranging from 0.76 to 0.95).

The high variability between midnight and midday surface albedo patterns on JD 167 can be attributed to the characteristics of the snowcover, and to the dependence of albedo on snow grain size. JD 167 preceded the start of the melt season, and the entire glacier surface was covered by new snow with a small grain size. Therefore, the main control on surface albedo at this time was the solar zenith angle. As the melt season progressed, snow grain sizes and the water content of the snow increased. As this happened, the snow grain radius became the most important control on surface albedo. This is illustrated for JD 195, at which time the difference between the surface albedo at midnight and midday was much less pronounced than on JD 167 (Figure 4.19). The surface albedo was only

slightly lower at midday on JD 195 than it was at midnight because the majority of the glacier consisted of melting snow with a large grain size.

Seasonal Variations: The surface albedo varied on a seasonal basis as a result of changes in the effective grain size, a parameter which accounts for the effects on the surface albedo of both the physical size of the snow particle and the snow water content. Daily average surface albedo predictions show that lower elevations on the glacier were the first to experience a decrease in albedo, because it is in these areas where melting first occurred (Figure 4.20). In general, seasonal trends in surface albedo closely followed seasonal trends in surface melt (compare Figure 4.20 and Figure 4.21). It appears that, regardless of their azimuth, steeply sloping areas had a higher daily average albedo than flatter sections of the glacier. For instance, the area marked with an arrow on Figure 4.20 is a steep, south facing slope where the model predicted higher albedo values than surrounding red (low albedo) areas. Although it's albedo was especially low at midday (see Figure 4.19 b), this area experienced higher than normal albedos throughout the rest of the day, resulting in a high daily average albedo.

Glacier ice was exposed on the lower sections of the glacier on JD 195 (see Figure 4.22 for a diagram of facies zones at the end of the melt season). These areas had a low daily average albedo, ranging from 0.5 to 0.6. The effects of a new snowfall on the surface albedo can be seen by comparing surface albedo predictions for JD 195 and JD 199. A snowfall event between 0200 and 1800 hrs. on JD 199 caused the surface albedo to increase across the catchment.

4.63 Spatial and Temporal Variations in Surface Melt

Testing of Model Output against UDG data from the 3 Weather Stations:

Surface melt predictions from the EB model are tested against UDG data from the 3 weather stations. The model version used to generate melt predictions in this section is

EBM-96 (i.e. the updated model with all the changes described in this paper), using the SI-P2 superimposed ice algorithm (this configuration will be known hereafter as the "standard configuration"). Because the EB model predicts changes in the water equivalent depth of snow or ice at the surface, and the UDG measures changes in surface height, the UDG data must be converted to water equivalent measurements before comparisons can be made with the EB model output. This is a difficult task given the fact that the upper and lower stations could not be visited frequently enough to monitor changes in snowpack density. Therefore, a prediction of average snowpack density is obtained from the SNTHERM model. The advantage of this approach is that SNTHERM provides a continuous record of snow density, whereas snowpit data are discontinuous, so that interpolation techniques must be used to estimate density values when measurements are not available. A comparison of SNTHERM predictions with measured average snowpack density from the M-AWS (where snow pits were analyzed on a regular basis) verifies the accuracy of the SNTHERM density predictions ($r^2 = 0.90$, with SE = 0.03 and p-value = 0.95; Figure 4.23).

Model performance may be evaluated according to how well predicted SWE simulates trends in measured SWE (as indicated by the coefficient of determination), and according to how well predicted SWE simulates the actual values in measured SWE (as indicated by comparing overall averages, standard and absolute error, and seasonal differences). Simulations for the L-AWS did the best job of predicting trends in measured SWE, since these simulations had the highest coefficient of determination (0.94) (Figure 4.24; Table 4.8). However, melt at the L-AWS was under-predicted. The run for the U-AWS was most successful at predicting the measured SWE values, but performed poorly at predicting the trends in SWE (coefficient of determination = 0.17). Predictions were best until about JD 196, when measured SWE dropped below predicted values until JD 202. This and other decreases in measured SWE may have been caused by wind scouring instead of melt. Simulations at the M-AWS did a good job at predicting both the trends and actual values in measured SWE.

Modelled Surface Melt for the Entire Glacier:

This section examines surface mass balance predictions, derived from the standard configuration of the EBM-96 model, for the entire glacier at different times during the melt season. The mass balance predictions represent the water equivalence of snow or ice remaining from the initial snow water equivalence at the start of the model run. Snow which melts but refreezes as superimposed ice is not subtracted from the cumulative mass balance; the mass balance is altered only once snow melt is removed from the system as runoff.

The mass balance across the glacier remained largely unaltered until after JD 181 (Figure 4.21). After this time, the most substantial melting occurred below ~500 m elevation, around the snout of the glacier. A profile of predicted specific mass balance with elevation (B_{sp}, see Equation 4.24), compared with ablation stake measurements, shows that the model accurately predicts the equilibrium line elevation (ELA), located at 600 m (Figure 4.25). The ELA for 1996 is probably low compared with previous years on John Evans Glacier. Contour curvature from a topographic map of John Evans Glacier (Section 4.21) and analysis of shallow ice cores (M. Sharp, *pers. comm.*) suggest the long-term equilibrium line is as high as 750 m. To compare the average specific balance of model predictions with measured average specific balance, it is necessary to interpolate and extrapolate measured stake data for each elevation band on the glacier. This is done by performing a linear regression of measured specific balance with elevation. The relationship (r^2 = 0.64, SE = 0.15, p-value = 0.001) predicts an average specific mass balance of 0.15 m WE, 0.134 m WE higher than the value of 0.016 m WE predicted by the energy balance model. However, given the low level of significance in the regression of measured specific mass balance with elevation, the prediction of average specific mass balance from measured data is questionable.

Facies Zones at the End of the Melt Season:

On JD 195, nearly 90% of the glacier was covered with superimposed ice (Figure 4.22 a). Of this superimposed ice, 29% was exposed at the surface, with the remaining 61%

covered by snow. 63% of the entire glacier was still covered with some amount of snow on JD 195 (Figure 4.22 b). Glacier ice was exposed on the lower 10% of the snout of the glacier, up to the 400 to 450 m elevation contour.

Patterns in snow depth remaining at the end of the melt season show that snowline retreat was not strictly dependent on elevation. There was no snow remaining in the corridor NE of the M-AWS (marked with an arrow on Figure 4.22 a), which was at a higher elevation than other areas of the glacier which still had snow. This was because this corridor was south-facing and was not shaded by the mountains when the sun was in its noontime position.

Information on the different facies zones across the glacier at the end of the melt season is useful in determining suitable locations for the extraction of ice cores from John Evans Glacier. Shallow ice cores extracted from the zone of superimposed ice formation allow for the examination of recent patterns in the mass balance of the glacier. These ice cores are ideally taken from areas where superimposed ice is exposed at the surface, but has not yet begun to melt substantially, so that observed superimposed ice thicknesses can be assumed to represent the maximum thickness formed in a given season. Based on the 1996 melt season, the corridor mentioned above would be an ideal location for the extraction of such ice cores, because the surface was snow free but still covered with a substantial amount of superimposed ice. However, although this area might be suitable for the 1996-1997 season, it is expected that patterns in facies zones vary between years. Analysis of multiple years of data are necessary to determine the optimum locations for the extraction of ice cores from John Evans Glacier.

Comparison of EBM-96 and EBM-94:

The old version of the energy balance model, EBM-94, was run with the 1996 dataset to test how its predictions compare with output from EBM-96. EBM-94 substantially over-predicted melt across the entire glacier (Figure 4.25; Table 4.10). EBM-94 predicted the ELA to be at 1350 m, 750 m above the observed ELA. Although the coefficient of determination was higher for EBM-94 than for EBM-96, the difference between observed

and EBM-94 predicted average specific mass balance was 0.43 m WE (c.f. difference of 0.134 m WE between observed and EBM-96 predicted average specific mass balance). Therefore, based on comparisons with measured stake data, EBM-96 was better at predicting the mass balance of John Evans Glacier than EBM-94.

4.7 Comparison with other Studies

There have been relatively few energy balance studies at high polar latitudes, and the majority of these studies have been concentrated along the margins of the Greenland ice sheet (e.g. Braithwaite and Olesen, 1990; Konzelmann and Braithwaite, 1995; van den Broeke, 1996). Although meteorological and ablation stake data have been collected from other glaciers in the high Arctic (e.g. the Devon and Agassiz ice caps), energy balance studies have been carried out primarily on White Glacier, often with manually collected meteorological data at sampling intervals of up to 4 hours (Keeler, 1963; Havens et al. 1965; Adams, 1966). Of the energy balance studies on the Greenland ice sheet and on glaciers in the Canadian Arctic islands, none have had as detailed a dataset, with as high a spatial resolution, as the one used to drive energy balance model simulations described in this paper. This model is the first of its type applied to high Arctic regions. No other spatially distributed energy balance model has made a detailed physical treatment of two key components of the mass balance of high Arctic glaciers, namely surface albedo and superimposed ice formation.

Although the energy balance model described in this paper may be an improvement over models previously used for Arctic regions, surface energy balance models applied to mid-latitude alpine glaciers probably still provide more accurate predictions of glacier mass balance (e.g. Arnold *et al.*, 1996). This is because most alpine glaciers are smaller, so that it is easier to obtain high resolution meteorological and ablation stake data to drive and verify the model. Also, a parameterization of superimposed ice formation is not required for alpine glaciers, reducing model complexity.

4.8 Conclusion

Mass balance simulations for John Evans Glacier using EBM-96 are substantially different from predictions made by EBM-94, the previous version of the model. Data from a limited stake network suggest EBM-96 model predictions are more accurate and that EBM-94 substantially over-predicts melt. The improvement in EBM-96 model performance was due improvements in the parameterization of components of the mass and energy balance. The physically-based surface albedo routine probably played the largest role in improving model performance, as shown by sensitivity tests using different surface albedo algorithms (see Chapter 2). The large discrepancy between EBM-94 and EBM-96 mass balance predictions suggests that models which use empirical methods to predict surface albedo and superimposed ice depths may significantly over-predict melt.

CHAPTER 4 TABLES

CALCULATION	EBM-94	EBM-96
surface albedo	empirically estimated based upon time after new snowfall and fraction of liquid water at the surface (van de Wal and Oerlemans 1994)	physically based bispectral model driven by effective grain size and solar zenith angle (Marks, 1987; Jordan, 1991; see Chapter 2)
fraction of direct to diffuse radiation	diffuse fraction set constant at 20% of direct fraction if cell is shaded (Oerlemans, 1993)	2-stream radiation model; atmosphere divided into 3-layers (Shapiro, 1987; see Chapter 2)
maximum superimposed ice depth	1) calculated as percentage of total snowpack water equivalence 2) calculated as a function of initial ice temperature and the time period of superimposed ice formation (Woodward *et al.*, in press)	1) calculated according to Woodward *et al.* with slight modifications 2) rate of formation calculated based on temperature profile to a depth of 14m (see Chapter 3)
transfer of thermal energy between the snowpack and the ice surface	set constant based on measurements made by Konzelmann and Braithwaite (1995)	calculated explicitly in superimposed ice routine (2) above
Temperature lapse rate	assumed constant lapse rate of $0.004°Cm^{-1}$	measured hourly lapse rates provided as input to the model
turbulent heat flux	assumed adiabatic stratification in Prandtl-type boundary layer with no stability corrections	bulk transfer technique (using Monin-Obukov similarity theorem) with corrections for stability
incoming longwave radiation	empirically estimated; cloud emissivity changes based on cloud type (Ohmura, 1981)	calculated as a residual from net radiation measurements, assuming a constant value for outgoing longwave radiation

Table 4.1: Modifications to the surface energy balance model. EBM-94 refers to model simulations with 1994 data using the model developed by Woodward (1995), while EBM-96 refers to model simulations with 1996 data using the modified model described in this paper.

Met. Station Name	Latitude	Longitude	Elevation (m a.s.l.)
L-AWS	79°37'52"	74°04'38"	261
M-AWS	79°40'17"	74°20'59"	824
U-AWS	79°42'35"	74°33'20"	1183

Table 4.2 Location and elevation of each automated weather station.

Measurement	Instrument and model	Measurement Range	Instrument Error
Air Temperature	Campbell 107F Temperature probe	-53°C to +48°C	±0.4°C
Relative humidity sensor	HMP35CF Vaisala RH probe	0 to 100% RH	±2% RH (0 to 90% RH) ±3% RH (90 to 100% RH)
Incoming short-wave radiation	LI200s Li-COR Pyranometer	0.280-2.80 μm	±5% maximum
Outgoing short-wave radiation	Kipp and Zonen CM7 Pyranometer	0.305-2.80 μm	±2%
Net Radiation	REBS Q7 net radiometer	0.250 to 6.0 μm	wind speed dependent
Air Pressure	CS105 Barometric Pressure Sensor	600 to 1060 mb	±0.5 mb (@ 20°C)
Wind Speed	05103 R.M. Young Wind Monitor	0 to 60 m/s	1.0 m/s threshold sensitivity
Wind Direction	05103 R.M. Young Wind Monitor	360°	1.0 m/s threshold sensitivity at 10° displacement
Height of snow/ice surface	UDG01 Ultrasonic Depth Gauge	0.6 to 10 m	±1 cm or 0.4% of distance to target (whichever is greatest)

Table 4.3 Specifications of meteorological instruments. These instruments were connected to a Campbell Scientific CR10 data logger and SM 192/716 storage module.

Station	Start of Hourly Measurements	End of Hourly/ Start of Daily Measurements	End of Daily Measurements
L-AWS	JD 172, 1996	JD 212, 1996	JD 143, 1997
M-AWS	JD 167, 1996	JD 202, 1996	JD 144, 1997
U-AWS	JD 169, 1996	JD 216, 1996	JD 144, 1997

Table 4.4 Time intervals of hourly and daily output of meteorological observations at each AWS.

Elevation (m)	Julian Day	Measured SWE, 1996 (cm)	Predicted SWE from Equation 4.21 (cm)	Difference between 1996 measurements and Equation 4.21 predictions (cm)
824	166	27.0	19.6	7.4
824	176	30.1	19.6	10.5
965	164	32.6	20.7	11.9
1182	176	29.8	22.5	7.3
			Average	9.3

Table 4.5 Snow water equivalence (SWE) at 3 sites on the glacier, prior to the start of the melt season. Column 4 is the predicted SWE using Woodward's (1995) regression equation, based on spring of 1995 snow depth and density profiles.

Stake Label	Elevation (m)	Found in 1997?
L0-A	184	Y
L0-B	219	Y
L1	261	Y
L2	288	Y
L3	314	Y
L4	370	Y
L5	460	Y
L6	501	Y
L7	418	Y
L8	561	Y
L9	612	N
L10	652	N
L11	672	Y
L12	704	Y
L13	749	N
U11	824	N
U10	803	N
U9	862	N

U8	920	Y
U7	965	N
U6	1025	Y
U5	1061	N
U4	1085	Y
U3	1164	N
U2	1190	Y
U1	1250	Y

Table 4.6: Ablation stakes set up at the start of the 1996 melt season, with associated elevations. Y indicates that the stakes were found during the spring of 1997, while N indicates they were not.

	Average Lapse Rate (°C m^{-1})	Standard Deviation
L-AWS to M-AWS	-0.000621	0.0039
M-AWS to U-AWS	-0.00565	0.0049

Table 4.7: Average and standard deviation of lapse rates determined from measured hourly air temperatures on John Evans Glacier. Negative lapse rates indicate a decrease in temperature with increasing elevation.

	L-AWS	M-AWS	U-AWS
Number of Data Pairs	582	816	960
Mean Observed	0.12	0.24	0.28
Mean Calculated	0.16	0.22	0.28
Coefficient of Determination	0.94	0.85	0.17
Seasonal Difference	-0.33	0.09	0.02
Standard Error	0.02	0.01	0.02
Absolute Error	0.00	0.01	0.00

Table 4.8: Statistical data for model runs testing comparing modeled SWE using the "standard" model run versus measured SWE from UDG data, converted to SWE from SNTHERM density predictions.

Coefficient of Determination = $\left[\sum(x_o - \bar{x}_o)^2 - \sum(x_c - x_o)^2\right] / \sum(x_o - \bar{x}_o)^2$

Seasonal Difference = $\left[\sum(x_o - x_c)\right] / \sum(x_o)$

Standard Error = $\left[\sum(x_c - x_o)^2 / n\right]^{0.5} / \bar{x}_o$

Absolute Error = $\sum(x_o - x_c) / n\bar{x}_o$

where x_c is the calculated value, x_o is the observed value, $\bar{x}$ is the mean value, and n is the total number of observations

	EBM-96
n	14
Average measured specific mass balance	0.15
Average predicted specific mass balance	0.016
Coefficient of Determination	0.44
Seasonal Difference	0.70
Standard Error	0.21
Absolute Error	0.01

Table 4.9: Statistical data for model run comparing standard run (EBM-96) with measured ablation stake data. Units are in m WE.

	EBM-94
n	14
Average measured specific mass balance	0.15
Average predicted specific mass balance	-0.28
Coefficient of Determination	0.72
Seasonal Difference	-3.75
Standard Error	0.06
Absolute Error	-0.04

Table 4.10: Statistical data for model run comparing the old version of the energy balance model (EBM-94) with measured ablation stake data. Units are m WE.

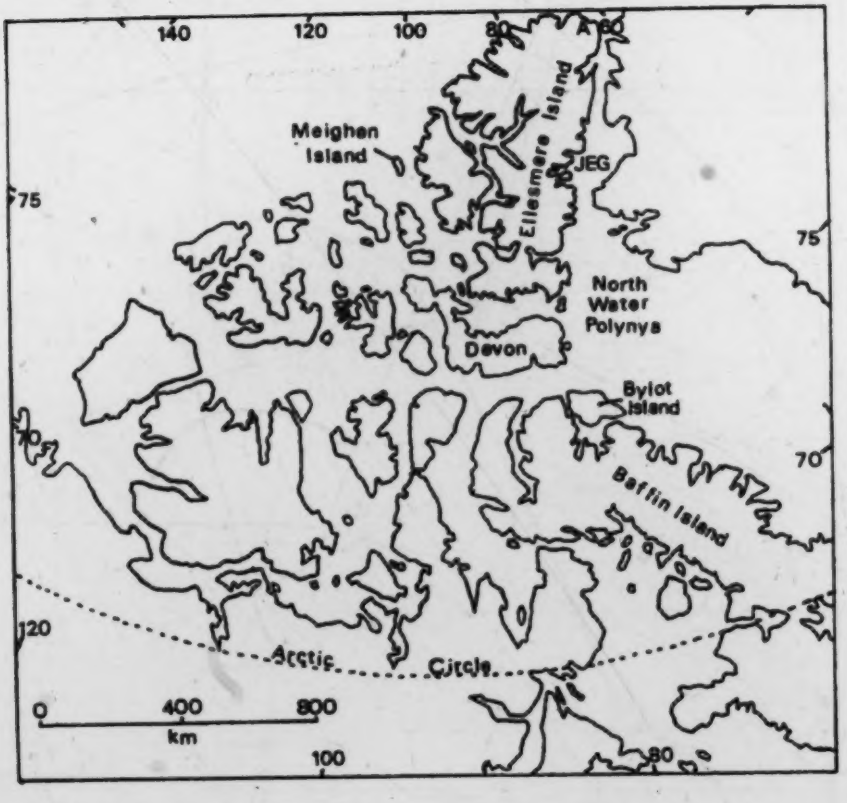

Figure 4.1:Map of the Canadian Arctic Islands. JEG = John Evans Glacier, A=AES Meteorological station at Alert.

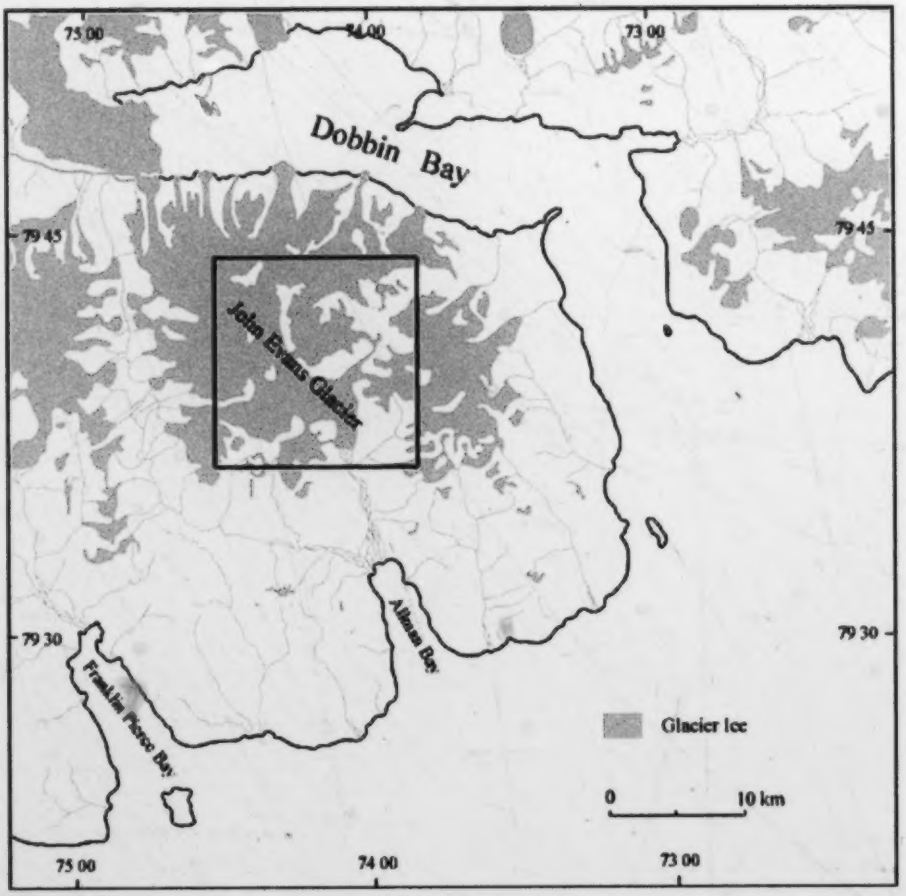

Figure 4.2: Location of John Evans Glacier, Ellesmere Island, Nunavut, Canada.

Figure 4.3: Contour map of John Evans Glacier with locations of lower, middle and upper automated weather stations (marked with arrows) and stake locations (marked with circles).

Figure 4.4: 3-dimensional model of John Evans Glacier.

Figure 4.5: Photograph of John Evans Glacier. "L-AWS" and "M-AWS" show the location of the lower and middle automated weather stations.

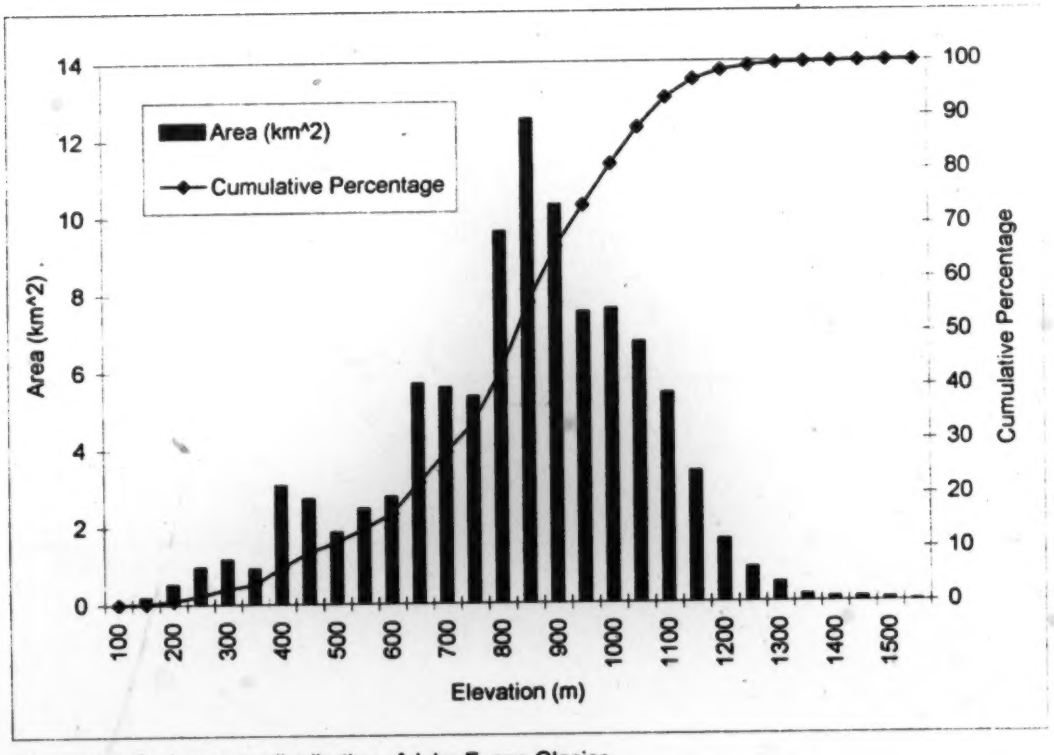

Figure 4.6: Surface area distribution of John Evans Glacier.

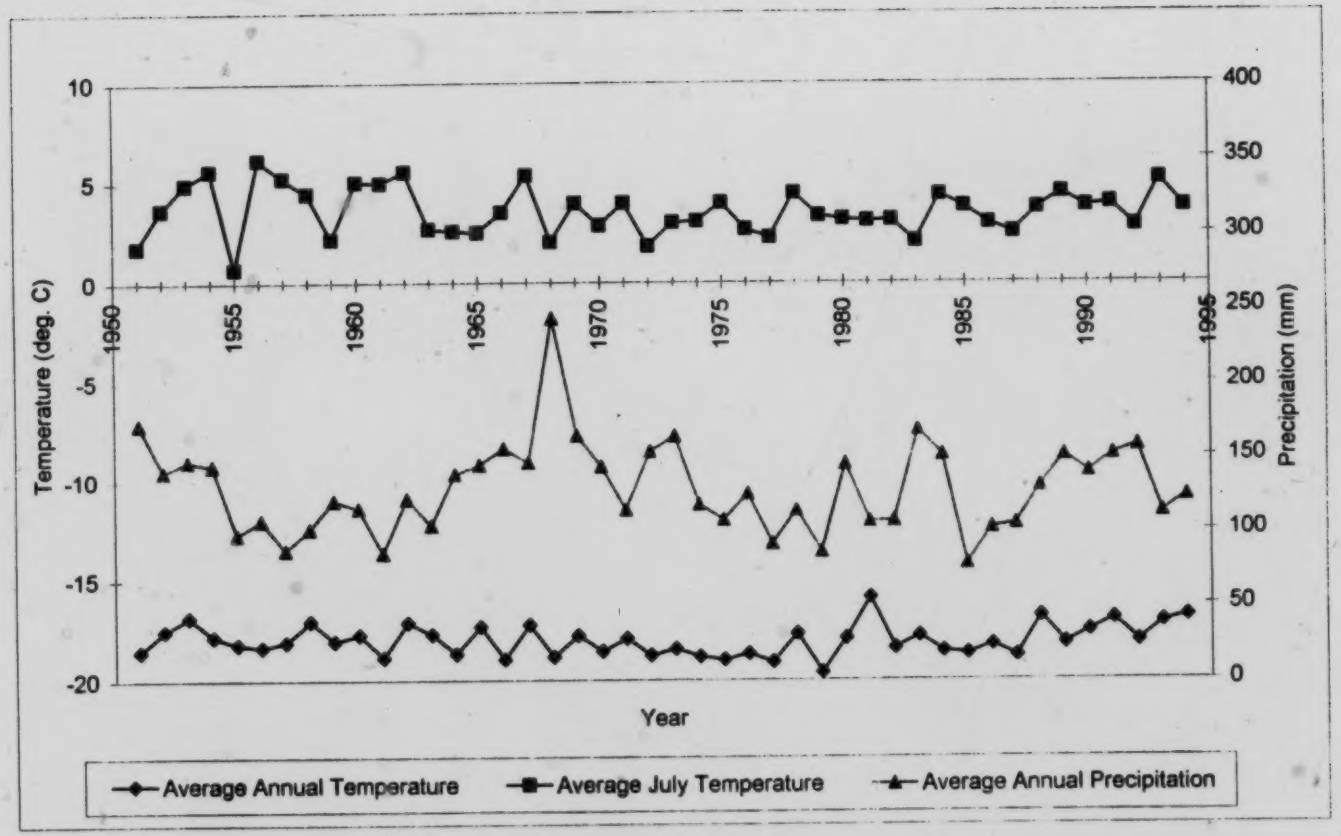

Figure 4.7 Temperature and precipitation records from AES meteorological station, Alert.

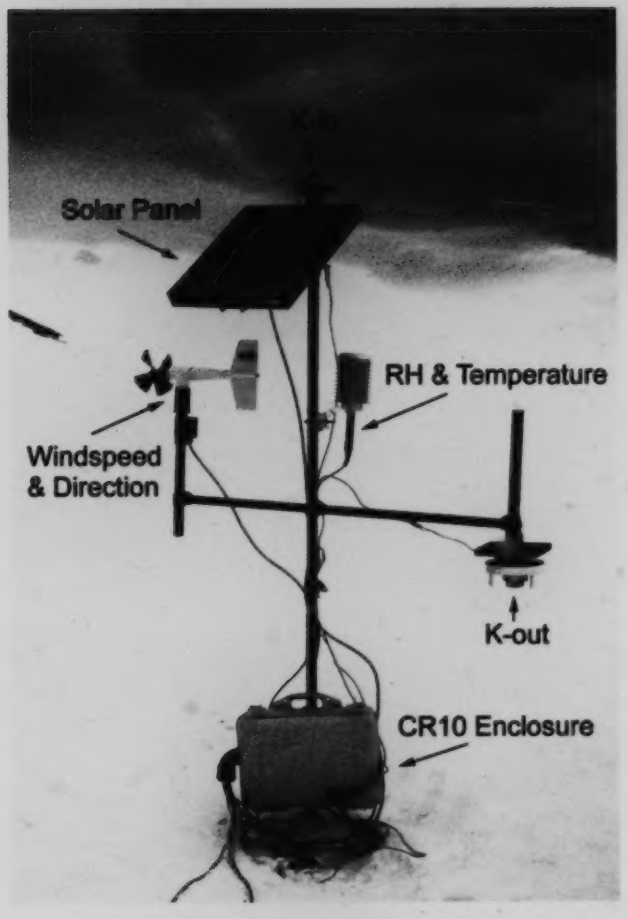

Figure 4.8: Photograph of the main mast at the M-AWS.

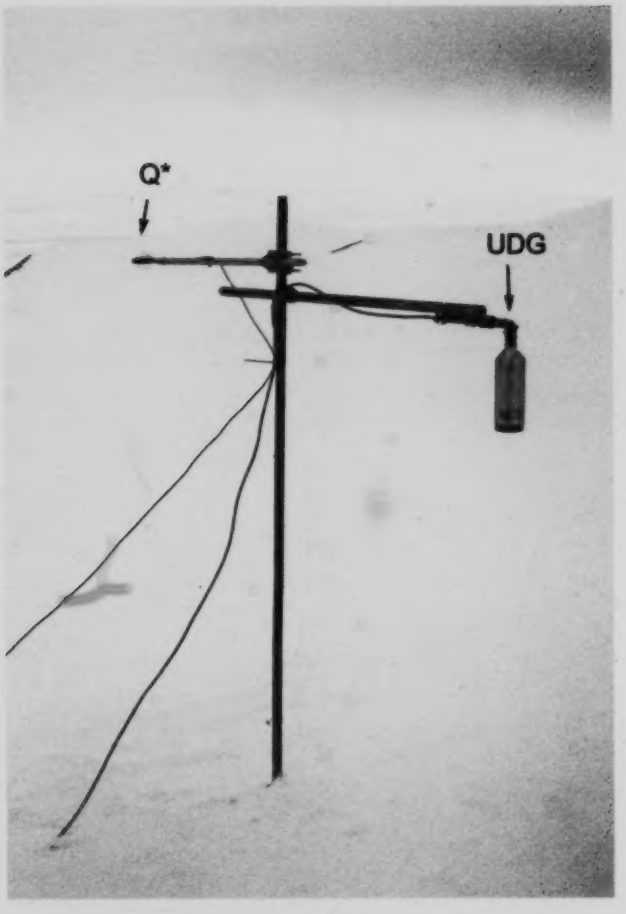

Figure 4.9: Photograph of the UDG and net radiometer mast at the U-AWS.

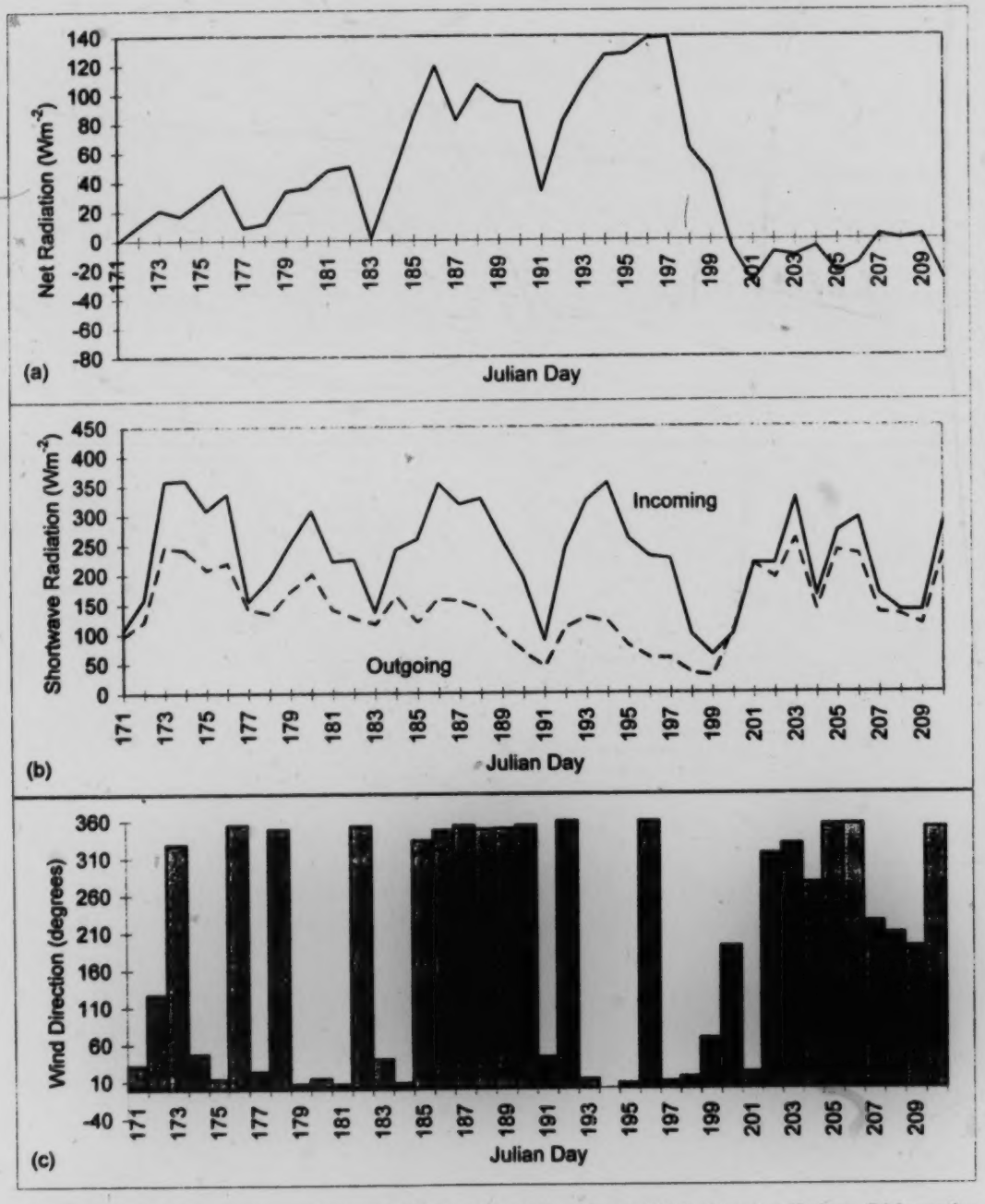

Figure 4.10: Daily averages meteorological measurements at the L-AWS. (a) net radiation; (b) incoming (solid line) and outgoing (dashed line) shortwave radiation; (c) wind direction

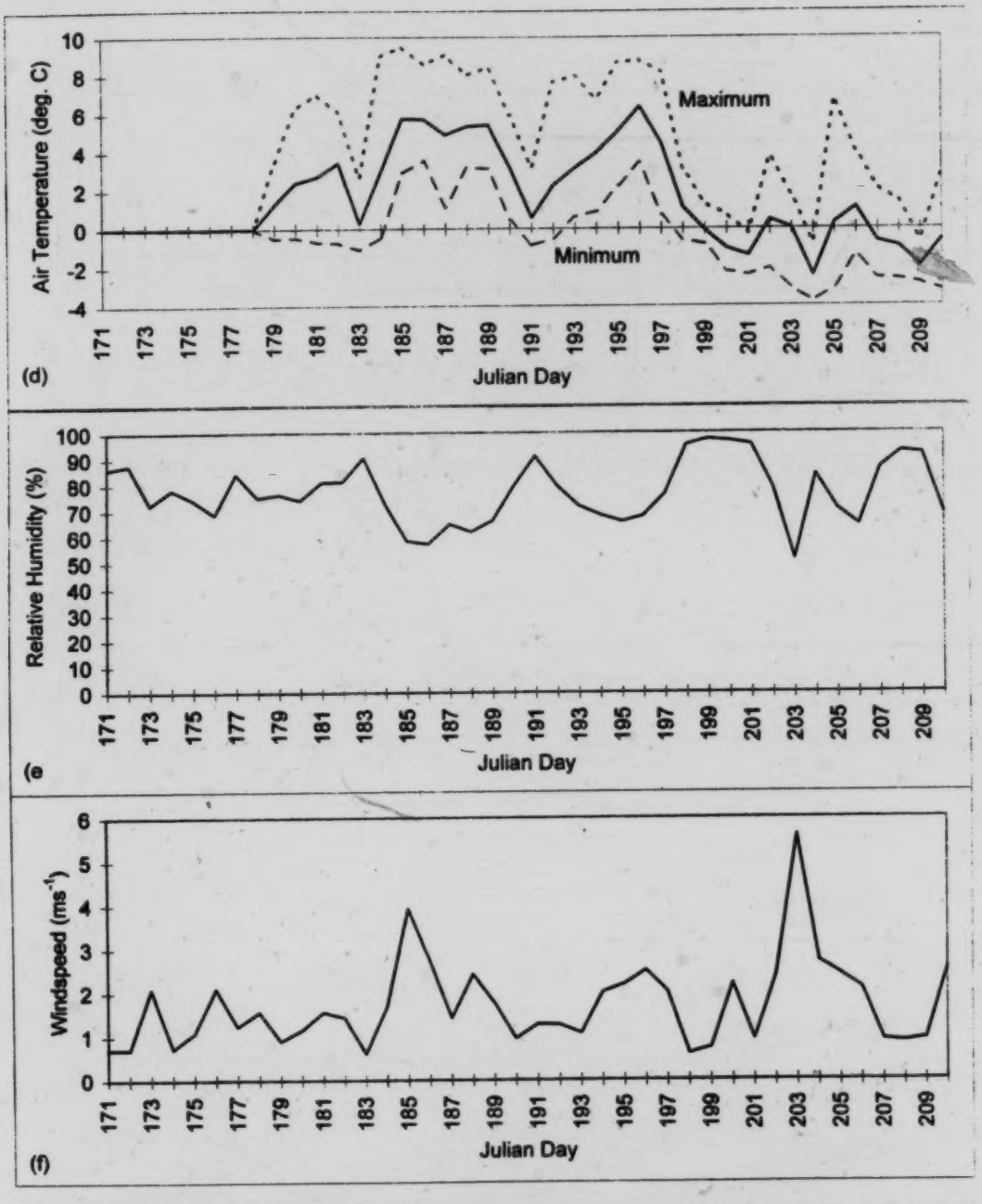

Figure 4.10 (con't): Daily averages meteorological measurements at the L-AWS. (d) daily average (solid line), maximum (dotted line) and minimum (dashed line) air temperature; (e) relative humidity; (f) windspeed

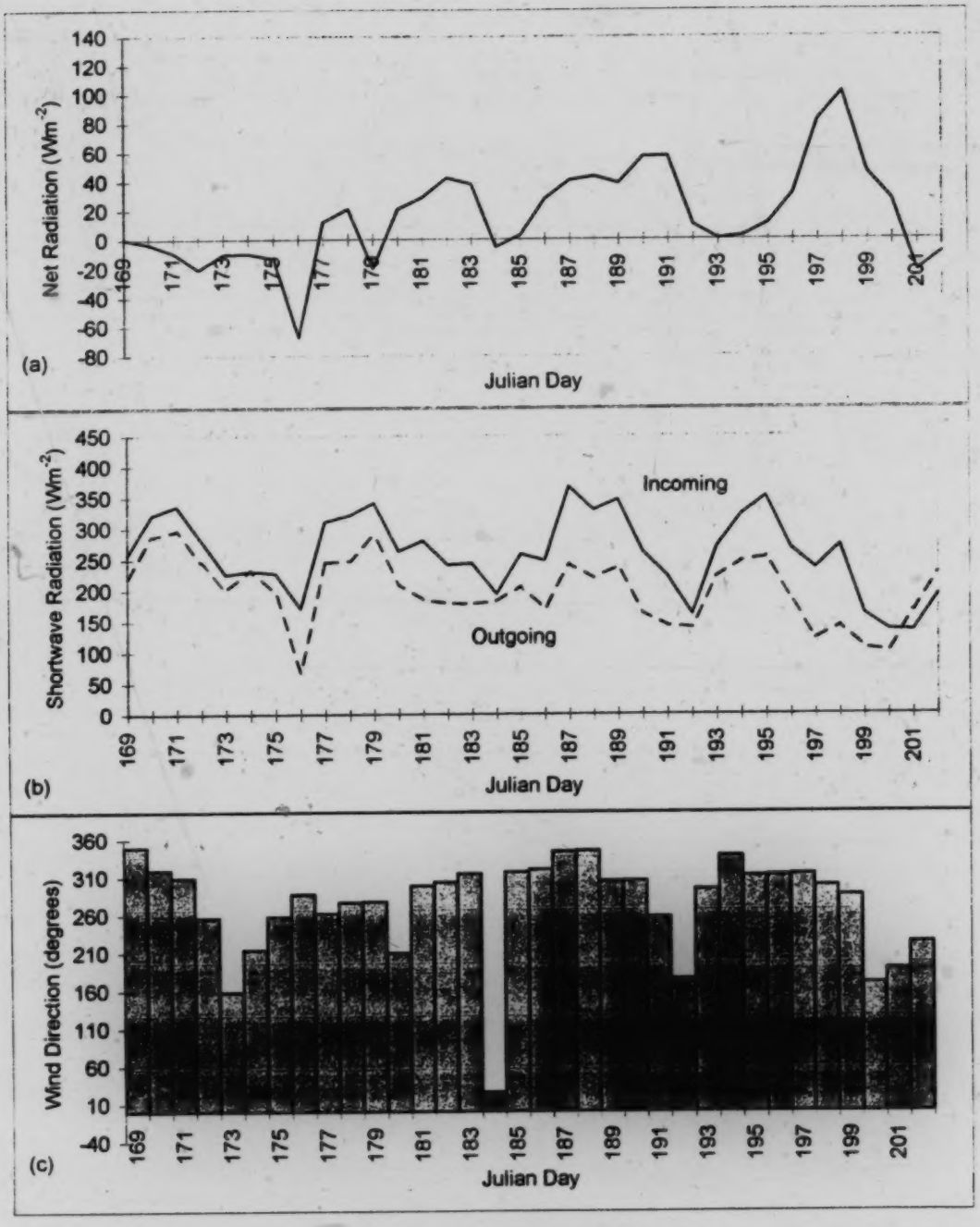

Figure 4.11: Daily averages meteorological measurements at the M-AWS. (a) net radiation; (b) incomir (solid line) and outgoing (dashed line) shortwave radiation; (c) wind direction.

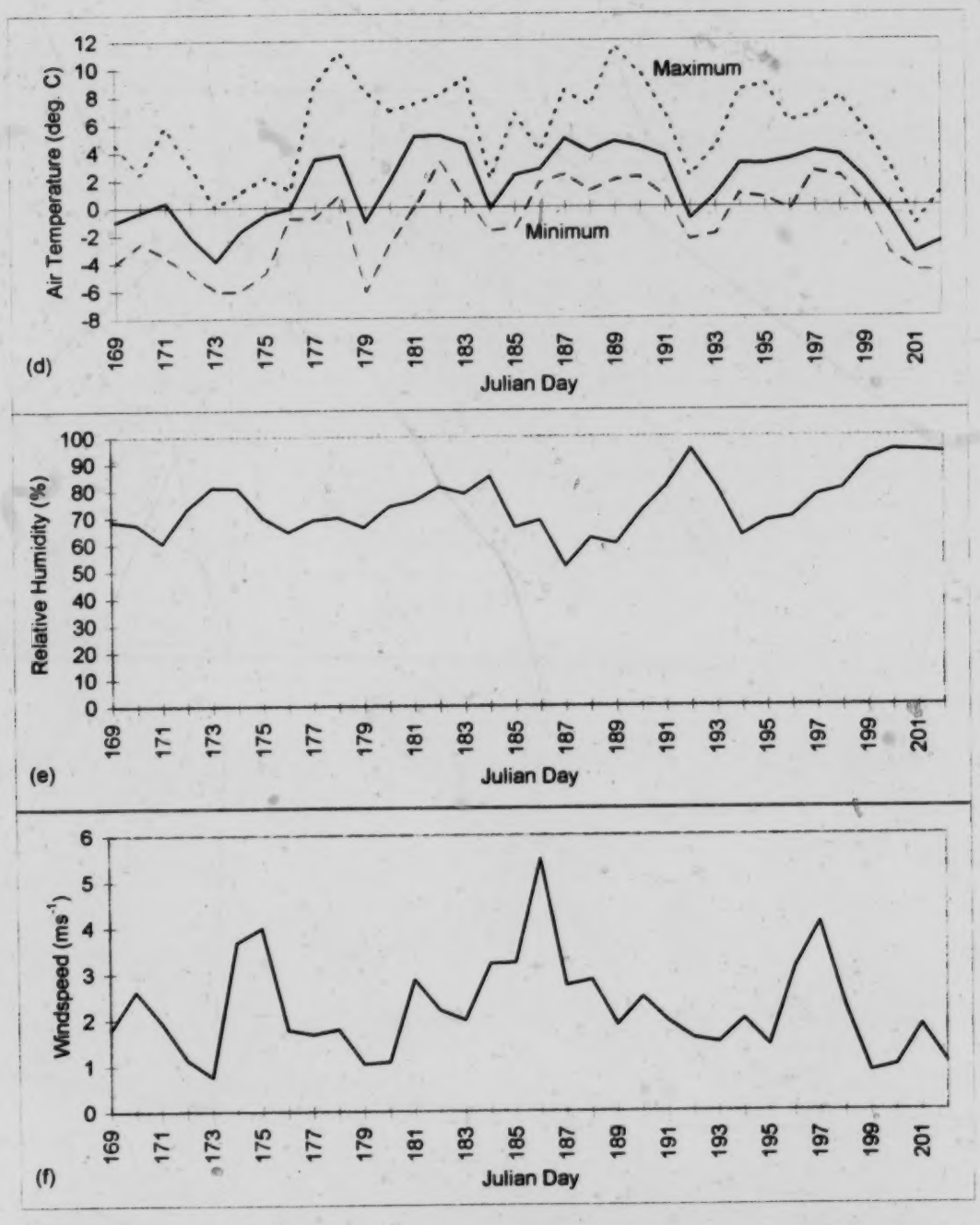

Figure 4.11 (con't): Daily averages meteorological measurements at the M-AWS. (d) daily average (soli line), maximum (dotted line) and minimum (dashed line) air temperature; (e) relative humidity; (f) windspeed

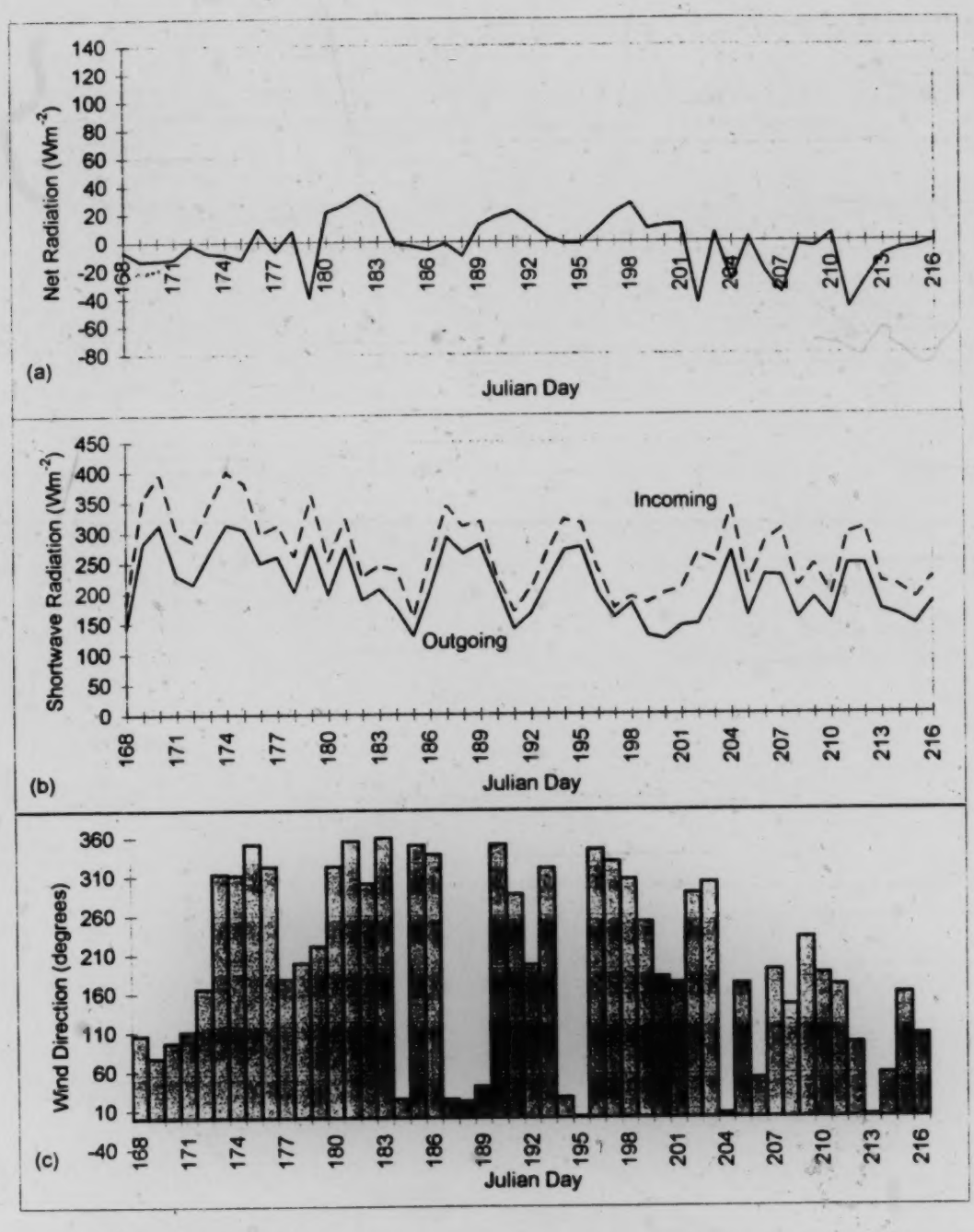

Figure 4.12: Daily averages meteorological measurements at the U-AWS. (a) net radiation; (b) incomin (solid line) and outgoing (dashed line) shortwave radiation; (c) wind direction

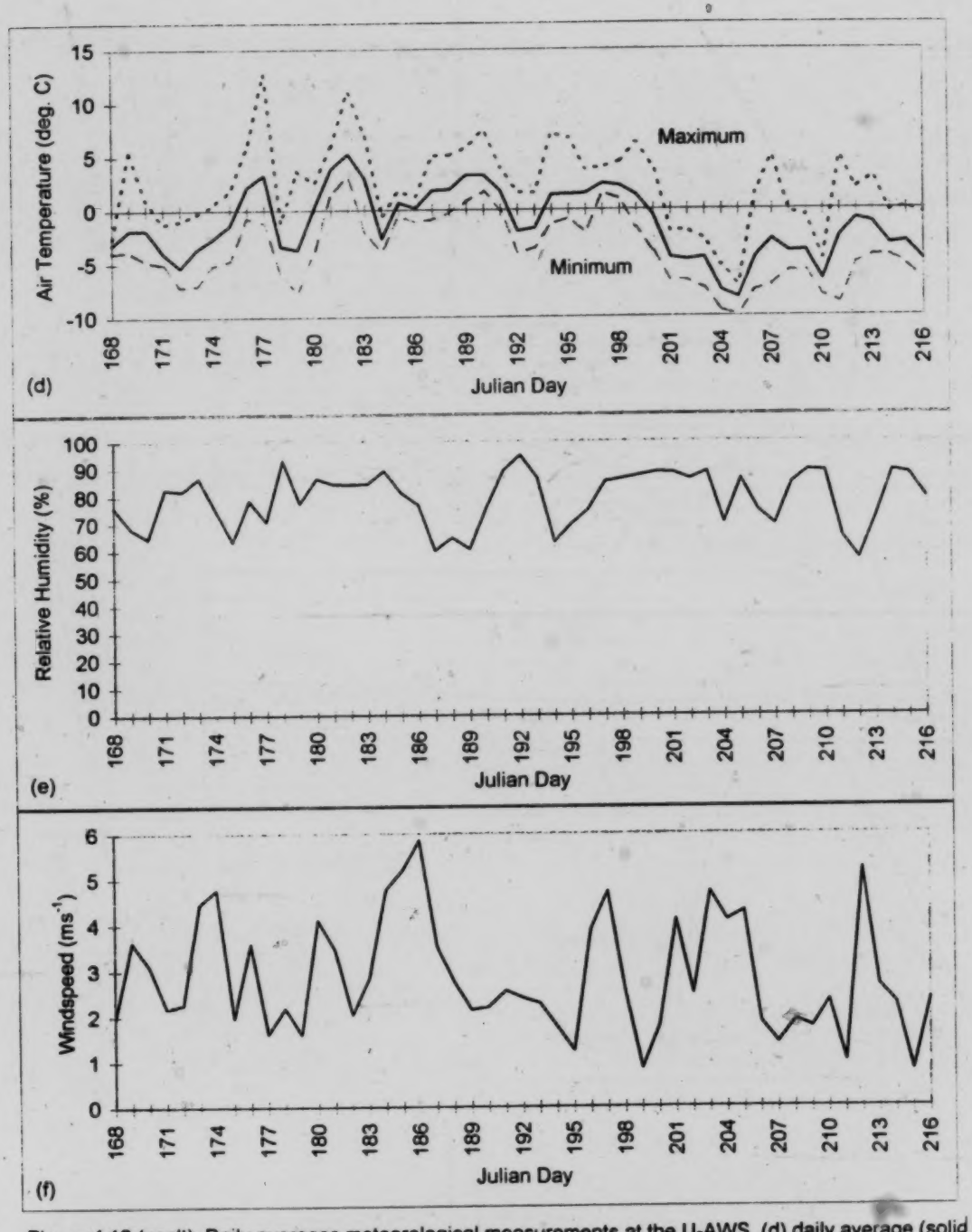

Figure 4.12 (con't): Daily averages meteorological measurements at the U-AWS. (d) daily average (solid line), maximum (dotted line) and minimum (dashed line) air temperature; (e) relative humidity; (f) windspeed.

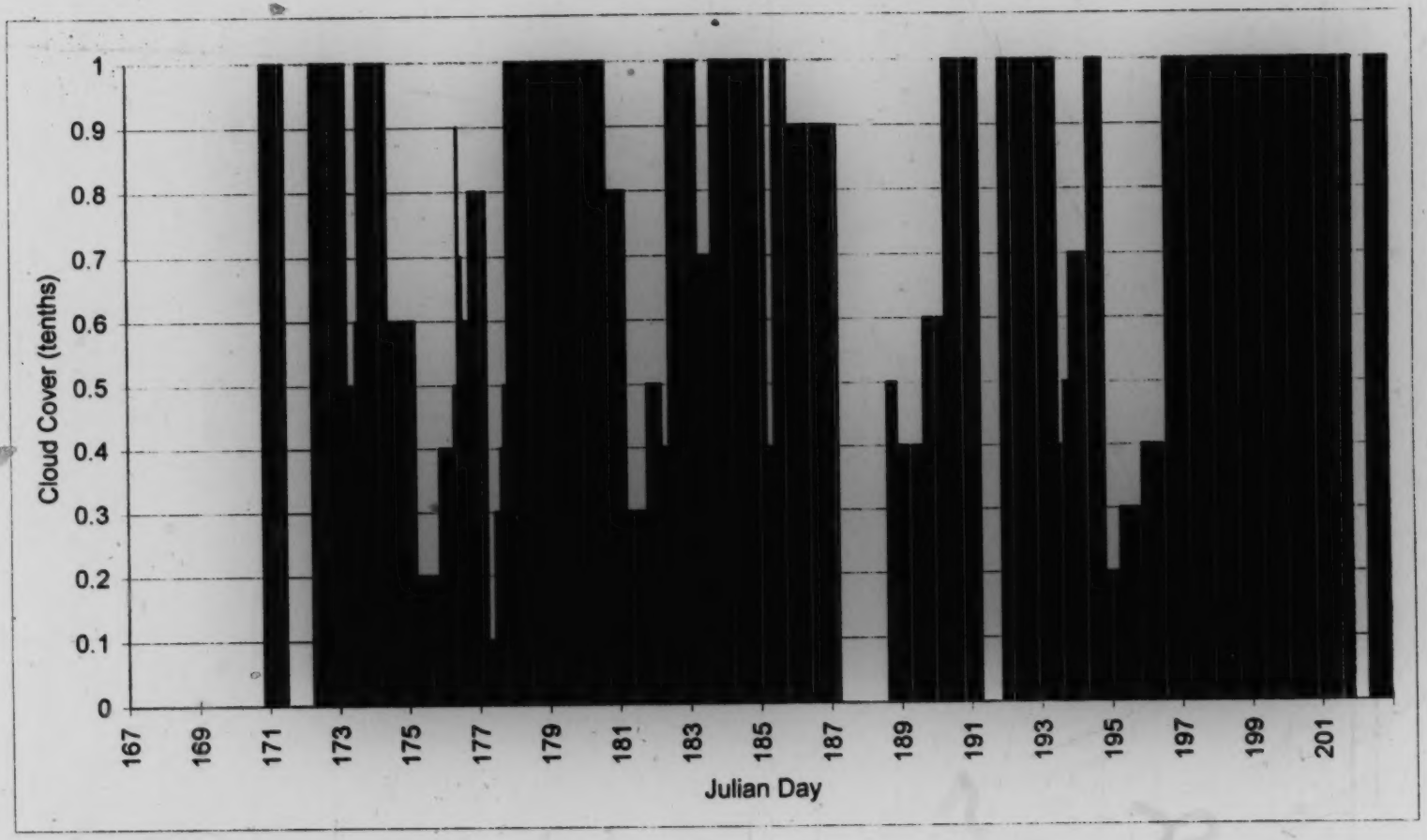

Figure 4.13: Cloud cover observations in tenths at the M-AWS.

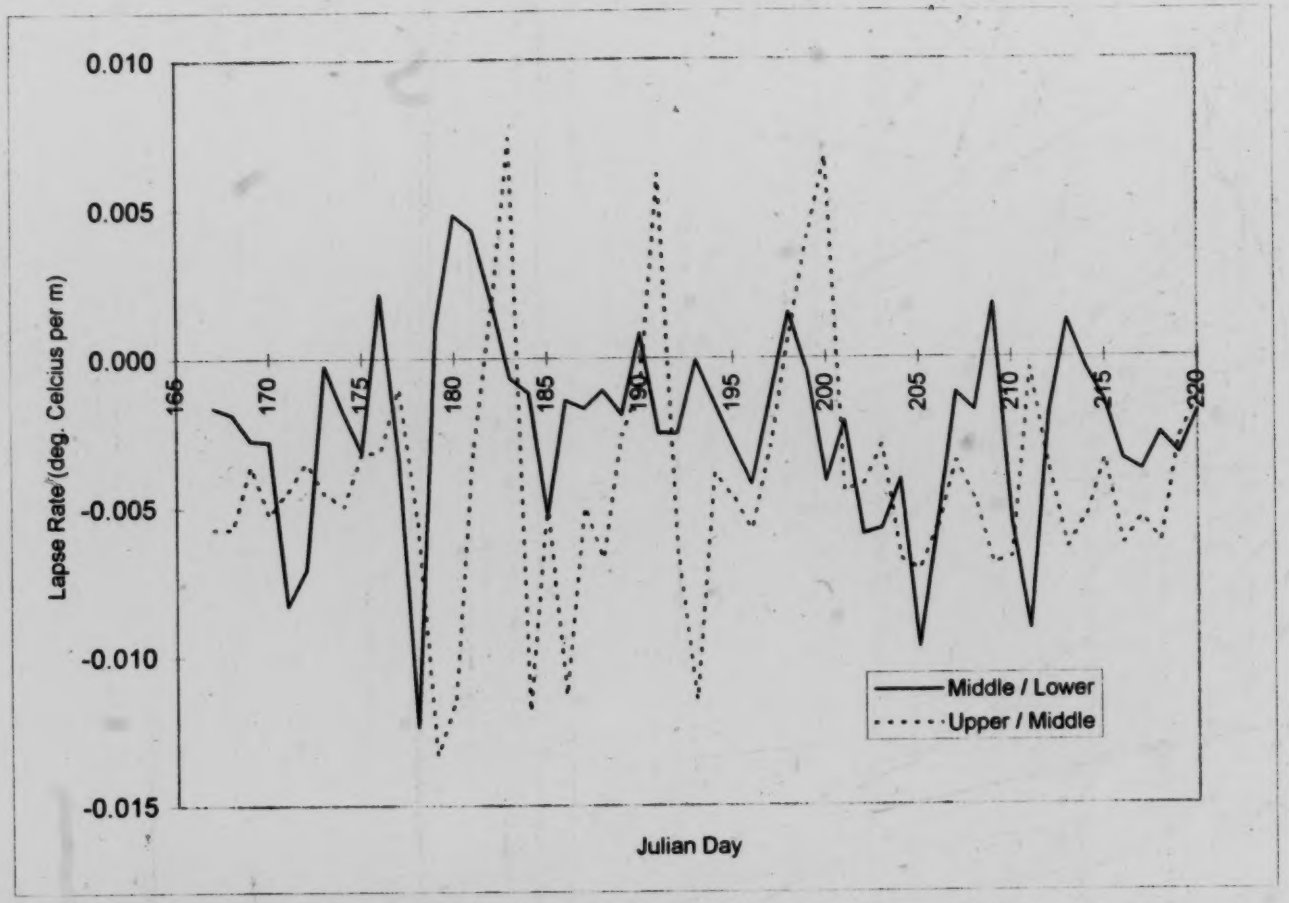

Figure 4.14: Daily average lapse rates ($^{o}C\ m^{-1}$) between the 3 automated weather stations. (Negative lapse rates indicate a decrease in temperature with elevation).

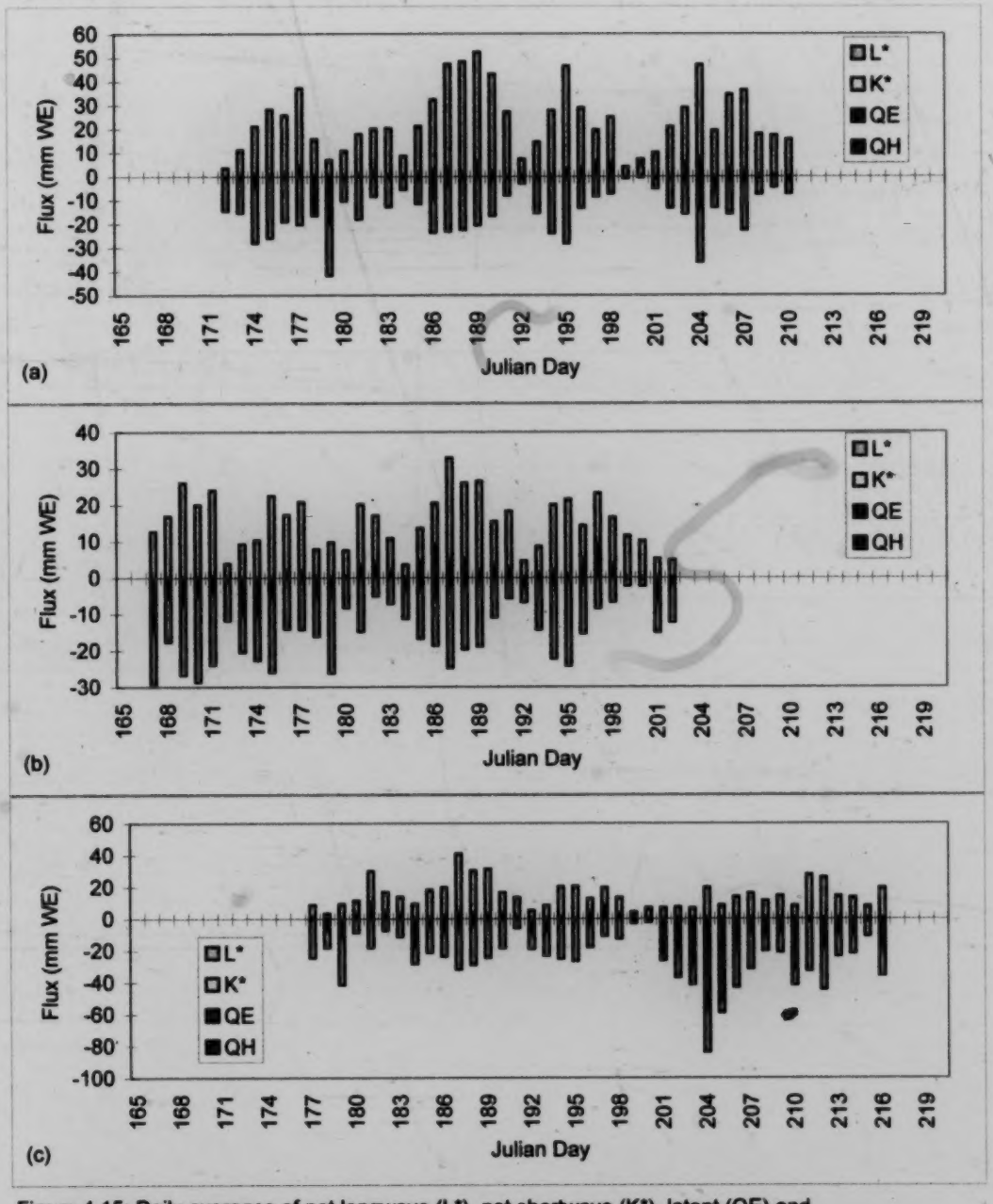

Figure 4.15: Daily averages of net longwave (L*), net shortwave (K*), latent (QE) and sensible heat (QH) fluxes at the (a) L-AWS, (b) M-AWS and (c) U-AWS. Positive fluxes indicate a downward flux of energy to the snowpack. Values are in mm WE. (Notice difference in y-axis scale between the 3 graphs).

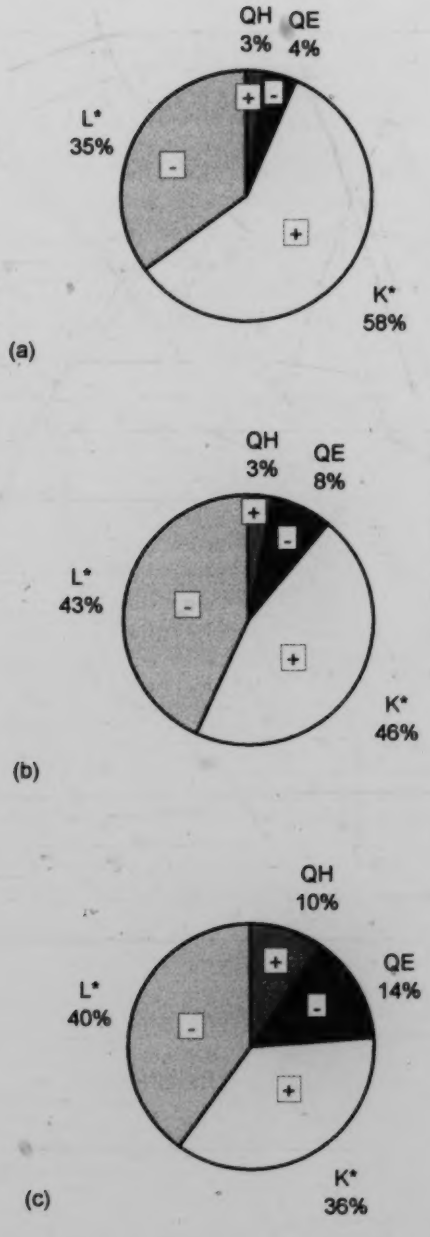

Figure 4.16: Partitioning of total melt energy at the (a) L-AWS, (b) M-AWS and (c) U-AWS. "+" indicates that the flux contributes to melt, and a "-" indicates a loss of melt energy at the surface.

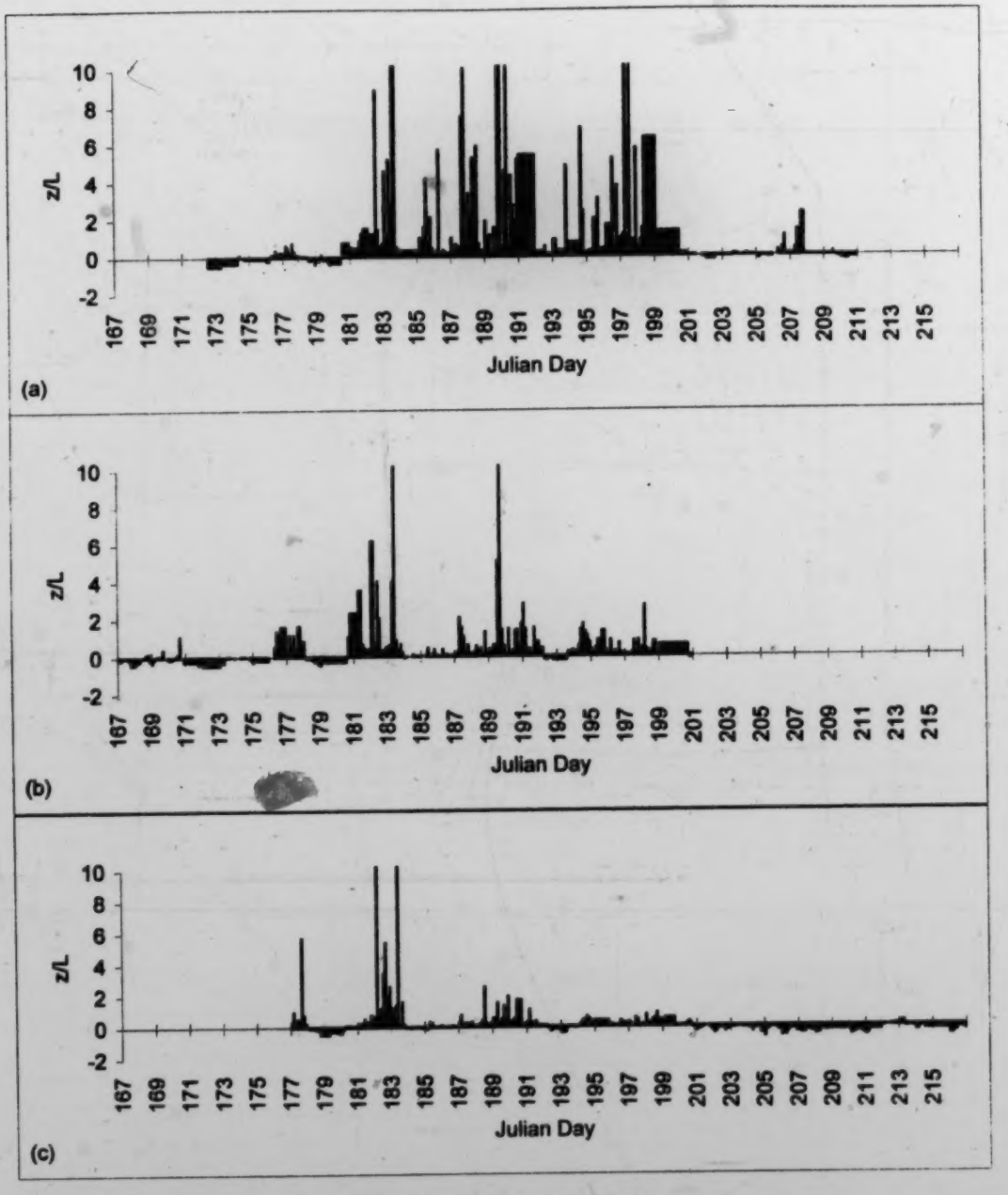

Figure 4.17: z/L (height of snow over the Monin-Obukov stability length scale) at the 3 weather station sites, as determined from the bulk transfer technique in turbulent flow. Positive z/L indicates stable conditions, while negative z/L indicates unstable conditions.

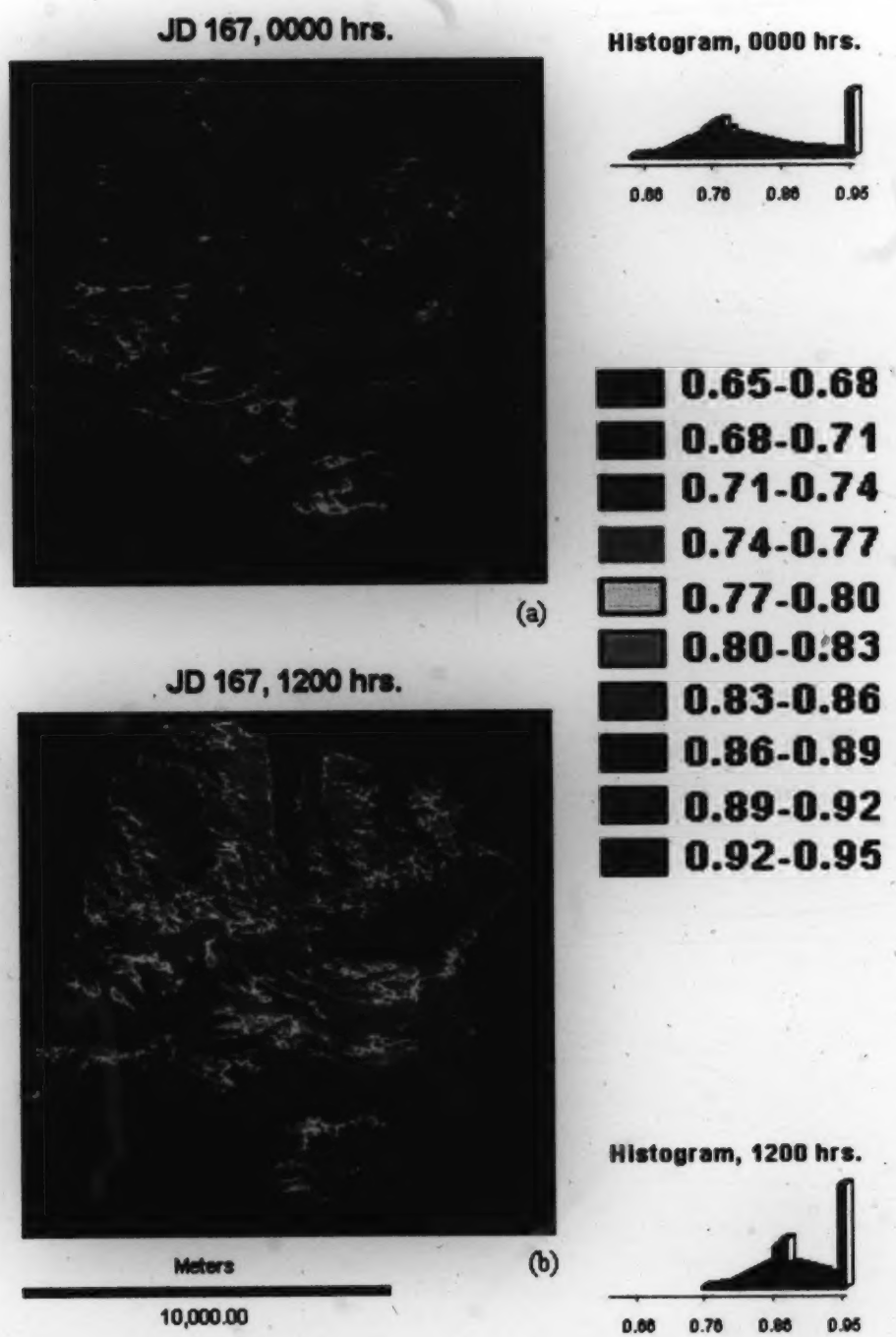

Figure 4.18: Variations in surface albedo on JD 167. (a) 0000 hrs. (b) 1200 hrs.

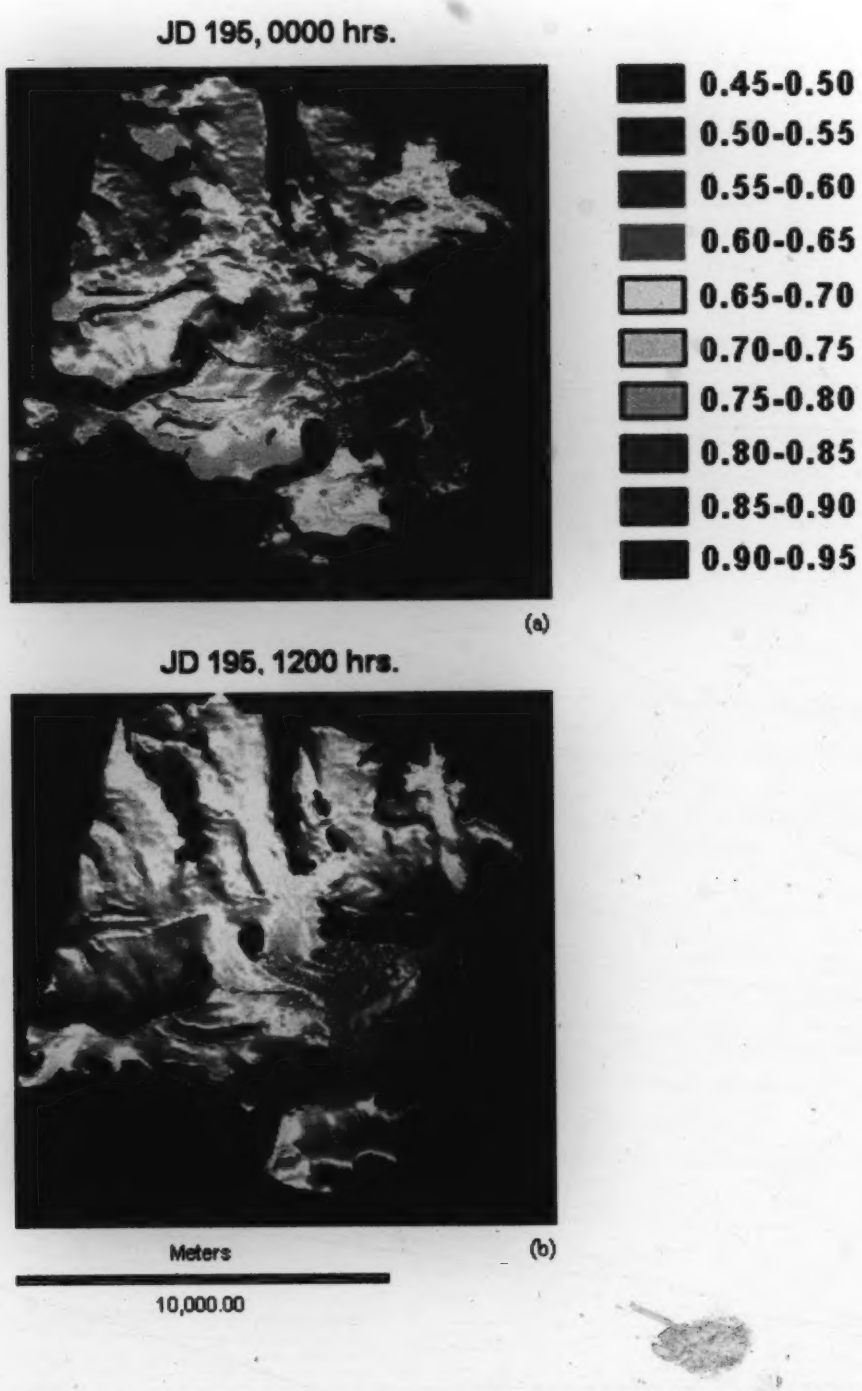

Figure 4.19Variations in surface albedo on JD 195. (a) 0000 hrs. (b) 1200 hrs.

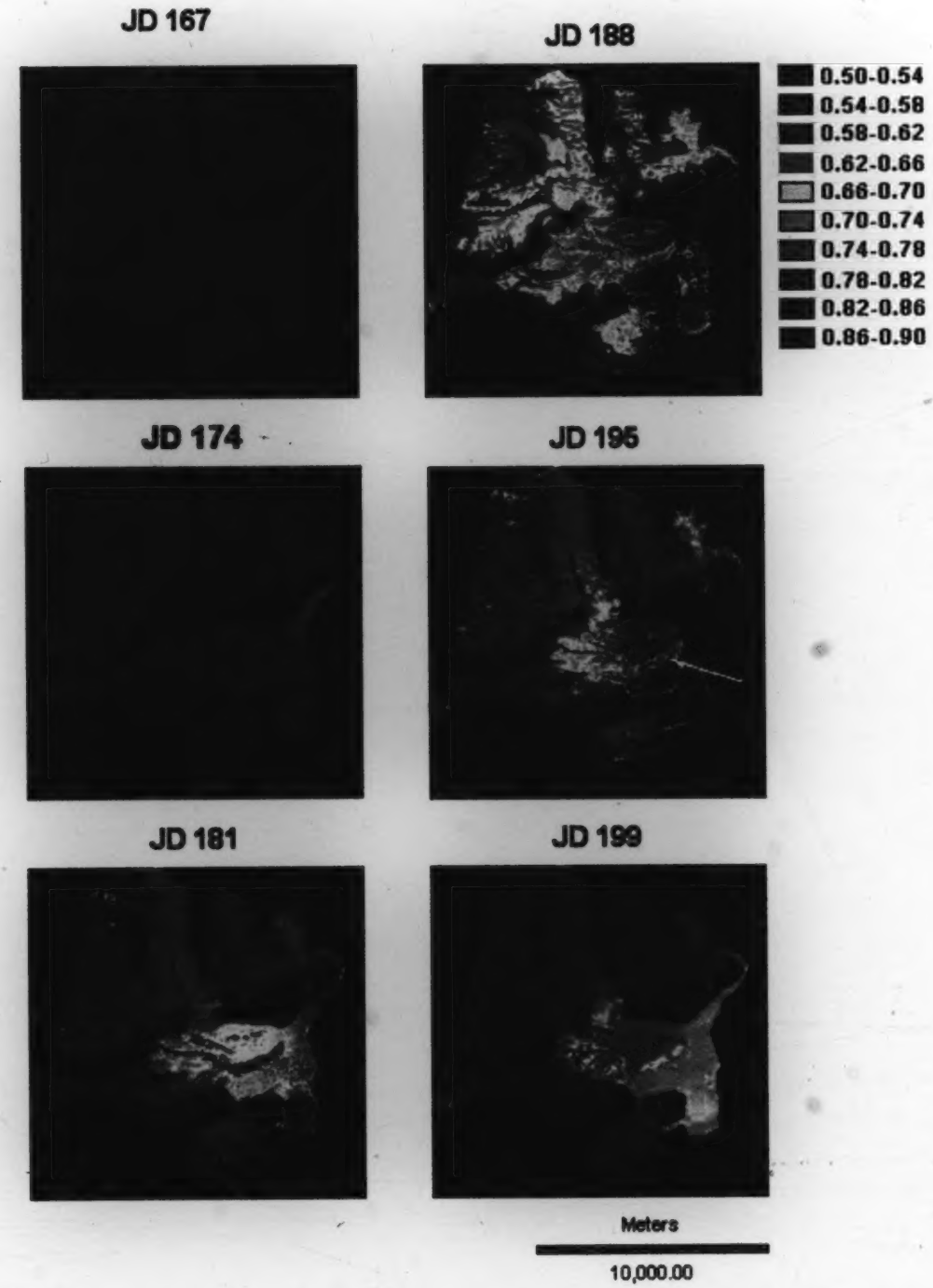

Figure 4.20: Seasonal variations in surface albedo.

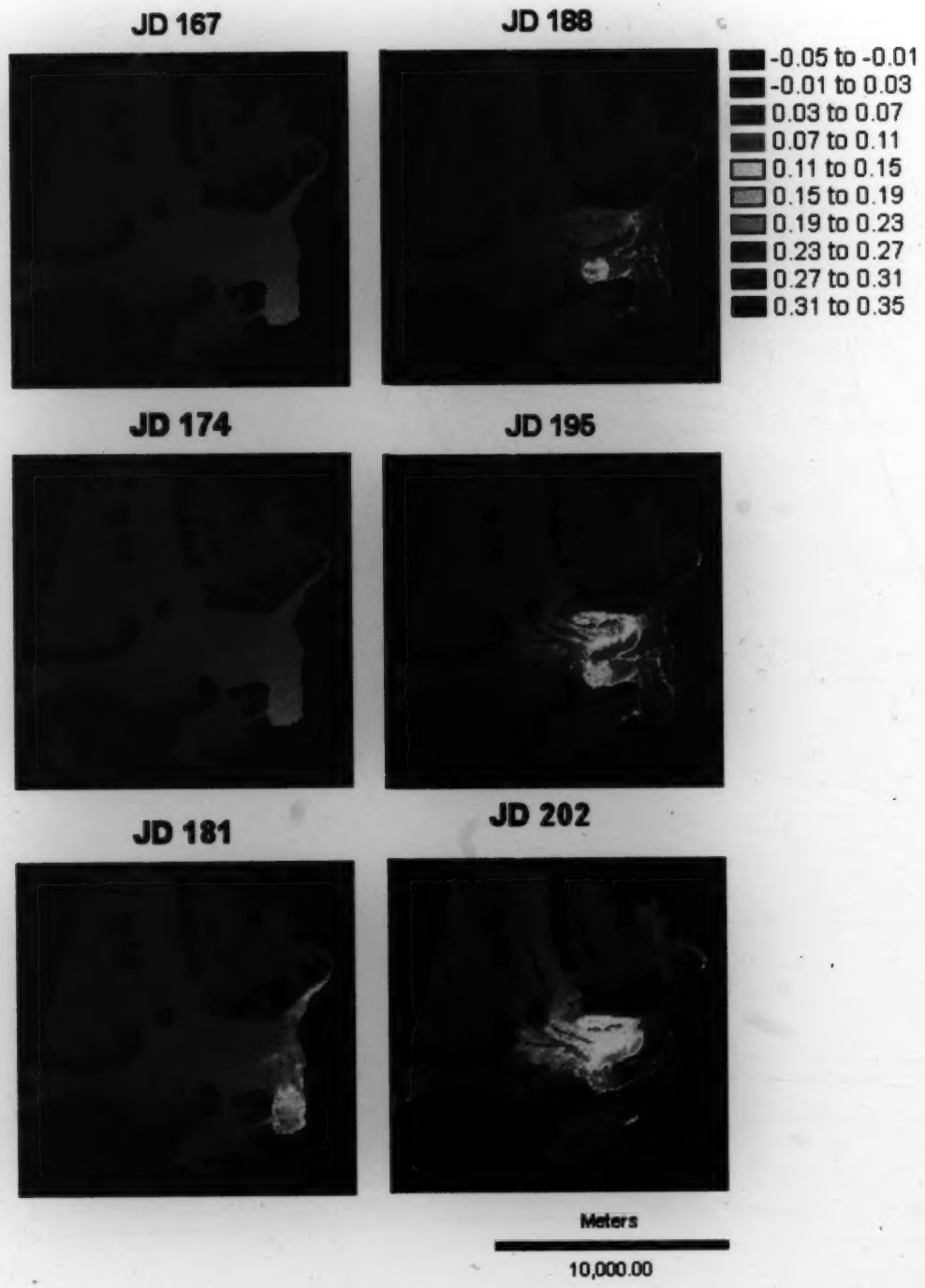

Figure 4.21: Seasonal variations in surface melt. (Units are m WE).

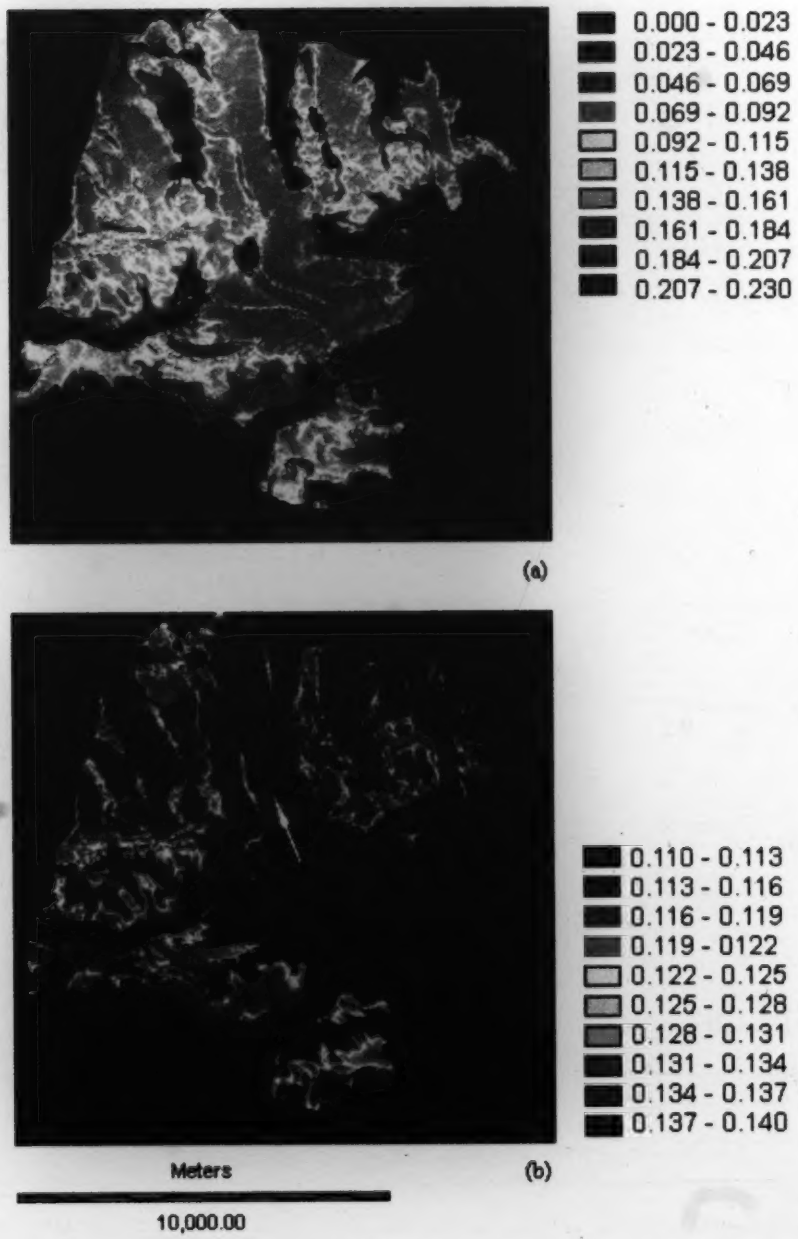

Figure 4.22: Facies zones at the end of the melt season (JD 195). (a) remaining snow, (b) remaining superimposed ice. (Units are m WE). Arrow in (b) marks ideal location for extraction of ice cores.

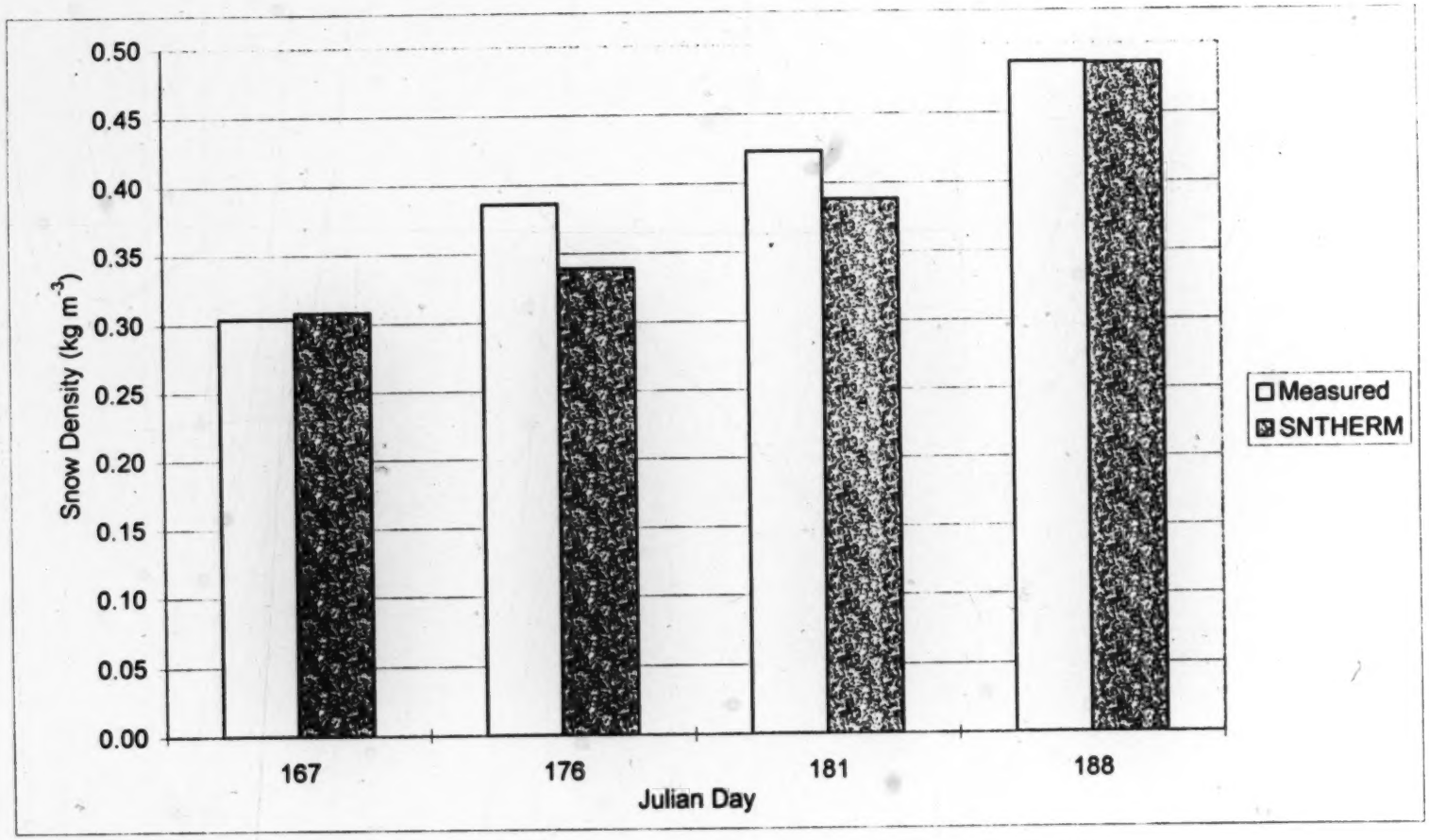

Figure 4.23: Comparison of measured and SNTHERM predicted total snowpack density.

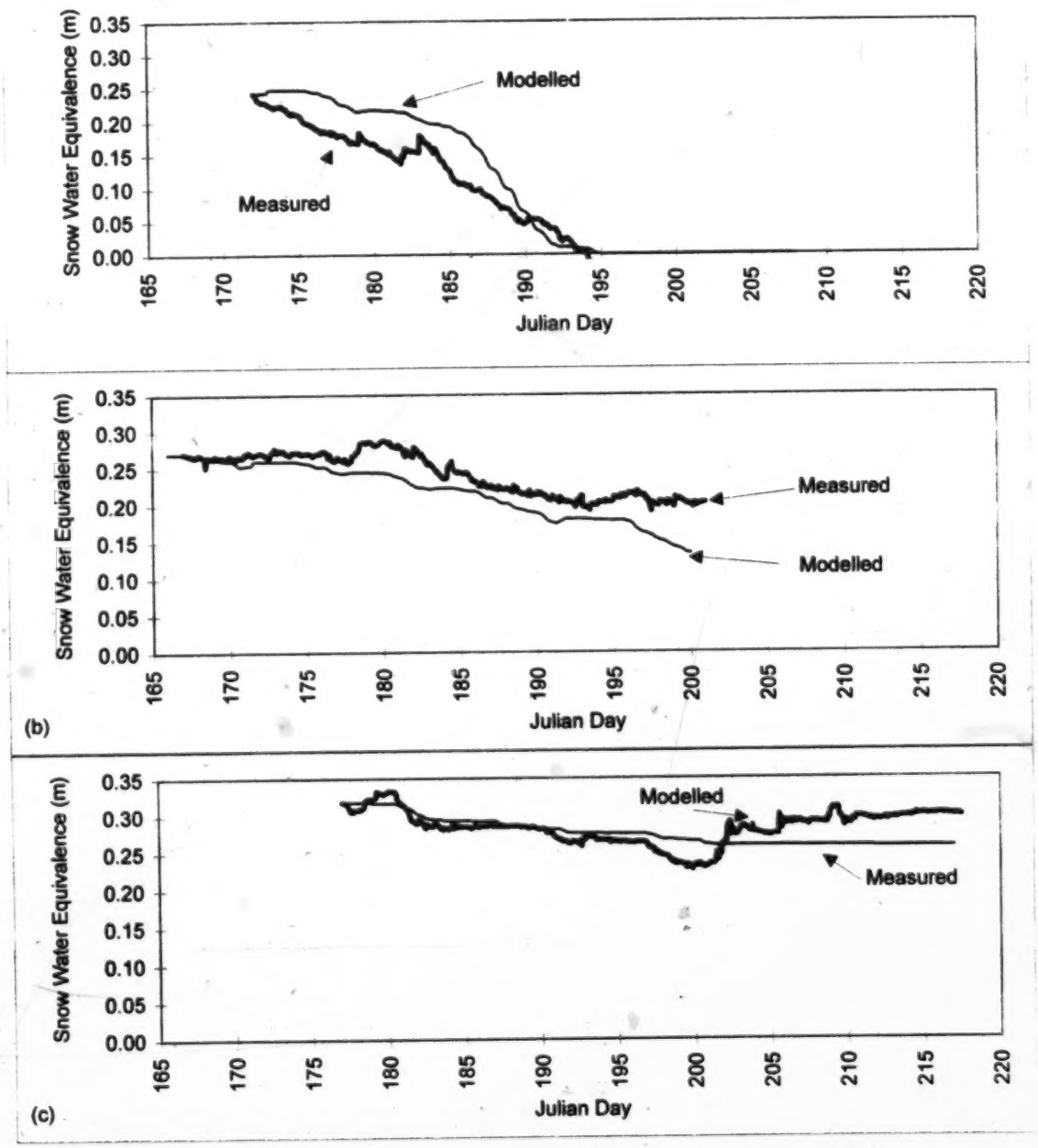

Figure 4.24: Comparison of modelled versus measured snow ablation using the "standard" model run at the (a) L-AWS, (b) M-AWS, and (c) U-AWS.

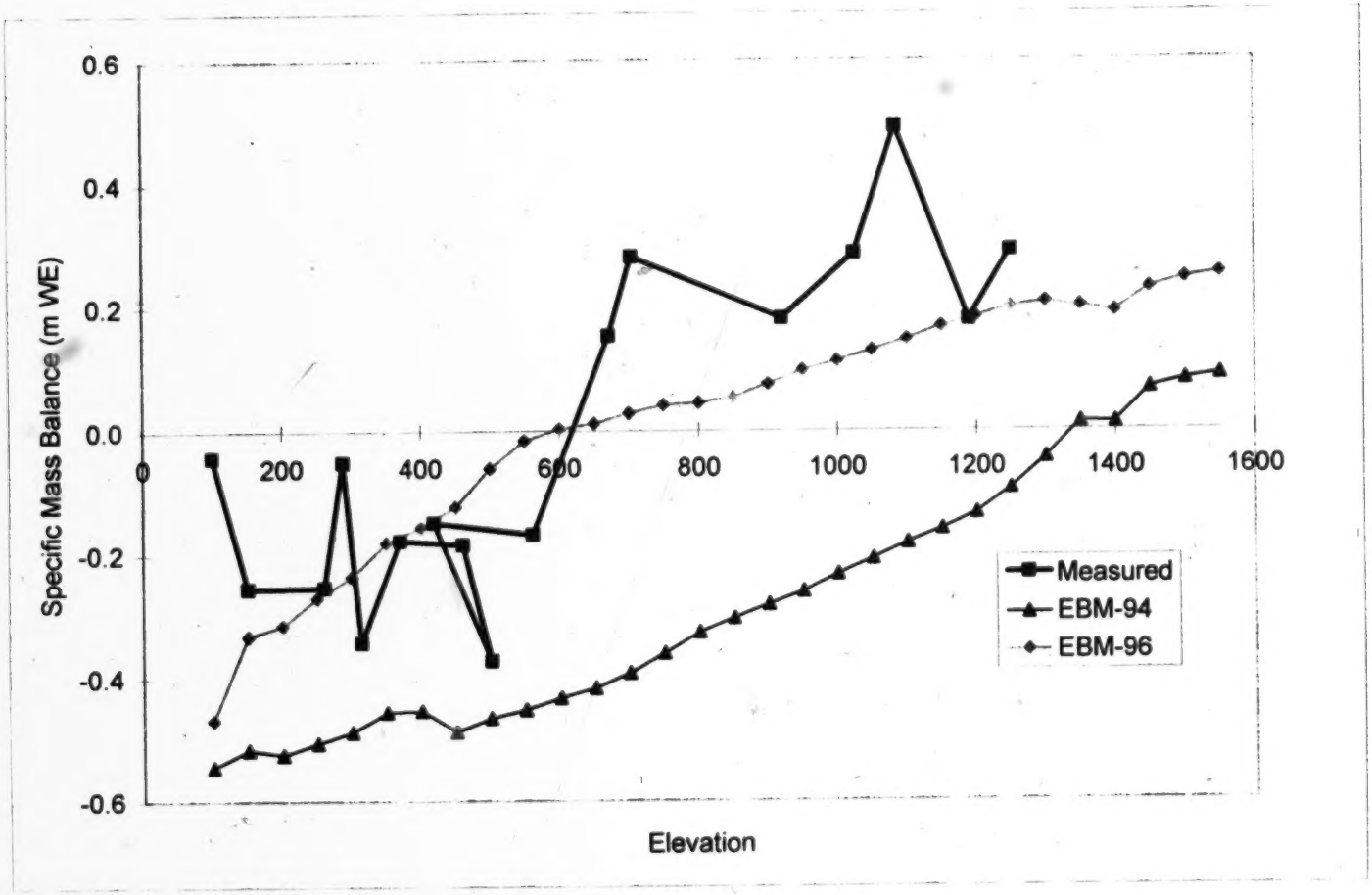

Figure 4.25: Predicted specific mass balance compared with measured mass balance from the ablation stake network.

4.9 References

Adams, W.P. 1966. Ablation and Run-off on the White Glacier, Axel Heiberg Island, Canadian Arctic Archipelago. Glaciology. No. 1. *Axel Heiberg Research Reports, McGill University, Montreal.* Jacobsen-McGill Arctic Research Expedition. 1959-1962. pp.77.

Ambach, W. 1986. Nomographs for the determination of meltwater from snow and ice surfaces. *Berichte des Wissenschaftlich-Medizinischen Vereins in Innsbruck.* 73: 7-15.

Ambach, W. and Kuhn, M. 1987. Altitudinal shift of the equilibrium line in Greenland calculated from heat balance characteristics. In Oerlemans, J. (ed.) *Glacier fluctuations and Climate Change.* Kluwer Academics. 281-288.

Arnold, N.S., Willis, I.C., Sharp, M.J., Richards, K.S. and Lawson, W.J. 1996. A distributed surface energy-balance model for a small valley glacier. I. Development and testing for Haut Glacier d'Arolla, Valais, Switzerland. *Journal of Glaciology.* 42(140): 77-89.

Bøggild, C.E., Reeh, N., and Oerter, H. 1994. Modelling Ablation and Mass-Balance sensitivity to Climate Change of Storstrømmen, Northeast Greenland. *Global and Planetary Change.* 9: 79-90.

Braithwaite, R. 1995. Aerodynamic stability and turbulent sensible-heat flux over a melting ice surface, the Greenland ice sheet. *Journal of Glaciology.* 41(139): 562-571.

Braithwaite, R.J. and Olesen, O.B. 1990. A Simple Energy-Balance Model to Calculate Ice Ablation at the Margin of the Greenland Ice Sheet. *Journal of Glaciology,* 36(123): 222-228.

Brock, B. 1997. Seasonal and spatial variations in the surface energy-balance of valley glaciers. *Unpublished PhD. Thesis.* University of Cambridge. 343p.

Hardy, R.L. 1971. Multiquadratic Equations of Topography and Other Irregular Surfaces. *Journal of Geophysical Research,* 76(8): 1905-1915.

Havens, J.M., Muller, F. and Wilmot, G.C. 1965. Comparative meteorological survey and a short term heat balance study of White Glacier, Canadian Arctic Archipelago-Summer 1962. *Axel Heiberg Island Research Reports, McGill University, Montreal.* Meteorology No. 4. pp.68.

Hemenway, D.D. 1995. An efficient analytical approach for generating DEM. *Unpublished Masters Thesis,* Department of Geography, University of Alberta.

Holmgren, B. 1971. Climate and Energy Exchange on a Sub-polar Ice Cap in Summer. Part. F. On the Energy Exchange of the Snow Surface at Ice Cap Station. Arctic Institute of North America Devon Island Expedition 1961-1963. *Meddelanden Från Uppsala Universitets Meteorologiska*. No.112.

Jordan, R. 1991. A one-dimensional temperature model for a snow cover. Technical documentation for SNTHERM.89. *Spec. Rep.* 91-16, USA-CRREL, Hanover, NH.

Keeler, C.M. 1963. Relationship between climate, ablation and run-off on the Sverdrup Glacier, 1963, Devon Island, N.W.T. *A final report to Arctic Institute of North America Devon Island Expedition*. pp.80.

Konzelmann, T. and Braithwaite, R.J. 1995. Variations of Ablation, Albedo and Energy Balance at the Margin of the Greenland Ice Sheet, Kronprins Christian Land, eastern North Greenland. *Journal of Glaciology*, 41(137): 174-182.

Marks, D. 1988. Climate, energy exchange, and snowmelt in Emerald Lake Watershed, Sierra Nevada. *Unpublished Ph.D. Thesis*, University of California at Santa Barbara. 158 p.

Oerlemans, J. 1993. A model for the Surface Balance of Ice Masses: part I. Alpine Glaciers. *Zeitschrift Für Gletscherkunde Und Glazialgeologie*, 27/28: 63-83.

Ohmura, A. 1981. Climate and Energy Balance on Arctic Tundra. *Zurcher Geographische Schriften*, 3. pp.437.

Ohmura, A., Konzelmann, T., Rotach, M., Forrer, J., Wild, M., Abe-Ouchi, A., and Toritani, H. 1994. Energy Balance for the Greenland Ice Sheet by Observation and Model Computation. Snow and Ice Cover: Interactions with the Atmosphere and Ecosystems (*Proceedings of Yokohama Symposia*, July 1993. IAHS Publications no.223: 85-94.

Ohmura, A., Wild, M., Lennart, B. 1996. Present and future mass balance of the ice sheets simulated with GCM. *Annals of Glaciology*. 23: 187-193.

Shapiro, R. 1987. A simple model for the calculation of the flux of direct and diffuse solar radiation through the atmosphere. ST Systems Corporation, Lexington, MA. Scientific Report No. 35. Under contract to Air Force Geophysics Laboratory, Report AFGL-TR-87-0200.

Sverdrup, H. U. 1935. Scientific results of the Norwegian-Swedish Spitsbergen Expedition in 1934. Part IV. The ablation on Isachsen's Plateau and on the Fourteenth of July Glacier in relation to radiation and meteorological conditions. *Geografiska Annaler*, 17(3-4): 145-166.

Trimble Navigation Limited 1994. Mapping Systems General Reference. Part No. 24177-00.

Revision A.

van de Wal, R.S.W. 1996. Mass-balance modelling of the Greenland ice sheet: a comparison of an energy-balance and a degree-day model. *Annals of Glaciology*. 23: 36-45.

van de Wal, R.S.W. and Oerlemans, J. 1994. An energy balance model for the Greenland Ice Sheet. *Global and Planetary Change*. 9: 115-131.

Woodward, J. 1995. Superimposed ice and glacier mass balance. *Unpublished M.Sc. Thesis*. University of Alberta. 96p.

Woodward, J., Sharp, M. and Arendt, A. *In Press*. The influence of superimposed ice formation on the sensitivity of glacier mass balance to climate change.

CHAPTER 5: Mass Balance Simulations Using a Degree-Day Model for a High Arctic Glacier

5.1 Introduction

In general, two methods have been adopted for modelling glacier mass balance from climate data. The energy balance method, described in Chapter 4, is used to calculate explicitly the structure of the turbulent boundary layer above a glacier surface, and to determine the net energy fluxes contributing to melt. Because they explicitly calculate the physical processes of melt at the surface, energy balance models (EBM's) are considered to be the most accurate method for modelling glacier mass balance (van de Wal, 1996). The drawback to EBM's is that they require a significant amount of computing time, as well as a large amount of input data to drive the model (e.g. net radiation, air temperature, wind speed, and relative humidity). A simpler method to calculate glacier mass balance is based upon the observed relationship between air temperature and glacier ablation. This 'degree-day' method is simpler because melt is calculated exclusively from air temperature measurements via degree-day factors which are different for varying surface conditions. For instance, the degree-day factor for snow may be in the range of 3.0 mm WE per degree-day, whereas the factor for ice is commonly around 8.0 mm WE per degree-day (Reeh, 1991).

Despite their relative simplicity, degree-day models have been used successfully in mass balance simulations for high polar glaciers and ice sheets. Degree-day based predictions have compared well with observed mass balance measurements for the Greenland ice sheet (Huybrechts, 1994) and glaciers in Iceland, Norway and Greenland (Johannesson et al., 1995). Degree-day models have also proven useful for predicting the likely effects of global climate change (in the form of increased air temperature) on the mass balance of high polar glaciers and ice sheets (Reeh, 1991; Laumann & Reeh, 1993). Degree-day models have been developed for and tested on high polar glaciers and ice sheets because these glaciers are so remote that it is costly to obtain detailed climatic data required to drive energy balance models. Although air temperature data to drive degree-day simulations should ideally be obtained from on-site meteorological stations, many studies have relied on air temperature data from nearby weather

stations as input to the degree-day model, and have still obtained accurate predictions of glacier mass balance. Therefore, there is a strong motivation to test and improve degree-day models, because such models provide a means of predicting glacier mass balance in regions which are remote or inaccessible, using data which are relatively easy to obtain.

Studies which model the mass balance of high polar glaciers have tended to focus exclusively on either the energy balance or degree-day approach. Often, the choice of model is dictated by data availability, and, for areas where only simple climatic data are available, modellers must use the degree-day approach. However, situations in which enough data are available to use both energy balance and degree-day models provide a unique opportunity to compare models, and, more importantly, to use output from the energy balance model to improve the accuracy of the degree-day method. The means by which degree-day models, driven exclusively by air temperature data, can incorporate influences on the surface energy balance, such as surface albedo and turbulence, is via the degree-day factor. Most degree-day studies have calculated degree-day factors for a given site by comparing ablation measurements with positive degree-days. This has yielded degree-day factors which vary according to glacier location and surface characteristics. Variations in degree-day factors reflect variations in the structure of the energy balance (i.e. the relative contribution of different components of the energy balance, such as radiative and turbulent heat fluxes, to the melt energy flux) between different locations, and differences in the melt rates of snow, superimposed ice, and glacier ice in response to a given energy input at the surface. However, Braithwaite (1994) compared energy balance and degree-day model simulations for the Greenland ice sheet, and showed that degree-day factors vary not only with location and surface type, but also with summer mean temperature, surface albedo and turbulence. The degree-day factor, therefore, is the key link between the stochastic degree-day and physically based energy balance approaches to modelling glacier mass balance.

In this paper, the summer mass balance of John Evans Glacier, Ellesmere Island, Nunavut is simulated with a degree-day model, using field data from the summer of 1996. The energy balance model developed in Chapter 4 is used to improve degree-day simulations by investigating the causes of variation in the degree-day factor as predicted from energy balance calculations. Degree-day factors are solved for at a given grid cell by: (1) using the energy

balance model to predict the daily melt in the grid cell, (2) calculating the daily positive degree-days from meteorological measurements and (3) dividing melt by daily positive degree days to obtain the degree-day factor. Step (3) produces the degree-day factor required for the degree-day model to predict the amount of melt simulated by the energy balance model. Seasonal and spatial variations in degree-day factors are investigated with the aim of developing simple parameterizations which could be used to incorporate variable degree day factors in the degree day model, allowing it to be used in situations where only air temperature data are available. Particular emphasis is placed upon parameterizing degree-day factors as a function of the effective grain size of snow or ice, a key parameter in the albedo model described in Chapter 2. Because the effective grain size is estimated empirically, it may be used to predict degree-day factors in the degree-day model.

Although degree-day models are ideally driven with local meteorological data, this paper will investigate the use of remote data to drive model simulations. The advantage to using remote data is that the degree-day model may be used to predict mass balance at locations for which there are no on-site meteorological data. For instance, on-site data from John Evans Glacier are available only for the 1994 and 1996 melt seasons. To simulate mass balance in years previous to this, it is necessary to use remote data. Remote data will be obtained from AES Alert weather station (82°30'N 62°20'W), where continuous air temperature records have been collected since 1951.

The use of remote data raises 2 issues which will be explored in this paper. The first is how to convert remote data to local data to drive degree-day model simulations. Two methods to convert remote data to local data will be investigated:

(1) A constant correction factor, based on the average difference between air temperature measured at John Evans Glacier and Alert, will be applied to the Alert dataset.

(2) Alert data will be modelled as a cosine curve of annual period with stochastic deviations, as a function of mean annual and mean July air temperature, also with a

constant correction factor as in (1) above.

The second issue investigated in this paper is how using remote data degrades model performance. Model simulations will be compared with measured mass balance data from 1996-1997, to determine the loss in model accuracy with the use of remote data.

5.2 Study Area

5.21 Site description

John Evans Glacier is a large valley glacier located at 79°40'N 74°00'W on an unnamed peninsula south of Dobbin Bay, eastern Ellesmere Island, Nunavut, Canada (Figure 5.1-5.3). Its catchment area is 211km^2, of which 47% is glaciated, and spans an altitudinal range of 50 to 1500 m (Figure 5.4). 77% of the ice surface area lies between 600m and 1100m. The catchment comprises a main trunk glacier fed from a number of sub-catchments in the western part of the basin, and 8 small valley glaciers feeding into a marginal lake 3 km from the snout of the main trunk glacier on its eastern side.

5.22 Local Climate

Mean annual and July temperatures recorded over the period 1951-1994 at the AES meteorological station at Alert, north-eastern Ellesmere Island (82°30'N 62°20'W) are shown in Figure 5.5. The mean annual sea level temperature at Alert was -17.8°C. During 1988-89, the average annual air temperature at Alert was -16.9°C. This is similar to the average annual air temperature (-17.3°C) measured for the same period at Allman Bay, located 5km south of John Evans Glacier (Figure 5.2) (G. Henry, *pers comm.*). However, July 1988 temperatures were approximately 3°C warmer at Allman Bay (located at sea level) than at Alert. Field data for the present study were collected during the summer of 1996, which was unusually cold. The mean 1996 July air temperature measured at the lower weather station (elevation 261 m) on John Evans Glacier was approximately 3°C colder than the mean July air temperature at Allman Bay in 1988 (note that some of this difference in temperature may be due to differences in surface type and elevation between Allman Bay and John Evans Glacier). Mean total precipitation

from 1 August 1995 to 1 August 1996 at Alert (165.4 mm WE) was 128% higher than the mean annual total precipitation at Alert over the period 1951-1994 (128.5 mm WE).

5.3 Model Summary

5.31 Calculation of Air Temperature

Most degree-day simulations carried out in this paper will be driven by measured air temperature data from either John Evans Glacier or the Alert weather station. However, a simple method to predict the annual air temperature cycle in the Arctic will also be used to drive degree-day model simulations. This method uses a cosine function to model the annual temperature cycle (TCA), based on the mean annual (TMA) and mean July (TJA) air temperatures (Reeh, 1991):

$$TCA = TMA + (TJA - TMA)\cos(2\pi t/A + \phi) \tag{5.1}$$

where t is the time, A = 1 year, and ϕ is the phase angle, determined using a least-squares curve fitting routine by fitting measured data to temperatures predicted from Equation 5.3 (see Section 5.53).

5.32 Positive Degree-Days

Method #1:

Two different methods are used to calculate positive degree-days for either measured or predicted air temperature data Method #1 uses daily or hourly air temperature data and assigns positive degree-days whenever the temperature is above 0°C:

$$\text{if } TCA > 0°C,\ DD = TCA \tag{5.2}$$

$$\text{if } TCA \leq 0°C,\ DD = 0 \tag{5.3}$$

For Equations 5.2 and 5.3, TCA represents the air temperature, whether measured or calculated from Equation 5.1, used to drive degree-day model simulations.

Method #2: Calculating Positive Degree-Days from Equation 5.1:

A problem with calculating positive degree-days from temperatures predicted by Equations 5.1 is that if TMJ < 0°C, then the positive degree day sum would be zero. In reality, there may be days when the temperature exceeds the zero degree mark, even if the average temperature of the warmest month is below 0°C (Reeh, 1991). Also, random temperature deviations from the average annual cycle are likely to cause positive temperatures in the spring or fall, although the average temperature in these seasons may be well below the freezing point. In the calculation of positive degree-days (PDD), these deviations of the actual temperature (T) from the long-term annual cycle (TCA) are accounted for by a statistic which is normally distributed, centered on the curve given by Equation 5.3, and having a standard deviation s:

$$PDD = \int_0^\infty \left(\frac{T}{s\sqrt{2\pi}} \exp\text{-}(T - TCA)^2 / (2s)^2 \right) dT \qquad (5.4)$$

5.33 Calculation of Degree-Day Factors

Rather than using prescribed degree-day factors which vary only with surface characteristics, as has been done in previous degree-day studies, degree-day factors are determined by comparing degree-days with surface melt at specific points along the centerline of the glacier. Surface melt is predicted using the EBM described in Chapter 3. Degree-day factors (DDF) at a given location are calculated as:

$$DDF = \frac{MELT}{PDD} \qquad (5.5)$$

where MELT is the water equivalent ablation predicted by the EBM. DDF's for a given location are associated with the surface type (snow, superimposed ice or glacier ice) present at that location based on melt predictions from the EBM. This is done in order to determine relationships between surface type and DDF's.

5.34 Snow and Ice Melt Algorithm

The algorithm for snow and ice melt is similar to that described by Braithwaite and Thomsen (1984), except that rainfall is neglected, i.e. precipitation is assumed to occur as snowfall only. Once the positive degree-days are calculated, they are multiplied by the degree-day factor determined in Section 5.32. The melting of snow or ice is then determined in the following sequence:

1) Snow (if present) is melted. The melt water is supposed to percolate into the snow cover and re-freeze immediately as superimposed ice. Runoff does not occur until the amount of superimposed ice exceeds a given fraction (Pmax) of the snow cover. Pmax is determined based on the theory of heat conduction in ice, used by Woodward (1995) and described in Chapter 3 (method SI-P1).

2)The superimposed ice is melted.

3)Glacier ice is melted.

5.4 Meteorological Data

Three automatic weather stations (AWS's) were set up at low (261 m a.s.l.), middle (824 m a.s.l.) and high (1183 m a.s.l.) elevation sites on John Evans Glacier (Figure 5.3; Table 5.1). Each AWS consisted of a central mast frozen into a ~1.5m deep hole drilled into the ice surface. Air temperature was measured at a height of 2m above the snow or ice surface at each weather station, using a Campbell Scientific 107F temperature probe. Measurements were taken every 10 sec. and averaged for hourly and daily output. Meteorological data required to drive the EBM were also collected at the 3 AWS's, as described in Section 3.5. The stations collected hourly data throughout the months of June and July, 1996, and collected daily data through the fall, winter and spring of 1996 - 97 (Table 5.2).

5.5 Results and Discussion

5.51 Air Temperature Measurements

Average hourly air temperature measurements at Alert weather station (Figure 5.6a) did not correlate well with air temperature measurements at John Evans Glacier (Figure 5.6b,c,d). The coefficient of determination between Alert data and each of the John Evans Glacier weather station sites was between -0.0006 and -0.3, to a level of significance of as low as <0.01 (Table 5.3). Single factor analysis of variance showed that the mean Alert air temperatures were most similar to mean air temperatures at the L-AWS ($p > 0.72$), but less similar to mean air temperature measurements at the M-AWS and L-AWS (Table 5.4).

5.52 Correction to Alert Air Temperature Data

Temperature data from the L-AWS were used for comparison with Alert data because the L-AWS (261 m a.s.l.) was closest in elevation to Alert (0 m a.s.l.), and because the analysis in Section 5.51 showed that the mean of Alert and L-AWS temperature measurements are the same to a moderately high level of significance ($p > 0.72$). Average air temperatures measured at the L-AWS for the period of instrumental record (JD 172 - JD 212) were first corrected for elevation for comparison with Alert data. This was done using the average of measured lapse rates between L-AWS and M-AWS (Table 5.5). The lapse rate from the L-AWS to the M-AWS was unusually low (-0.000621°C m^{-1}). This was probably due to fog in Allman Bay which, in summer 1996, commonly covered lower sections of the glacier up to an elevation of 300 to 400 m, creating cooler conditions at the snout than at higher elevations on the glacier. The lapse rate between the M-AWS and the U-AWS was slightly higher than the lapse rate of -0.004°C m^{-1} measured by Bøggild *et al.* (1994) for Storstrømmen, North Greenland.

Assuming that the lapse rate between the L-AWS and M-AWS applied to areas of the glacier below the L-AWS, this lapse rate is used to extrapolate L-AWS air temperature measurements to sea level. Average sea level air temperatures at Alert were 1.08°C higher than average air temperatures at L-AWS (corrected to sea level), for the period of instrumental record at L-AWS. The Alert dataset was therefore adjusted by -1.08°C before being used to drive model simulations for John Evans Glacier.

For all degree-day simulations, hourly temperature lapse rates are read as input to the model. These are calculated from differences between measured temperatures at the 3 weather stations. The glacier is split into 2 sections: an upper section between the M-AWS and U-AWS, and a lower section between the L-AWS and M-AWS. Each grid cell is assigned a lapse rate based on the difference in hourly mean temperature at the 2 weather stations between which the grid cell is located. Locations above the U-AWS are assigned the lapse rate calculated for the section between the U-AWS and M-AWS, while locations below the L-AWS are assigned the lapse rate calculated for the section between the M-AWS and L-AWS.

5.53 Temperature Prediction Using Cosine Function

Equation 5.1 was used to predict air temperature at Alert using mean annual and mean July air temperatures. TMA was assigned a value of -17.7°C based on air temperature data from Alert from 1951 to 1994. TMJ was given a value of 2.94°C as determined from the 1996 Alert dataset (the entire 1995-1996 Alert dataset was not available to determine TMA for the year of model simulations). The phase angle ϕ was determined by least-squares fitting of the predicted air temperature, TCA, to the Alert data. This produces a phase angle of 3.49. All predictions from Equation 5.1 were adjusted by -1.08°C before being used to drive model simulations for John Evans Glacier, to account for differences between conditions at Alert and John Evans Glacier as described in Section 5.52. Equation 5.1 did a good job at predicting the overall trend in the Alert dataset ($r^2 = 0.58$, $p < 0.05$) (Figure 5.7).

5.54 Positive Degree-Days

This section compares positive degree-days calculated for John Evans Glacier using different methods. Three different air temperature datasets are used: (1) the local data from the L-AWS at John Evans Glacier; (2) remote data from Alert, adjusted for conditions at John Evans Glacier as described in Section 5.52; and (3) remote data from Alert modelled as a cosine function, as described in Section 5.53, also adjusted for

conditions at John Evans Glacier. Calculations of degree-days for all Alert simulations (datasets (2) and (3) above) are carried out using both methods described in Section 5.32, and comparisons are made between results from each method.

Total positive degree-days, calculated from hourly data at the L-AWS for the period of instrumental record, were 1897.1 degree-days (Figure 5.8). Positive degree-day calculations with the TCA dataset using Method # 2 best predicted the total positive degree-days at the L-AWS (Figure 5.8, Table 5.6). The relationship between the positive degree-days calculated with the TCA dataset using Method # 2, and those predicted from hourly data at the L-AWS, has the lowest standard error and highest coefficient of determination. Positive degree-day calculations using the measured Alert dataset do seem to simulate the temporal patterns in positive degree-days at L-AWS better than the TCA dataset, although there is a lag of several days between patterns in the degree-days at John Evans Glacier and similar patterns at Alert (Figure 5.8). Presumably it is this lag which reduces the coefficient of determination for the Alert calculations. This lag should be investigated in future studies so that Alert air temperatures may be adjusted to simulate more accurately temperatures at John Evans. Such a lag may be the result of weather systems bringing warm weather to John Evans Glacier before reaching Alert. For the present model, positive degree-days are calculated from the TCA dataset using Method # 2.

5.55 Average Degree-Day Factors at the 3 Weather Stations

The slope of the regression line relating total ablation in a day to the positive degree-day sum for that day is the average degree-day factor (Figure 5.9). In this analysis, ablation values are predicted from hourly energy balance calculations. The average degree-day factor for snow is highest at the L-AWS and lowest at the M-AWS (Table 5.7). (The few days during which superimposed ice or glacier ice were exposed at the L-AWS are omitted from this analysis, because most of these days had very few positive degree-days). The relationship between ablation and positive degree-days, which is the basis upon which degree-day models are developed, is poor for all 3 sites on John Evans Glacier, especially

for the M-AWS, for which $r^2 = 0.05$ (Table 5.7).

Average degree-day factors determined for John Evans Glacier in 1996 are low compared to values used in most other studies (Table 5.8). However, Braithwaite (1994) tested the sensitivity of positive degree-day factors to the summer mean temperature, and predicted low positive degree-day factors for snow for cold summers. Interpolating from Braithwaite's graph (Figure 5 in Braithwaite, 1994), a summer (June-August) mean temperature at John Evans Glacier in 1996 of 0.33°C gives a value of ~2.0 mm WE $d^{-1}\,°C^{-1}$ for the positive degree-day factor for snow. This is close to the value determined for the U-AWS (1.99 mm WE $d^{-1}\,°C^{-1}$).

5.56 Spatial and Temporal Variations in Predicted Degree-Day Factors

Degree-day factors for melt at each AWS were determined using the method described in Section 5.32. Degree-day factors increased with time after a new snowfall at each of the stations (Figure 5.10a). Highest degree-day factors occurred at the U-AWS and M-AWS around JD 195. In general, degree-day factors followed the patterns in modelled effective grain radius (Figure 5.10b), as determined by the EBM. The effective grain radius is a parameter used in the EBM to represent the optical properties of snow or ice crystals. It is based on the "true" grain radius that would be measured in the field, but also accounts for the effects of free water and snow contaminants. Thus for snow crystals of similar size (as measured in the field), a sample which has a high free water content would have a higher effective grain size than one which is dry. Different grain radii are predicted for visible and near-infrared wavelengths because certain components of the grain growth affect specific optical properties of the snowpack. For instance, snowpack contamination primarily reduces surface reflection in the visible portion of the spectrum, so an increase in the snow contamination increases the visible effective grain size only (see Section 2.83 for description of effective grain radius algorithm).

It is not surprising that degree-day factors follow the patterns in effective grain size, since grain size is one of the main parameters which drives the surface albedo algorithm (described in Chapter 2), and surface albedo is in turn an important parameter in energy

balance calculations. However, factors other than grain size may be influencing the positive degree-day factor. Braithwaite (1994) found a relationship between summer mean temperature and degree-day factors for snow and ice. For instance, large positive degree-day factors were found to occur at lower temperatures and with low albedo. Albedo variations (0.3-0.7) had the greatest effect on degree-day factors at low temperatures, while variations in turbulence had a greater effect at higher temperatures. Relationships between surface albedo, air temperature and positive degree-day factors were examined in this study, but no significant correlations were found.

The relationship between grain size and predicted degree-day factors was examined for each weather station. The strongest relationship is between visible effective grain size and degree-day factor at the M-AWS ($r^2 = 0.58$), followed by the relationship between visible effective grain size and degree-day factor at the L-AWS ($r^2 = 0.50$) (Table 5.9). At the U-AWS, there is a weak negative relationship between grain size and degree-day factors. This may be explained by the fact that the U-AWS was located at a very windy site (see Figure 4.12 f) where grain size was strongly affected by wind scouring, a process not considered in the present grain growth algorithm. However, as wind conditions at the U-AWS are likely not representative of conditions over most of the glacier, data from the U-AWS can justifiably be omitted from the present analysis. Grain size is therefore used as a basis for predicting spatial and temporal variations in degree-day factors. The advantage to this approach is that the grain growth algorithm developed in Chapter 2 is an empirical model, and simply requires a knowledge of the timing of snowfall events on the glacier. Thus it can be readily incorporated into the degree-day model.

By plotting predicted grain sizes against predicted degree-day factors at the L-AWS and M-AWS, it is possible to develop a simple parameterization of degree-day factors for snow as a function of snow grain size. At both the L-AWS and M-AWS, there is a linear increase in degree-day factor with increasing grain size (Figure 5.10a & b). The slope of the relationship between degree-day factors and grain size is an order of magnitude higher at the L-AWS than at the M-AWS, because snow grains grew to a much larger "effective" size at the L-AWS (largely as a result of increased melt and hence increased free water

content within the snowpack). To develop a parameterization of degree-day factors, data from both the M-AWS and L-AWS for the visible and near-infrared effective grain radii will be used (Figure 5.11).

A multiple regression comparing visible and near-infrared effective grain radii for both the M-AWS and L-AWS produces the following relationship:

$$DDF = 0.0607 r_{vis} + 0.0737 r_{nir} + 1.447 \quad (5.6)$$

where r_{vis} is the effective grain radius for the visible part of the spectrum, and r_{nir} is the effective grain radius for the near-infrared part of the spectrum.

The degree-day factor parameterization developed using Equation 5.6 applies to snow surfaces only. Although the EBM predicts that there were up to 12 days at the L-AWS when the surface consisted of superimposed ice or glacier ice, these data suggest an average positive degree-day factor of only 1.4 mm WE d^{-1} $°C^{-1}$. This is very low compared with values suggested in the literature, which range from 5.5 to 13.8 mm WE d^{-1} $°C^{-1}$, and is especially unusual considering that the relationship shown by Braithwaite (1994, Figure 5) predicts a value of 13 to 14 mm WE d^{-1} $°C^{-1}$ for the observed summer mean temperature at John Evans Glacier. It is not clear whether the low degree-day factor calculated from the L-AWS is correct, and given the lack of data to address this problem, there is little choice but to assign a constant value of 6.3 mm WE d^{-1} $°C^{-1}$ to the degree-day factor for ice and superimposed ice, based on measurements made by Braithwaite (1981) in the Canadian high Arctic. Given that the melt season at John Evans Glacier in 1996 was short, and few areas of the glacier were snow-free for very long, errors in the degree-day factor for ice should not greatly affect overall calculations of summer mass balance. However, since in other years, superimposed ice and glacier ice are exposed at the surface for longer periods of time than during the 1996 melt season, the problem of determining accurate degree-day factors for ice needs to be addressed in the future.

5.57 Comparison of Degree-Day and Energy Balance Model Simulations for the 3 AWS's

To test the positive degree-day factor parameterization developed in Section 5.56, the

degree-day model was run for each of the 3 AWS's. Results from the degree-day model are compared with results from the energy balance model, and with measured snow water equivalence from UDG data (see Section 4.63 for description of converting UDG data to water equivalence values). All of these simulations use hourly air temperature and precipitation data collected at each of the respective weather stations. The energy balance simulation uses the "standard configuration" described in Chapter 4. Since the degree-day factor parameterization was developed using snow melt data, these simulations show changes in snow water equivalence only. Model simulations were therefore stopped once the snowpack was removed. At each of the 3 AWS's, degree-day simulations were carried out both with a constant degree-day factor for snow of 3.0 mm d^{-1} C^{-1} (labelled "Constant DDF" in Figure 5.12), and a degree-day factor for snow calculated using Equation 5.6 (labelled "Variable DDF" in Figure 5.12).

At all sites, the degree-day simulations using a variable degree-day factor predicted measured snow ablation more closely than degree-day simulations using a constant degree-day factor, since variable degree-day factor simulations had a lower standard and absolute error than simulations using constant degree-day factors (Figure 5.12; Tables 5.10-5.12). The degree-day model, using a variable degree-day factor, was able to simulate the patterns in measured snow ablation at each of the weather station sites, as shown by the higher coefficient of determination for variable degree-day factor simulations compared with energy balance simulations. The possible exception to this was at the L-AWS where the energy balance simulation better predicted the timing of snow melt.

5.58 Comparison of Degree-Day Simulations for John Evans Glacier

In this section, the degree-day model is used to simulate mass balance for all of John Evans Glacier. All degree-day simulations are compared with ablation stake data from John Evans Glacier. Alert and TCA data are used as inputs, and the model is run with both constant and variable degree-day factors. All simulations are run for the full period of instrumental record at the M-AWS, and therefore include melt of superimposed ice and glacier ice. TCA and Alert simulations are adjusted by -1.08°C to correct them for

conditions at John Evans Glacier. Table 5.13 summarizes the simulations discussed in this section.

Simulations using local data from John Evans Glacier performed better than simulations using remote data (Figure 5.13 and 5.15; Table 5.14). Of the simulations which used local data, JEG #1 (constant positive degree-day factor for snow of 3.0 mm WE d^{-1} $°C^{-1}$) provided the closest prediction of average specific mass balance (0.13 m WE compared with 0.15 m WE measured value). Simulations using variable positive degree-day factors for snow (JEG #3) had a higher coefficient of determination than JEG #1 simulations, and improved mass balance simulations below 600 m elevation (Figure 5.13 a), but over-predicted melt (average specific mass balance for JEG #3 was 0.06 m WE).

Using variable degree-day factors instead of a constant degree-day factor for snow had the effect of lowering the predicted mass balance for the TCA and Alert simulations, particularly at lower elevations. Mass balance simulations using remote data and a constant degree-day factor of 4.0 mm WE $d^{-1}°C^{-1}$ (TCA #1 and Alert #1) were nearly identical (average specific mass balance of 0.29 m WE). However, when variable degree-day factors were used (TCA #2 and Alert #2), the average specific mass balance dropped from 0.29 m WE to 0.20 m WE for Alert #2, but only to 0.27 m WE for TCA #2. The TCA and Alert datasets predict similar total positive degree-days, and the main difference between these 2 datasets was the distribution of positive degree-days throughout the melt season: the Alert #2 simulation was driven by Alert air temperatures whose trend varied throughout the season, while the TCA #2 simulation was driven by temperatures predicted from a cosine function which smoothed out any natural air temperature variations. The fact that using a variable degree-day factor had a greater affect upon the Alert simulation than the TCA simulation suggests that the temporal distribution of positive degree-days through the season affects overall mass balance predictions when using variable degree-day factors. During periods of especially warm temperatures, as predicted from the Alert dataset, melt rates increased the free water content at the surface, increasing the effective grain size. Under such conditions, due to the relationship described by Equation 5.6, the variable degree-day factor would also increase rapidly. Therefore, using the method of

variable degree-day factors described in this paper, it makes a difference whether positive degree-days are concentrated within a few select weeks or days (which is the case in reality), or whether positive degree-days are distributed evenly throughout the melt season (which is the case for a method which approximates air temperature based on a cosine curve, such as the TCA method).

5.59 Comparison with Energy Balance Model

Assuming ablation stake data are correct, the degree-day model was able to provided better estimates of the mass balance of John Evans Glacier for the summer of 1996 than the energy balance model described in Chapter 4. The average specific mass balance from ablation stake data was 0.15 m WE. The average specific mass balance using the energy balance model was 0.016 m WE (Table 4.9, Chapter 4) compared with 0.13 m WE using the degree-day model with a constant degree-day factor for snow of 3.0 mm WE d^{-1} $°C^{-1}$ (run JEG #2). However, the use of variable degree-day factors (run JEG #3) brought the degree-day prediction of average specific mass balance (0.06 m WE) closer to the value predicted by the energy balance model (0.016 m WE). Therefore, if the energy balance model provided an estimate mass balance which was more accurate than the ablation stake data, then the degree-day simulations using a variable degree-day factor performed better than the degree-day simulation using a constant degree-day factor for snow of 3.0 mm WE d^{-1} $°C^{-1}$.

5.6 Comparison with Other Studies

Of all degree-day studies, only Braithwaite (1994) has considered the variability of positive degree-day factors with meteorological and surface conditions over a glacier. Braithwaite found that degree-day factors over the Greenland ice sheet varied with mean temperature, surface albedo and turbulence. In the present study, no relationship could be found between mean temperature and degree-day factors. However, a relationship was found between effective grain size, one of the main controls on surface albedo, and degree-day factors. The parameterization developed in this paper relates increases in effective grain size (which decreases surface albedo) to increases in degree-day factors.

This is in agreement with Braithwaite's finding that degree-day factors increase with a decrease in surface albedo. It is also in agreement with a recent study by Vincent and Vallon (1997), who examined the relationship between long-term historical mass balance records and climatic data. They found that, in establishing the empirical relation between mass balance fluctuations and climatic variation, it was impossible to ignore glacier surface conditions. Surface albedo was shown to be an important parameter in relating ablation to mass balance via positive degree-days.

The majority of degree-day model simulations for Arctic glaciers and ice sheets have focused on predicting mass balance responses to climate change (e.g. Braithwaite and Olesen, 1990; Laumann and Reeh, 1993; Bøggild *et al.*, 1994; van de Wal, 1996). All of these studies have assumed constant positive degree-day factors in predicting surface melt from positive degree-days. If the relationship between historical mass balance and climatic data was sensitive to surface characteristics such as surface albedo, as suggested by Vincent and Vallon (1997), it seems likely that future mass balance fluctuations might also be sensitive to surface conditions. This seems especially likely given that climatic changes due to an increase in atmospheric CO_2 are predicted to change the climate of the high Arctic more rapidly than in the recent historical past (Hansen *et al.*, 1981; Cao *et al.*, 1992; Manabe *et al.*, 1992; McGinnis and Crane, 1994; Lynch *et al.*, 1995), and rapid increases in air temperature would likely alter the surface conditions on polar glaciers and ice sheets.

Variable degree-day factors provide a means of incorporating important feedback mechanisms into degree-day mass balance simulations which examine the effects of climate change on glaciers and ice sheets. Several degree-day simulations tested under various climate change scenarios have considered the effect of an increase or decrease in accumulation through time on the mass balance of polar glaciers and ice sheets (e.g. Braithwaite and Olesen, 1990; Bøggild *et al.*, 1994). The use of a variable degree-day factor algorithm, which considers grain size variations after a new snowfall, would allow for the incorporation of the albedo feedback mechanism into degree-day models, since snow grain size is a major control on surface albedo. A rise in air temperatures could lead

to more rapid melt at the surface, increasing the free water content of the snow and increasing effective grain size. This would lower surface albedo and increase degree-day factors, leading to a more rapid removal of the snowpack and exposing glacier ice more quickly than normal. Such models would not only be sensitive to the quantity of accumulation in a given year, but would also be sensitive to the timing and frequency of snowfall events.

5.7 Conclusions

Degree-day model simulations for John Evans Glacier provided more accurate predictions of the average specific mass balance of John Evans Glacier, assuming data from a limited ablation stake network are correct. Degree-day simulations using a constant degree-day factor for snow (3.0 mm WE $d^{-1}°C^{-1}$) and for ice and superimposed ice (6.3 mm WE $d^{-1}°C^{-1}$) produced the best estimates of measured mass balance. Using a variable degree-day factor improved the model's ability to simulate spatial variations in measured ablation, especially in the lower ablation zone.

This paper has tested a degree-day model for John Evans Glacier using both on-site and remote air temperature data. Simulations using on-site data provided much better estimates of the mass balance of John Evans Glacier for the summer of 1996 than simulations driven by remote data. If only remote data are available to drive glacier mass balance simulations using a degree-day model, the best approach is to apply a correction factor to the remote data to account for difference in climatic conditions between the different locations. Simulating air temperature using a cosine function substantially decreases model performance when degree-day factors are calculated as a function of effective grain size. This suggests degree-day models which use variable degree-day factors must not only predict total seasonal positive degree-days, but they must also simulate temporal variations in positive degree-days.

Met. Station Name	Latitude	Longitude	Elevation (m a.s.l.)
L-AWS	79°37'52"	74°04'38"	261
M-AWS	79°40'17"	74°20'59"	824
U-AWS	79°42'35"	74°33'20"	1183

Table 5.1: Location and elevation of each automatic weather station.

Station	Start of Hourly Measurements	End of Hourly/ Start of Daily Measurements	End of Daily Measurements
L-AWS	JD 172, 1996	JD 212, 1996	JD 143, 1997
M-AWS	JD 167, 1996	JD 202, 1996	JD 144, 1997
U-AWS	JD 169, 1996	JD 216, 1996	JD 144, 1997

Table 5.2: Time periods during which hourly and daily meteorological observations were made at each AWS.

Weather Station	r^2	p-value
L-AWS	-0.0006	<0.01
M-AWS	-0.3	0.01
U-AWS	-0.004	0.09

Table 5.3: Coefficients of determination and significance levels (p-value) between Alert data and each of the John Evans Glacier weather stations for the period of JD 177 to JD 202.

Weather Station	Total degrees of freedom	Computed F	p-value	Critical F
L-AWS	1245	0.13	0.72	3.85
M-AWS	1245	0.72	0.40	3.85
U-AWS	1245	149.55	<0.01	3.85

Table 5.4: Analysis of variance table comparing means air temperatures at each of the John Evans Glacier weather stations with mean air temperature at Alert for the period of JD 177 to JD 202.

	Average Lapse Rate (°C m^{-1})	Standard Deviation
L-AWS to M-AWS	-0.000621	0.0039
M-AWS to U-AWS	-0.00565	0.0049

Table 5.5: Average and standard deviation of lapse rates determined from measured hourly air temperatures on John Evans Glacier. Negative lapse rates indicate a increase in temperature with increasing elevation.

	Alert (Method #1)	Alert (Method # 2)	TCA (Method # 1)	TCA (Method # 2)
n	960	960	960	960
Total Observed	1897.1	1897.1	1897.1	1897.1
Total Calculated	2332.0	2415.0	1651.8	2098.6
Coefficient of Determination	0.88	0.92	0.90	0.94
Seasonal Difference	0.18	0.04	0.49	0.18
Standard Error	224.63	182.33	143.77	135.98
Absolute Error	0.22	0.05	0.97	0.23

Table 5.6: Statistical attributes comparing the patterns in predicted positive degree-days through time using remote data with those using local data from the L-AWS for the period of JD 177 - 202.

Coefficient of Determination = $\left[\sum(x_o - \bar{x}_o)^2 - \sum(x_c - x_o)^2\right] / \sum(x_o - \bar{x}_o)^2$

Seasonal Difference = $\left[\sum(x_o - x_c)\right] / \sum(x_o)$

Standard Error = $\left[\sum(x_c - x_o)^2 / n\right]^{0.5} / \bar{x}_o$

Absolute Error = $\sum(x_o - x_c) / n\bar{x}_o$

where x_c is the calculated value, x_o is the observed value, $\bar{x}$ is the mean value, and n is the total number of observations

Station	Average Degree-Day Factor for Snow	Coefficient of determination	p-value
L-AWS	3.58	0.27	0.007
M-AWS	1.35	0.05	0.28
U-AWS	1.99	0.31	0.02

Table 5.7: Average degree-day factors for snow melt at the 3 AWS sites (units are mm WE d^{-1} $°C^{-1}$), and the coefficient of determination and p-value between ablation and positive degree-days at each weather station.

Degree-Day Factor for Snow	Location	Reference
5.4	Gr. Aletschgletscher	Lang and others (1976)
3.0	Franz Josef Glacier	Woo and Fitzharris (1992)
5.7	Satujokull	Johannesson and others (1993)
4.4	Nigardsbreen	Johannesson and others (1993)
4.5	Ålfotbreen	Laumann and Reeh (1993)
4.0	Nigardsbreen	Laumann and Reeh (1993)
3.5	Hellstugubreen	Laumann and Reeh (1993)

Table 5.8: Positive degree-day factors for snow ablation on glaciers. Units are mm WE d^{-1} $°C^{-1}$. Reproduced from Braithwaite (1994).

	L-AWS		M-AWS		Combined L-AWS and M-AWS		U-AWS	
	r^2	SE	r^2	SE	r^2	SE	r^2	SE
vis	0.50	0.179	0.58	0.017	0.47	0.013	-0.07	0.72
nir	0.14	0.522	0.14	0.218	0.14	0.188	-0.07	0.72
vis & nir	0.57	0.171	0.74	0.017	0.47	1.57	-0.07	0.72

Table 5.9: Correlation coefficients (r^2) and standard errors for relationship between visible (vis) and near-infrared (nir) effective grain radii as predicted by the EBM, and solved positive degree-day factors at each of the weather stations. SE is the standard error, and vis & nir refers to a multiple regression of the both effective grain radii datasets with positive degree-day factors.

	EB	Variable DDF	Constant DDF
n	864	864	864
Observed Final Julian Day with Snow	193	193	193
Calculated Final Julian Day with Snow	195	189	207
Mean Observed Specific Mass Balance	0.13	0.13	0.13
Mean Calculated Specific Mass Balance	0.10	0.13	0.10
Coefficient of Determination	0.92	0.94	0.90
Seasonal Difference	0.00	0.00	0.00
Standard Error	0.02	0.01	0.03
Absolute Error	0.00	-0.01	0.00

Table 5.10: Statistical comparison of energy balance (EB) and degree-day simulations at the L-AWS for JD 177 - JD 202. Variable DDF and Constant DDF are degree-day simulations using variable and constant degree-day factors respectively (units are in m WE).

	EB	Variable DDF	Constant DDF
n	817	817	817
Mean Observed Specific Mass Balance	0.26	0.26	0.26
Mean Calculated Specific Mass Balance	0.24	0.24	0.21
Coefficient of Determination	0.85	0.88	0.89
Seasonal Difference	0.00	0.00	0.00
Standard Error	0.01	0.02	0.02
Absolute Error	0.01	0.00	0.01

Table 5.11: Statistical comparison of energy balance (EB) and degree-day simulations at the M-AWS for JD 167 - JD 202. Variable DDF and Constant DDF are degree-day simulations using variable and constant degree-day factors respectively (units are in m WE).

	EB	Variable DDF	Constant DDF
n	864	864	864
Mean Observed Specific Mass Balance	0.28	0.28	0.28
Mean Calculated Specific Mass Balance	0.26	0.27	0.23
Coefficient of Determination	0.28	0.31	0.32
Seasonal Difference	0.00	0.00	0.00
Standard Error	0.02	0.02	0.04
Absolute Error	0.01	0.00	0.01

Table 5.12: Statistical comparison of energy balance (EB) and degree-day simulations at the U-AWS for JD 172 - JD 210. Variable DDF and Constant DDF are degree-day simulations using variable and constant degree-day factors respectively (units are in m WE).

Model Name	Data Source	Positive Degree-Day Factor for Snow
JEG # 1	M-AWS	3.0
JEG # 2	M-AWS	4.0
JEG # 3	M-AWS	Variable (Equation 5.6)
TCA # 1	cosine function using Alert data (Equation 5.1)	4.0
TCA # 2	cosine function using Alert data (Equation 5.1)	Variable (Equation 5.6)
Alert # 1	Alert	4.0
Alert # 2	Alert	Variable (Equation 5.6)

Table 5.13: List of model simulations run to test the degree-day model against measured mass balance from the ablation stakes.

	JEG #1	JEG #2	JEG #3	TCA #1	TCA #2	Alert #1	Alert #2
n	16	16	16	16	16	16	16
Measured Average Specific Mass Balance	0.15	0.15	0.15	0.15	0.15	0.15	0.15
Calculated Average Specific Mass Balance	0.13	0.05	0.06	0.29	0.27	0.29	0.20
Coefficient of Determination	0.52	0.60	0.66	0.63	0.43	0.63	0.52
Seasonal Difference	0.98	0.59	0.34	1.63	1.72	1.31	1.72
Standard Error	0.10	0.11	0.15	0.02	0.05	0.02	0.07
Absolute Error	0.00	0.00	0.00	-0.07	0.01	-0.07	-0.04

Table 5.14: Statistical attributes of comparisons between degree-day simulations and observed mass balance data from ablation stakes. Units are in m WE.

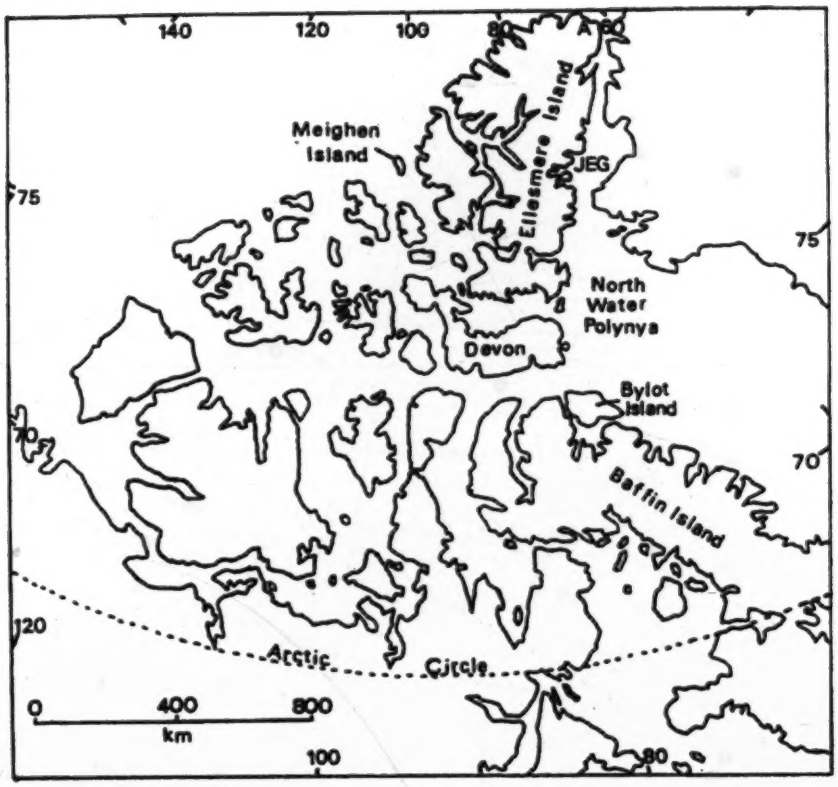

Figure 5.1: The Canadian Arctic Islands. JEG = John Evans Glacier, A = AES Meteorological Station at Alert.

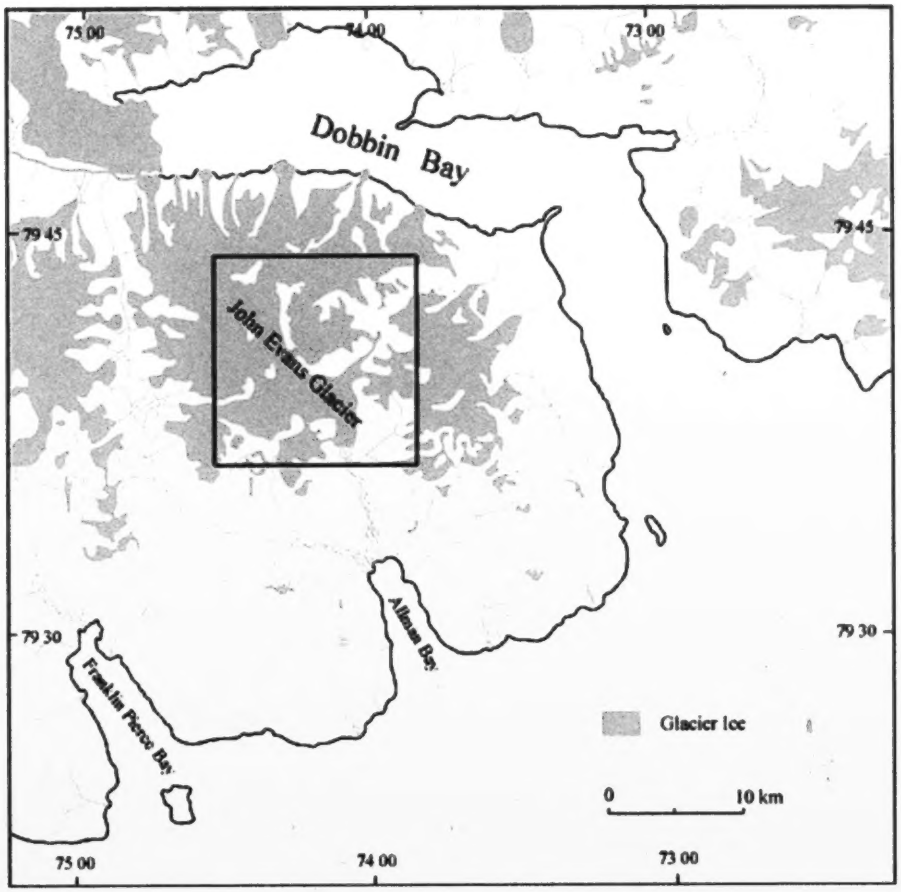

Figure 5.2: Location of John Evans Glacier, Ellesmere Island, Nunavut, Canada.

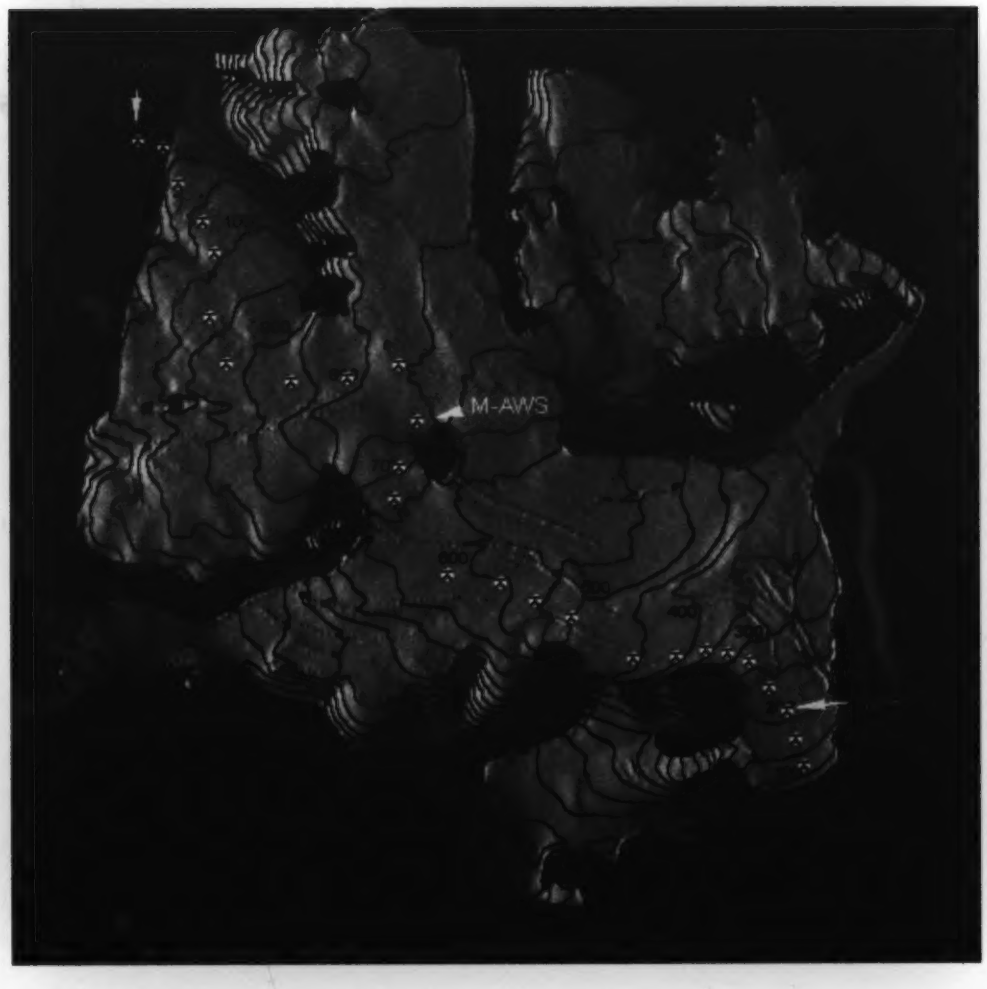

Figure 5.3: Contour map of John Evans Glacier with locations of lower, middle and upper automated weather stations (marked with arrows) and stake locations (marked with circles).

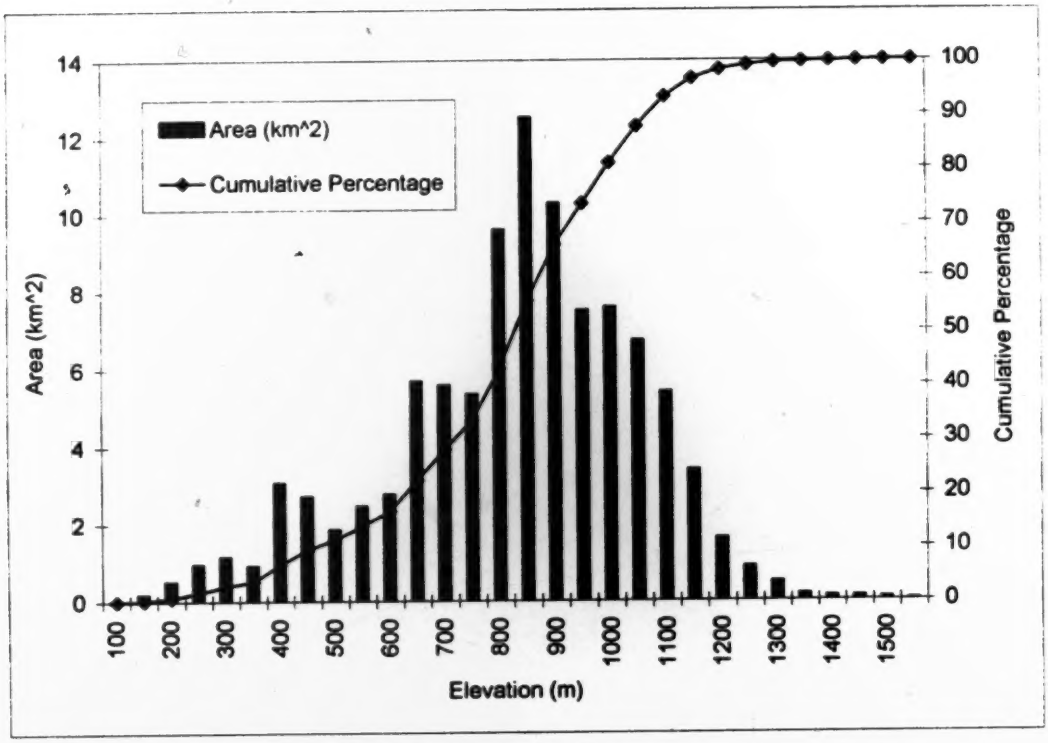

Figure 5.4: Surface area distribution of John Evans Glacier.

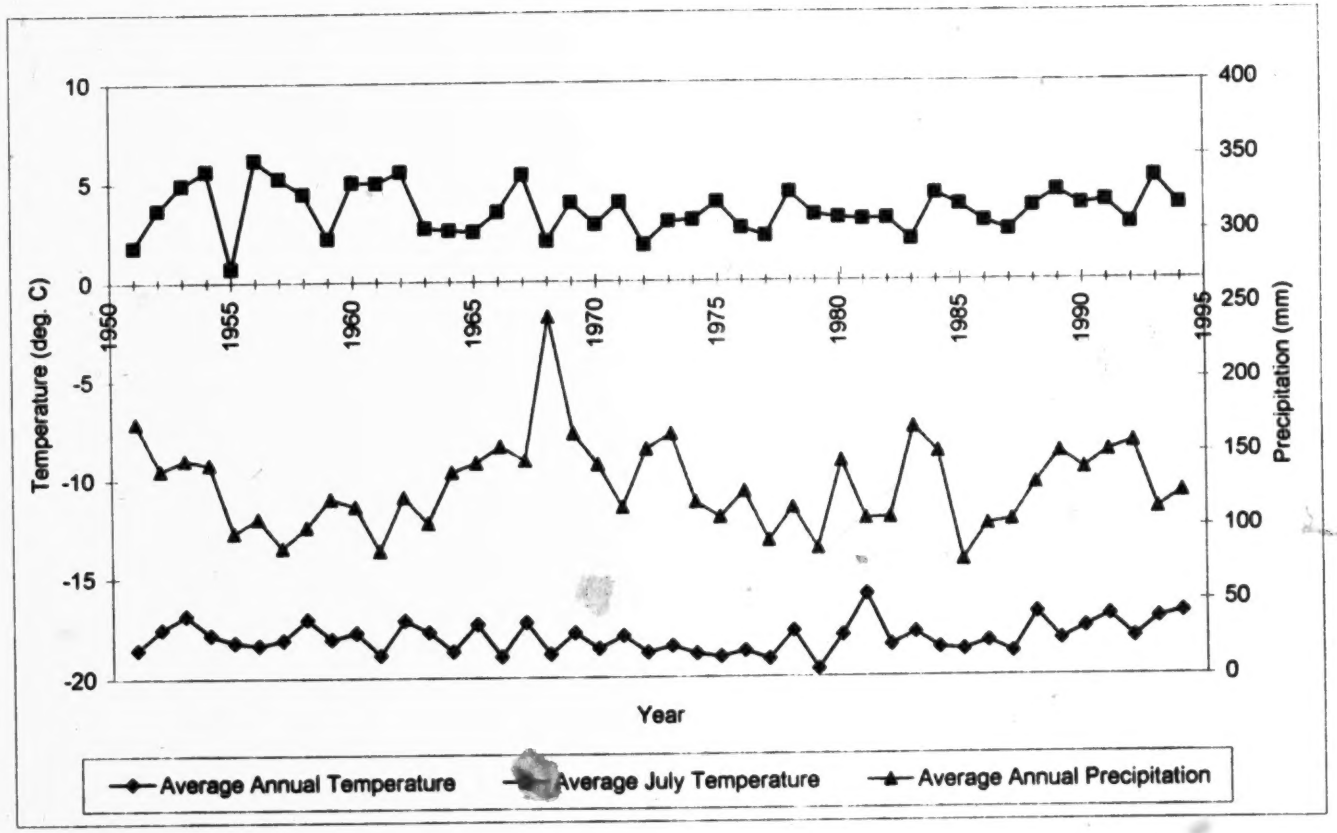

Figure 5.5: Temperature and precipitation records from AES meteorological station, Alert.

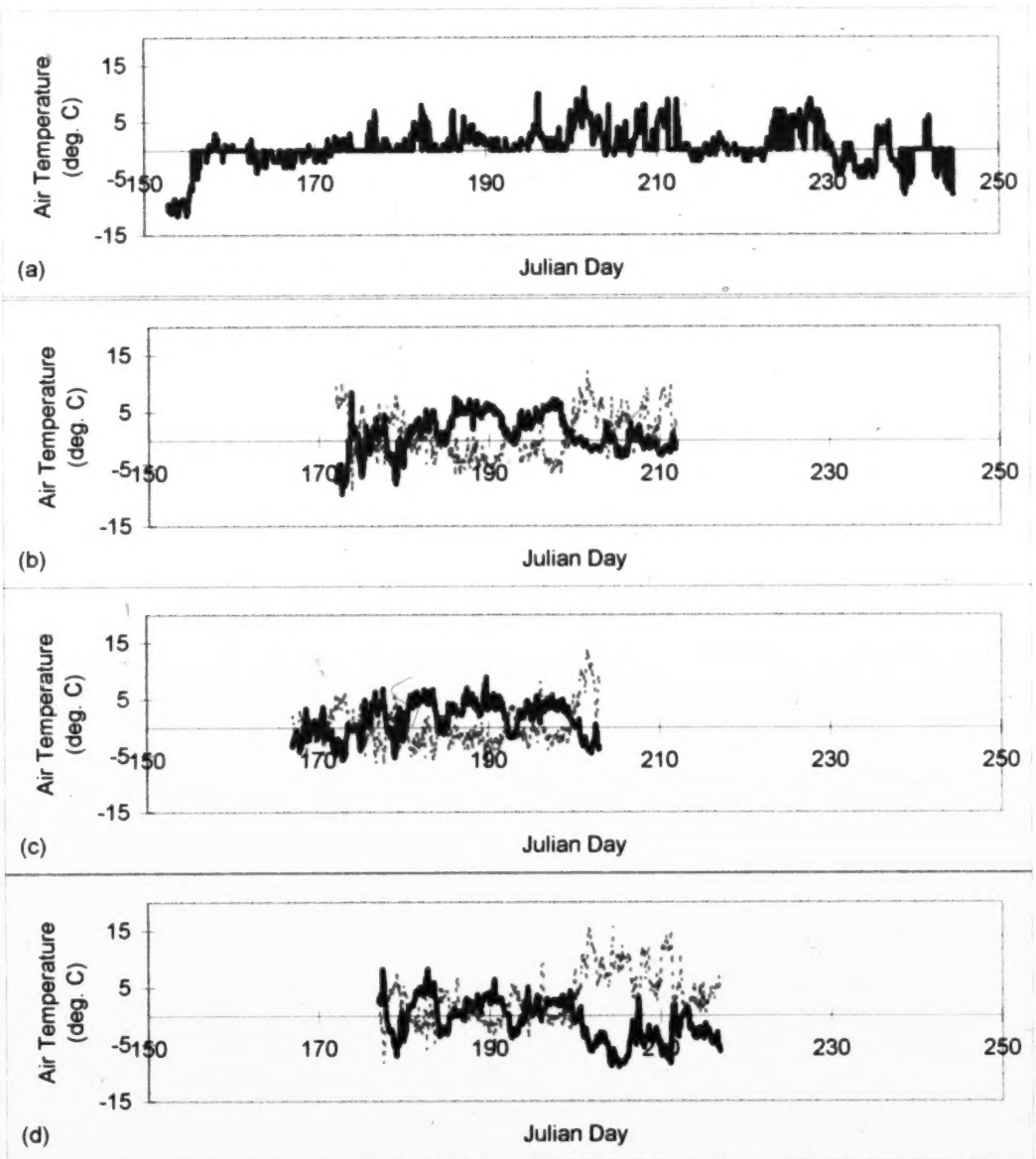

Figure 5.6: (a) Average hourly air temperatures measured at (a) Alert weather station, (b) L-AWS, (c) M-AWS and (d) U-AWS. Graphs (b), (c) and (d) show measured air temperature (solid black line) and the difference between Alert air temperature and that measured at the weather station (dotted red line).

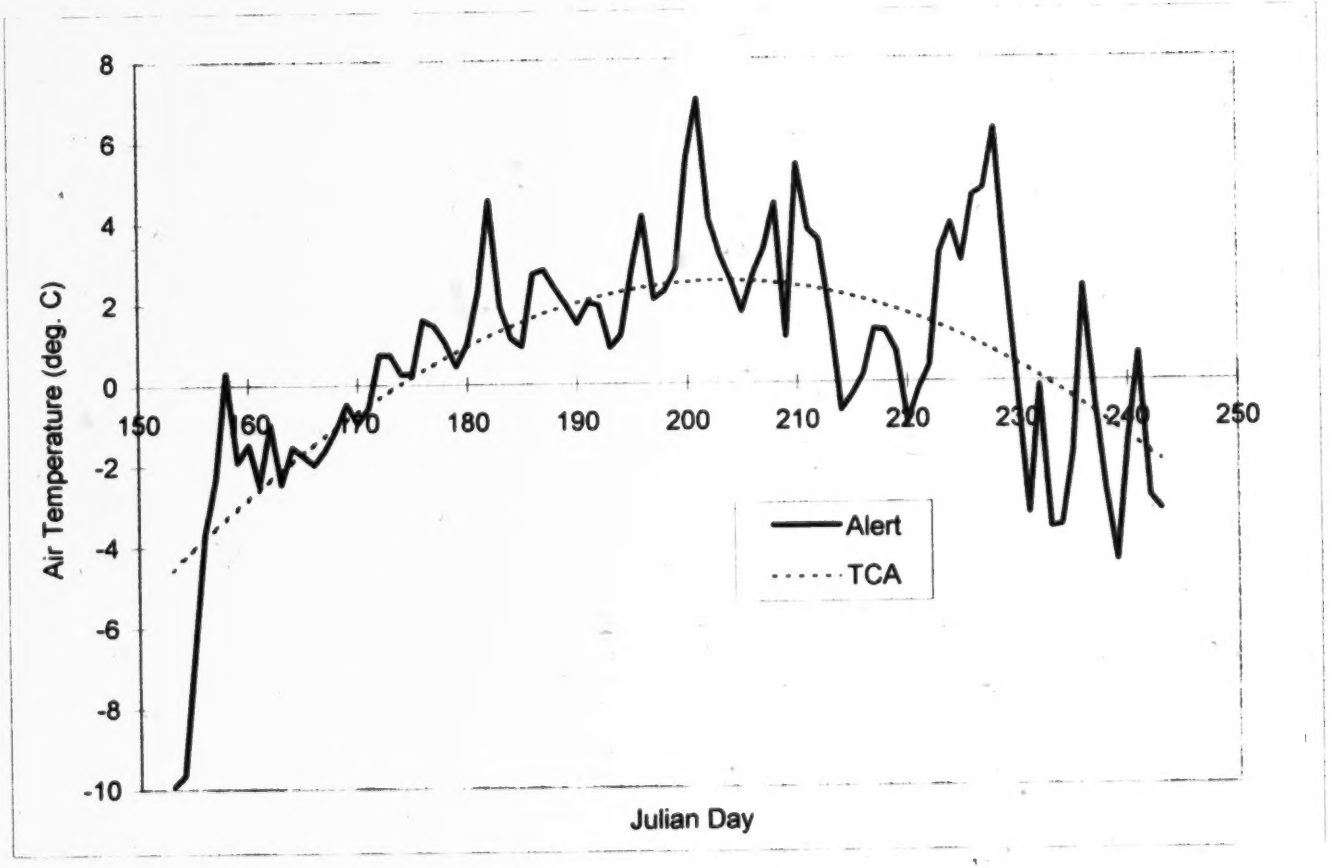

Figure 5.7: Comparison of predicted daily air temperature using cosine function (TCA Equation) and measured daily average air temperature at Alert.

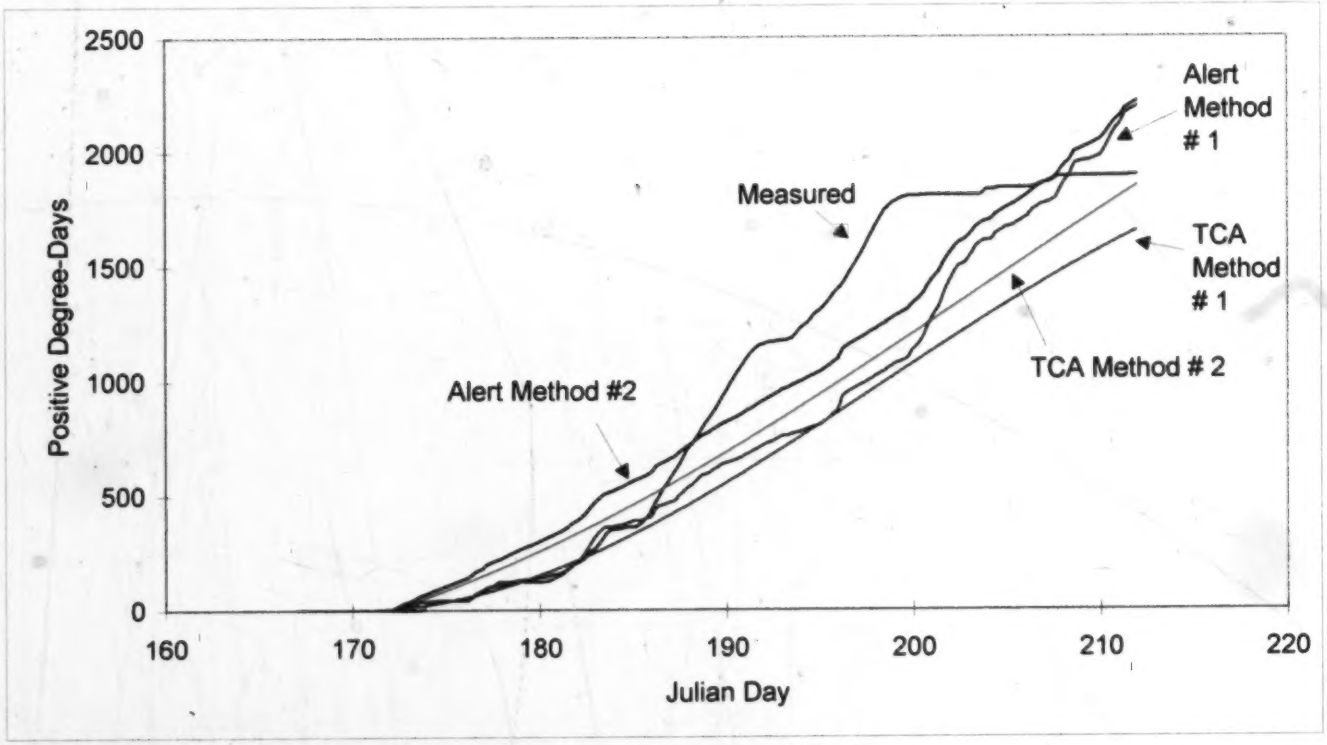

Figure 5.8: Measured and predicted positive degree-days at the L-AWS.
(See text for description of different simulations).

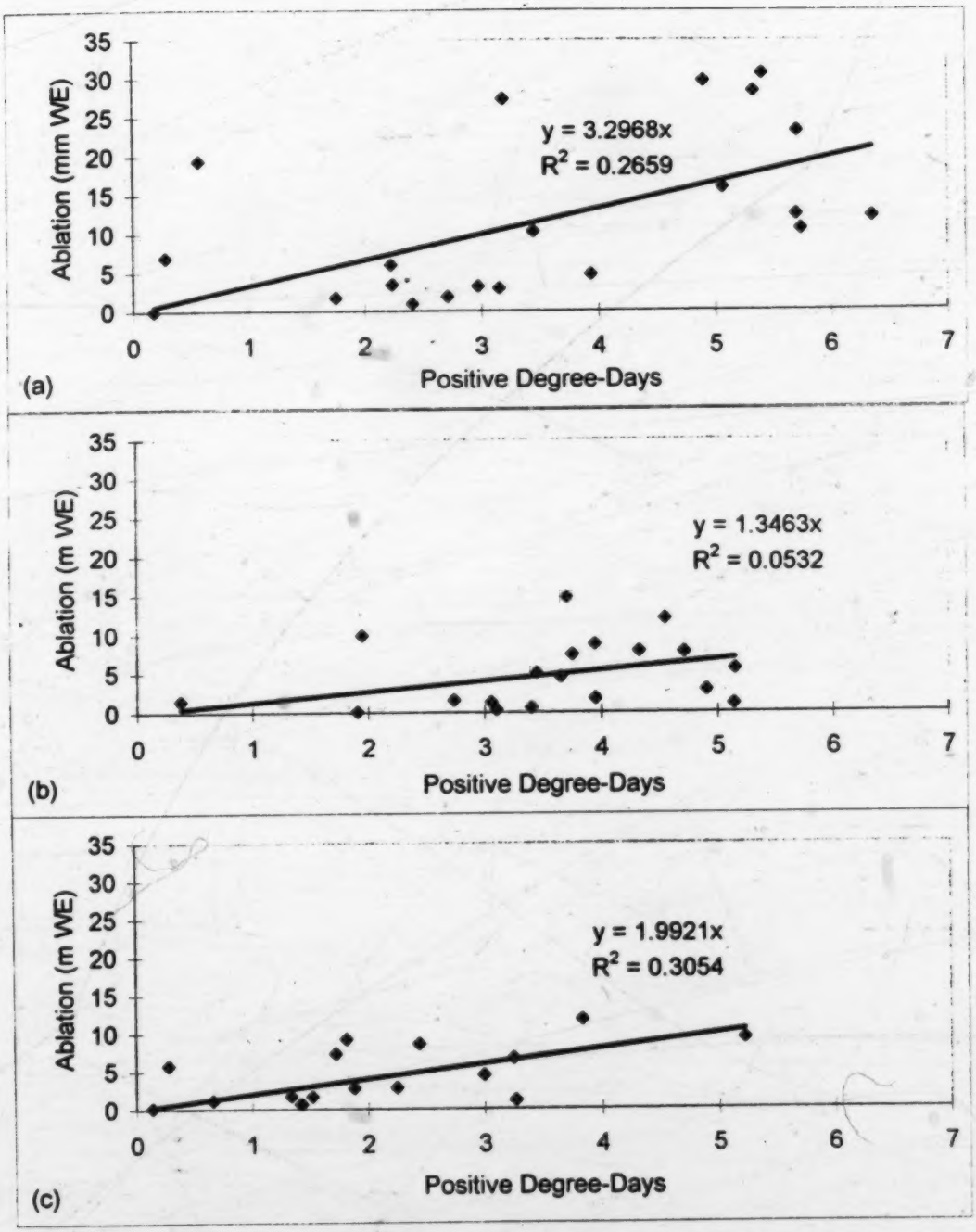

Figure 5.9: Total daily ablation for snow versus positive degree-days at each of the weather stations. (a) L-AWS; (b) M-AWS; (c) U-AWS.

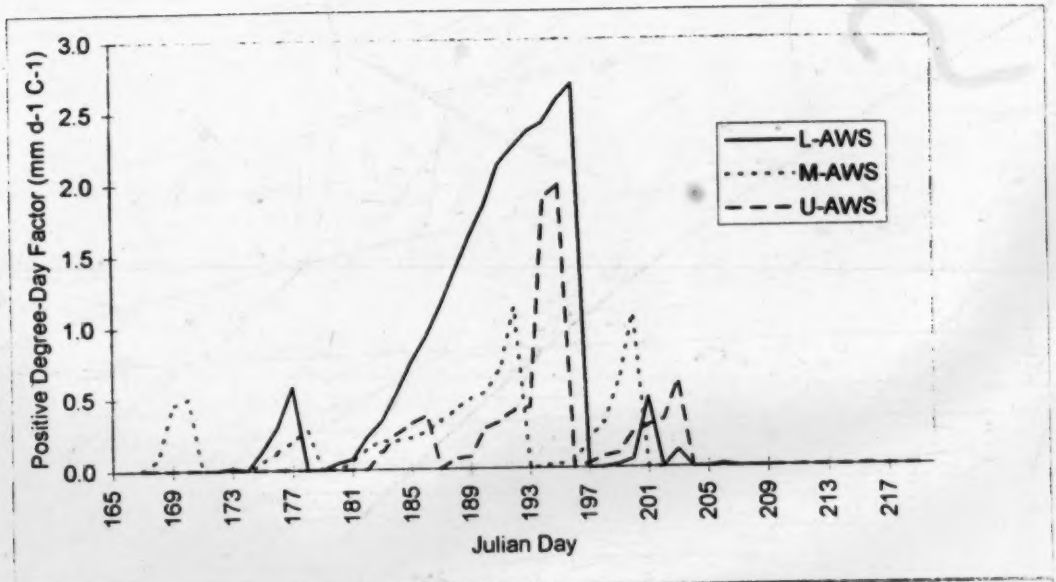

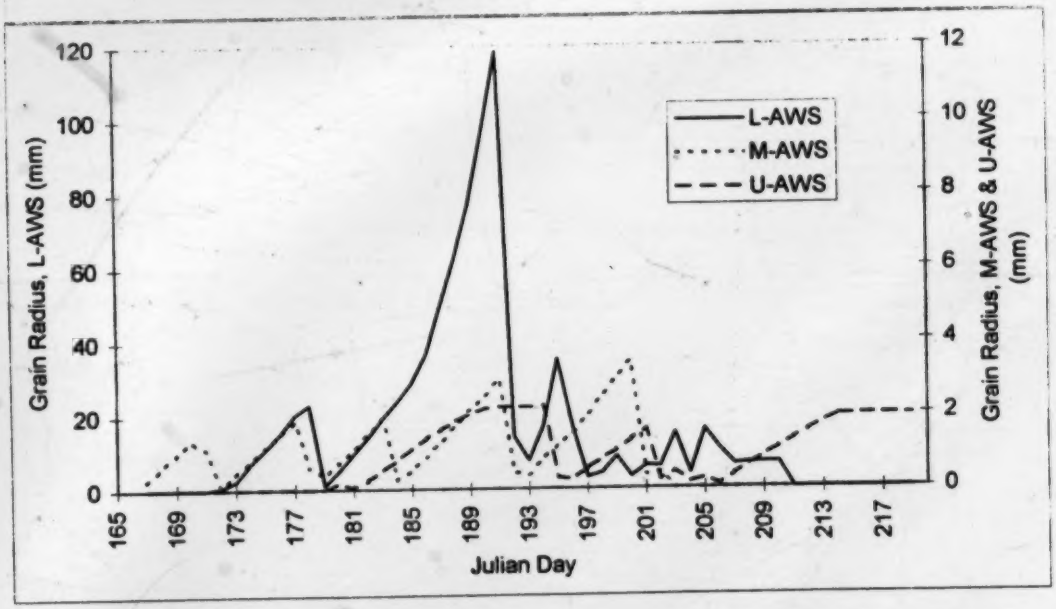

Figure 5.10: (a) Predicted positive degree-day factors for snow at the 3 weather stations.
(b) Predicted effective grain radii at the 3 weather stations.

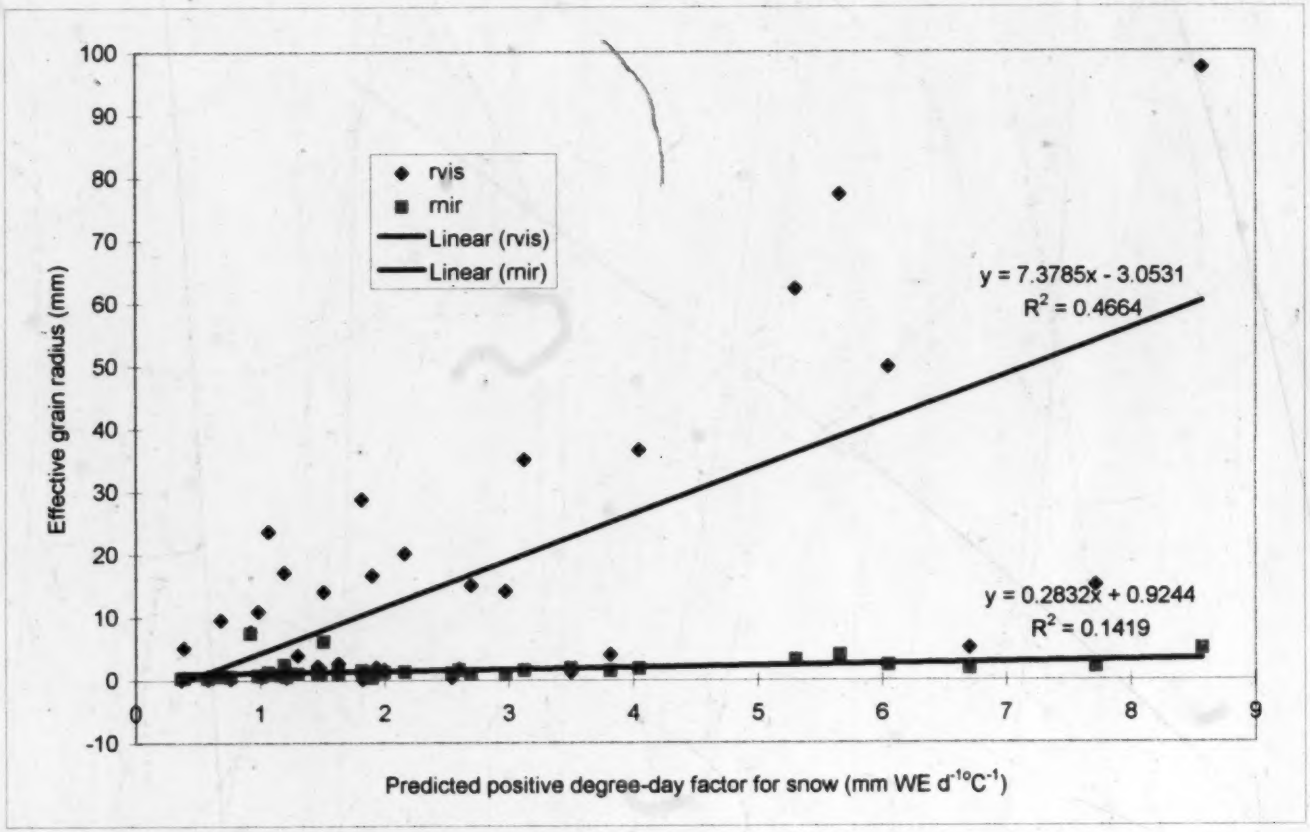

Figure 5.11: Effective visible and near-infrared grain radii versus predicted positive degree-day factors for snow, using combined data from the L-AWS and M-AWS.

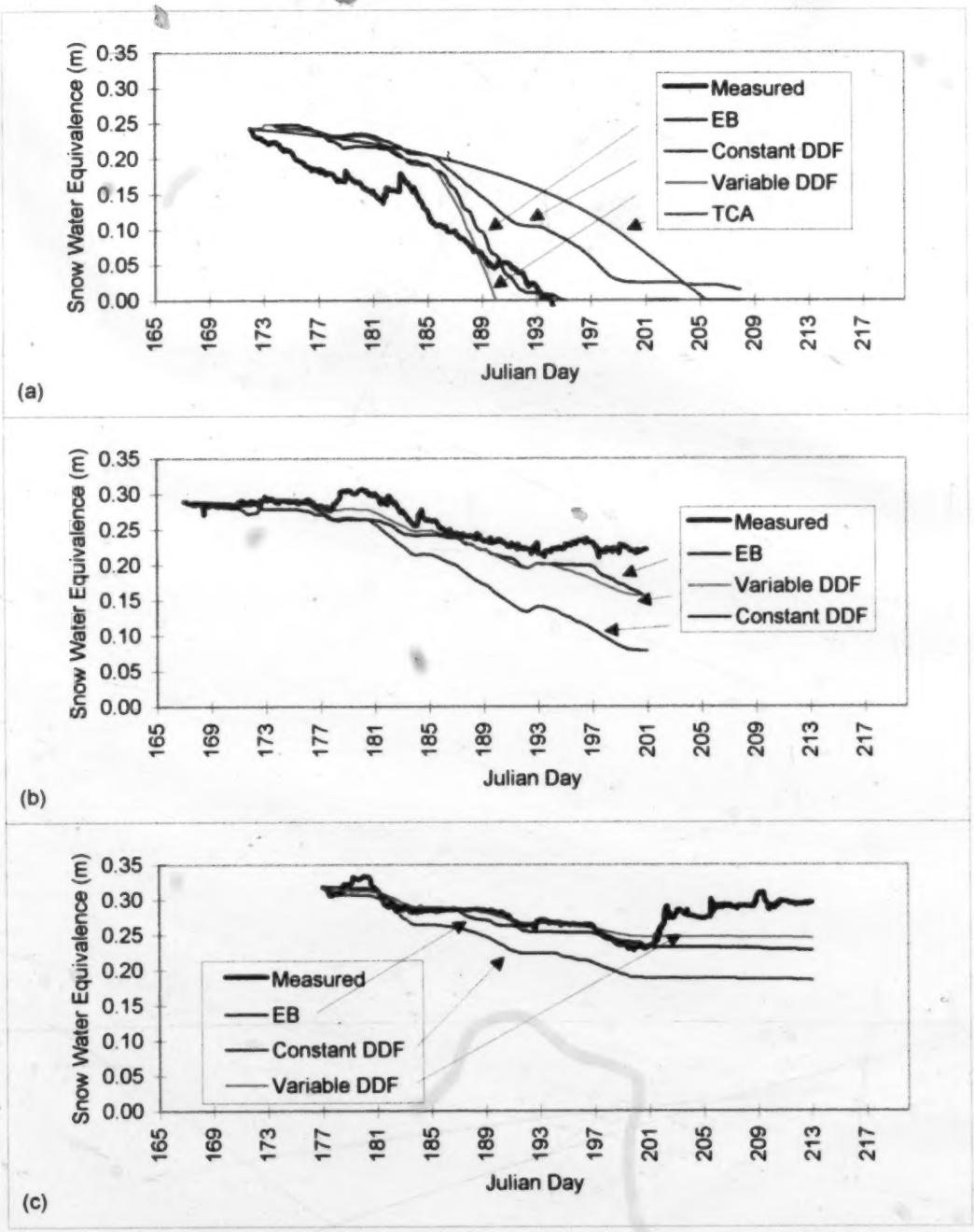

Figure 5.12: Comparison of degree-day model simulations at each of the weather station sites. (a) L-AWS; (b) M-AWS; (c) U-AWS.

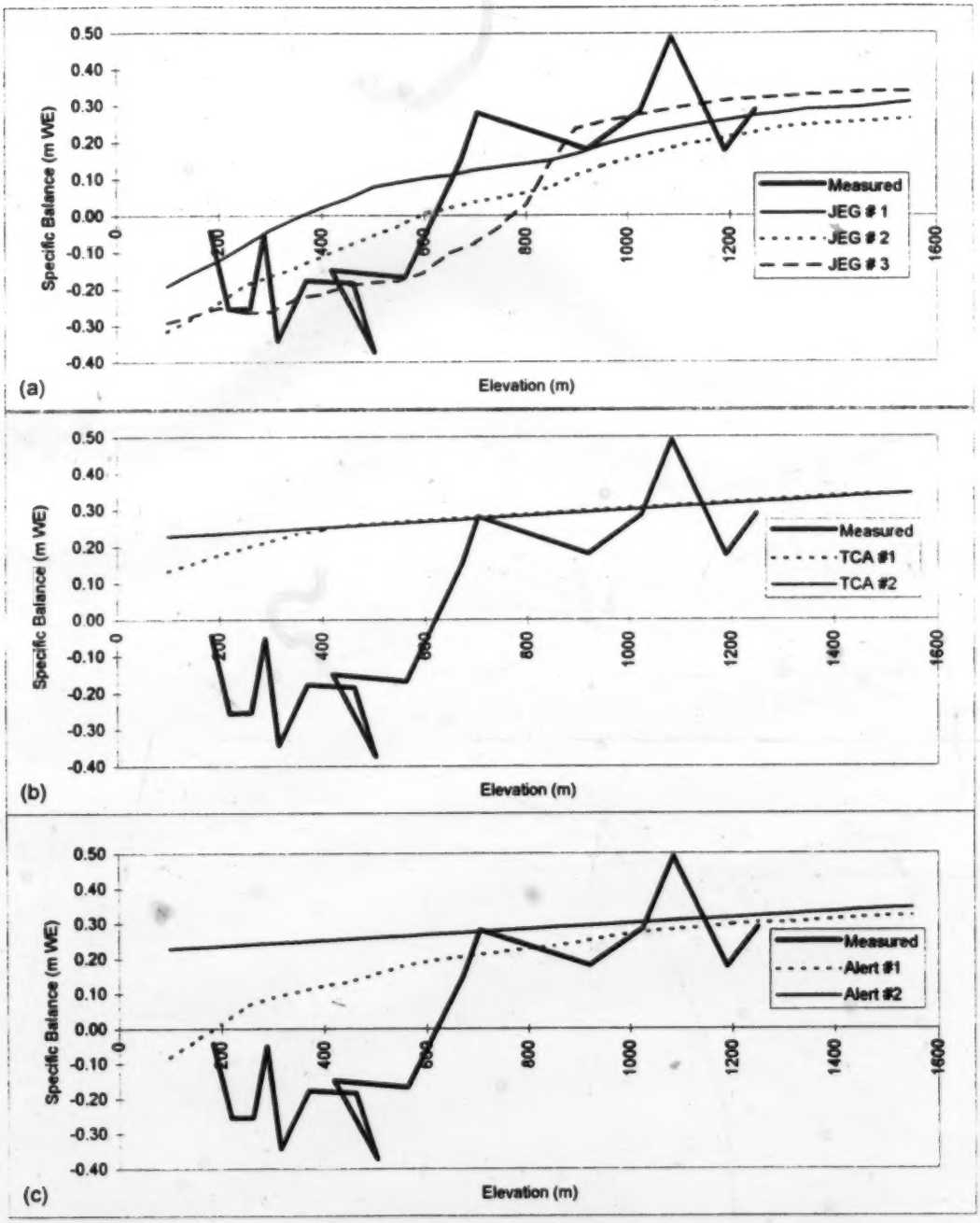

Figure 5.13: Comparison of specific mass balance predictions from degree-day calculations with measured mass balance from ablation stakes. (a) Degree-day simulations with local (John Evans Glacier) air temperature data. (b) Simulations with remote (Alert) data, modelled with TCA Equation. (c) Simulations with remote (Alert) data.

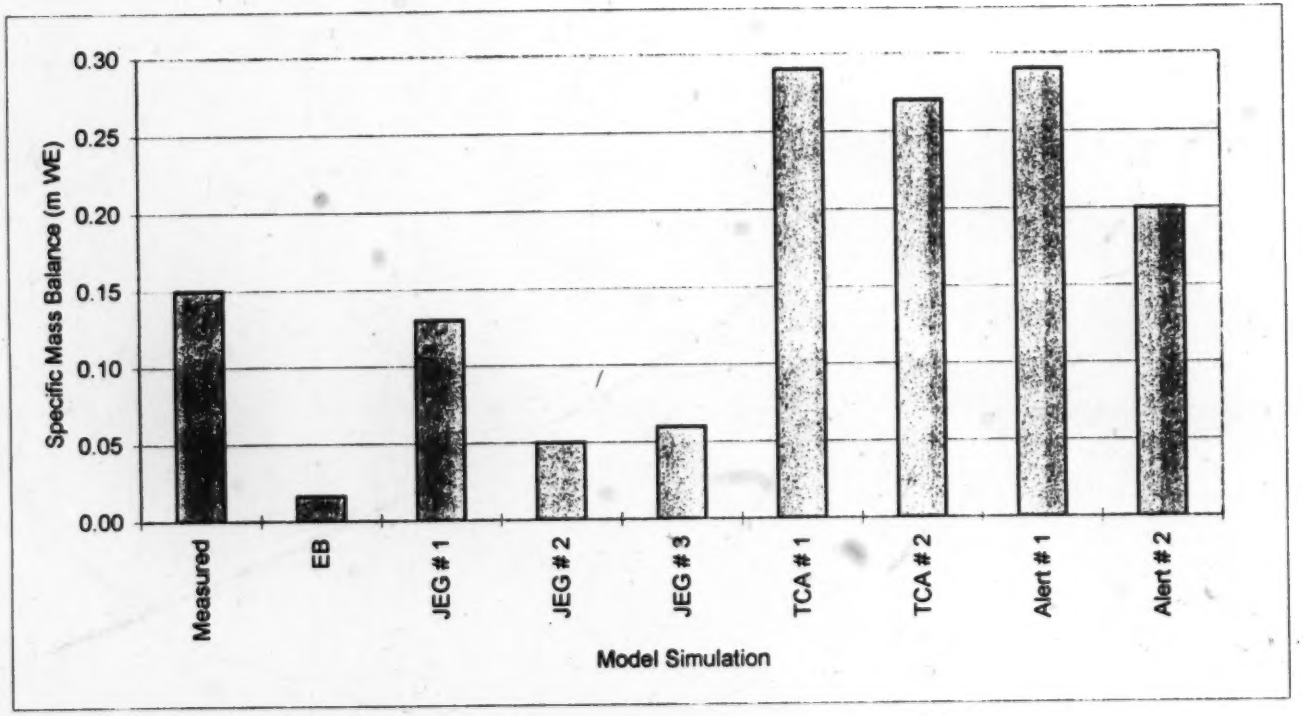

Figure 5.14: Average specific mass balance for various degree-day model simulations. (see text for description of model runs).

5.8 References

Bøggild, C.E., Reeh, N., and Oerter, H. 1994. Modelling Ablation and Mass-Balance sensitivity to Climate Change of Storstrømmen, Northeast Greenland. *Global and Planetary Change*. 9: 79-90.

Braithwaite, R.J. 1981. On glacier energy balance, ablation, and air temperature. *Journal of Glaciology*. 27(97), 381-391.

Braithwaite, R.J. 1994. Positive degree-day factors for ablation on the Greenland Ice Sheet studied by energy-balance modelling. *Journal of Glaciology*, 40(135): 153-160.

Braithwaite, R.J. and Thomsen, H.H. 1984. Runoff conditions at Paakitsup Ajuliarusersua, Jakobshaven, estimated by modelling. *Gronlands Geol. Unders. Gletscher-hydrol. meddr*. 84(3): 22 p.

Braithwaite, R.J. and Olesen, O.B. 1990. A simple energy-balance model to calculate ice ablation at the margin of the Greenland Ice Sheet. *Journal of Glaciology*, 36(123): 222-228.

Cao, H.X., Mitchell, J.F.B., and Lavery, J.R. 1992. Simulated Diurnal Range and Variability of Surface Temperature in a Global Climate Model for Present and Doubled CO_2 Climates. *Journal of Climate*, 5: 920-943.

Hansen, J., Johnson, D., Lacis, A., Lebedeff, S., Lee, P., Rind, D., and Russell, G. 1981. Climate Impact of Increasing Atmospheric Carbon Dioxide. *Science*, 213(4511): 957-966.

Huybrechts, P. 1994. The present evolution of the Greenland ice sheet: an assessment by modelling. *Global and Planetary Change*. 9: 39-51.

Johannesson, T., Sigurdsson, O., Laumann, T., and Kennett, M. 1995. Degree-day glacier mass-balance modelling with applications to glaciers in Iceland, Norway and Greenland. *Journal of Glaciology*, 41(138): 345-358.

Jung-Rothenhausler, F. 1993. Prospects for Remote Sensing of the Annual Mass Balance: White Glacier, Axel Heiberg Island, N.W.T., Canada. *Unpublished M.Sc. Thesis*, Watershed Ecosystems Graduate Programme, Trent University, Peterborough, Ontario, Canada. 189p.

Lang, H., Schädler, and Davidson, G. 1977. Hydroglaciological investigations on the Ewigschneefeld - Gr. Aletschgletscher. *Zeitschrift Für Gletscherkunde Und Glazialgeologie*.12(2), 1976: 109-124.

Laumann, T. and Reeh, N. 1993. Sensitivity to climate change of the mass balance of glaciers

in southern Norway. *Journal of Glaciology*. 39(133): 656-665.

Lynch, A.H., Chapman, W.L., Walsh, J.E, Weller, G. 1995. Development of a Regional Climate Model of the Western Arctic. *Journal of Climate*, 8: 1555-1570.

Manabe, S., Spelman, M.J., and Stouffer, R.J. 1992. Transient Responses of a Coupled Ocean-Atmosphere Model to Gradual Changes of Atmospheric CO_2. Part II: Seasonal Response. *Journal of Climate*, 5: 105-126.

McGinnis, D.L. and Crane, R.G. 1994. A Multivariate Analysis of Arctic Climate in GCMs. *Journal of Climate*, 7: 1240-1250.

Reeh, N. 1991. Parameterization of melt rate and surface temperature on the Greenland Ice Sheet. *Polarforschung*, 59(3): 113-128.

van de Wal, R.S.W. 1996. Mass-balance modelling of the Greenland ice sheet: a comparison of an energy-balance and a degree-day model. *Annals of Glaciology*. 23: 36-45.

Vincent, C. and Vallon, M. 1997. Meteorological controls on glacier mass balance: empirical relations suggested by measurements on glacier de Sarennes, France. *Journal of Glaciology*. 43(143): 131-137.

Woo, M.-k. and Fitzharris, B.B. 1992. Reconstruction of mass balance variations for Franz Josef Glacier, New Zealand, 1913-1989. *Arctic and Alpine Research*. 24(4): 281-290.

Woodward, J. 1995. Superimposed ice and glacier mass balance. *Unpublished M.Sc. Thesis*. University of Alberta. 96p.

Chapter 6: General Discussion and Conclusions

6.1 Surface Energy Balance Models for High Arctic Glaciers

The surface energy balance model described in this thesis (EBM-96) produced mass balance predictions that were substantially closer to measured mass balance data than the previous version of the model (EBM-94). EBM-96 predicted an average specific mass balance of 0.016 m WE, compared with a values of -0.283 m WE predicted by EBM-94.

This study suggests that surface albedo plays an important role in surface energy balance calculations, supporting findings made by numerous other workers (e.g. Munro, 1990; Paterson, 1994; Knap and Oerlemans, 1996). The importance of incorporating surface slope and azimuth measurements into surface albedo calculations is of crucial importance in the Arctic. Even small deviations of surface slope from the horizontal were shown to have a large impact on surface albedo, as was found by Grenfell *et al.* (1994) and Wiscombe and Warren (1980).

The approach adopted by Woodward (1995) to predict the maximum thickness of superimposed ice formed on John Evans Glacier produced a very accurate prediction of superimposed ice thickness at the M-AWS. The fact that the heat flux equations upon which Woodward's method was based are able to simulate trends in the near surface ice temperature support the validity of this approach. The Pmax method for predicting superimposed ice (with Pmax = 0.60 as suggested by Reeh, 1991) over-predicted the superimposed ice thickness at the M-AWS. Results suggest a lower value for Pmax (0.47).

6.2 Degree-Day Models for High Arctic Glaciers

An alternative approach has been presented for the determination of positive degree-days. Most degree-day models have simply assigned a constant value to the degree-day factors of snow, superimposed ice or glacier ice. This study has discovered a relationship between effective grain size and positive degree-day factors for snow, allowing degree-day factors to be changed according to surface characteristics. Degree-day simulations using

variable positive degree-day factors provided an accurate estimate of mass balance on John Evans glacier, predicting an average specific mass balance of 0.13 m WE (with a constant degree-day factor for snow of 3.0 mm WE d^{-1} $°C^{-1}$). This prediction was closer to measured mass balance data than the energy balance model prediction, and suggests simple degree-day models may be used to provide as accurate simulations of glacier mass balance as more computationally intensive energy balance models. Degree-day simulations using local data performed better than simulations driven by remote data.

6.3 Wider Implications

This thesis has shown that the present-day mass balance of glaciers and ice sheets in the high Arctic is governed by complex interactions between local climatic conditions and surface characteristics. Surface energy balance and degree-day models which treat glacier surface characteristics as static during the course of a melt season, or as alternating between 2 or 3 phases (such as snow, superimposed ice and glacier ice), may not be accurately predicting the present-day mass balance of glaciers in the Arctic. When applied to simulations of the future effects of global climate on glacier mass balance, such models might not simulate important feedback mechanisms between the surface and the atmosphere. For instance, an increase in air temperature in the Arctic could increase melt rates on high Arctic glaciers, thereby reducing the surface albedo through the effect of meltwater on the effective grain size of snow. This decrease in albedo would force an additional increase in surface melt, and models which do not simulate these processes would not accurately model such an effect.

6.4 Suggestions for Future Work

6.41 Surface Albedo

Because of the strong dependence of surface albedo on effective grain size, substantial improvements to the accuracy of the albedo algorithm developed in this paper could be achieved by improving the grain size algorithm. The grain size algorithm could be improved by obtaining detailed measurements of snow crystal sizes throughout different phases of the melt season. The effects of water on the effective grain size could be

determined through periodic measurements of the free water content of the upper snowpack layers. Albedo measurements during years when superimposed ice and glacier ice are exposed at the surface would help in determining accurate effective grain sizes for these surfaces. Such measurements should be combined with some measure of the dirtiness of the ice surface.

In the future, if albedo measurements are made over a sloping surface, the radiometers should be set up with their cosine collectors aligned parallel to the surface, rather than parallel to the horizon. This would eliminate the need for corrections to measured albedo data which probably introduce errors. Accurate measurements of surface slope are essential to ensure modelled values are properly corrected for the effects of a sloping surface.

6.42 Superimposed Ice Formation

More detailed profiles of near surface ice temperatures would aid in the testing of physically-based superimposed ice algorithms. Ice temperatures should be measured to a depth of at least 14m to determine whether the basic assumption that ice temperatures do not fluctuate below this depth is correct. If not, calculations should be made to a greater depth to allow for seasonal variations in ice temperatures. Additional measurements of superimposed ice thickness are necessary to validate model predictions. Ideally, a method which allows superimposed ice thickness to be monitored at regular intervals throughout the melt season, and which does not disturb the overlying snowpack, should be used.

6.43 Surface Energy Balance Modelling

There are several ways in which surface energy balance simulations could be improved. The first is to develop a method for predicting snowdepth variations across the catchment. Terrain analysis used to classify representative terrain features across the glacier may be compared with snowdepth measurements to determine whether similar terrain features have similar snow depths. If so, terrain features may be used to parameterize snow depth variations across the catchment, so that spot measurements of snowdepth may be extrapolated to areas where measurements were not made. It may also be possible to

simulate other processes responsible for the accumulation or redistribution of snow, such as wind scour and drifting, which could also be modelled according to surface topography.

Variations in meteorological parameters across the catchment should be modelled in a more realistic fashion than in the current approach, which assumes a linear change in all meteorological measurements between the automatic weather stations. Additional meteorological measurements at locations other than the automatic weather stations may provide a basis for dividing the glacier into zones with similar characteristics. For example, upper exposed areas of the glacier could be classified into a zone of high wind speed, whereas lower sheltered areas could be classified into a zone of low wind speed.

6.44 Degree-Day Modelling

A more accurate parameterization of effective grain size variations would not only improve surface albedo simulations, it would also improve predictions of variable degree-day factors. Additional meteorological datasets from John Evans Glacier may reveal a relationship between degree-day factors and temperature, concurrent with the findings of Braithwaite (1994). Meteorological data should be collected from areas on the glacier where superimposed ice and glacier ice are exposed for a long enough period of time to determine appropriate positive degree-day values for these surface types.

6.45 Model Validation

A difficulty in this study has been the proper validation of model predictions. Its intrinsically problematic to compare an areally averaged model output with a point stake measurement, due to the large range in predicted specific balances across a given elevation band. In the future it may be more useful to plot a range of specific balances for a given elevation band against point specific balance measurements.

Degree-day and energy balance models could be validated with greater confidence if a higher density of ablation stake measurements were made across the glacier. More accurate mass balance measurements could help in deciding whether differences between model predictions and observations are entirely due to model deficiencies, as is generally

assumed, or whether they are caused by measurement errors or lack of measurements.

6.5 References

Braithwaite, R.J. 1994. Positive degree-day factors for ablation on the Greenland Ice Sheet studied by energy-balance modelling. *Journal of Glaciology*, 40(135): 153-160.

Grenfell, T.C., Warren, S.G. and Mullen, P.C. 1994. Reflection of solar radiation by the Antarctic snow surface at ultraviolet, visible, and near-infrared wavelengths. *Journal of Geophysical Research*. 99(D9): 18,669-18,684.

Knap, W.H. and Oerlemans, J. 1996. The surface albedo of the Greenland ice sheet: satellite-derived and in situ measurements in the Søndre Strømfjord area during the 1991 melt season. *Journal of Glaciology*. 42(141): 364-374.

Munro, D.S. 1990. Comparison of melt energy computations and ablatometer measurements on melting ice and snow. *Arctic and Alpine Research*. 22(2): 153-162.

Reeh, N. 1991. Parameterization of melt rate and surface temperature on the Greenland Ice Sheet. *Polarforschung*, 59(3): 113-128.

Paterson, W.S.B. 1994. The Physics of Glaciers. Pergamon Press, 250 p.

Wiscombe, W.J. and Warren, S.G. 1980. A model for the spectral albedo of snow. I: Pure snow. *Journal of the Atmospheric Sciences*. 37(12): 2712-2733.

Woodward, J. 1995. Superimposed ice and glacier mass balance. *Unpublished M.Sc. Thesis*. University of Alberta. 96p.